

School of Civil and Mechanical Engineering

**Development of representative volumetric element
method for analysis of interlocking brick system**

Tingwei Shi

0000-0001-5094-7057

This thesis is presented for the Degree of

Doctor of Philosophy

of

Curtin University

May 2023

Declaration

To the best of my knowledge and belief this thesis contains no material previously published by any other person except where due acknowledgment has been made.

This thesis contains no material which has been accepted for the award of any other degree or diploma in any university.

Signature:

Date: 21/07/2023

Abstract

Masonry structure is one of the most popular structural forms all over the world especially for low-rise buildings. Conventional masonry structure is made of mortar and bricks. Due to the relatively low strength of mortar, damage always initiates in the mortar or the interfaces between bricks and mortar when subjected to shear loading. Therefore, mortar-less masonry construction with interlocking bricks have gradually attracted much attention because of their advantages, such as improving the construction efficiency, reducing labour cost, and providing better mechanical performance.

Different interlocking bricks have been developed which nevertheless are mostly designed to provide easy alignment only. The effect of interlocking mechanism on the mechanical performance of interlocking bricks is not utilized. The mechanical performance of interlocking bricks with large shear keys have rarely been thoroughly investigated. Moreover, for dry-stacking interlocking bricks, the contacts between adjacent bricks are complex. Imperfections inevitably exist on bricks owing to imperfect manufacture, construction quality control and construction error, as well as minor damages caused during transportation. It is necessary to properly understand the effect of small gaps between bricks due to imperfections that are randomly distributed over the masonry wall on the loading capacity of the wall. Last but not the least, when analysing and designing interlocking brick structures, conventional numerical modelling method using detailed modelling approach requires very large amount of computational resource; there needs a suitable numerical approach with improved simulation efficiency and acceptable accuracy.

In response to the above challenges, this thesis employs experimental and numerical approaches to study the fundamental mechanical properties of a new type of interlocking bricks, to investigate the influence of brick imperfections using statistical analysis methods, and to develop a new numerical modelling method using

representative volumetric element method. This thesis consists of the following parts:

In Part 1, the compressive properties and shear properties of interlocking bricks are studied. Laboratory compressive tests are performed on interlocking brick prisms made of different numbers of bricks. A detailed numerical model of interlocking brick prisms is generated and validated with lab testing data. Intensive parametric study is then carried out to quantify the influence of brick number, brick material strength, etc. An empirical design formula is generated to predict the compressive strength of interlocking bricks. A semi-analytical formula is also derived to estimate the axial stiffness of interlocking brick prisms. Experimental and numerical simulation are then conducted to investigate the shear capacity of the interlocking prism. The effects of axial pre-compression, concrete strength, surface roughness and friction coefficient between the neighbouring interlocking bricks are investigated through parametric numerical analysis. Similarly, an empirical design formula is derived to predict the shear strength of interlocking brick prisms.

Part 2 of this thesis investigates the influence of brick imperfection on mechanical properties of interlocking brick wall. Detailed numerical models of interlocking brick walls with spatially varying imperfections are simulated. Stochastic analysis is carried out to predict the compressive properties of interlocking brick walls with spatially varying randomly distributed brick imperfections. Monte-Carlo analysis is performed. The number of brick imperfections is assumed to follow the Binominal distribution in massive brick production process, where the probability of imperfection is categorized according to the manufacturing quality, i.e., high-quality, high-medium, medium-low, and low-quality, using the stratified sampling method. The imperfection sizes are assumed to follow truncated normal distribution. Based on these hypotheses, the damage and crack development mechanism of interlocking brick walls with different imperfection distributions are investigated. The influences of imperfection size and its coefficient of variation (COV) on the compressive strength, equivalent compressive

stiffness and linear stiffness of interlocking brick walls are discussed.

Part 3 develops a representative volumetric element method for analysis of interlocking brick systems. A representative volume element (RVE) is extracted from interlocking brick walls on the basis of periodic construction patterns. Detailed numerical modelling of the RVE and simulations are carried out considering the nonlinear material properties and different stress states. The equivalent material properties of the RVE are derived from the numerical simulation results. Compressive and tensile damage scalars according to the theory of continuum damage mechanics are used to analyse the hardening behaviour, the softening behaviour, and the failure of the RVE. To verify the obtained equivalent material properties, interlocking brick walls modelled with the homogenized material properties subjected to the uniaxial compressive loading and the combined compression-shear loading are analysed. The results are compared with those obtained from the detailed modelling of the interlocking brick wall. The accuracy and the efficiency of using the derived equivalent material properties in modelling the interlocking brick wall are demonstrated. Furthermore, this part also explores the application of the homogenization technique for dry-stacking interlocking brick structures under blast loading, such as TNT and gas explosions. The developed approach, which takes into account the nonlinear material properties and strain rate effects, is found to yield reliable modeling accuracy with reduced computational resources. In brief, the outcomes of this research provide insights into the mechanical properties of the dry-stacking interlocking structures made of the interlocking bricks. The outputs derived from this thesis can provide suggestions for the analysis of interlocking brick system using the representative volumetric element method.

Acknowledgement

First and foremost, I would like to thank my esteemed supervisors Professor Hong Hao and Dr Xihong Zhang for all their guidance and help during my PhD journey.

I would like to thank and acknowledge the group members in the Centre for Infrastructural Monitoring and Protection (CIMP) at Curtin University, including Dr Cheng Yuan, Dr. Haoran Zhuo, Mr Guanyu Xie, Mr Chong Chen, Mr Liuliang Cui for assisting with the numerical modelling and experimental test during my PhD study. I am also thankful to Dr Hexin Jin and Dr Zhijie Huang for their comments and suggestions.

I acknowledge the financial support from the Australian Research Council (ARC) and Tetraloc Pty Ltd under ARC Linkage Project LP170100846 to carry out the research. I also gratefully acknowledge the financial support from Curtin International Postgraduate Research Scholarship (CIPRS) to support my PhD study.

Last but not least, I would like to express my deepest gratitude to my parents, for unconditional love and support.

List of published work and work prepared for publication

The list of published paper and work prepared for publications, with the full bibliographic citations in the thesis, are listed below.

Shi T, Zhang X, Hao H, Chen C. Experimental and numerical investigation on the compressive properties of interlocking blocks. *Engineering Structures*, 2021, 228: 111561.

Shi T, Zhang X, Hao H, Xie G. Experimental and numerical studies of the shear resistance capacities of interlocking blocks. *Journal of Building Engineering*, 2021, 44: 103230.

Shi T, Zhang X, Hao H, Xie G. Influences of Random Imperfection Distribution on the Compressive Properties of Interlocking Brick Wall. (Accepted)

Shi T, Zhang X, Hao H, Xie G. Numerical Derivation of Homogenized Constitutional Relation for Masonry Wall Made of Mortar-less Interlocking Bricks. (Under review)

Shi T, Zhang X, Hao H, Xie G. Numerical Derivation of Homogenized Constitutional Relation for Masonry Wall Made of Mortar-less Interlocking Bricks under Dynamic Loading. (Under review)

List of relevant additional publications

The additional publications relevant to the thesis but not forming part of it with the bibliographical details are listed below.

(None)

Statement of contribution of others

The work presented in this thesis was primarily conducted by the PhD candidate, Tingwei Shi, which include developing numerical simulation, conducting analytical analysis, carrying out experimental test, analysing results and preparing the manuscripts. Contributions by others are described as follows. The signed contribution forms are attached in the appendix.

Chapter 3

Prof. Hong Hao and Dr. Xihong Zhang defined the scope of the experimental tests, revised the manuscript and provided intellectual input towards data analysis and discussion of the results. Mr. Chong Chen helped with the experiments at Curtin University. The financial support was provided by Australian Research Council via LP170100846.

Chapter 4

Prof. Hong Hao and Dr. Xihong Zhang defined the scope of the experimental tests, revised the manuscript and provided intellectual input towards data analysis and discussion of the results. Mr. Guanyu Xie helped with the numerical modelling at Curtin University. The financial support was provided by Australian Research Council via LP170100846.

Chapter 5

Prof. Hong Hao and Dr. Xihong Zhang revised the manuscript and provided intellectual input towards data analysis and discussion of the results. Mr. Guanyu Xie helped with the numerical modelling at Curtin University. The financial support was provided by Australian Research Council via LP170100846.

Chapter 6

Prof. Hong Hao and Dr. Xihong Zhang contributed to the revision of the manuscript,

offering intellectual insights for data analysis and result discussions. Guanyu Xie assisted with numerical modeling at Curtin University. The research was financially supported by the Australian Research Council through grant LP170100846.

Chapter 7

Prof. Hong Hao and Dr. Xihong Zhang played key roles in revising the manuscript, providing valuable input for data analysis and discussions of the findings. At Curtin University, Guanyu Xie offered support in the area of numerical modeling. Financial backing for this research was generously provided by the Australian Research Council via grant LP170100846.

Table of Contents

Declaration	I
Abstract	II
Acknowledgement.....	V
List of published work and work prepared for publication.....	VI
List of relevant additional publications.....	VII
Statement of contribution of others.....	VIII
Table of Contents	X
List of Figures	XV
List of Tables.....	XXI
Chapter 1 Introduction	1
1.1 Background	1
1.2 Research objective.....	2
1.3 Research outline	3
Chapter 2 Literature review	5
2.1 Introduction	5
2.2 Fundamental mechanical properties and influencing factors.....	6
2.2.1 Mechanical performances of masonry.....	6
2.2.2 Shear properties	7
2.3 Rough surface.....	10
2.3.1 The influence of geometric imperfection	11
2.3.2 The influence of contact behaviour	12
2.4 Stochastic analysis of masonry structure response	13
2.5 Numerical modeling approaches for masonry structure	15
2.6 Dynamic brick material properties	16
2.7 Summary	18
Chapter 3 Experimental and numerical investigation on the compressive properties of	

interlocking blocks	20
3.1 Introduction	20
3.2 Interlocking bricks.....	21
3.2.1 Brick configuration.....	21
3.2.2 Theoretical compressive strength	21
3.3 Experimental investigation.....	24
3.3.1 Material property test.....	24
3.3.2 Prism test	25
3.4 Numerical modelling.....	27
3.4.1 Material model.....	28
3.4.2 Model details	30
3.4.3 Convergence study	30
3.4.4 Contact algorithm	31
3.5 Results and analysis	35
3.5.1 Force-displacement curves	35
3.5.2 Crack propagation.....	38
3.5.3 Failure modes	41
3.6 Parametric study	42
3.6.1 Effect of block number	43
3.6.2 Effect of brick surface roughness amplitude	44
3.6.3 Effect of material strength	45
3.6.4 Modified design formula for compressive strength.....	46
3.6.5 Semi-empirical method for prism compressive stiffness	48
3.7 Summary	50
Chapter 4 Experimental and Numerical Studies of the Shear Resistance Capacities of Interlocking Blocks	52
4.1 Introduction	52
4.2 Laboratory tests	52

4.2.1	Material property	53
4.2.2	Shear test setup	53
4.3	Numerical Simulation	55
4.3.1	Model details	55
4.3.2	Material model.....	56
4.3.3	Contact algorithm	57
4.4	Results and Analysis.....	59
4.4.1	Load-displacement curves	59
4.4.2	Failure mode and crack propagation	62
4.4.3	Stress distribution and crack evolution.....	64
4.4.4	Shear capacity.....	66
4.4.5	Comparison with design formula	68
4.5	Parametric study	70
4.5.1	Effects of axial pre-compression and concrete strength	71
4.5.2	Effect of surface roughness and friction coefficient.....	72
4.6	Empirical Formula.....	75
4.6.1	Material failure model	75
4.6.2	Modified design formula	77
4.7	Summary	79
Chapter 5 Influences of Random Imperfection Distribution on the Compressive Properties of Interlocking Brick Wall		
		81
5.1	Introduction	81
5.2	Numerical Model.....	81
5.2.1	Brick configuration.....	81
5.2.2	Finite element model	82
5.2.3	Model validation.....	84
5.2.4	Size effect	86
5.3	Probabilistic Models.....	87

5.3.1 Brick and joint imperfection.....	88
5.3.2 Stochastic analysis with Monte-Carlo simulation	89
5.3.3 Convergence study	91
5.4 Crack Development and Failure Mode	92
5.4.1 Cracking pattern	92
5.4.2 Initial crack and crack development in a wall	94
5.4.3 Failure mode	97
5.5 Results and Analysis.....	99
5.5.1 Stress-strain curves	99
5.5.2 Compressive strength and probability distribution.....	103
5.5.3 Equivalent stiffness and probability distribution.....	107
5.5.4 Linear stiffness and probability distribution.....	111
5.6 Conclusion.....	114
Chapter 6 Numerical Derivation of Homogenized Constitutional Relation for Masonry Wall Made of Mortar-less Interlocking Bricks	117
6.1 Introduction	117
6.2 Methodology	117
6.3 Numerical Modelling of Interlocking Bricks	119
6.3.1 Material model.....	119
6.3.2 Contact properties.....	120
6.3.3 Mesh convergence study	121
6.4 Numerical Results of RVE	123
6.4.1 Stress-strain curves under different stress states	123
6.4.2 Equivalent material properties of RVE.....	129
6.4.2.1 Elastic properties	129
6.5 Size Effect and Model Validation.....	137
6.5.1 Size effect	137
6.5.2 Model validation.....	139

6.6 Summary	144
Chapter 7 Numerical Derivation of Homogenized Constitutional Relation of Mortarless Interlocking Brick Wall for Dynamic Response Prediction.....	146
7.1 Introduction	146
7.2 Numerical Modelling	146
7.2.1 Material model.....	147
7.2.2 Strain rate effect.....	148
7.2.3 Contact model.....	149
7.2.4 Mesh convergence	149
7.3 Numerical Results	150
7.3.1 Stress-strain relations.....	150
7.3.2 Derivation of equivalent properties	157
7.4 Model Validation	168
7.4.1 TNT explosion.....	169
7.4.2 Gas explosion loading	174
7.4.2.2 Two-way wall	176
7.5 Summary	178
Chapter 8 Conclusions and Recommendations.....	180
8.1 Main findings	180
8.2 Recommendations	184
References	186
Appendix I Interlocking shear resistance model.....	200
Appendix II Statement of contribution of co-authors	206
Appendix III Copyright Clearance.....	208

List of Figures

Figure 3-1. Configuration of interlocking blocks.	21
Figure 3-2. Illustration of force analysis of a fundamental unit.....	22
Figure 3-3. Material properties.	25
Figure 3-4. Compressive test setup for 2-block prism.	26
Figure 3-5. Typical damage-to-failure progress of 1-block prism: (i) tensile wing cracks initiate; (ii) cracks extend from key and propagate downwards; (iii) crack coalescence; (iv) more cracks occur near the contact region	26
Figure 3-6. Comparison of experimental and analytical compressive loads.	27
Figure 3-7. Time histories of reaction force and inertia force.....	29
Figure 3-8. Surface roughness examination and modelling.....	33
Figure 3-9. Results of the roughness surface	34
Figure 3-10. Load-displacement curves from laboratory test and numerical simulation.	38
Figure 3-11. Prism crack initiation and development in the experiments and numerical simulations.	41
Figure 3-12. Comparison of prism damage modes.	42
Figure 3-13. Ultimate compressive strength for interlocking brick prisms with different numbers of brick.	44
Figure 3-14. Ultimate compressive strength for interlocking brick prisms with different roughness amplitudes.	45
Figure 3-15. Ultimate compressive strength for interlocking brick prisms with different material strength.....	46
Figure 3-16. a) Comparison of the prism compressive strength estimated from the	

proposed formula and the test and the numerical results; b) predictions of different compressive strengths of interlocking imperfection prisms.....	47
Figure 3-17. The equivalent vertical stiffness of the interlocking prism.	48
Figure 3-18. Equivalent compressive stiffness of interlocking brick prisms.....	50
Figure 4-1. Determination of brick material properties.	53
Figure 4-2. Experimental and numerical models for the prism shear test	55
Figure 4-3. Definitions of concrete damage plasticity (CDP) model [53].....	57
Figure 4-4. Evaluation of brick surface roughness.	59
Figure 4-5. Load-displacement curves from numerical simulation and laboratory test.	61
Figure 4-6. Comparison of prism damage modes between numerical modelling and laboratory test.....	63
Figure 4-7. Prism cracks evolution in the numerical simulations and experiments (Specimen 2 under 10 kN axial pre-compression).....	64
Figure 4-8. Crack evolution of prism stress contours.	65
Figure 4-9. Load analysis for the wedging action on interlocking bricks.....	67
Figure 4-10. Relationships between a) prism equivalent shear strength with axial compressive stress; b) prism equivalent shear strength with concrete strength. 72	
Figure 4-11. Effect of surface friction coefficient on a) shear load-displacement curves and b) peak shear load and initial stiffness.	73
Figure 4-12. Shear load versus displacement curves for interlocking brick with different surface roughness (a) under 10kN axial pre-compression; (b) 20 kN pre-compression; (c) 30 kN pre-compression; (d) 40 kN pre-compression.	74
Figure 4-13. Effect of the surface roughness on (a) peak shear load; and (b) initial	

stiffness.	74
Figure 4-14. Coefficient C ₁ with respect to different geometries of interlocking key	76
Figure 4-15. Coefficient C ₂ with varying material strength.....	77
Figure 4-16. Comparison between different design models.	79
Figure 5-1. Configuration of interlocking blocks.	82
Figure 5-2. Experimental setup and numerical model	84
Figure 5-3. Comparison of compressive force versus axial displacement curves from laboratory test and numerical modelling.....	85
Figure 5-4. Comparison of prism damage and failure patterns.....	86
Figure 5-5. Influences of size effect.....	87
Figure 5-6. Illustration of interlocking wall with random spatial imperfections.	89
Figure 5-7. Convergence of Monte-Carlo simulations	92
Figure 5-8. Crack patterns for interlocking brick with different imperfections.....	94
Figure 5-9. Initial crack and load path at the stage of OA	97
Figure 5-10. Damage contours of interlocking brick wall at peak compressive loads	99
Figure 5-11. Stress-strain curves of interlocking brick walls with spatially varying imperfections.....	103
Figure 5-12. Distribution of wall compressive strengths corresponding to different COVs of brick imperfections	105
Figure 5-13. Histograms of compressive strength for interlocking walls.....	107
Figure 5-14. The definition of equivalent stiffness and linear stiffness.....	109

Figure 5-15. Distribution of wall equivalent stiffness corresponding to the different COVs of brick imperfection size distributions.....	109
Figure 5-16. Histograms of equivalent stiffness for interlocking brick walls.....	111
Figure 5-17. Distribution of wall linear stiffness corresponding to different COVs of brick imperfection size distributions.....	112
Figure 5-18. Histograms of linear stiffness for interlocking walls	114
Figure 6-1. Configuration of interlocking brick.....	118
Figure 6-2. Homogenization of an interlocking wall.....	119
Figure 6-3. Uniaxial compressive and tensile behaviors of brick material in the CDP model.....	120
Figure 6-4. Mesh convergence study	123
Figure 6-5. Stress-strain relations under compression-compression loadings.....	126
Figure 6-6. Stress-strain relations under compression-tension and tension-tension loadings	128
Figure 6-7. Stress-strain relations of RVE under compression-shear loadings.....	129
Figure 6-8. Biaxial failure envelope in plane stress space	131
Figure 6-9. Failure surface in the deviatoric and meridian planes.....	132
Figure 6-10. a) The plastic potential in the meridian plane; and b) confined uniaxial stress-strain relations under different pressures in the Y-direction	133
Figure 6-11. Stress-strain relations of the RVE under uniaxial stress states a) compression; b) tension.....	135
Figure 6-12. Material damage based on the continuum damage mechanics theory [191-193]	136
Figure 6-13. Models for examining the size effect	138

Figure 6-14. Size effect of the RVE	139
Figure 6-15. Result comparison of mesh dependence study	141
Figure 6-16. Comparison of stress-strain curves of the homogenization method and the detailed modelling method for the interlocking brick wall under uniaxial compression	142
Figure 6-17. Comparison of shear stress-strain curves of the homogenization method and the detailed modelling method for the interlocking brick wall under compression-shear loading.....	143
Figure 6-18. Comparison of damage contours of the homogenization method and the detailed modelling method for the interlocking brick wall under compression- shear loading	144
Figure 7-1. Uniaxial compressive and tensile behaviors of brick material in the CDP model.....	148
Figure 7-2. Uniaxial stress-strain curve of brick.....	149
Figure 7-3. Mesh convergence study	150
Figure 7-4. Stress-strain curves of RVE under uniaxial compressions	151
Figure 7-5. Stress-strain curves under uniaxial tension	152
Figure 7-6. Stress-strain curves under shear loading	153
Figure 7-7. Stress-strain curves under biaxial compression.....	154
Figure 7-8. Stress-strain curves under compression with two constraints	155
Figure 7-9. Stress-strain curves under bi-axial compression with constraint	156
Figure 7-10. Stress-strain curves under triaxial loading	157
Figure 7-11. Biaxial failure envelope in plane stress space for different strain rates	159

Figure 7-12. Failure surface in the deviatoric and meridian planes	160
Figure 7-13. DIF of a) uniaxial compressive strength; and b) uniaxial tensile strength	161
Figure 7-14. Stress-strain relations of the RVE under uniaxial stress states a) compression; b) tension.....	165
Figure 7-15. An overview of the interlocking brick wall models	169
Figure 7-16. Illustration of interlocking brick wall under TNT explosion (Case 2)	170
Figure 7-17. Comparison of damage contours under 40kg TNT at 5m stand-off distance.....	172
Figure 7-18. Comparison of damage contours under 10kg TNT at 1m stand-off distance.....	173
Figure 7-19. Recorded pressure-time histories [195].....	175
Figure 7-20. Comparison of damage contours and central displacement time histories for one-way wall under gas explosion	176
Figure 7-21. Comparison of damage contours and central displacement time histories for two-way wall under gas explosion	178

List of Tables

Table 3-1. Brick material properties.....	29
Table 3-2. Material constants for the CDP model in Abaqus	29
Table 3-3. Mesh size convergence study	30
Table 3-4. Properties of interface	35
Table 4-1. Material properties of interlocking brick	57
Table 4-2. Material constants of concrete damage plasticity model	57
Table 4-3. The results obtained from the shear tests	68
Table 4-4. Comparison of shear capacities between laboratory testing results, numerical modeling and existing empirical and design formulae	70
Table 5-1. Material properties of interlocking brick	83
Table 5-2. Summary of wall compressive strengths from Monte-Carlo analysis	105
Table 5-3. Summary of wall equivalent compressive stiffness from Monte-Carlo analysis.....	109
Table 5-4. Summary of wall linear stiffness from Monte-Carlo analysis	112
Table 7-1. Information of selected tests [195]	174

CHAPTER 1 INTRODUCTION

1.1 Background

Masonry structure is one of the most predominate structure forms throughout the world particularly for low-rising residential structures. This is mainly because of its relatively low cost comparing with reinforce concrete and steel structures, outstanding thermal and sound insulation performance, and robust structural performance in comparison to timber and other structural forms. Conventional masonry construction comprises of clay bricks bonded together by a layer of mortar or cementitious material. Because of the relatively low strength of mortar, failure in conventional masonry structures always initiates in the mortar or at the bonding interfaces with bricks. As a result, masonry structures made of conventional bricks normally exhibit poor structural performance particularly against extreme loading conditions such as earthquake, impact and blast loading [1, 2]. The structure quality and construction efficiency are very much dependent on the performance of brick layers.

Considering the above deficiencies, the advancements of masonry structure in the past decades include (but not exclusively) introducing thin-bed or mortar-less (dry stacking) construction methods to improve construction efficiency, and using interlocking bricks to replace conventional plain bricks in order to improve structure mechanical performance. Combining the above features, dry stacking interlocking masonry blocks could lead to significant reductions in construction time, minimization of labour cost, and increasing the shear resistance [3, 4], and improvement in construction quality [5-8], which therefore have attracted much interests from the construction industry. Various types of interlocking bricks have been developed to improve construction efficiency and quality [8-16]. Anand and Ramamurthy compiled the development of available interlocking bricks [17]. It was reported that the production rate with interlocking brick could be 2.5~5 times higher than conventional

brick, and 60%~80% labour saving during construction by employing different interlocking bricks [18]. Apart from the great construction efficiency that can be achieved by using interlocking bricks, construction quality as well as the demand of brick layers' skill could be substantially reduced as the interlocking mechanism of bricks can help to ensure alignment, robustness and strength requirement. This feature was also found to suit particularly to most rural areas where skilled labours for conventional brick construction are in short which may lead to shabby masonry structures especially facing nature disasters [19].

1.2 Research objective

The objective of this study is to quantify the fundamental mechanical properties of interlocking bricks of a particular design and to develop a numerical analysis method using representative volumetric element. To achieve the objective, numerical simulations, analytical analyses, and experimental tests are carried out. The detailed scopes of works are included as follows:

- (1) To examine the fundamental mechanical properties of interlocking bricks under uniaxial compression and direct shear loading.
- (2) To carry out numerical modelling and perform parametric study to investigate the performance of structures constructed with interlocking bricks.
- (3) To study the influence of brick surface roughness condition on the performance of dry-stacking interlocking bricks.
- (4) To develop a Representative Volumetric Element (RVE) model for interlocking bricks.
- (5) To study the influence of element size effect and structural effect on the modeling accuracy of RVE for interlocking bricks under quasi-static and dynamic loading conditions.

1.3 Research outline

There are eight chapters in this thesis. The outline of this thesis is presented as follows:

Chapter 1 presents the background, research objective, and research outline.

Chapter 2 reviews the existing relevant studies.

Chapter 3 investigates the compressive properties of interlocking brick prism based on the analytical analysis, laboratory testing and numerical modelling. Different methods are used and compared for modelling the interlocking brick prism. A semi-empirical formula based on fracture mechanics theory is derived to predict the compressive strength of interlocking brick prisms.

In Chapter 4, analytical derivation, laboratory testing and numerical modelling are carried out to investigate the shear properties of interlocking brick prism. Different modelling methods are used and compared for modelling the interlocking brick prism. An empirical design formula is proposed for prediction of the shear strength of the interlocking brick.

In Chapter 5, Monte-Carlo simulations are conducted to investigate the influence of spatially varying randomly distributed brick imperfections on the compressive behaviour of dry-stacking interlocking brick walls. The crack pattern and load path of interlocking brick walls under different imperfection distributions are studied; the influences of the mean value and discreteness of imperfection sizes on the compressive strength and stiffness of the interlocking brick wall are quantified.

In Chapter 6, a representative volume element (RVE) is extracted from dry-stacking interlocking brick walls based on their periodic construction patterns. The equivalent material properties of the RVE, considering the nonlinear behaviour and damage evolution, are then derived under various stress states based on continuum damage mechanics. Finally, comparisons are made through examining the numerically modelled interlocking brick wall responses using the developed RVEs with the equivalent

material model and detailed interlocking brick models. The accuracy and computation efficiency of the RVE model in predicting the behaviour of interlocking brick walls are assessed.

In Chapter 7, similar to above utilizing the periodic construction pattern, a representative volume element (RVE) of interlocking brick is developed with consideration of strain rate effect for modeling wall dynamic response. The equivalent material properties of the RVE is determined via numerical modeling of various stress states and different strain rates. Nonlinear material properties are considered, where the hardening and softening behavior of the RVE are expressed using compressive and tensile damage scalars based on continuum damage mechanics theory. To validate the accuracy and appropriateness of the derived equivalent material properties, the responses of interlocking brick walls subjected to both solid explosive blast and gas explosion loading are modeled employing the RVE element and homogenized material properties. A comparison of the results with a detailed numerical model of the interlocking brick wall reveals that the proposed homogenization technique offers reliable modeling accuracy while significantly reducing computational demands.

Chapter 8 concludes the findings of this thesis, and provides recommendations for future research.

CHAPTER 2 LITERATURE REVIEW

2.1 Introduction

Mortar-less (dry-stacking) block allows masonry units being laid without using any mortar layers. The elimination of mortar obviously reduces material cost and enables cold weather construction to proceed through the winter months with much less elaborated requirements for weather protection. Dry-stacking method could also eliminate the problem of shrinkage cracking in concrete masonry units, and most important of all it requires much less skilled and experienced labour forces which can be a major advantage in light of the shortage of skilled labours. It also increases the productivity and speed of construction. All of these advantages translate into a greater economic benefit, while maintaining the inherent characteristics of masonry construction [20-22]. The mechanical performance of dry-stacking masonry blocks is also largely influenced by the joints between neighbouring bricks. For mortar-free interlocking brick system, the interlocking blocks could move slightly when it is subjected to in-plane shear load. This relative movement could help to improve energy dissipation capacity of the brick system under lateral loads. The lack of bedding mortar also removes the lateral tensile stresses in masonry blocks, which initiates early splitting at a low stress level when masonry is subjected to axial compression [23]. Interlocking bricks have been developed to improve the structural performance and ease construction. The introduction of shear keys could improve the shear resistance capacity at the brick joints. Because of the shear keys, interlocking blocks could exhibit better self-centring capacity after the applied shear force is removed. Combining the above advantages of interlocking bricks and mortarless construction thus is very attractive. However, since the interlocking mechanism of mortar-less connection differs significantly from conventional mortar connection, the current understandings about the mechanical behaviour of the conventional masonry structures could not be simply adopted to analyse and design the masonry structures

with interlocking bricks. In this chapter, fundamental mechanical properties of interlocking structure are reviewed, including compressive properties and shear properties, and the factors that influence the capacities of interlocking structures. In addition, the influences of imperfection of the interlocking bricks on the performance of dry-stacking interlocking brick structures are reviewed. Existing stochastic analysis on the response of masonry structures are reviewed. Moreover, popularly used numerical modelling approaches are summarized with focus on homogenization techniques applied into masonry structures. Last but not least, dynamic material properties for brick materials are also reviewed for derivation of homogenized material properties of interlocking bricks under dynamic loading.

2.2 Fundamental mechanical properties and influencing factors

2.2.1 Mechanical performances of masonry

Different interlocking mechanisms were introduced over the past few years. The interlocking mechanism can be provided in either horizontal, vertical or both directions. Plate-like assemblies of tetrahedral or osteomorphic bricks were also proposed in recent studies [4]. The mechanical performances of bricks with different interconnections were experimentally investigated by different researchers. For example, with direct shear tests on interlocking bricks comprising two shallow truncated cones, Sturm et al. [6] proved the effectiveness of shear key in improving the shear resistance capacity. It shall be noted that most current designs of interlocking brick systems are featured with small shear keys for construction easiness. Because the projection area of the shear tenon is relatively small, the shear resistance between interlocking blocks is therefore not significantly improved [24]. Faidra et al. [25] investigated interlocking assemblies of glass components with imperfect contacts. It was found that the osteomorphic blocks showed good multifunctionality and the dry-

stacked glass columns could still carry a considerable amount of compressive load after some of the components were broken. Recently, some researchers carried out preliminary tests on interlocking connections with large tenon and mortise to improve the shear resistance. Damages to the tips of tenon and mortise were observed when the bricks were under low axial compression; complete breakage of tenons was found when the applied axial force was large [26, 27]. The influence of interlocking connection on brick axial loading capacity was also studied, mainly by experimental tests [28, 29]. Some researchers found low axial loading capacity of interlocking bricks because of the relatively small contact area due to joint imperfection [30, 31]. Crack and failure of stacked pier with interlocking bricks initiated from the mortise of the connection due to lateral expansion and stress concentration [23, 32-34]. Studies on the flexural bending capacity of interlocking brick are rare because without axial pre-compression, no bending resistance could be provided by mortar-less interlocking bricks. Some preliminary laboratory tests found that when prestress was applied, similar flexural bending capacity was reported as compared to conventional brick with prestress [35]. There is still a lack of systematic study on the mechanical properties of interlocking brick structures.

2.2.2 Shear properties

The effect of interlocking connection on brick compressive load bearing capacity has been investigated primarily through experimental methods [28, 29, 36-40]. Some researchers reported low compressive load bearing capacity of interlocking bricks due to the relatively small contact area because of joint imperfection [30, 41]. Apart from compressive capacity, the shear mechanisms of brick with different interconnections have also been studied and reported [5, 6, 17, 23, 32, 33, 42-44], which nevertheless are mostly for validation of particular products. It shall also be worth noting that most current structures comprised of interlocking bricks are characterized by small shear keys for easiness in construction, i.e., easy alignment. The shear tenons do not

remarkably improve the shear resistance of these bricks since the projection area of the keys is relatively small [24]. Recently some laboratory tests were conducted on interlocking bricks with large shear keys. Total shear off failure was found on these interlocking bricks under large axial force; and damages to the tips of the keys were discovered under low axial compression [26, 45]. Besides, recent studies by Zhang et al. [46, 47] also observed damages induced by stress concentration at shear keys of segmented columns comprised of concrete blocks with shear keys under impact and cyclic loading, which reduced column load bearing capacity against impact and seismic load. Apart from the above studies on the performances of particular designs by different researchers, the mechanical properties of interlocking brick still needs comprehensive studies.

2.2.2.1 The influence of interlocking mechanism

Various types of interlocking mechanism have been developed to improve the capacity of the interlocking bricks [48-50]. Ahmed and Aziz found that dry joints with multiple keys performed better than single key without epoxy, because multiple keys enable uniform stress transfer between adjacent bricks and thus lead to better mechanical performance [51]. Although increasing the number of interlocking keys improves the shear capacity of joints, the equivalent shear capacity of mortar-less joints with multiple keys is less than that of mortar-less joints with single key. For example, Alcalde et al. [52] analysed the fracture behaviour of mortar-less keyed joints subjected to shear load, and found that the averaged shear strength decreased with the increase in the number of keys, because the keys failed sequentially. Nevertheless, this effect became less apparent as the axial prestress increased to 3.0 MPa. Because a higher normal compressive stress increased the friction resistance and improved the integrity of the key group. Similar results were observed by Zhou et al. [53] and Jiang et al. [54]. Moreover, changing the key geometry may also greatly influence the shear performance of keyed joints [55]. Zhang et al. [56] examined the direct shear

resistances of four different shaped shear keys and concluded that they have very different shear resistance capacity and shear stiffness because of the difference in shear flow mechanism of different shaped shear keys.

2.2.2.2 The influence of contact surfaces

For dry interlocking joints, surface roughness condition could strongly influence the shear performance of keyed joints [36, 41, 63, 64]. Martínez et al. [38] found that the uneven surface despite small could change stress distribution at the interface, and therefore affect contact pressure. Fan et al. [65] studied the contact behaviour of rock and observed both shear failure and friction failure modes, which are influenced by surface roughness condition. These previous studies indicated that for mortar-less masonry construction, surface roughness condition at the joint could significantly influence the mechanical performance, which are also proved by some recent studies on mortar-less masonry prisms [66-68]. However, the influence of the surface roughness on the shear capacity has not been properly studied. It is critical for engineering application to appropriately investigate the effect of contact surface on the failure modes, as well as stress concentration in the dry-stacking masonry constructions. To investigate the effect of contact surface roughness, different methods have been applied to model rough contact surfaces. For example, Bahaaddini [69] employed discrete element method to reproduce the shear behaviour of saw-tooth triangular joints. Homogenization of the random rough surface into regular rough surface has also been a popular approach for modelling rough steel surface [70, 71]. The study of influences and modelling approaches of rough concrete and brick surface is very limited.

2.2.2.3 Shear capacity prediction formulae

Different formulae for prediction of ultimate shear capacity of interlocking joints have been proposed, where the difference could be substantial [51]. Some researchers proposed theoretical derivation [72, 73], while others derived empirical formulae

based on laboratory testing and numerical modelling data [57, 74, 75]. Most popularly used design codes such as AASHTO [76] assume the shear force is transferred through the interlocking joint by both the shear key and the surface friction [49]. Some researchers evaluated the accuracy of AASHTO method in prediction of the shear resistance capacity of different keyed joints. For example, Ahmed and Aziz [77] carried out direct shear test to study the shear behaviour of mortar-less connections with single and multiple keys. It was found that the AASHTO design formula could conservatively predict the shear strength of joints with single key, but overestimate the shear strength of mortar-less connection with multiple keys. Similar results were also reported by Zhou et al. [53]. However, opposite conclusion was reported by Jiang et al. [54] who found AASHTO method underestimated the shear load of joints with single key made of steel fibre reinforced concrete (SFRC) but more accurately predicted that of three-keyed dry joints. For interlocking brick comprising multiple keys, the accuracy of AASHTO and other prediction methods are not known yet.

2.3 Rough surface

Imperfection unavoidably exists in dry-stacked interlocking bricks resulted from brick manufacturing error/tolerance and the quality of workmanship. Unlike traditional masonry constructions, the imperfections on brick surfaces are remedied by mortar that joins the adjacent bricks. The imperfections of bricks in mortar-less masonry structure result in gaps between interlocking bricks, which affect the structural strength, stiffness, and deformation capacities. Therefore, the influences of imperfections on the performances of interlocking brick structures should be investigated. Moreover, as the mechanical properties depend on the design of interlocking keys, which varies from one design to another. There is no design standard or recommended practice for the design of mortar-less interlocking brick wall in engineering applications yet. Since the imperfections affect the loading capacity and stiffness of the wall, it is necessary to properly evaluate the influence of imperfection on interlocking brick structures

constructed with the mortar-less method.

2.3.1 The influence of geometric imperfection

The mechanical performance of dry-stacking masonry blocks is largely influenced by the geometric imperfection of the blocks as a result of the contact surface imperfection [31, 63, 64]. Since clay bricks are normally manufactured in kiln, the high temperature burning of extruded clay mixture process leads to irregular brick surface topography and unit height difference (irregular surface topology) of up to a few millimetres. For conventional brick-laying method with thick mortar layer (approximately 10 mm), the effects of brick height difference and irregular surface topography at the connections can be moderated by mortar. For mortar-less method, the influence of brick geometric imperfection on its mechanical properties cannot be ignored. Casapulla and Portioli [78] experimentally investigated the contact behaviour at the interface between dry-stacked masonry blocks, and found the joint behaviour of two rough blocks passing over each other was strongly dependent on surface roughness. Agaajani [64] discovered that the height of manufactured blocks followed a Gauss statistical distribution, which thereby caused an indubitably height variation when blocks are aligned in a wall. Jaafar et al. [31] examined the height difference (± 0.25 mm) of a batch of blocks from local major brick manufacturers and conducted compressive tests on dry-stacking brick prisms. It was found that the difference of compressive displacement at different locations in the same plane section of the prism can be up to 0.90 mm. This is mainly due to variation in the behaviour of contact at the dry joints. This difference in compressive displacement could result in internal shear stress which reduces prism compressive strength. Despite the absolute value of surface imperfection appears to be small, these imperfections on the joints could lead to stress concentration in the block connections and therefore decrease the ultimate load-carrying capacity of a masonry system.

2.3.2 The influence of contact behaviour

The contact behaviour at the interface between dry-stacked masonry blocks is also affected by the micro-scale phenomena, including cohesion, contact pressure and friction [24, 30, 57, 79-81]. Bosro et al. [82] modelled the interface properties between the blocks using the surface-to-surface contact with a friction coefficient of 0.603. Ayed et al. [30] used the Coulomb friction criterion to describe the interface failure between blocks through the numerical model, which considered the linear elastic behaviour of the material and ignored the material non-linear behaviour. Zahra and Dhanasekar [79] generated a micro-scale finite element model to simulate the rough surfaces of the dry-stacking interface by adjusting the location of the nodal coordinate and assigning rock properties to the peaks at the bed joints. Several other researchers [33, 83-86] also emphasised that the ultimate load-carrying capacity of a dry-stacking masonry prism was significantly dependent on the extent of imperfection at the dry interface. Jaafar et al. [13] found that contacting behaviour between the dry joints of interlocking bricks presented nonlinear progressive closure when the wall was subjected to gradually increased compressive load. Some studies investigated the contact behaviour of dry-stacking bricks, and examined its influence on the overall behaviour of masonry systems [87]. For example, Zahra et al. [88] used matrix based tactile surface sensors (MBTSS) to obtain the contact area and contact pressure of the dry-stacking brick prism under compression. Rekik et al. [28] employed non-contact digital image correlation (DIC) technique to ascertain both the contact area and the contact pressure. Zahra et al. [88] used carbon paper image imprints to trace the loading increments, and each imprint was then analysed to find out the contact surface area. The contact surface of mortar-less brick system was also simplified into a two-dimensional numerical model by some researchers [29, 89, 90]. However, the simplified 2D model could not capture cracks occurring out of the plane. Ngapeya et al. [1] generated a 3D model of dry-stacking blocks, and studied the influence of block height imperfection on the axial load-carrying capacity of prism. Comparison was also

made between analytical approaches and finite element analysis results. Mousavian and Casapulla [91] extended the limit analysis method with a concave contact model for the interlocking interfaces to the design of structurally feasible assemblages of interlocking blocks. These above studies demonstrated that for dry-stacking masonry construction, block geometric imperfection caused by surface topography and brick height variation could lead to significant mechanical performance variation [66-68]. Nevertheless, previous studies only considered non-spatial variability of imperfections in which the same imperfection was assumed throughout the brick pier/wall. This simplification apparently would not properly represent the real condition of brick structures, where the size of imperfection of each brick unit varies; the locations of these imperfections also vary across the structure [41]. Therefore, a proper study that considers the random spatial variations of imperfection of each brick and location within a structure should be performed.

2.4 Stochastic analysis of masonry structure response

Stochastic analysis has been commonly used to investigate the influences of random variables on structural performance of masonry structures [92-94]. For example, the influence of material uncertainties on the axial compressive strength of masonry wallets was investigated through probability analysis based on Monte-Carlo simulations [95]. Stewart and Lawrence [96] generated a probabilistic model to assess the structural reliability of masonry walls subjected to concentrically compressive loading considering variations in mortar type, live-to-dead load ratio, brick material compressive strength and tributary area. The accuracy of design code, i.e., the Australian masonry design code AS3700-2001 [97], was examined based on the reliability analysis. Existence of spatial variability of brick joint flexural bond-wrench strengths was also studied using stochastic analysis. For example, the influence of spatial correlation among unit brick joint flexural bond-wrench strengths was experimentally studied by Heffler et al. [98]. It was found that the flexural bond-

wrench strength of each brick unit is statistically independent of its neighbouring unit. Li et al. [99] found that there are obvious differences between spatial and non-spatial analysis of the flexural bond-wrench strength of brick wall in terms of wall performance and failure mode. Non-spatial simulation was found to overestimate the mean of wall compressive strength compared with spatial simulation. Some previous studies also investigated the influence of workmanship quality on the strength of masonry structures [100, 101]. For instance, Stewart and Lawrence [101] studied the effect of workmanship quality, discretising of masonry unit thickness and wall width on the reliability index, which concluded that the structural reliabilities were very susceptible to these above factors. Martínez et al. [38] discussed the impacts of random variation in the rough surfaces of brick. Shi et al. [102] investigated that the compressive behavior of interlocking prisms comprised of interlocking block with non-spatially varied imperfections. No seating effect was observed in the numerical simulation. Ngapeya et al. [1] estimated the load bearing capacity considering the height imperfection of each brick. It was found that the height imperfection of individual brick plays a critical role in the failure mechanism and the load bearing performance of a dry-stacked brick wall subjected to compressive load. This is because the height imperfection controls the actual contacting area between the neighbouring masonry courses, and thus it dominates the load percolation system in the wall. Gooch et al. [103] established numerical modellings, which were found to overestimate the elastic stiffness of masonry structures as compared to laboratory testing results. Therefore, it is necessary to properly understand and interpret the numerical modelling results. Till now, only very few studies investigated the structural performance of dry-stacked interlocking structures with consideration of the spatial variation of imperfections. Critical structure performance factors such as the stiffness and compressive strength of dry-stacked interlocking brick wall are not understood well yet.

2.5 Numerical modeling approaches for masonry structure

Finite element (FE) method is predominately employed for modelling masonry structures. Methods for modelling masonry structures using FE method can be divided into three categories: (i) micro-modelling method (direct simulation), where brick units, mortar, and brick/mortar interfaces are modelled in detail. It enables the observation of localized damage of brick, mortar and joint [104-106]. Since this method always involves a large number of elements, it is very time consuming and therefore is not well applicable to large scale structures; (ii) simplified micro-modelling method, where the brick units are simulated as continuum elements while mortar joints as well as brick/mortar interfaces are lumped and modelled using surface contact algorithms [107-110]. This is because the bricks are much stiffer than the mortar and joints. Comparing with the detailed micro-modelling method, the simplified method is less computational resource demanding; (iii) macro-modelling method, where representative element is employed and assumed as a homogeneous material to model the brick structure. Macro-modelling method is regarded as a transition from the micro-scale detailed material modelling to structural-scale modelling according to the homogenization theory. Many homogenization techniques are applied to model masonry structures due to the periodic layouts and properties. For example, representative volume elements (RVE) are extracted from large-scale masonry structures for derivation of the homogenized macro material properties of the masonry [111].

Pande et al. [112] were probably the first group of researchers who attempted to homogenise a masonry structure, and proposed a two-step homogenization scheme: firstly, the masonry bricks and vertical mortar joints are homogenised in the horizontal direction. The RVE is further homogenised in the vertical direction considering the horizontal joints. Choudhury et al. [113] carried out numerical modelling to analyse three masonry shear walls with different opening configurations based on the two-step

homogenization approach. It was found that the homogenization method could reasonably predict the global response and crack patterns of the masonry walls. Based on the homogenisation technique, the close-form expressions of the governing equilibrium equations for masonry structures were proposed [114-116]. It assumes the various constituents to compose a set of homogeneous interconnected units simulated by classic elasticity theory [117, 118]. Gabor et al. [119] applied this technique to obtain the elastic properties of the homogenized RVE. Wu et al. [120] inherited the above method and applied it to hollow concrete block masonry. It was then used to model the response of hollow concrete block masonry subjected to blast loading [121]. Ma et al. [122] derived the two-dimensional RVE for masonry structures with nonlinear inelastic constitutive properties, where the strength envelope and the damage rule of RVE were derived. Wei and Hao [123] integrated this method to include strain rate effects and implemented it in the commercial software LS-DYNA as a user-defined subroutine for efficiently simulating masonry wall responses subjected to blast loads. Peng et al. [124] generated a RVE for masonry structures with a Drucker-Prager (DP) strength envelope for the homogenized model, and performed shear-compression experiments to verify the accuracy of the developed RVE. Silva et al. [125] also developed an RVE for masonry structures to determine the curvature-bending moment relationships. The numerical modelling results were found to agree well with the experimental results. However, this method is only suitable for masonry structures subjected to out-of-plane loadings [126]. It should be noted that RVEs developed in previous studies are based on conventional masonry structures [127, 128].

2.6 Dynamic brick material properties

With the above-mentioned approaches, various researchers have performed numerical modelling to predict the response of brick structures under blast loading. For instance, Wu and Hao [129] developed a three-dimensional homogenized constitutive model for conventional mortar-bonded masonry by applying various stress states to the three-

dimensional representative volume element (RVE) and applied this homogenized constitutive model to the simulation of a masonry wall subjected to blast loads, obtaining results close to those of the detailed numerical model. As the static material properties may exhibit an increase in strength in response to high strain rates [130]. Similarly, Hashemi Rafsanjani [131] proposed a novel strain rate dependent anisotropic continuum model, which can be used for simulating masonry structures. This composite plasticity model has been implemented as a user-defined subroutine in the ABAQUS finite element code, employing 3D solid elements to simulate masonry behavior. Recently, Sahli et al. [132] developed a homogenized constitutive model for mortarless interlocking masonry. However, the shear key of the considered interlocking blocks used in the latter study was small, providing mainly alignment in construction but limited shear resistance of the masonry structure. Moreover, the study focused on the applicability of the developed homogenised constitutive model for mortarless interlocking masonry structures under seismic loads, where strain rate effect is not crucial.

To accurately simulate brick wall response under blast loading, it is necessary to properly account for dynamic material properties of brick materials. There is limited research on dynamic properties of brick materials, where discrepancies could be found among the testing results. Dynamic increase factor (DIF) of bricks is generally from 1.2 to 3.0 for compressive strength and above 3 for tensile strength. Larcher et al. [133] conducted Split-Hopkinson Pressure Bar test on bricks and found DIF of 1.38 at a strain rate of about 190s^{-1} . Hao and Tarasov [134] carried out quasi-static and dynamic impact test using a triaxial dynamic testing machine. The unconfined compressive strengths of clay bricks at strain rates between $2.1 \times 10^{-6}\text{s}^{-1}$ and 160s^{-1} were determined. Zhang et al. [135, 136] conducted a series of dynamic tests using SHPB tests to reveal the dynamic compressive and tensile properties of clay bricks. Empirical relations of DIF for both brick compressive and tensile strengths were derived. Till now, there is no study in the literature yet to derive the homogenized material properties for mortar-

less interlocking brick structures under dynamic loading considering the strain rate effect.

2.7 Summary

This chapter presents a comprehensive literature review on the fundamental mechanical properties and influencing factors of masonry structure made from interlocking bricks, the effect of rough surfaces, stochastic analysis of masonry structure response, numerical modeling approaches for simulating masonry structure, and dynamic brick material properties. The research gaps are identified as follows.

(1) In the previous studies, different researchers investigated compressive and shear properties of masonry structures, as well as the influencing factors on the performance of masonry structures, e.g., the influence of various types of joints, the influence of axial pre-compression, the influence of contact surfaces and various method to predict shear capacity. However, there is no systematic study to investigate compressive properties and shear mechanism of dry-stacking masonry structures made from interlocking bricks. Empirical formulae are also desired to predict compressive capacity and shear capacity of interlocking structures for engineering application.

(2) Due to the difficulty in the assessment of the contact between dry-stacking interlocking bricks, various assessment methods of imperfections and numerical methods for simulating imperfections have been observed in the previous studies. However, very limited attention has been paid to interpreting the performance of contacts between dry-stacking interlocking bricks including stress-strain curves, stiffness and compressive strength using stochastic method. Moreover, the influencing factors, e.g., the numbers of imperfections and the size of imperfections, on the compressive strength of interlocking structures should be quantified. There is a research gap in the probability-based analysis to quantify the influence of imperfections on the behavior of dry-stacking interlocking brick structures.

(3) Due to complicated contact, nonlinear material properties and complicated stress state and failure between neighbouring bricks, detailed numerical modelling is very time-consuming and inefficient. Existing studies developed RVEs for conventional masonry structures; there is a research gap on study of dry-stacking masonry wall made of interlocking bricks using the representative volumetric element method. Therefore, it is essential to develop RVE of dry-stacking interlocking masonry wall for efficient numerical modelling of interlocking masonry structures under different loadings.

CHAPTER 3 EXPERIMENTAL AND NUMERICAL INVESTIGATION ON THE COMPRESSIVE PROPERTIES OF INTERLOCKING BLOCKS

3.1 Introduction

As reviewed in Chapter 2, existing interlocking bricks are mostly designed to provide easy alignment only. The effect of interlocking mechanism on the mechanical performance of the interlocking block is not well investigated. In this chapter, laboratory tests and numerical simulations are performed to quantify the compressive properties of a new type of interlocking brick featured with large shear keys. The theoretical compressive strength of a unit interlocking brick prism is derived using fracture mechanics theory, which is validated with laboratory compressive test. Then, tests are conducted to investigate the influence of brick numbers on prism compressive strength. Detailed 3D numerical models of interlocking brick prisms are generated using ABAQUS and validated with experimental test results. The damage modes and localised stress concentration of the interlocking bricks are numerically and experimentally studied. Parametric study is then carried out to quantify the influences of different design parameters including the number of bricks, brick surface roughness amplitude (due to brick manufacturing tolerance and surface unevenness), and material strength. The analytical formula is modified through the numerical simulation and experimental results to predict the compressive capacity of interlocking brick prisms. A semi-empirical prediction method is also derived to predict the axial stiffness of the interlocking brick prism for use in design analysis of masonry structures made of mortar-less interlocking bricks.

The related work in this chapter has been published in Engineering Structures.

Shi T, Zhang X, Hao H, et al. *Experimental and numerical investigation on the compressive properties of interlocking blocks*[J]. *Engineering Structures*, 2021, 228: 111561.

<https://doi.org/10.1016/j.engstruct.2020.111561>

3.2 Interlocking bricks

3.2.1 Brick configuration

Figure 3-1 illustrates the configuration of the interlocking blocks of dimension 200 mm × 180 mm × 100 mm (length × height × thickness). As shown, the blocks have large protruded mortise and tenon of dimension 35 mm length × 30 mm height × 35 mm thickness. This is different from other existing interlocking blocks that usually have small keys primarily for alignment only rather than resisting shear force. The tenons are inclined, which enable the assembled blocks to slide under lateral loading. The blocks are made of cement, sand and gravel through high pressure moulding, therefore have concrete-like constitutive properties.

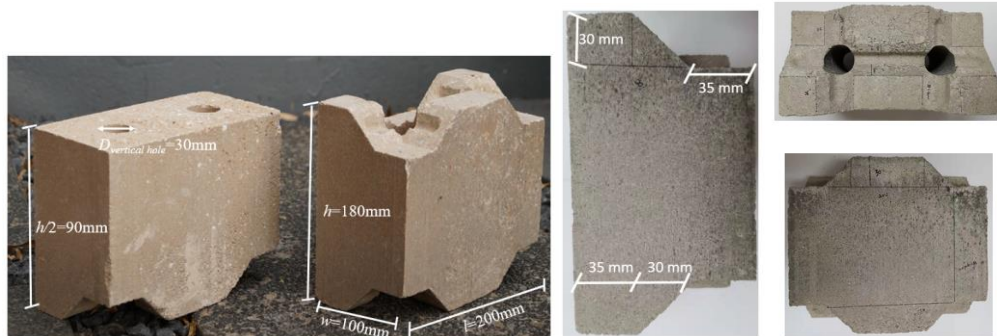


Figure 3-1. Configuration of interlocking blocks.

3.2.2 Theoretical compressive strength

With the introduction of interlocking keys to the joint, the compressive load-carrying capacity of brick prisms made of interlocking bricks could be influenced. Fracture mechanics theory is employed to analyse the compressive strength of interlocking brick prism. A one-block prism comprising of a full interlocking brick and

two half bricks as shown in Figure 3-2 is taken as the fundamental unit for analysis here.

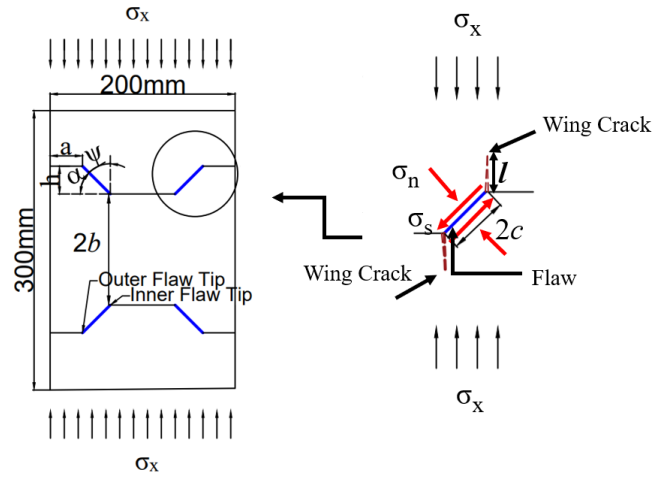


Figure 3-2. Illustration of force analysis of a fundamental unit.

The compressive force on the prism produces vertical stress across the interlocking joint. When acting on the inclined section of the shear key ($2c$), the vertical stress can be decomposed to a normal and a shear component as shown in Figure 3-2, delamination could be triggered due to the normal component. Taking this delamination as a ‘pre-existing’ flaw, a shear crack could further develop at its tips, whose faces slide under shear stress $\tau = \sigma_x(\sin\alpha\cos\alpha - \tan\phi\cos^2\alpha)$, where σ_x is the compressive stress, and the expression represents the shear stress induced on the plane of the contact interface minus the frictional stress (cohesion is ignored) [4]. If the effective shear stress is high enough to endure the frictional stress along the closed inclined interlocking key, the frictional sliding will result in tensile stress concentrations at the flaw tips of the interlocking key, therefore trigger the initiation and propagation of the wing cracks that are mainly induced by a high shear stress concentration in the bridge area and coalescence [137, 138]. For the one-block prism shown in Figure 3-2, there are four flaws on the front elevation view of the prism. According to the hypothesis proposed by Wong and Chau [139], the ultimate strength of flawed specimens is not influenced by the total number of pre-existing flaws, but

only by the geometric shape of the interlocking brick. The total stress intensity factor K_I for the growth of wing cracks can be expressed as:

$$\frac{K_I}{\sigma_x \sqrt{\pi c}} = \frac{(\sin 2\psi - \mu + \mu \cos 2\psi)}{(1 + L)^{\frac{3}{2}}} \left[0.23L + \frac{1}{\sqrt{3}(1 + L)^{\frac{1}{2}}} \right] + \left[\frac{2\varepsilon_0(L + \cos\psi)}{\pi} \right]^{\frac{1}{2}} \quad (3-1)$$

where ψ is the angle calculated from the σ_x -direction to the direction along the flaw surface (i.e. $\psi=90^\circ-\alpha$), $2c$ denotes the length of the pre-existing flaw, $L=l/c$ stands for the normalized length of the wing cracks (l denotes the length of the growth of wing crack), μ is the frictional coefficient along the frictional or shear flaw, and the flaw density ε_0 is measured from Nc^2/A (N is defined as the number of flaw for a unit area A). Wing cracks initiate when $K_I=K_{IC}$, where K_{IC} denotes the fracture toughness of the material of the brick [4, 140]. And hence the maximum compressive strength σ_x^{\max} of a flawed prism can be expressed as:

$$\sigma_1^{\max} = \frac{K_{IC}}{\sqrt{\pi c}} \left\{ \frac{[\sin 2\psi - \mu + \mu \cos 2\psi]}{(1 + L_{cr})^{\frac{3}{2}}} \times \left[0.23L_{cr} + \frac{1}{\sqrt{3}(1 + L_{cr})^{\frac{1}{2}}} \right] + \left[\frac{2\varepsilon_0(L_{cr} + \cos\psi)}{\pi} \right]^{\frac{1}{2}} \right\}^{-1} \quad (3-2)$$

where K_{IC} denotes the fracture toughness [139, 141] (0.5784 MPa \sqrt{m} for the material), $L_{cr}=l_{\max}/c$ (l_{\max} is defined as the peak possible value for the length of the coalesced wing cracks, and $2b$ means the distance between the two flaws). In this paper, the initial flaw density of the prism containing four flaws is $\varepsilon_0=0.03$ ($\varepsilon_0=Nc^2/A$ denotes that $N=4$, $A=0.2\text{m} \times 0.3\text{m}$ and $c=0.0212\text{ m}$). Using Eq. (3-2) the compressive strength of the unit interlocking brick is calculated to be 6.43 MPa, which corresponds to 119.59 kN for this 1-block prism.

As illustrated in Eq. (3-2), the theoretical compressive strength for interlocking prism comprising of multiple bricks would be identical because the flaw density ε_0 is

the same for one-block and multiple-block prisms. However, this may not necessarily be true because brick prisms comprising of more bricks have more interlocking joints, which could weaken the compressive load-carrying capacity. Laboratory test is conducted to validate the above theoretical derivation. Tests are extended from 1-block prism to 2-block and 4-block prisms in Section 3.

3.3 Experimental investigation

Laboratory testing results are presented in this section. Firstly, the material properties for the interlocking bricks are quantified. Then, uniaxial compressive tests are carried out on 1-block interlocking brick prism to verify the above analytical solution. Tests are then extended to 2-block and 4-block prisms to further verify the accuracy and suitability of the above solution.

3.3.1 Material property test

To characterize the compressive properties of the brick material, uniaxial unconfined compressive tests are carried out using a SHIMADZU-50 machine. Three 50 mm diameter by 100 mm length specimens are core-drilled from the bricks and finely grinded on both ends (see Figure 3-3a). Strain gauges are glued on the specimens to measure the axial strain. Following ASTM C140 [142], unconfined uniaxial compressive test is conducted at a constant speed of 0.03 mm/s using displacement control method. Figure 3-3b) shows the measured compressive stress-strain curves, where the stress is defined as the measured axial force divided by the specimen cross-

sectional area, and the strain is recorded using the strain gauges.

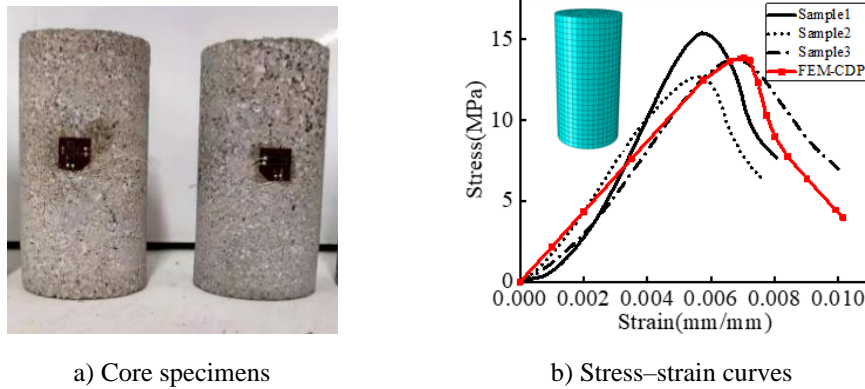


Figure 3-3. Material properties.

3.3.2 Prism test

Brick prisms comprising of one block, two blocks and four blocks are tested under uniaxial compression. The prisms are built by stacking the blocks on top of each other without mortar. Brick prism compressive tests are conducted with reference to EN1052-1 [143]. It is worth noting that there is no testing or design standard available yet for interlocking brick.

SHIMADZU-300 Universal Testing System at Curtin University is used for the compressive test. A stiff steel plate (150 mm ×300 mm ×20 mm) is used to distribute the compressive load from the loading platen to the prisms. A constant loading rate of 0.03 mm/s is applied through the loading platen to the brick prism specimens. Two laser LVDTs (linear variable differential transducers) are installed at the two sides of the brick prisms to measure the compressive displacements of the prisms during testing. The averaged values measured from two laser LVDTs are taken as the compressive displacement. The compressive load is monitored by a load cell embedded in the loading machine. A typical prism set-up is shown in Figure 3-4 (2-block prism). Three specimens for each type of prisms are tested.

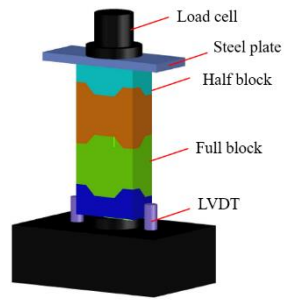


Figure 3-4. Compressive test setup for 2-block prism.

3.3.2.1 Failure modes

Figure 3-5 shows the typical compressive failure process of the 1-block prism. The initial crack appears at the inner flaw tip of the concaved shear keys of the central brick at approximately 80% of its peak load, which propagates downwards with the increase in compressive load. This is consistent with the theoretical assumption and formation of wing crack (Figure 3-2) in Section 2. The crack develops into crack coalescence till the peak load is reached. Then more cracks appear both in the central brick of the top convex interlocking key. The cracks continue to develop until the applied load is stopped.

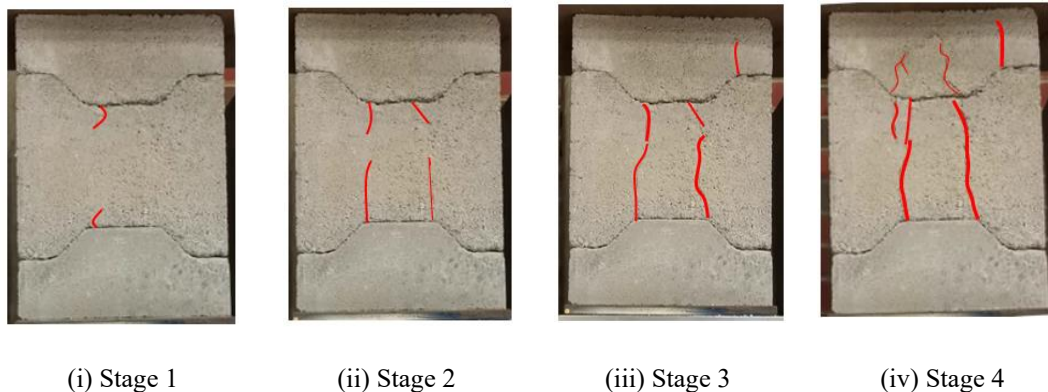


Figure 3-5. Typical damage-to-failure progress of 1-block prism: (i) tensile wing cracks initiate; (ii) cracks extend from key and propagate downwards; (iii) crack coalescence; (iv) more cracks occur near the contact region

3.3.2.2 Compressive load-carrying capacity

Figure 3-6 summarizes the ultimate compressive load-carrying capacities of the 1-block, 2-block and 4-block prisms. The theoretical predictions are also included for

comparison. An averaged compressive capacity of 128.3 kN is measured for the 1-block prism, which is very close to the theoretical prediction of 119.59 kN. It is apparent that the compressive capacity of the interlocking brick prism decreases with the increased number of blocks, indicating the compressive strength of interlocking blocks is influenced by the number of blocks. For example, an averaged compressive capacity of the 2-block prisms is 108.5 kN, and that of the 4-block prisms is 102.9 kN. This is because the increased number of interlocking joints introduces more weak sections for the prisms. The theoretical prediction is based on the analysis of 1-block prism, therefore could not take this into consideration, hence results in a +10.22% and +16.22% overestimation of loading capacities of the 2-block and 4-block prisms, respectively. Considering more bricks in the theoretical derivation is not straightforward because of more weak sections and flaws. In the subsequent sections, numerical models of prisms with different number of bricks are developed, and numerical analyses are carried out to investigate the influences of the number of bricks on the load-carrying capacities of interlocking masonry blocks.

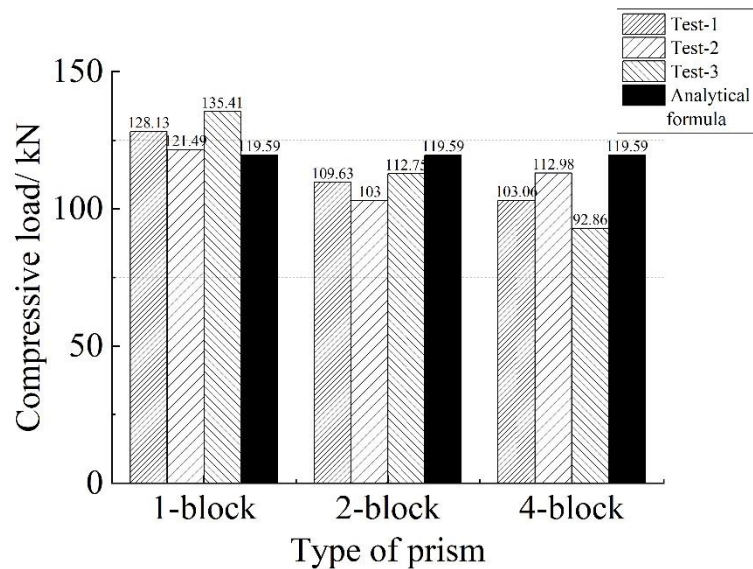


Figure 3-6. Comparison of experimental and analytical compressive loads.

3.4 Numerical modelling

To better understand the behaviour of interlocking bricks and facilitate further

parametric study, detailed three-dimensional numerical models of interlocking brick prisms are generated. The models are used to simulate the laboratory tests and the results are compared with those recorded in the tests to verify the accuracy of the numerical model. The material model is firstly described, followed by the details of the numerical models of the interlocking prisms. As discussed above, contacts between interlocking bricks affect the performances of mortar-less masonry blocks made of interlocking bricks, which are not straightforward to be accurately modelled. To investigate the modelling accuracy and efficiency, three different contact methods are used and compared. The numerical results are presented and compared with the laboratory testing results.

3.4.1 Material model

The commercial software ABAQUS [144] is used in this study. To simulate the nonlinear behaviour and damage of the interlocking prisms, the concrete damage plasticity (CDP) model proposed by Lubliner et al. [145] to predict the behaviour of concrete and other brittle materials is used. Crushing in compression or cracks in tension from micro- to macro-levels can both be modelled. CDP model assumes that the uniaxial compressive and tensile failures of the material are characterized by damaged plasticity (see Figure 3-7). Material hardening and softening behaviour can also be incorporated by this model.

The compressive strength, tensile strength, initial Young's modulus and the relationship between stress and strain are defined. The compressive strength of the material is obtained from the material tests presented above. The initial Young's modulus is taken as a secant modulus and is measured from the slope at a stress extent equal to 40% of the ultimate compressive strength. Poisson's ratio is determined at the same extent of the stress, which is obtained by the ratio of the transversal strain over the longitudinal strain. The material properties adopted for the interlocking blocks are given in Table 3-1, where E_0 is the initial Young's modulus; ν is the Poisson's ratio;

and f_t is the tensile strength. The tensile strength is obtained as $f_t=0.1f_c$, which is a relation often used for concrete material [38, 146].

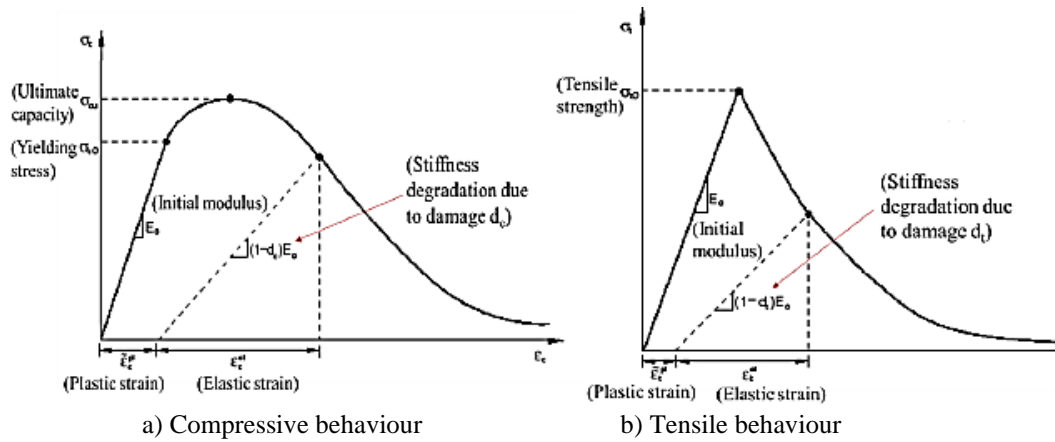


Figure 3-7. Time histories of reaction force and inertia force.

Table 3-1. Brick material properties.

Mass density (kg/m ³)	Elasticity		Plasticity				Viscosity Parameter
	Initial Young's modulus, E_0 (MPa)	Poisson's ratio ν	Dilatation angle ψ (°)	Eccentricity	Biaxial stress ratio f_{b0}/f_{c0}	K	
2565	2184.58	0.2	35	0.1	1.16	0.65	5E-5

Note: K is the ratio between the second stress invariant on the tensile meridian and compressive meridian at initial yield.

Table 3-2. Material constants for the CDP model in Abaqus

Compressive behaviour		Tensile behaviour	
Yield stress (MPa)	Inelastic strain	Yield stress (MPa)	Cracking strain
12.74	0	1.38	0
13.78	0.0003	1.24	0.0012
13.05	0.0015	1.19	0.0014
10.81	0.0034	1.14	0.0016
8.64	0.0052	1.09	0.0018
7.10	0.0067	0.80	0.0030
1	0.0200	0.56	0.0040

To evaluate the accuracy of the model and material parameters, uniaxial compression tests on the 50 mm length by 100 mm diameter core specimen is numerically modelled. As shown in Figure 3-3b), the column is meshed with solid element of size 4 mm × 4 mm × 4 mm in longitudinal, transverse and thickness direction respectively, and the material parameters are presented in Table 3-2. As

shown in Figure 3-3b, the stress-strain curve from the numerical results (as highlighted in the red curve – FEM-CDP) agrees reasonably well with the laboratory testing results.

3.4.2 Model details

Three-dimensional models of the interlocking brick prisms with solid elements are generated to model the interlocking block prisms. The C3D8R type element (3D 8-node linear with reduced integration) is selected which is an eight-node solid element with three translational degrees of freedom per node. The reduced integration is calculated by the incorporation of the lower-order rigidity of the unit, while the distributed loads and the mass matrix are determined by full integration. This element can be used to improve the calculation efficiency, and to obtain more accurate stress fields and displacements. For the interlocking brick prism, the axial and horizontal degrees of freedom at the base are restrained, whereas the nodes of the top block are restrained to prevent lateral movements and vertical movement is allowed. Displacement control loading method is used, which follows the loading method used in the tests. Nonlinear analysis is used in the numerical modelling.

3.4.3 Convergence study

Mesh convergence study is conducted by gradually reducing the mesh size from 56 mm to 3.5 mm. As shown in Table 3-3, further reducing mesh size from 7 mm to 3.5 mm yields minor changes in the computed maximum peak compressive force but the computational time increases substantially. Therefore, 7 mm mesh size is adopted for the numerical model in this study.

Table 3-3. Mesh size convergence study

Mesh size (mm × mm × mm)	Peak compressive force (kN)
56 × 56 × 56	177.82
28 × 28 × 28	152.27
14 × 14 × 14	138.81
7 × 7 × 7	118.29
3.5 × 3.5 × 3.5	112.46

3.4.4 Contact algorithm

Three different modelling methods, i.e. perfect contact, imperfect contact and cohesive element contact are considered herein to simulate the contact behaviour at the interlocking brick joints. The perfect contact is the fundamental method used by most engineers, which assumes the brick surfaces are smooth and in perfect contact condition with adjacent bricks. The imperfect contact method considers predefined gaps at the joint to model the imperfect surface condition of the brick. The cohesive contact method employs a cohesive element to deal with the non-linear behaviour at the joint. These three different types of contact model are detailed below:

3.4.4.1 Perfect contact

Perfect contact assumes the two surfaces of adjacent blocks match perfectly and ignore surface roughness condition. A contact pair is composed of the neighbouring contact surfaces, which can prevent penetration between the interlocking bricks. It provides a method for ensuring an appropriate transformation of forces between two interlocking bricks on the basis of tangential and normal contact behaviour. This study takes into account of both the normal contact behaviour, which dominates the penetration between the two interlocking bricks, and the tangential contact behaviour used to model sliding between adjacent bricks depending on the friction coefficient [147].

For tangential behaviour, the Mohr-Coulomb criterion is applied into the contact model. $\tau_{lim} = \mu\sigma + c_c$, where τ_{lim} denotes the limit for shear stress at which sliding starts, μ denotes the coefficient of friction, σ denotes the pressure of normal contact, and c_c denotes the cohesion of contact. There is no relative sliding between the contact surfaces before the tangential force reaches the critical shear stress, while the contact surface slides when the shear stress exceeds τ_{lim} . In this study, the friction coefficient is set to be 0.3 between the interlocking blocks and 0.15 between blocks and steel plates [38, 148], and for dry joints, contact cohesion is negligible ($c_c=0$) [149].

3.4.4.2 Imperfect contact

As discussed in the introduction, due to unavoidable manufacture error/tolerance and surface roughness, imperfect contact with small invisible gaps at the interfaces occurs most of the time between bricks. Rough surfaces involve lots of asperities (or valleys and peaks). For modelling the uneven surface roughness, the imperfection distributions existing in the interlocking blocks are firstly examined and quantified experimentally.

Experimental measurements of surface unevenness

Fifteen interlocking bricks are selected randomly from the same batch of bricks in this study. The experimental setup is illustrated in Figure 3-8a). The specimen is mounted on a flat table which provides a flat reference surface for measurement of imperfections. A surface height dial indicator is used to measure the absolute height of the brick surface along the key joint at 0.25 mm intervals along the section of the brick to map out the profile of the cross-section. As shown in Figure 3-8b), the mortises are surface S1, S5 and S6, and tenons are surface S2, S3 and S4. A total of 60 tenons and 30 mortises are measured. Figure 3-9 shows the surface unevenness measurement results. With respect to the lowest point of each surface, the asperity height varies from 0 mm to 0.2 mm for the mortise (S1,5,6), while tenons (S2,3,4) are rougher with the roughness amplitude varying from 0 mm to 0.3 mm with over 55% frequency of 0.1 mm. For a typical joint comprising of two interlocking blocks, to obtain the average gap length between the mortise and tenon, from the baseline of a brick (Figure 3-8b), the absolute roughness amplitudes from all measured points on each surface are averaged to obtain the average roughness amplitude of the surface. The average relative gap width Gap_2 between S2 and S5 can then be calculated as $Gap_2=h_5-h_2$, in which h_5 and h_2 are the average roughness amplitude of S5 and S2, respectively. Similarly, the average gap width between S1 and S4, and S6 and S3 can be calculated as $Gap_1=h_4-h_1$ and $Gap_3=h_6-h_3$, respectively. As shown in Figure 3-9, compared to the

Gap₁ and Gap₃ of the tenons, the Gap₂ could be ignored. Therefore, the S1 and S4 contact is assumed as perfect contact, hence it is idealized that there is no pointwise contact due to uneven surfaces. As illustrated in Figure 3-8c), once the joint is under compression, the compressive force will push the central gap between S1 and S4 to close, but leave a gap between S2 and S5, as well as S3 and S6. Therefore, an idealized imperfect contact model is generated with the central contact surfaces being fully closed but the two adjacent contact surfaces have a uniform gap of width 0.1 mm. The uniform gap width of 0.1 mm is an assumed value based on the measured roughness amplitude shown in Figure 3-9. Because the roughness profile on each brick surface is basically random, it is not possible to exactly model them in the numerical model, therefore simplification is made. In this study the gap width is based on the average roughness amplitudes measured from the brick surfaces. This simplification allows engineering assessment of the influence of surface unevenness in numerical simulations.

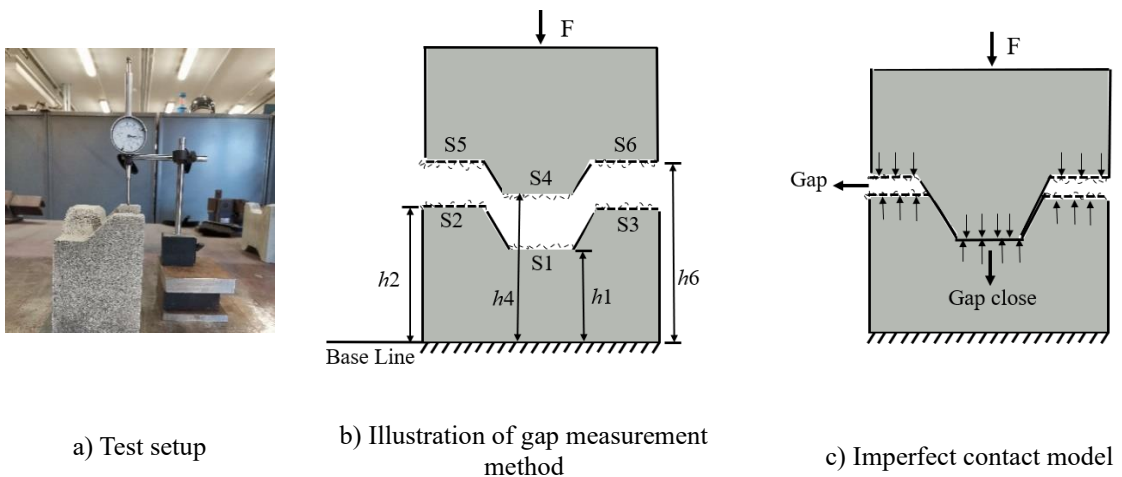
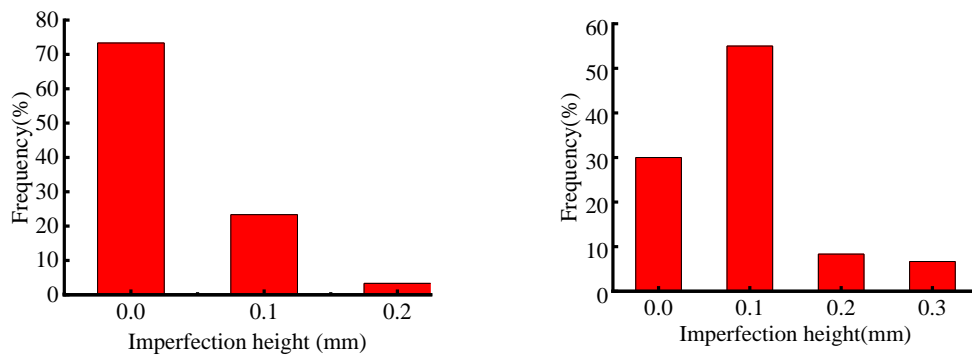


Figure 3-8. Surface roughness examination and modelling.



a) Mortise

b) Tenons

Figure 3-9. Results of the roughness surface

3.4.4.3 Cohesive contact

Cohesive element can be introduced to model the complex contact behaviour between two adjacent surfaces, whose stiffness could degrade after the pre-defined threshold criteria due to the shear and tensile deformations [81]. It enables the study of the cohesive behaviour and damage for the interlocking bricks to consider the surface unevenness and friction interaction.

In this study, a cohesive element of zero-thickness is used to model the interaction between two interlocking bricks. The constitutive model for the cohesive element employs the traction-separation law in ABAQUS. It assumes an initially linear elastic behaviour at the interface. As the compressive load increases and reaches the pre-defined stress, interface evolution and damages are triggered. Then, the friction model is activated which attributes to the shear stress [79]. The friction behaviour is modelled based on the Mohr-Coulomb failure criterion. The compressive stiffness is taken as 10 times that of the Young's modulus of the interlocking brick following reference [1]. The in-plane and out-of-the plane shear stiffnesses are taken as 0 since only the compression behaviour is considered. The maximum nominal stress for damage propagation is used here. The selected properties of interfaces available in the numerical simulation are tabulated in Table 3-4.

Table 3-4. Properties of interface

Interface Properties	Interface behaviour
Normal stiffness (N/mm)	21800
Shear stiffness (N/mm)	0
The coefficient of friction	0.3
Maximum tensile stress (MPa) [79]	0.68
Maximum shear stress (MPa)	0

3.5 Results and analysis

The laboratory testing results and numerical modelling results are presented in this section. Compressive force versus axial displacement curves, brick prism damage and failure modes, and ultimate compressive load-carrying capacity are compared and examined.

3.5.1 Force-displacement curves

Figure 3-10 shows the axial load-displacement curves for the 1-block, 2-block and 4-block prisms under compression. As shown, for the 1-block prism, the load increases slowly to about 20 kN at about 1.3 mm axial displacement, which is because of seating effect [38] that the gaps between the bricks close. As joints gradually close, the slope of the curve increases, and the compressive load also quickly rises almost linearly with displacement till the ultimate load at about 128 kN, after which it begins to drop, indicating the damage of the block. Among the three tested 1-block specimens, differences can be found in the force-displacement relations, which are because of the inherent variability at the interface of dry-stacking bed joints block and the variations between units in material properties [38]. Similar behaviour can be observed for the 2-block and 4-block prisms that the initial displacement for seating effect increases with the increase in the number of blocks hence the number of gaps. This is because asperity interactions at prism interfaces increase with the increase in the number of blocks. More asperities could be worn when more blocks are under compression. For the 4-block prisms, peak loads of about 100 kN are achieved at around 4mm displacement. Larger vertical displacements are observed on the 4-block prisms as compared to those of the 1-block and 2-block prisms. After reaching the peak load, the load quickly

decreases with further increased displacement.

Figure 3-10 compares the load-displacement curves of the numerical models using the above-mentioned three contact methods. Since the numerical model could not accurately represent the seating effect, their axial force-displacement curves are aligned with the experimental load-displacement curves after the initial gap is believed to be closed. It can be found that the numerical models with perfect and imperfect contacts could closely represent the stiffness of load-displacement curves after the gaps at the joints are fully closed as well as the ultimate compressive load. For example, for 1-block prisms the numerical load-displacement curves match the test curves relatively well if they are shifted by 1.3 mm, i.e., the initial seating displacement of the tested 1-block specimen. The compressive load increases almost linearly with displacement till about 80% of the ultimate strength, and then the stiffness begins to degrade indicating the damage of the brick. The predicted ultimate compressive loads with the three contact models, namely perfect contact model, imperfect contact model and cohesive model are 118.29 kN, 114.93 kN and 97.19 kN, respectively. The corresponding stiffnesses are 99.98 N/mm, 95.97 N/mm and 88.11 N/mm. As shown in Figure 3-10b) and 10c), as the number of brick increases, more apparent seating effect can be observed. The numerically modelled load-displacement curves for the 2-block and 4-block prisms are shifted by 1.5 mm and 2 mm respectively to align with the experimental curves. For the perfect and imperfect contact models, the load increases quickly to about 110 kN at about 3 mm axial displacement for the 2-block prism and about 105 kN at about 4 mm axial displacement for the 4-block prism. As shown, for the 2-block and 4-block prisms, the perfect contact model predicts a compressive stiffness of 71.18 N/mm and 44.71 N/mm, and the corresponding values from the imperfect contact model are 65.73 N/mm and 41.71 N/mm, respectively. The cohesive contact model gives the lowest compressive stiffnesses of 63.71 N/mm, 40.49 N/mm with the ultimate compression capacity of 93.96 kN and 91.67 kN, respectively. As shown in the above figures, the numerical models can reasonably well predict the

stiffness and ultimate load-bearing capacity of the masonry blocks, although they cannot simulate the process of asperities compaction from the initial surface contact to complete contact. Furthermore, the post-peak behaviour of the interlocking prisms cannot be fully modelled with the numerical methods which drops quicker and has less residual capacity in comparison to the laboratory test results. This is probably because of the material model used. Nevertheless, for design purpose since only compressive stiffness and ultimate compressive capacity are of primary interests, further modification of the numerical model to achieve better post peak behaviour is not conducted in this paper.

Through the above comparisons it can be found that the perfect contact model omits the rough surface effect in terms of varying peak height of the asperities. Slightly larger stiffness and ultimate load are therefore predicted by the perfect contact model as compared to the imperfect contact model. It is clear from Figure 3-10 that the cohesive contact model considerably underestimates the stiffness and the ultimate strength of the interlocking prisms, which is probably because the stiffness of the cohesive element is underestimated in the numerical model in comparison to that of the actual contact surface. Therefore, the numerical models with perfect and imperfect contact predict reasonably good result for both the compressive stiffness and ultimate load-carrying capacity of the interlocking brick prisms. Further studies with advanced numerical modelling technique to describe the roughness and imperfect contact surface so as to model the seating effect is under development.

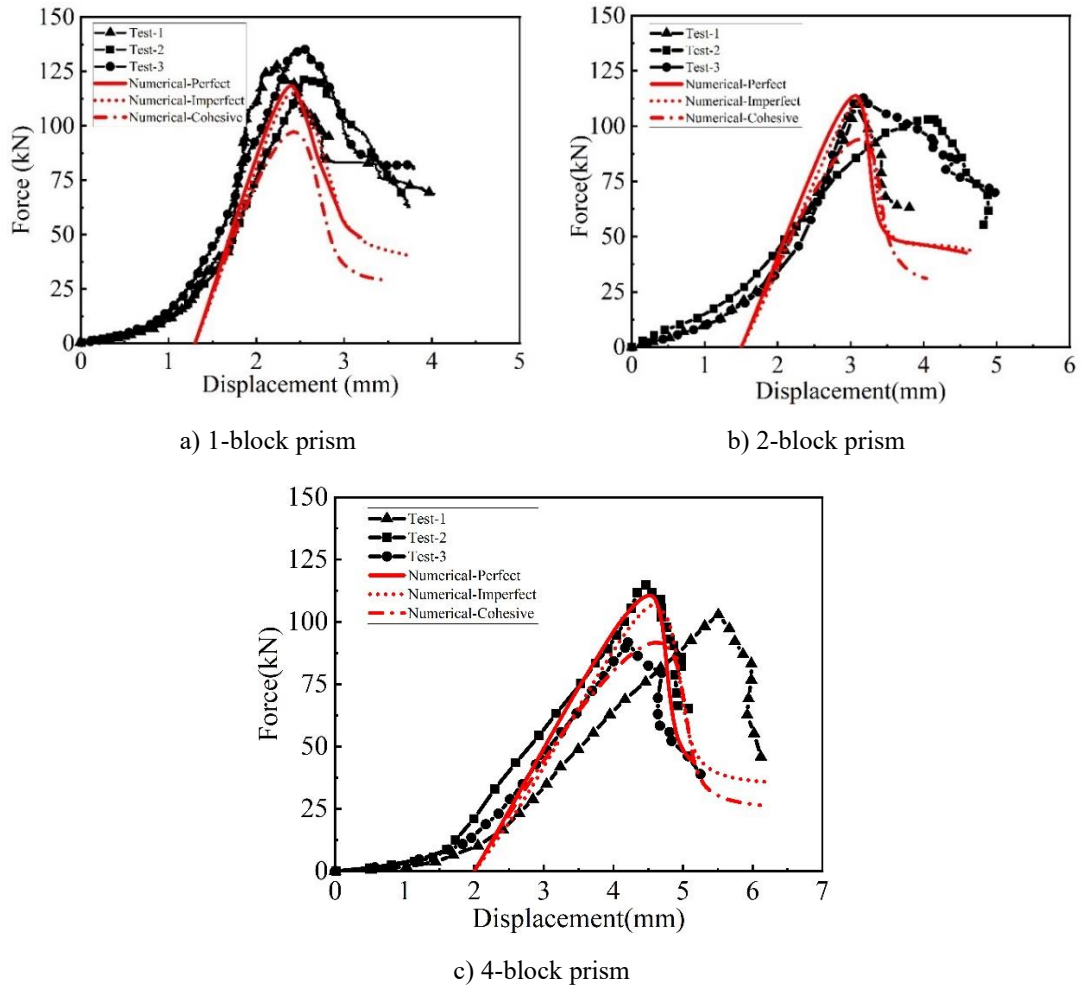
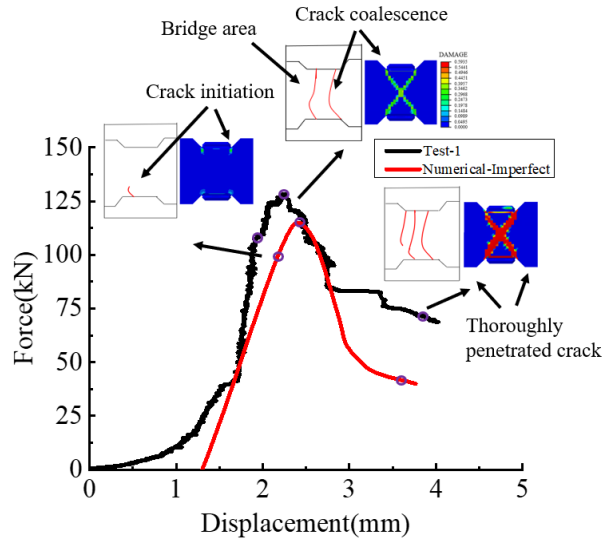


Figure 3-10. Load-displacement curves from laboratory test and numerical simulation.

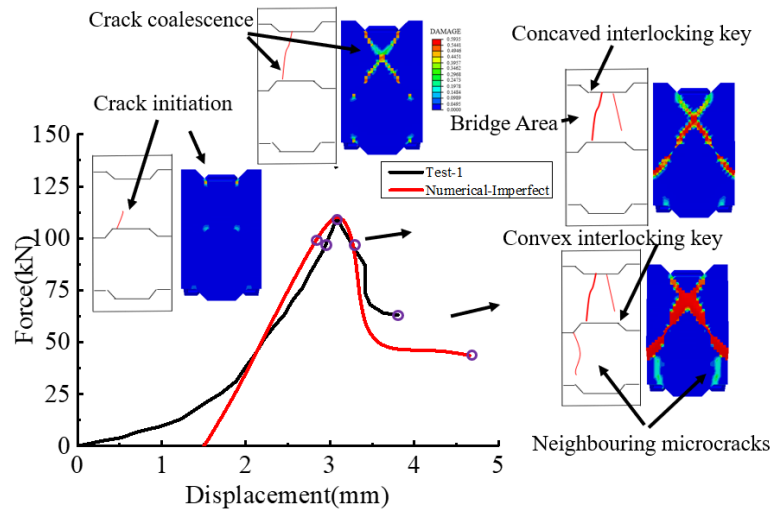
3.5.2 Crack propagation

Figure 3-11 illustrates the crack propagation processes of the prisms in stages with respects to the load-displacement curves. Tensile wing cracks can be found near the tenon and mortise, which initiate from flaw tips and extend in a steady pattern towards the direction of maximum compression [150]. It can be observed that for the 1-block prism wing cracks initiate from around the corner of the shear tenon when the applied compressive load is about 105 kN, and extend slowly along the compressive loading direction until the ultimate compressive force of 115 kN is reached. Two thorough vertical cracks are developed. With further increased vertical displacement, the cracks further extend vertically and interact with neighbouring microcracks, which lead to crack coalescences as well as ultimate failure of the prism [137, 151]. In the numerical

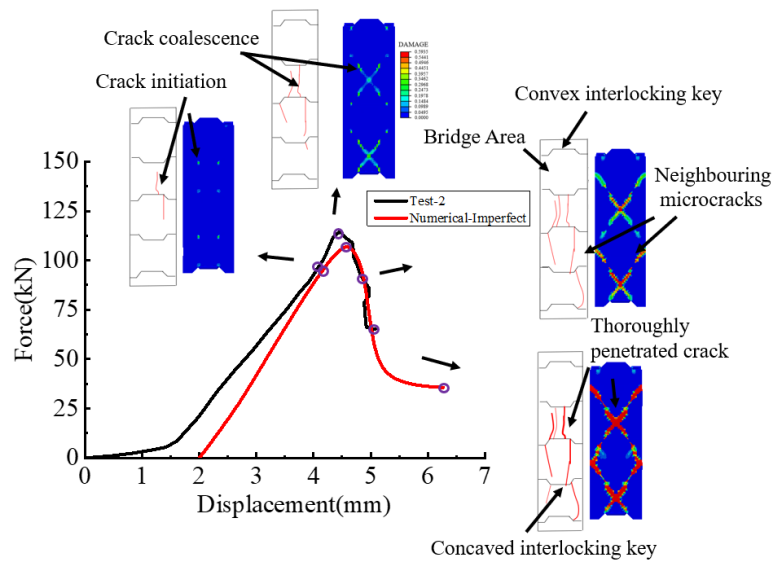
model, the initiation and growth of crack are both controlled by the stress field near the existing interlocking key. The numerical simulation agrees with experimental observations in that cracks initiate at about 80% of the peak load around the shear tenon, and extend along the vertical direction and result in the crack coalescence till the peak load is reached. Then these cracks grow wider with the increased load. Similarly, for the 2-block prisms, from both the numerical simulations and experimental observations it can be found that crack initiation occurs at 80% of the peak load and crack coalescence at the peak load is firstly presented on the concaved shear keys. With the increase in the applied displacement and load, a growing wing crack is developed at the outer tip in the middle of the bridge area [139] of the convex block, which is associated with wider and more cracks. The growth of cracks at the inner tips is faster than those shown at the outer tips, which agrees with that in the experimental observation. This is due to the higher stress concentration near the inner joint tip which enables the crack to propagate further. For the 4-block prisms, similar crack initiation and development can be observed. For multi-block prisms when the maximum compressive load is reached (corresponding to the second point in the figure), crack coalescence initiation occurs in the inner tip of the concaved interlocking key, and then these cracks propagate up and down forming a thoroughly penetrated crack. The crack pattern agrees well between numerical modelling and experimental observation.



a) 1-block prism



b) 2-block prism


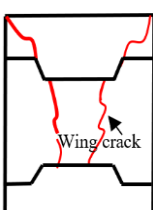
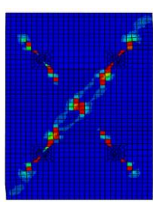
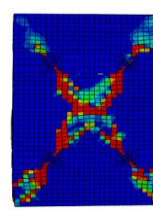
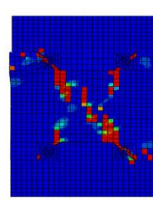


c) 4-block prism

Figure 3-11. Prism crack initiation and development in the experiments and numerical simulations.

3.5.3 Failure modes

Figure 3-12 summarizes and compares the damage modes of the interlocking prisms from the laboratory tests and numerical modelling. Both the laboratory test and the numerical model show wing cracks occur around the shear keys. For the perfect contact model, cracks at the unit interface propagate up and down from the flaw tips at an angle of 45° , exhibiting an X shape failure mode across the prism. The numerical models with cohesive contact model predict inclined cracks through the full block, which differs from the test observations. Through the comparisons, it can be found that the predictions from imperfect contact model most closely match the observed damages in the test among the three models, although some deviations are obvious. For example, the damages predicted by the numerical model is basically symmetric, whereas they are not necessarily symmetric in the tests. These differences can be attributed to the non-perfect contact conditions between adjacent interlocking bricks, and also possibly non-uniform material properties of the brick. Nonetheless, it can be concluded that the simplified imperfect model yields the closest predictions of the failure pattern of the interlocking brick prisms under compression.

Prism No.	Laboratory test	Cracking pattern	Damage contour		
			Perfect contact	Imperfect contact	Cohesive contact
1-block prism					

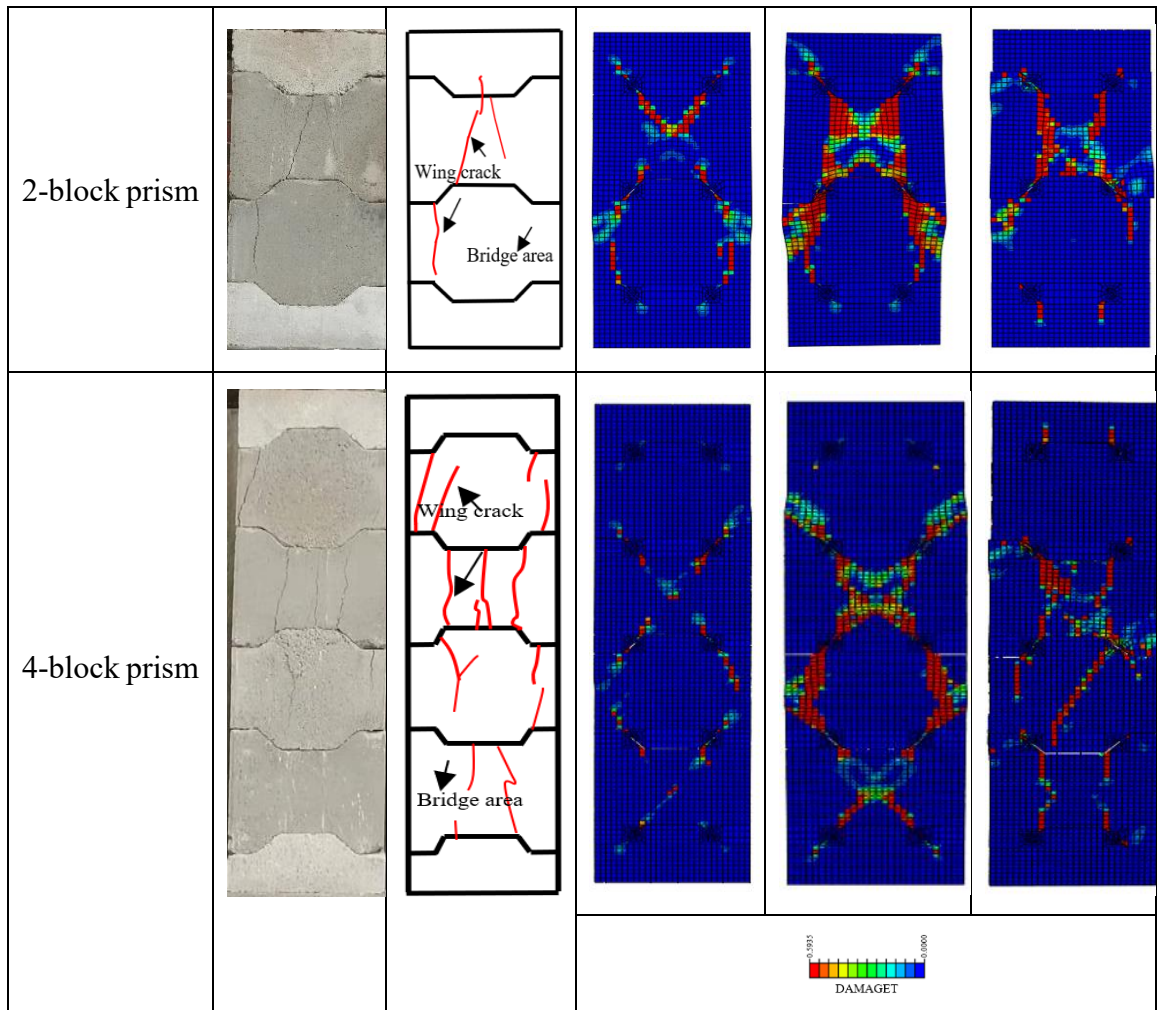


Figure 3-12. Comparison of prism damage modes.

The above results and analyses show the compressive behavior of interlocking brick prism is strongly influenced by the number of blocks. The compressive strength decreases with more blocks in prisms. Wing cracks are initiated from the protruded key tenon and mortise which is similar to the assumption of fracture mechanism theory. The developed numerical models could reasonably predict the behavior of the interlocking brick prisms. The imperfect contact modeling method gives the closest prediction.

3.6 Parametric study

Parametric study is carried out in this section to examine the influences of the number of blocks, the level of brick surface roughness amplitude, and material strength on the compressive load-carrying capacity of the interlocking brick prism. An

empirical formula is derived based on the numerical modeling results, experimental results, and analytical solution to predict the compressive load-carrying capacity of the interlocking brick prism. A semi-empirical method is also generated to estimate the compressive stiffness of the interlocking brick prism.

3.6.1 Effect of block number

A series of numerical simulations are carried out with gradually increased number of blocks for the prism until the ultimate compressive load converges. In the meanwhile, roughness amplitude due to brick surface imperfection and unevenness is assumed to be 0.1 mm, and the material compressive strength is 13.78 MPa in the numerical modellings. The cross-section area, brick size and interlocking key dimension are kept the same.

Figure 3-13 shows the results combining the prism ultimate compressive load with the number of blocks. It can be observed that as expected the influence of the number of blocks on the compressive load-carrying capacity of prisms is significant. For example, the equivalent compressive strength drops quickly from 6.18 MPa for 1-block prism to 5.93 MPa for 2-block prism, and further to 5.75 MPa for 4-block prism. Nevertheless, as the number of bricks in the prism increases, the decreasing speed also gradually reduces. The compressive strength reduces from 5.59 MPa for 8-block prism to about 5.52 MPa for 10-block prism (-1.3%), which further reduces to about 5.51 MPa for 12-block prism, indicating an ignorable -0.2% decrease.

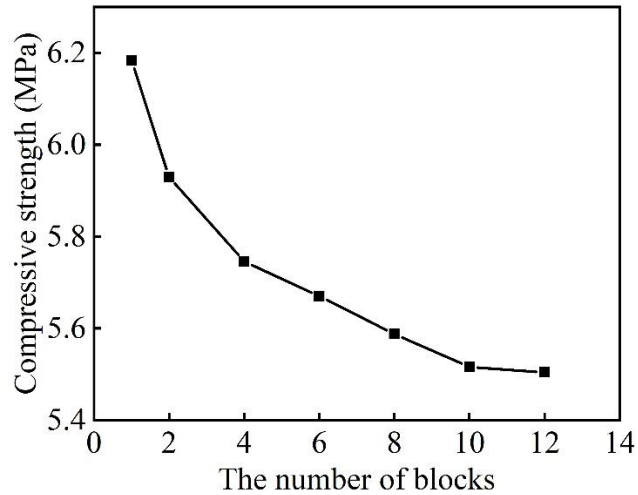


Figure 3-13. Ultimate compressive strength for interlocking brick prisms with different numbers of brick.

3.6.2 Effect of brick surface roughness amplitude

As demonstrated above in the laboratory test and numerical simulation, since joint imperfection due to brick manufacturing error/tolerance and surface unevenness could strongly influence the interlocking prism compressive strength, the interlocking bricks with surface roughness amplitude varying from 0 mm to 0.25 mm with a 0.05 mm increment are numerically modeled to quantify its influence on prism compressive strength. The cross-section area, brick size and interlocking key dimension are kept the same. The material compressive strength is also 13.78 MPa in the numerical simulations.

Figure 3-14 shows the results combining the prism ultimate compressive load with imperfection roughness amplitude and the number of blocks in the prisms. It can be observed that the compressive capacity of the interlocking brick prism with the same number of bricks decreases with the increased roughness amplitude. For example, for the 6-block model with roughness amplitude of 0.1 mm and 0.25 mm, the ultimate capacity decreases to approximately 5.09 MPa from 5.67 MPa; for the 12-block prism, the ultimate capacity decreases from 5.51 MPa when the roughness amplitude is 0.1 mm to 4.87 MPa when the roughness amplitude is 0.25 mm. These results indicate that

the roughness amplitude also has strong influence on the prism compressive capacity.

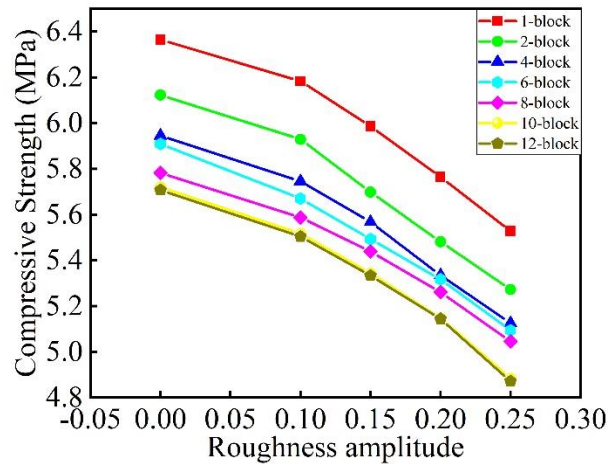


Figure 3-14. Ultimate compressive strength for interlocking brick prisms with different roughness amplitudes.

3.6.3 Effect of material strength

To examine the influence of material strength (f_{brick}) on the compressive strength of the interlocking prism, numerical simulation is conducted with f_{brick} varying between 13.8 MPa and 30 MPa with around 5 MPa increment. The Young's modulus is taken as 160 times the compressive strength of the material, and the material tensile strength is $0.1f_{brick}$ [38]. The roughness amplitude is assumed to be 0.1 mm.

Figure 3-15 presents the compressive strength of the prisms of different number of blocks with respect to the material compressive strength. For instance, for the 10-block model the ultimate compressive strength increases from approximately 5.52 MPa to 9.30 MPa when the material strength increases from 13.8 MPa to 30 MPa. As expected, the compressive strength of interlocking brick prisms is strongly influenced by the material strength, and the prism loading capacity shows a near-linear relation with the material compressive strength. Moreover, the ratio of the prism strength to the material strength is approximately 0.23, and is dependent on other parameters such as the brick surface roughness amplitude and the number of bricks as discussed above. However, the influence of these parameters is not as significant as the material strength.

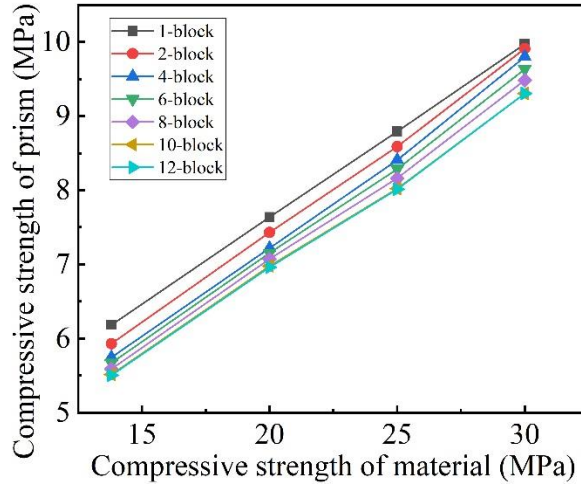


Figure 3-15. Ultimate compressive strength for interlocking brick prisms with different material strength.

3.6.4 Modified design formula for compressive strength

To account for the influence of the number of blocks, and the brick surface roughness amplitude as demonstrated above in engineering analysis and design, modification to the analytical solution of Eq. (3-2) is made by introducing to correction factors, i.e. $f(n_{block})$ and $g(h_{imp})$. In addition, to account for the variation of material strength, another term $\mu(f_{brick})$ is also introduced. The compressive strength of an interlocking brick prism, $\sigma_{n,h}$, could be expressed using the following equation

$$\sigma_{n,h} = \sigma_1^{max} * f(n_{block}) * g(h_{imp}) * \mu(f_{brick}) \quad (3-3)$$

where σ_1^{max} is the unit block compressive strength of the analytical solution given in Eq. (3-2).

Regression analysis on the laboratory testing and numerical modeling results is conducted to derive the above modification components in the proposed formula. Regression models are considered to achieve a best-fitted formula. The adequacy of regression models is evaluated with the coefficients of determination (R^2). The Eq. (3-4) with high R^2 of 94.7% is therefore chosen, which reflects the prism strength is positively proportioned to material strength, and negatively related to the number of bricks and roughness amplitude.

$$\sigma = \sigma_1^{max} * (0.199f_{brick} + 2.238) * \left(0.133 + \frac{1}{1.933 * n_{block} + 22.076}\right) * \frac{1}{0.784h_{imp} + 0.855} \quad (3-4)$$

To evaluate the accuracy of the proposed formula, Figure 3-16a) compares the formula predicted prism strength with those obtained from tests and numerical calculations. It can be found that the prediction using the proposed formula could closely predict those from the numerical simulations and experimental tests with the ratio of $\sigma_{test}/\sigma_{pred.}$ consistently distributing around the surface of 1.0.

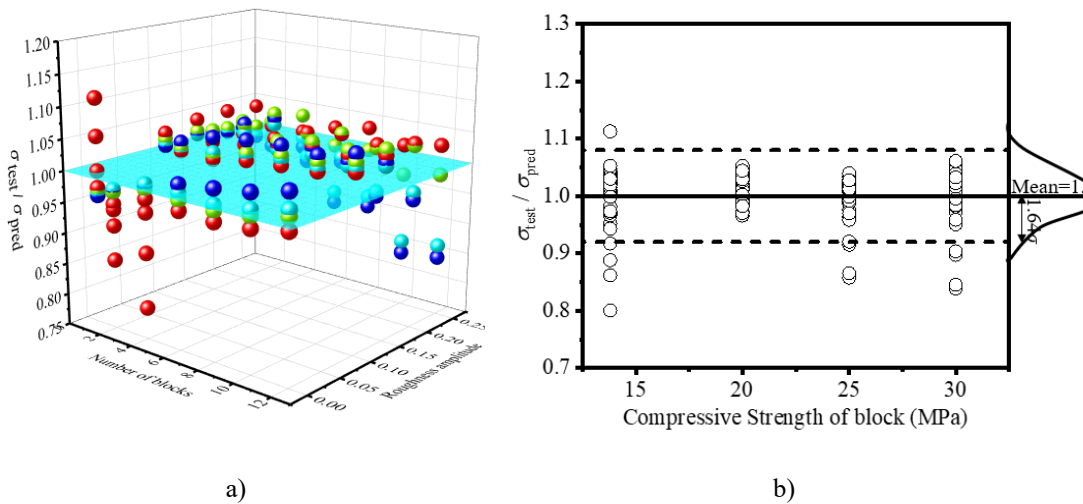


Figure 3-16. a) Comparison of the prism compressive strength estimated from the proposed formula and the test and the numerical results; b) predictions of different compressive strengths of interlocking imperfection prisms

For engineering design purpose, to account for uncertainties such as material strength, the above proposed prediction formula is further integrated with a safety margin by setting a confidence limit. Following CSA-S304.1 [152], the specified compressive strength for the interlocking brick prism can be determined with 95% confidence. Assuming the ratio of $\sigma_{test}/\sigma_{pred.}$ to follow normal distribution, the 95% confidence can be determined by subtracting 1.64 times the standard deviation from the arithmetic mean. Therefore, the confidence lower limit for a standard deviation of

0.047 and a mean of 1.00 can be estimated to be 0.92 (as shown in Figure 3-16b). Therefore, Eq. (3-5) can be presented appropriately for engineering assessment though re-evaluating as:

$$\sigma = 0.92 \sigma_1^{max} * (0.199 f_{brick} + 2.238) * \left(0.133 + \frac{1}{1.933 * n_{block} + 22.076} \right) * \frac{1}{0.784 h_{imp} + 0.855} \quad (3-5)$$

3.6.5 Semi-empirical method for prism compressive stiffness

A semi-empirical analysis method is proposed herein for simplified design purpose of interlocking prisms under uniaxial compression loads. A homogeneous prism is derived with an equivalent axial stiffness to predict the compressive properties for prisms comprised of different numbers of interlocking bricks.

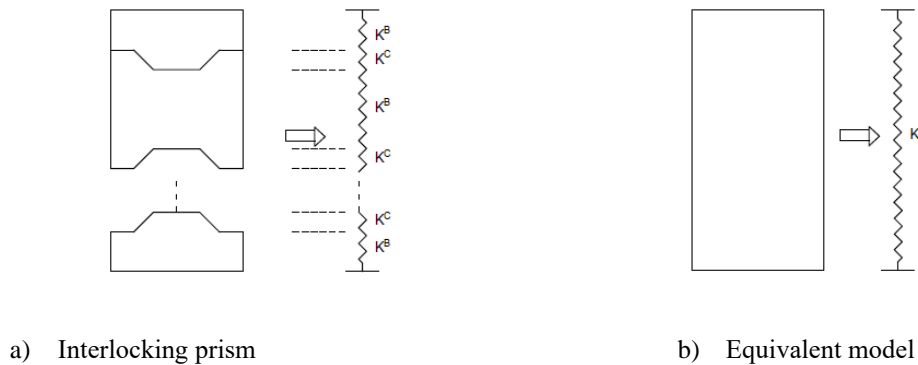


Figure 3-17. The equivalent vertical stiffness of the interlocking prism.

As demonstrated in Figure 3-17a), an interlocking brick prism with n pieces of bricks can be represented by a series of springs, i.e. K^B and K^C for the block stiffness and the interlocking contact stiffness, respectively. The equivalent spring stiffness K^n for a homogenous model (Figure 3-17b) can be written in the following forms:

$$1/K^n = n/K^B + (n + 1)/K^C \quad (3-6)$$

For each block, its stiffness K^B can be calculated by

$$K^B = \frac{E_{mat} A_{block}}{L_{block}} \quad (3-7)$$

where E_{mat} is the Young's modulus of the material, A_{block} is the cross-sectional area of the brick, and L_{block} is the height of the brick. By using material constants and brick dimension, K^B is 338.37 kN/mm.

The equivalent axial stiffness of n-block prism K^n can also be expressed as

$$K^n = \frac{EA}{L} = \frac{\int_x F(x) dx}{\Delta l_n \times L_n} \quad (3-8)$$

where F is the peak compressive load, Δl_n is the corresponding axial displacement, and L_n is the height of the prism. The equivalent stiffness of 1-block prisms can be calculated with the laboratory testing data. And Eq. (3-8) is applied to the case of 1-block prism, the stiffness of contact surface K^C can be written by

$$K^C = \frac{2K^1 \times K^B}{K^B - 2K^1} \quad (3-9)$$

So it can be calculated that K^C is 263.28 N/mm. With the above-derived K^B and K^C , the equivalent axial stiffness of the interlocking brick prism comprising of n-block can be easily estimated. Figure 3-18 presents the experimental tested prism stiffness and the estimated prism stiffness using the semi-analytical approach. It shows the equivalent stiffnesses predicted by Eq. (3-6) and those from the experiments agree reasonably well.

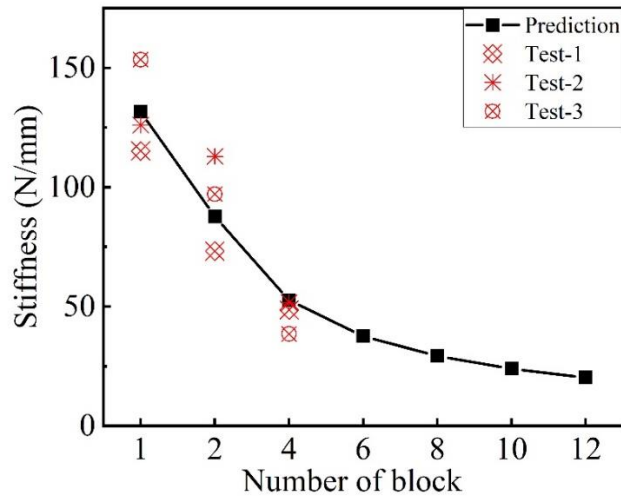


Figure 3-18. Equivalent compressive stiffness of interlocking brick prisms.

3.7 Summary

This chapter presents analytical analysis, laboratory testing and numerical modelling to investigate the compressive properties of interlocking brick prisms. The damage and failure modes of dry-stacking interlocking brick prisms are studied. Detailed numerical models of interlocking brick prisms are generated using different contact modelling methods, which are validated and verified with the laboratory tests. Parameter study is carried out to quantify the influences of the number of blocks, joint roughness amplitude due to brick surface unevenness, and brick material strength on the compressive load-carrying capacity. Combining the numerical simulation and testing results, an analytical prediction formula is derived to predict the compressive strength of interlocking brick prisms. A semi-empirical approach is also developed to estimate the compressive stiffness of interlocking brick prisms. The following conclusions are drawn from this study:

1. Fracture mechanism based analytical solution could closely predict the compressive strength of unit interlocking brick. However, because the strength of prism is strongly influenced by the number of blocks, the analytical solution based on a unit interlocking block could not well predict the compressive strength of the prism.

2. Laboratory compressive tests are conducted on a series of multiple block prisms. Strong seating effect of the dry-stacking interlocking brick prisms on their compression performance is observed. It is found that the ultimate strength decreases with the increase in the number of blocks because of the increased number of interlocking joints.
3. Detailed numerical models using different contact modelling methods are generated which could reasonably predict the behaviour of interlocking brick prisms. The imperfect contact model gives the closest prediction considering the initial stiffness, the ultimate compressive load-carrying capacity and damage modes. However, none of these methods could replicate the seating effect.
4. Both laboratory tests and numerical simulation reveal the damage and failure patterns of interlocking brick prisms.
5. Parametric study quantifies the influence of the number of bricks, joint roughness amplitudes and material compressive strength on the prism compressive capacity. A modified formula is derived to predict the compressive strength of interlocking brick prisms with consideration of the number of blocks, joint roughness amplitudes, and material strength. And a semi-empirical prediction method is also derived to predict the axial stiffness of the interlocking brick prisms.

CHAPTER 4 EXPERIMENTAL AND NUMERICAL STUDIES OF THE SHEAR RESISTANCE CAPACITIES OF INTERLOCKING BLOCKS

4.1 Introduction

In this chapter, the shear performance of the same type of interlocking brick is investigated in detail. Laboratory shear test is firstly conducted to study the damage mode and shear capacity of interlocking brick prisms. Numerical model is then generated with consideration of contact imperfection and validated with test results. Intensive parametric studies are conducted to quantify the influences of material strength, axial pre-compression force, friction coefficients, and contact imperfection at brick interfaces on the shear response of interlocking prisms. The accuracy of existing methods for predicting the shear capacities of shear key by design standard and empirical formula are evaluated. Based on the numerical and laboratory results, an empirical design formula is proposed to predict the shear capacity of the interlocking brick.

The related work in this chapter has been published Journal of Building Engineering.

Shi T, Zhang X, Hao H, et al. Experimental and numerical studies of the shear resistance capacities of interlocking blocks[J]. Journal of Building Engineering, 2021, 44: 103230.

<https://doi.org/10.1016/j.job.2021.103230>

4.2 Laboratory tests

Laboratory shear test is carried out to experimentally examine the shear behaviour of

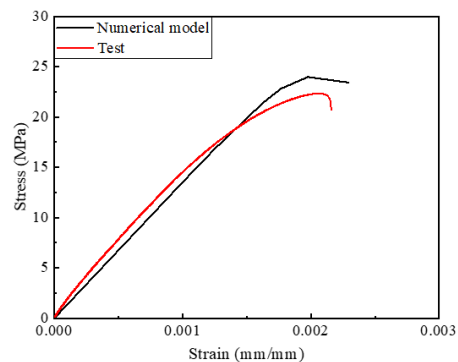
interlocking bricks. Considering the large variation in brick material properties, the material strength of the studied interlocking bricks is firstly tested through unconfined uniaxial compressive test. Then, shear test on interlocking brick prisms is setup and performed to investigate the shear behaviour of interlocking bricks.

4.2.1 Material property

It should be noted that the material of the bricks used in the experiments of this chapter differs from that in Chapter 3 due to adjustments of the proportions of each source material. Consequently, a material property test was conducted once again. The experimental procedure is consistent with that described in Section 3.3.1. The averaged axial stress-strain curve measured in the tests are shown in Figure 4-1b, where the axial stress is calculated by dividing the measured axial compressive load by the cross-sectional area of the specimen. Strain gauges are used to measure the axial strain. The numerical prediction of the corresponding stress-strain curve is also presented in the figure, details of numerical model will be presented in the subsequent sections.



(a) Uniaxial compressive test



(b) Stress-strain curves

Figure 4-1. Determination of brick material properties.

4.2.2 Shear test setup

Following BS EN 1052-3 [153], shear tests are setup to examine the shear properties of the interlocking bricks. Figure 4-2a and b illustrates the test setup, where the specimen dimension is 600mm × 200mm × 200mm (length × height × thickness). The prism comprises of three dry-stacking interlocking blocks of 200mm × 100mm

×180mm (length ×thickness×height) and two pieces of half bricks as end blocks. The interlocking blocks have large interlocking keys (35 mm length × 35 mm thickness× 30 mm height), which provide shear resistance at the interlocking joints, as shown in Figure 4-2c. The prism is firstly pre-loaded axially in the horizontal direction. Then, the two side blocks are fixed using two steel plates to the bottom supporting frames. To minimize the flexural bending deformation in the prism, flat bars and wide-angle plates are used to fix the two end bricks firmly to the bottom support frame. The rotation of the two side bricks is therefore effectively restrained. The central brick is loaded to move downwards. Two shear planes are therefore created through this setup. Because of the non-symmetric layout of the interlocking keys on the brick, the damage and failure of the testing brick prism vary on the frontal surface (Side I) and rear surface (Side II).

One LVDT (linear variable differential transformer) is installed to record the vertical displacement of the central brick. Another LVDT is used to measure the vertical movement of one side brick, so as to monitor the rotational movement of the side brick. One loadcell is used to monitor the axial pre-compressive force applied. Another loadcell is used on the central brick to measure the shear force applied to the shear planes. Two loadcells are installed beneath the two side bricks to ensure the same amount of tying forces is applied. Two groups of tests are conducted with 10 kN and 30 kN axial pre-compression applied to the brick prisms, corresponding to 0.538 MPa and 1.614 MPa axial stress, which are the typical vertical stress in masonry wall for a single-storey and low-rise masonry building. Three specimens are tested for each group in the study.

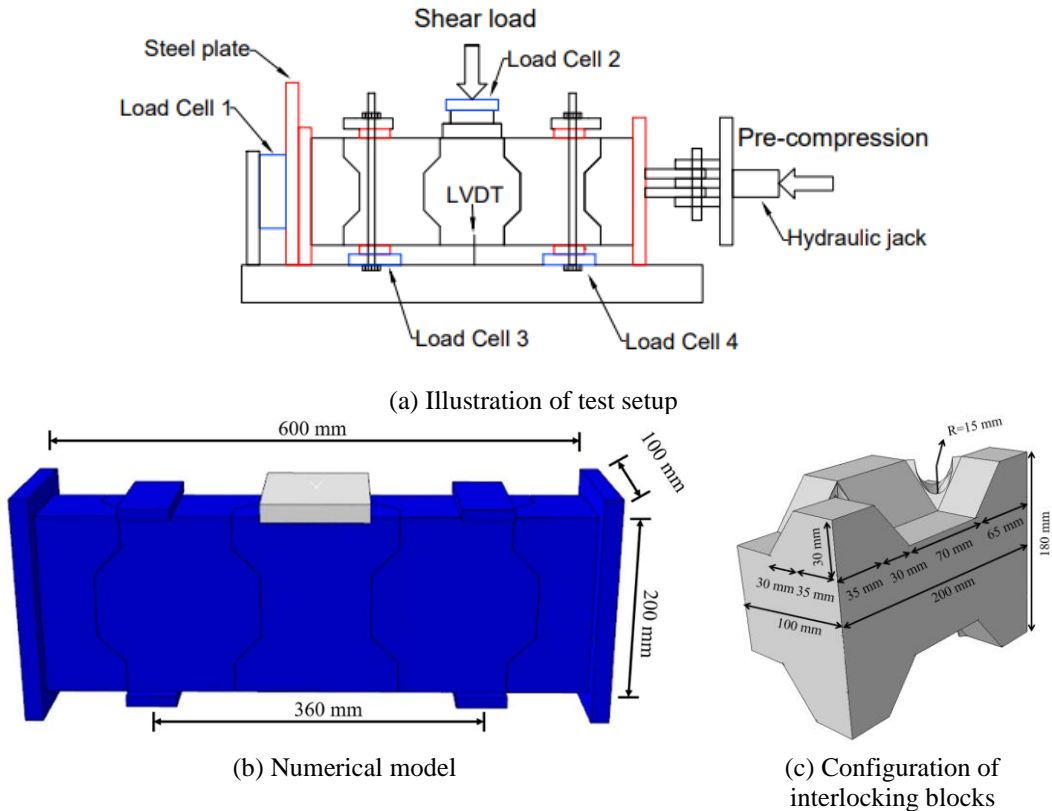


Figure 4-2. Experimental and numerical models for the prism shear test

4.3 Numerical Simulation

A three-dimensional finite element model of the interlocking brick prism is developed in Abaqus [144] to further investigate the shear behaviour of the interlocking bricks.

4.3.1 Model details

Figure 4-2b presents the numerical simulation of the interlocking prism, which replicates the laboratory test setup. Steel strips of the same dimensions as in the test are modelled to fix and load the brick prism, where a friction coefficient of 0.15 is adopted between steel and the bricks [38]. Solid element C3D8R in Abaqus is adopted for the interlocking brick. In the numerical modelling, three loading steps are implemented, i.e., axial pre-compression of the interlocking prism, fixing the two side bricks with vertical pre-tying force onto the two supports, and application of vertical load on the central brick. The axial pre-compressive force and pre-tying force are applied using force control method. For the vertical force, displacement-controlled

loading method is used as in the laboratory test. Convergence study is implemented by step-reducing the mesh sizes. It is found that when the mesh size reduces from 5 mm to 2.5 mm, the maximum compressive force in the prism does not change much but it requires a significantly higher computation resource. Therefore, 5 mm mesh size is used in this study for the numerical simulation.

4.3.2 Material model

The material model of concrete damage plasticity (CDP) is employed to simulate the nonlinear behaviour and damage of the brick, which is proposed by Lubliner et al. [145]. Crushing in compression and cracking in tension can both be modelled. As shown in Figure 4-3, in CDP model, the compressive and tensile stress-strain relationships are defined, which are featured by damaged plasticity parameters. The unconfined uniaxial compressive strength is acquired via the laboratory material tests depicted in Section 4.2.1. The elastic modulus (E_0) is taken as the secant modulus determined from the origin to the point with a stress level equivalent to 40% of the compressive strength. The Poisson's ratio is determined at the same stress level. Table 4-1 and Table 4-2 show the material properties of the interlocking brick, where E_0 represents the elastic modulus; ν denotes the Poisson's ratio. The tensile strength is taken as $f_t=0.1 f_c$ following previous studies [38, 146]. The unconfined uniaxial compressive behaviour of the brick core is modelled to verify the brick material constitutive model. The stress-strain curve from the numerical calculation using the CDP model agrees reasonably well with that in the laboratory test (see Figure 4-1b). An elastic perfect plastic material model is adopted for the steel, whose Young's modulus of 210 GPa as well as Poisson's ratio of 0.3 are used.

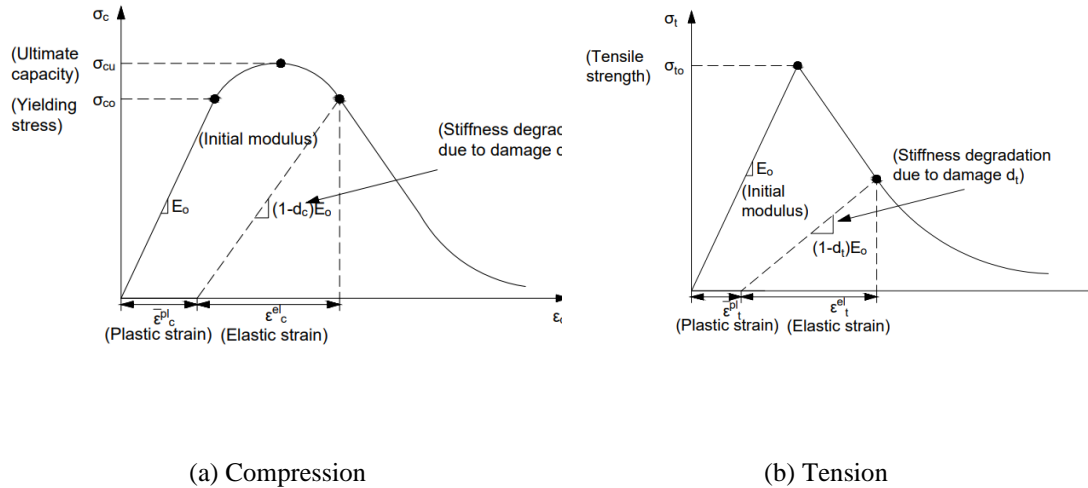


Figure 4-3. Definitions of concrete damage plasticity (CDP) model [53].

Table 4-1. Material properties of interlocking brick

Elasticity			Plasticity		
Initial Young's modulus, E_0 (GPa)	Poisson's ratio ν	Dilatation angle ψ ($^\circ$)	Eccentricity	Biaxial stress ratio f_{ho}/f_{co}	K
13.49	0.2	30	0.1	1.16	0.67

Table 4-2. Material constants of concrete damage plasticity model

Behaviour in compression		Behaviour in Tension	
Yield stress (MPa)	Inelastic strain	Yield stress (MPa)	Cracking strain
15.12	0	1.78	0
15.96	0.00002	0.93	0.0007
16.84	0.00006	0.78	0.0008
17.84	0.00012	0.63	0.0009
10	0.0010	0.48	0.0010
		0.18	0.0012

4.3.3 Contact algorithm

Contact surface strongly influences the behaviour of mortar-less joint of interlocking bricks [36]. Three different modelling approaches: perfect contact, random rough contact and simplified rough contact, are used to simulate the contact behaviour between the mortar-less joints.

4.3.3.1 Perfect contact

The perfect contact is the simplest approach used in the engineering field. It assumes that contact surfaces between neighbouring bricks are smooth, which leads to perfect connection. The surface-to-surface contact is used to simulate the connections between the neighbouring interlocking bricks. The tangential behaviour is defined by Mohr-Coulomb criterion, the friction coefficient is taken as 0.3 [38, 148]. And the normal behaviour is defined by hard contact. The hard contact ensures contact surfaces between the adjacent interlocking bricks be in contact without penetration.

4.3.3.2 Random and simplified rough contact

The random rough contact considers brick natural surface condition due to material and manufacture tolerance. To examine the true brick surface condition, laboratory test is carried out using a laser profile scanner to quantify the surface profile of the bricks. As shown in Figure 4-4a, each brick is cut into halves and placed on a flat testing table, and the laser scanner installed on a rigid steel frame scans the top surface profile of the interlocking brick. The laser scans the surface for three times, and the averaged value of profile is taken as the actual surface roughness. Figure 4-4b shows one of the typical brick surface contours scanned from the test. The above experimentally measured contour at the interlocking bricks is then numerically generated with fine mesh as illustrated in Figure 4-4c. To improve computational efficiency, and also to reasonably model surface roughness without the need to measure every surface of the interlocking bricks, the random surface roughness is simplified by the mean surface roughness value and trapezoidal shape roughness profiles (Figure 4-4c).

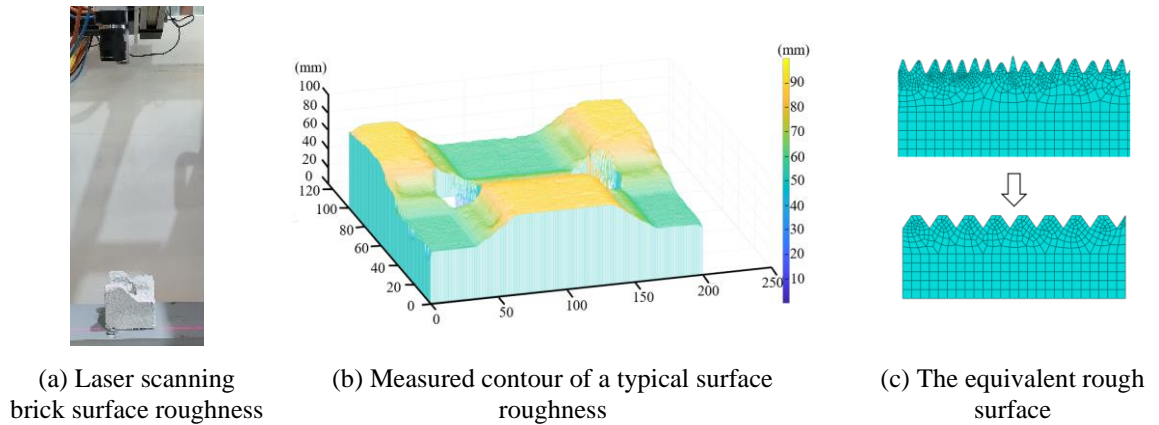


Figure 4-4. Evaluation of brick surface roughness.

4.4 Results and Analysis

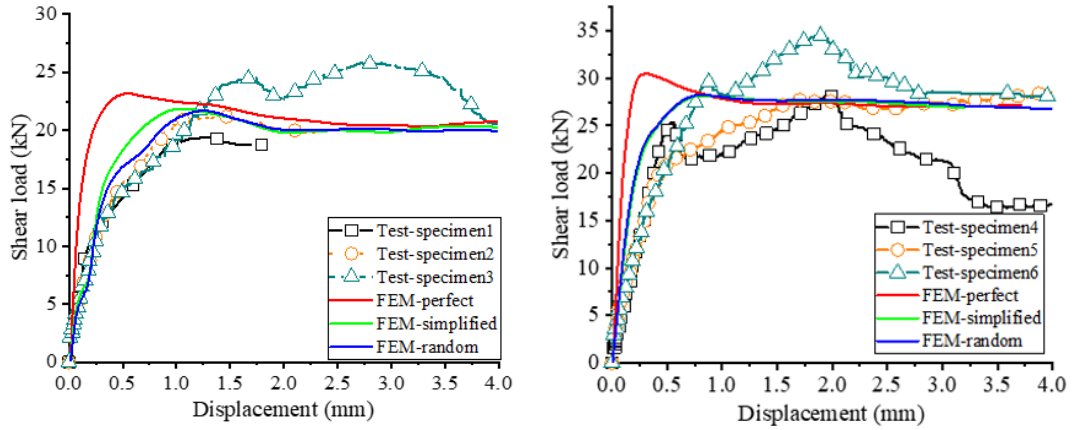
Numerical modelling and laboratory testing results are provided in this section. Shear load-displacement relationship, failure modes of the interlocking brick, and shear capacity are compared to demonstrate the shear behaviour of interlocking bricks.

4.4.1 Load-displacement curves

Figure 4-5 presents the shear load versus central brick vertical displacement. In this paper, a half of the applied vertical force is taken as the “shear force” experienced by the interlocking joint due to the two symmetric shear planes, and this shear force is taken as the shear capacity of the interlocking joint. When a 10 kN axial pre-compression is applied to the brick prism, the shear force increases linearly to about 6.27 kN at about 0.11 mm displacement, reflecting an initial stiffness of 56.43 kN/mm, and it corresponds to about 30% of the maximum shear load of the prism. As the shear load further increases, the slope of the curve drops. The shear load increases non-linearly as it approaches the maximum shear load of 21.18 kN at a displacement of around 1.46 mm, after which it begins to decrease, reflecting the failure of the interlocking prism. It is worth noticing that on Specimen 3 after the initial peak load is reached, a 2nd peak load is developed. The first peak corresponds to the damage of intact prism at the weakest shear key and the sharp drop reveals shearing off on one side of the shear key that provides the shear strength τ_1 . Afterwards, stress at the

interlocking connection is redistributed, where block rotation can be observed. The test might be influenced by the flexural bending deformation of the prism, which was observed in the lab test. The second peak represents the combined contributions from the shear strength of the second interlocking key, some friction force in the first interlocking key connection due to bending, and membrane effect due to the prism deformation and axial pre-compression. Therefore, a higher shear force is recorded for the 2nd peak load. Similar observation was reported by previous researchers on the concrete shear key [154]. Nevertheless, it is worth noting that because of the large depth, the prism can be considered as a deep beam, whose flexural deformation is therefore not significant. Some variations among the three prisms tested can be observed, which are due to the inherent variability of contact surfaces between mortar-less interlocking bricks and the non-simultaneous damages of the interlocking bricks at the two shear planes.

When the prisms are subjected to 30 kN axial pre-compression, similar behaviours can be observed, but a larger initial stiffness of 88.30 kN/mm is observed due to the higher axial pre-compression. A peak shear load of about 29.58 kN is achieved at around 0.88 mm displacement. After reaching the maximum shear force, the applied force decreases steadily with further increased displacement until residual strength is maintained. Larger peak shear resistance is observed on the 30 kN pre-compressed prisms as compared to that of the 10 kN pre-compressed prisms because the increased axial compression leads to higher inter-surface friction [50].



(a) 10 kN axial pre-compression

(b) 30 kN axial pre-compression

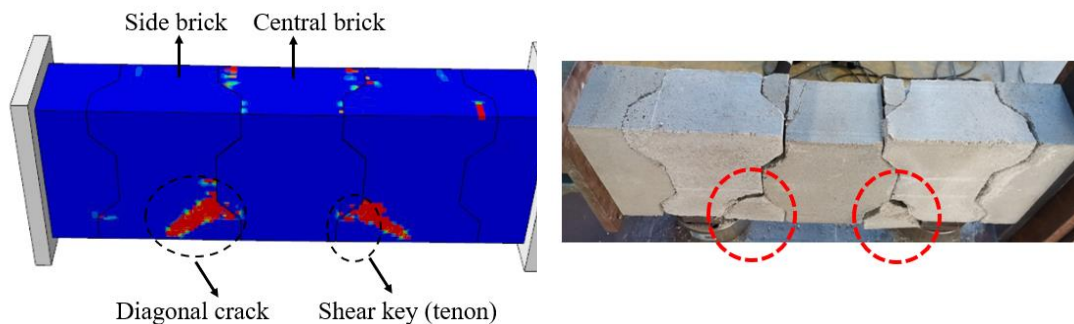
Figure 4-5. Load-displacement curves from numerical simulation and laboratory test.

The numerically modelled shear force-displacement curves are compared with those from the laboratory tests, as shown in Figure 4-5. It can be observed that the perfect contact models largely overestimate the initial stiffness of the interlocking prisms under both 10 kN and 30 kN axial pre-compression cases. In comparison, the numerical models with random and simplified rough surfaces could more closely replicate the stiffness of the prism. For example, under 10 kN axial pre-compression, the perfect contact model predicts an initial stiffness of 136.87 kN/mm, while the simplified and random rough contact models predict 50.86 kN/mm and 38.88 kN/mm, respectively. Similarly, under 30 kN axial pre-compression, an initial stiffness of 188.31 kN/mm is predicted by the perfect contact model, which is much higher than those of 102.96 kN/mm and 107.75 kN/mm by the random and simplified contact model. Nevertheless, these three models predict similar shear loading capacities. For example, under 10 kN axial pre-compression, the perfect contact model predicts a maximum shear load of 23.17 kN in comparison to 21.86 kN and 21.69 kN for the simplified and random rough contact models indicating less than 10% difference. Similar trend can be found for the interlocking bricks under 30 kN axial pre-compression. It is evidenced that modelling of contact surface is crucial for accurate prediction of interlocking brick shear stiffness and capacity, under higher axial pre-compression, the difference between the random and simplified rough surface models

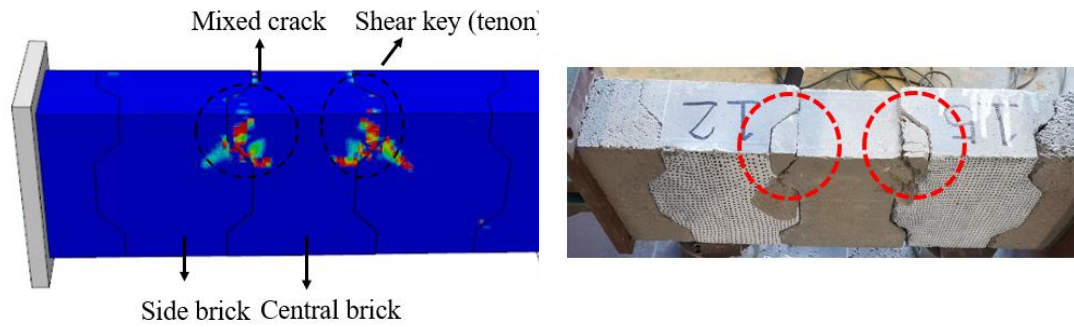
is smaller. The simplified and detailed random rough surface models predict very similar shear capacity because shear resistance is primarily provided by the shear key, while the contribution of the surface friction that is closely related to surface roughness condition is not pronounced. These results indicate that the random rough surface can be approximately modelled by simplified trapezoidal rough surface, which give similar predictions of the shear capacity, and close predictions of the shear stiffness especially when the axial compression force is relatively large.

4.4.2 Failure mode and crack propagation

Because of the unique shape of the interlocking bricks, there are two different failure patterns on the frontal and rear sides of the interlocking brick prism as shown in Figure 4-6, i.e., Side I and II. On Side I diagonal cracks are developed on the bottom shear keys of the two side bricks. This is accompanied by a brittle shear failure at the shear keys because of the principle stress on the plane reaching the failure strength [73]. Similarly, on Side II cracks initiate on the corner of the tenon of the central brick, and then the cracks extend shortly in the direction perpendicular to the inclined surface after which the cracks propagate vertically. Thus, the crack pattern on Side II is a mixed crack mode (Figure 4-6b). The excessive shear stress leads to the eventual damages of these tenons. After the failure of these tenons, only surface friction at the interfaces resists the shear load which provides the residual shear capacity.



(a) Side I



(b) Side II

Figure 4-6. Comparison of prism damage modes between numerical modelling and laboratory test.

The crack initiation and propagation processes of the interlocking brick prism modelled numerically and recorded in the lab test are plotted in the shear force versus displacement curve as shown in Figure 4-7. As can be observed on Side I diagonal cracks initiate on the bottom shear keys of the two side bricks at Stage A. They extend diagonally at about 45° , associated with the slight decrease in the stiffness of the specimen. With further applied vertical displacement on the central block, cracks further develop leading to the further damage of the interlocking brick prism. Unlike the numerically modelled cracks occurred simultaneously and symmetrically on both sides of the interlocking brick prism, crack in the laboratory tested specimen occurred only on one side first because of unavoidable asymmetry of the tested specimens owing to imperfectness in preparing the bricks and interlocking specimens. But at the maximum shear load, the crack patterns converge between numerical modelling and experimental observation. It can also be observed from Figure 4-7 that on Side II the shear key of the central brick cracks under the applied shear load at Stage A, which extend diagonally at about 45° angle. With the further increased shear load, the cracks then extend vertically and penetrate through the central brick at the maximum shear load.

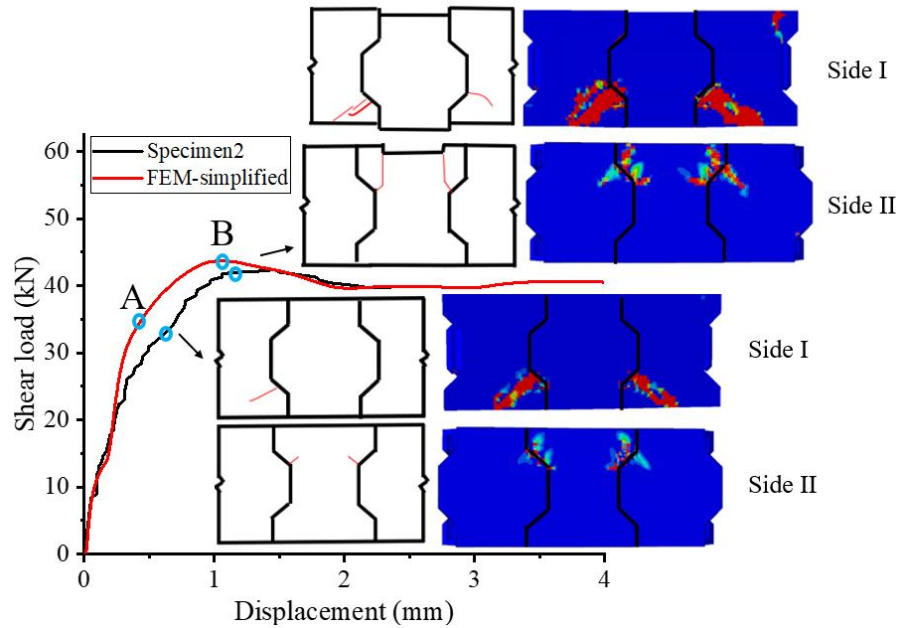
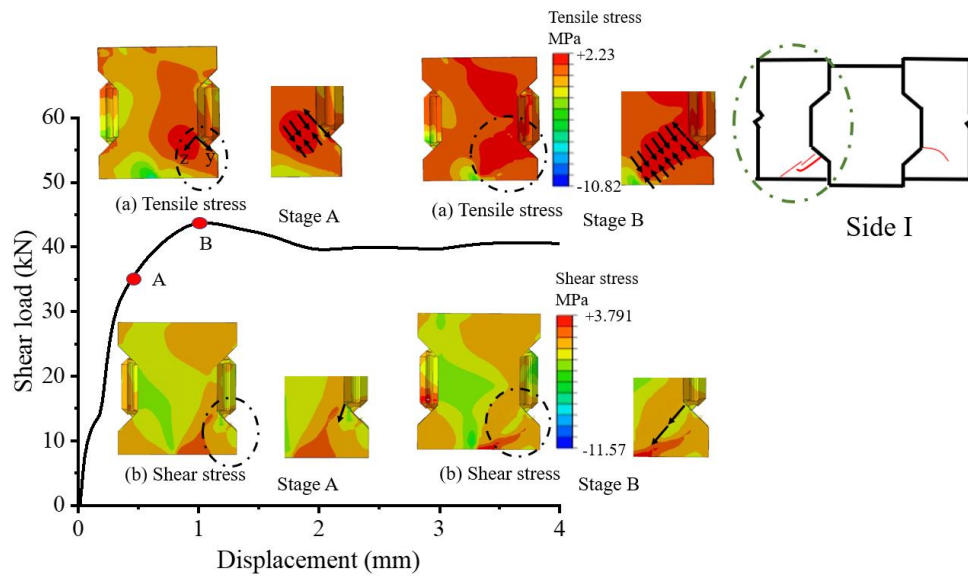


Figure 4-7. Prism cracks evolution in the numerical simulations and experiments (Specimen 2 under 10 kN axial pre-compression).

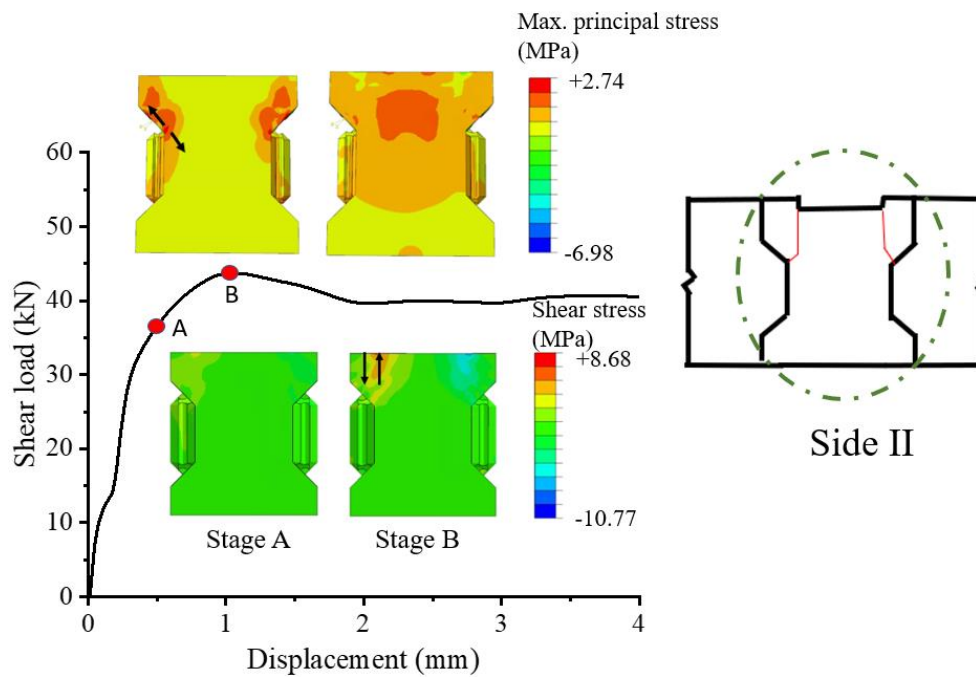
4.4.3 Stress distribution and crack evolution

To better understand the stress distribution in the interlocking brick prism, the tensile stress and shear stress contours generated from the numerical modelling using the simplified rough surface model are plotted along with the shear load versus displacement curves in Figure 4-8. On Side I, the applied shear force on the shear plane induces a large tensile stress around the shear key of the side brick. At Stage A, diagonal crack appears due to excessive tensile stress at the shear key, which extends and propagates under the further increased shear force on the interlocking joint. For the central block on Side II (Figure 4-8b), a large tensile stress is generated around the shear key because of geometry change induced stress concentration. Tensile cracks (mode I) are initiated at Stage A, which extend diagonally at about 45° . As the applied shear load gradually increases, the propagation of diagonal cracks ceased because it enters a low tensile stress field which therefore would release less strain energy. The formation and propagation of the diagonal crack results in the rotation of the shear key and varies the boundary condition of the stress zone. As a result, as can be seen in Figure 4-8b, a large shear stress is induced around the shear key, which consequentially

leads to the further development of the crack under the shear stress (mode II crack) until the total failure of the shear key on the central block at Stage B.



(a) The diagonal crack evolution in the side brick on Side I



(b) The mixed crack evolution in the central brick on Side II

Figure 4-8. Crack evolution of prism stress contours.

4.4.4 Shear capacity

To examine the shear capacity of the interlocking prism, the wedge crack model (WCM) [155] is employed. As illustrated in Figure 4-9, the vertical force from the shear load on the interlocking joint is F and the horizontal force from axial compression is F' , which leads to the crack initiation. The stress intensity factor of mode I crack [156] at the crack tip, generated by the wedging forces F and F' (K_{Ia}), can be given as follows:

$$K_I = 2(F\sin\theta - F'\cos\theta) \sqrt{\frac{\pi}{(\pi^2 - 4)l}} \quad (4-1)$$

where l stands for the length of the diagonal crack; F' is calculated as the horizontal pre-compressive load acting on the cracking area, and F is the shear load acting on the cracking area; subscription I represents mode I crack. The crack angle θ is assumed to be 45° following laboratory observation and previous studies [157-159]. For mode I fracture, crack is initiated when the stress intensity factor K_I reaches K_{IC} , where $K_{IC} = 0.0443 \text{ MPa}\cdot\text{m}^{1/2}$ denotes the fracture toughness of material [160]. Therefore, the maximum shear capacity V for the interlocking brick at the joint can be expressed as:

$$V = F_{pre}\mu + \left(K_{IC} \sqrt{\frac{(\pi^2 - 4)l_1}{\pi}} \times \frac{1}{2} + F'_1\cos\theta \right) \frac{1}{\sin\theta} + \left(K_{IC} \sqrt{\frac{(\pi^2 - 4)l_2}{\pi}} \times \frac{1}{2} + F'_2\cos\theta \right) \frac{1}{\sin\theta} \quad (4-2)$$

where F_{pre} is the axial pre-compressive force on the interlocking prism, and μ is the surface friction coefficient, which equals to 0.3. The term $F_{pre}\mu$ in Eq. (4-2) accounts for the friction resistance force at the interlocking joint. Substituting crack lengths $l_1=10\text{mm}$ for the central brick and $l_2=88\text{mm}$ for the side bricks, the maximum shear capacity V for the interlocking brick can be calculated.

The theoretical predictions are compared with the laboratory testing results in Table

4-4. When subjected to 10kN axial pre-compression, an averaged shear capacity of 22.04 kN is predicted, which is very close to the laboratory testing data of 21.7kN (+1.5% error). But when the axial pre-compression level is high (30kN), the theoretical prediction overpredicts the shear capacity by +16.4% (32.1kN) comparing to the laboratory testing data (27.56kN). This is probably because the quality of contact between the interlocking brick is not probably considered in the theoretical derivation.

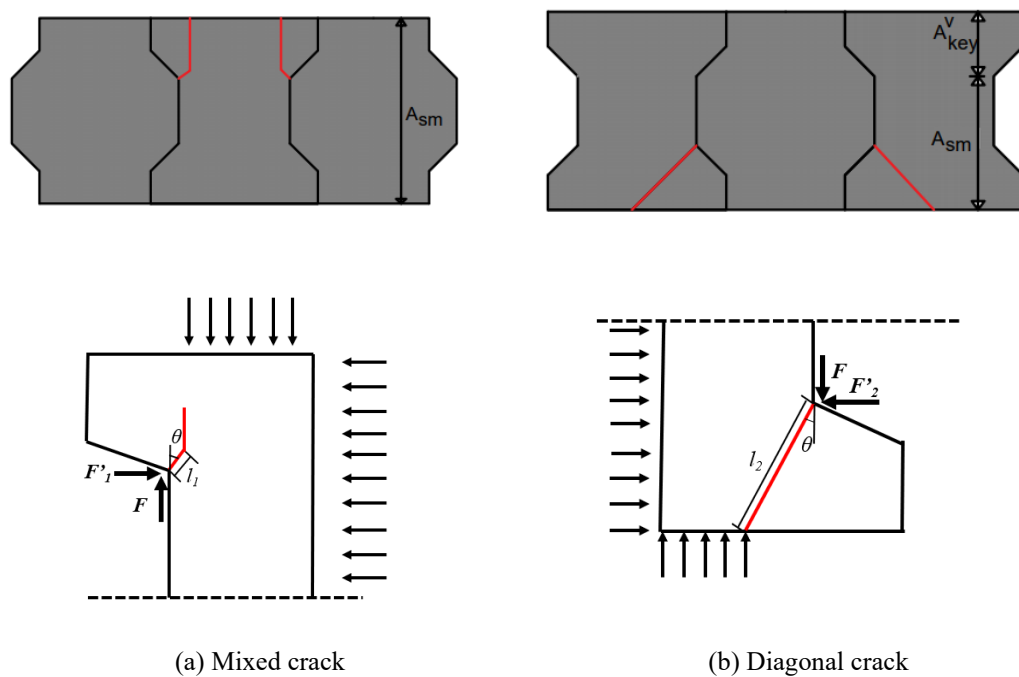


Figure 4-9. Load analysis for the wedging action on interlocking bricks.

In the meanwhile, following design code EN-1052-3 [153], the equivalent shear strength for the interlocking bricks can be calculated for simplified engineering application by assuming two shear planes created between the central block and the two side blocks as shown in Figure 4-6. The equivalent shear strength is calculated using the shear load on the interlocking joint (one shear plane) dividing the cross-sectional area of the joint (200mm height \times 100mm depth minus the area of two holes). Table 4-3 summarizes the peak shear load on the interlocking joint (V_1), the equivalent shear strength (τ_1), the associated displacement (δ_1) and the initial shear stiffness. Among the three specimens of each group of tests, a coefficient of variation (CoV)

about 10% is found which indicates that the test results vary in an acceptable small range. When subjected to 10 kN axial compression, an averaged equivalent shear strength of 1.17 MPa is measured, which is 27% lower than that under 30 kN axial pre-compression (1.48 MPa). This is expected as axial pre-compression could influence both the friction resistance and the shear resistance of the shear key. Therefore, axial pre-compression level should be considered when evaluating the shear strength of interlocking bricks.

Table 4-3. The results obtained from the shear tests

Prisms	V1/kN	τ_1 /MPa	δ_1 /mm	Initial shear stiffness/(kN/mm)
Preload-10-1	19.42	1.04	1.31	57.12
Preload-10-2	21.18	1.14	1.46	56.42
Preload-10-3	24.51	1.32	1.74	53.00
Average	21.70	1.17	1.50	55.51
Preload-30-1	25.31	1.36	0.54	107.40
Preload-30-2	27.80	1.50	1.75	164.00
Preload-30-3	29.58	1.59	0.88	163.51
Average	27.56	1.48	1.06	144.97

4.4.5 Comparison with design formula

Comparison is made between the above tested shear capacity for the interlocking brick and existing empirical formula and design method to evaluate the accuracy and suitability of these existing methods. In engineering practice, AASHTO design code (in Eq. (4-3)) [76] and the semi-empirical formula proposed by Rombach and Specker [53, 161, 162] (in Eq. (4-4)) are the commonly used methods. As shown, both methods separate the shear capacity V of a keyed joint into two parts: a) resistance from the interlocking key; and b) interface friction.

$$V = A_{key}^V (0.006792 f_{cm})^{0.5} \times (12 + 2.466 \sigma_n) + u A_{sm} \sigma_n \quad (4-3)$$

$$V = 0.14 f_{cm} A_{key}^V + 0.65 (A_k + A_{sm}) \sigma_n \quad (4-4)$$

where A_{key}^V is the projection area of shear keys on the failure plane (mm^2); and A_{sm} is the contacting area between flat contact surfaces in the failure plane (mm^2), as shown

in Figure 4-9; f_{cm} is the characteristic compressive strength of material (MPa); σ_n is the average compressive stress across the key base area (MPa); and μ is the friction coefficient between the contacting surfaces, which AASHTO recommends as 0.6. Table 4-4 compares the shear capacity of the interlocking bricks under different axial pre-compressions and those estimated by AASHTO, Rombach and Specker's formula and the theoretical derivation presented above. Rombach and Specker carried out parametric study using numerical modelling and provided an empirical formula for estimation of the shear capacity of interlocking joint [162, 163]. Comparing the prediction results using their formula with the current testing results, it can be found that Rombach and Specker's formula substantially underestimates the shear capacity by about 30% when the prism is subjected to 10 kN axial pre-compression. This is because in their study, very small concrete shear keys were considered and direct key shear off failure was the primary failure mode, which differs to the failure mode of the interlocking brick prisms in this study. As the axial pre-compressive force applied to the prism increases, the prediction error using Rombach and Specker's formula reduces, which only slightly overestimates the 30kN pre-compression cases by 2.64%. This is because the contribution percentage of friction resistance in the overall shear capacity increases and that of shear key reduces with the increase in axial pre-compression. As a result, the relative error reduces. The AASHTO formula predicts different shear capacities of the interlocking brick prism, which slightly underestimates the shear capacity of the interlocking prism by -2.37% when 10 kN axial pre-compression is applied, but it overestimates the prism shear capacity by 23.96% when it is subjected to 30 kN axial pre-compression. This prediction error by AASHTO formula could be attributed to the following two reasons: firstly, AASHTO formula is empirically derived based on a large amount of testing data on concrete joints with small shear keys, which being similar to the Rombach and Specker's method is not necessarily suitable for prediction of the shear capacity of large shear key. Secondly, AASHTO specifies a large friction coefficient of 0.6, which could overestimate the

friction resistance at the joint between interlocking bricks. Therefore, under low axial pre-compression, AASHTO method underestimates the shear resistance of the shear key but overestimates the friction coefficient, whose effects cancel each other and ends up a closer match with the lab testing results. But when the axial pre-compression level is high, when the contribution of friction becomes more pronounced, the AASHTO method gives a much higher prediction on the shear capacity of interlocking bricks, which is very similar to the observation given by Zhou et al. on the precast concrete joint, who reported consistently higher shear capacity was predicted using AASHTO method than that using the Rombach and Specker’s formula. Therefore, the existing methods may not accurately predict the shear capacity of interlocking bricks. The theoretical derivation based on fracture mechanics theory overestimates the shear capacities of the interlocking brick prism by +1.57% and +16.44% when subjected to 10 kN and 30 kN pre-compression, respectively. This is possibly because the rough surface of the interlocking bricks is not considered, and thus the friction resistance estimation is not accurate.

Table 4-4. Comparison of shear capacities between laboratory testing results, numerical modeling and existing empirical and design formulae

Pre-load kN	Maximum shear force kN	Numerical simulation kN	error %	AASHTO kN	error %	Rombach & Specker kN	error %	Theoretical prediction kN	error %
10	21.70	21.86	0.74	21.19	-2.37	15.29	-29.55	22.04	1.57
30	27.56	28.16	2.18	34.16	23.96	28.29	2.64	32.09	16.44

4.5 Parametric study

To evaluate the influence of several design parameters on the shear capacity of interlocking bricks, and to derive an empirical formula for prediction of the shear capacity of interlocking bricks for engineering applications, parametric studies are carried out by varying the axial pre-compression level, surface friction coefficient, contact surface roughness, and concrete strength.

4.5.1 Effects of axial pre-compression and concrete strength

To quantify the influences of axial pre-compression and brick material compressive strength on the maximum shear load bearing capacity of the interlocking brick prism, a number of numerical simulations are conducted. The dimension of the brick is 200 mm × 100mm ×180 mm (length ×thickness ×height) as default. The mean brick surface roughness is assumed as 0.3 mm, and the coefficient of friction is 0.3, which are based on the default brick configuration. Four different axial pre-compression levels are modelled, i.e. 0.538 MPa, 1.073 MPa, 1.614 MPa and 2.152 MPa, which correspond approximately to the axial stress level in a ground floor wall for single- to low rise multiple-storey building [164]. Three different material strengths with $f_c=10$ MPa, 18 MPa, and 25 MPa are considered which are commonly used for concrete masonry units. Figure 4-10a) shows the equivalent shear strength versus axial pre-compressive stress. As shown, the equivalent shear strength increases with the axial pre-compressive stress. For example, for the interlocking prism with material strength of 25 MPa, the equivalent shear strength is 1.56 MPa when it is subjected to a 0.538 MPa axial pre-compressive stress, and it increases to 2.09 MPa when axial pre-compressive stress is 2.15 MPa. The relationship between concrete strength and the equivalent shear strength is shown in Figure 4-10b). As expected, brick material strength also strongly influences the brick shear strength. For instance, as the material compressive strength increases from 10 MPa to 25 MPa, the equivalent shear strength of the interlocking brick prisms (under 2.152 MPa axial pre-compressive stress) increases by +62.06%.

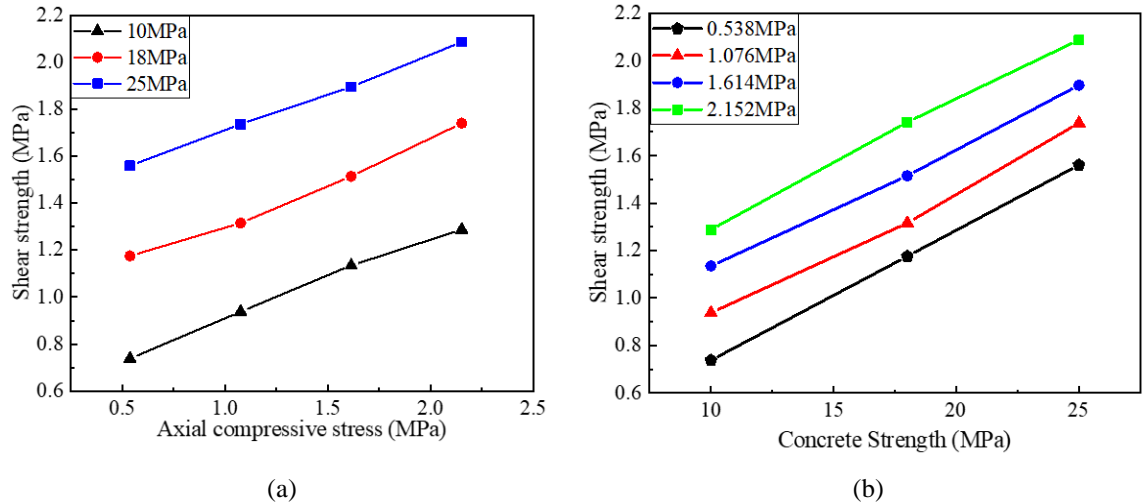


Figure 4-10. Relationships between a) prism equivalent shear strength with axial compressive stress;
b) prism equivalent shear strength with concrete strength

4.5.2 Effect of surface roughness and friction coefficient

Both the shear resistance of the interlocking shear key and interface friction contribute to the shear resistance at interlocking joint. Interface friction as a macro-level effect and surface roughness as a micro-level effect could both influence the friction induced shear resistance of interlocking bricks. To quantify the influence of interface friction coefficient on the prism shear capacity, a sensitivity analysis is carried out, where mean brick surface roughness is assumed to be 0.3 mm, axial pre-compression is 30 kN, material strength is 18 MPa, and the dimension of the interlocking brick is as default. Friction coefficient μ is varied from 0.1 to 0.6 with a 0.1 increment. Figure 4-11 shows the modelling results. It can be observed that with the increase of friction coefficient from 0.1 to 0.6, the initial stiffness increases from 71.74kN/mm to 126.29kN/mm by 76%. This is because a large shear force is needed to initiate the inter-block slip when the friction coefficient increases. The peak shear resistances of the interlocking brick prisms also increase as the friction coefficient increases. With friction coefficient increases from 0.1 to 0.6, the peak shear load increases from 26.12kN to 32.19kN by 23.24%. This is expected because friction resistance contributes to the shear capacity of the interlocking brick.

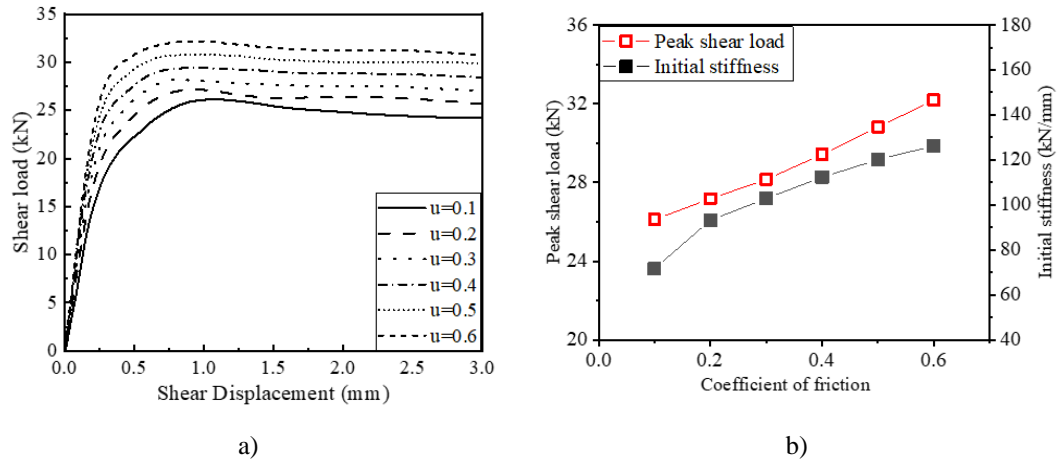
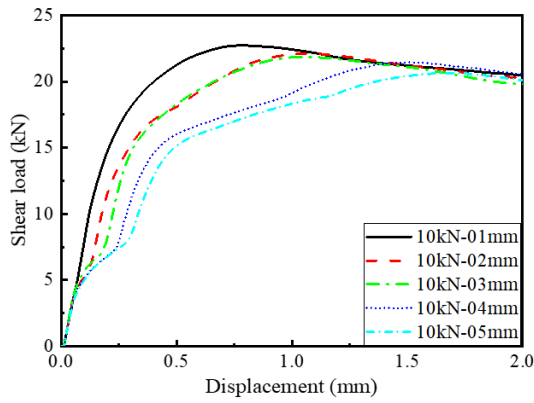
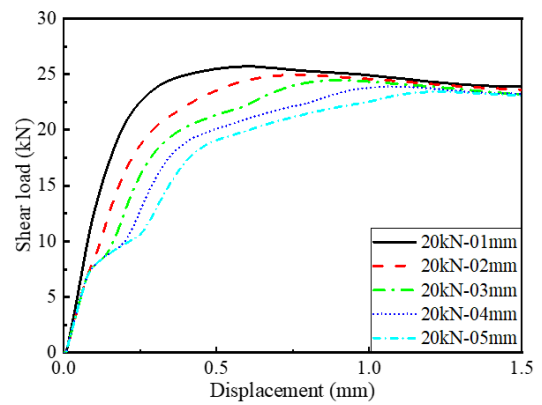


Figure 4-11. Effect of surface friction coefficient on a) shear load-displacement curves and b) peak shear load and initial stiffness.

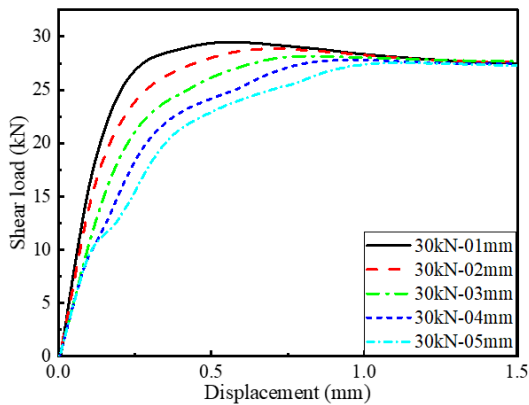
To quantify the influence of brick surface roughness on the shear resistance of the interlocking prism, surface roughness with height ranging between 0.1 and 0.5mm at an interval of 0.1mm is numerically modelled on the interlocking bricks. The unconfined uniaxial compressive strength of the brick material is 18MPa; the axial pre-compression varies from 10 kN to 40 kN, and the friction coefficient is 0.3. The shear force versus displacement relationships of specimens with different surface roughness as shown in Figure 4-12. For the interlocking brick prisms under 10 kN and 20 kN axial pre-compression, non-linear behaviour can be observed in the rising sections of the curves when the surface roughness is above 0.2 mm. This is because of the local compaction of the rough surfaces under axial compression, which is not obvious when surface roughness is 0.1 mm. Under higher axial pre-compression, this non-linear behaviour becomes unrecognizable. It can also be observed that with increased surface roughness, the displacement at peak shear load increases. This is because a larger displacement is needed for the asperities in the rough surface to achieve the maximum shear resistance. Similar influence of surface roughness can be found on initial stiffness. As summarized in Figure 4-13, under 20 kN axial pre-compression, the initial stiffness is 128.42 kN/mm for the interlocking brick prism with 0.1 mm surface roughness, which decreases to 83.55 kN/mm and 43.77 kN/mm when surface roughness increases to 0.2 mm and 0.5 mm.



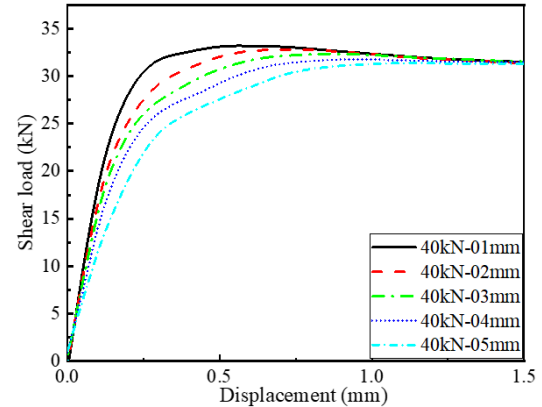
(a)



(b)

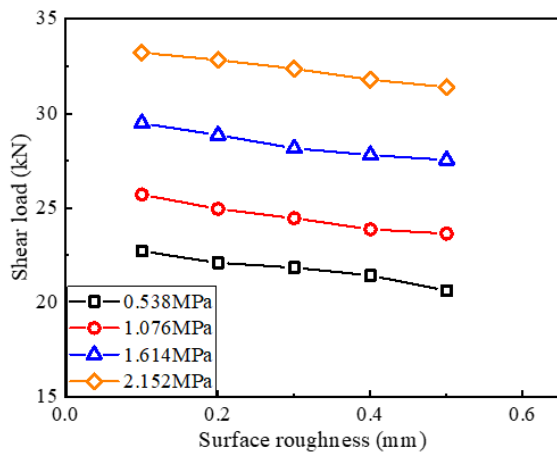


(c)

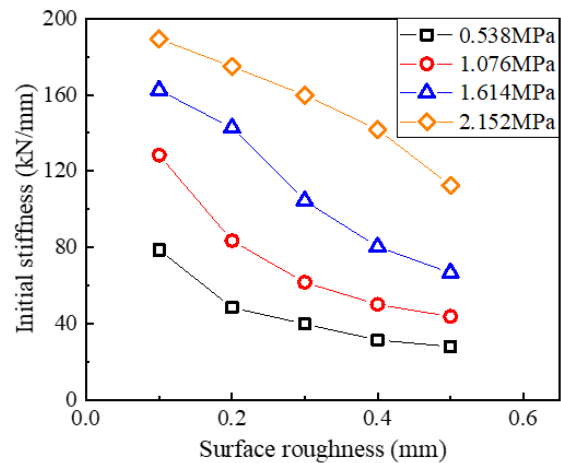


(d)

Figure 4-12. Shear load versus displacement curves for interlocking brick with different surface roughness (a) under 10kN axial pre-compression; (b) 20 kN pre-compression; (c) 30 kN pre-compression; (d) 40 kN pre-compression.



(a)



(b)

Figure 4-13. Effect of the surface roughness on (a) peak shear load; and (b) initial stiffness.

4.6 Empirical Formula

The above results demonstrate existing analysis and design formulae may not provide accurate predictions of the shear resistance of the interlocking brick prism. This could be attributed to the different shear key failure mechanism, inappropriate surface friction coefficient used in the calculation, and lack of consideration of contact surface roughness [40]. Based on the laboratory test results and numerical parametric study results, a material failure based empirical prediction formula is proposed herein.

4.6.1 Material failure model

The following equation with reference to AASHTO is employed to define the shear resistance capacity of the interlocking brick prism as:

$$V_j = A_{key}^V f'_c (C_1 + C_2 \sigma_n) + \mu A_{sm} \sigma_n \quad (4-5)$$

where $A_{key}^V f'_c (C_1 + C_2 \sigma_n)$ defines the contribution from the shear keys, and $\mu A_{sm} \sigma_n$ is the contribution from the friction resistance.

With large shear keys in interlocking bricks, the damage and failure of shear keys differ from those of small shear keys as defined in AASHTO. It is therefore necessary to properly re-examine the stress state and define the failure.

The failure envelope is employed herein which is based on the modification suggested by Hofbeck et al.[165]. The detailed derivation is presented in Appendix A. C_1 is the coefficient of shear strength, which takes into account the strength provided by interlocking keys ignoring the axial pre-compression, C_1 , can be written as

$$C_1 = \frac{0.2125 \cos \theta}{\sqrt{\left(\frac{1}{2} \times \frac{7A_{key}^V}{10A_{key}^H}\right)^2 + 1} - \frac{1}{2} \times \frac{7A_{key}^V}{10A_{key}^H} \sin \theta} \quad (4-6)$$

where θ is the inclined angle of the line L_2 relative to stress axis σ , which is tangent to the Mohr's circle at failure under uniaxial tension (see Figure A-2); A_{key}^H is the

horizontal projection area of the interlocking key along the direction of pre-compressive force, A_{key}^V is the vertical projection area of the shear key along the direction of applied vertical force.

Considering brick material characteristic compressive strength $f_{cu,k}$ varying from 10 MPa to 30 MPa which are common range for concrete masonry units, and various interlocking brick geometry A_{key}^V/A_{key}^H , the coefficient factor C_1 can be calculated and shown in Figure 4-14. A conservative $C_1=0.14$ is determined with the current brick material strength and shear key geometry. As derived in the Appendix, when axial pre-compression exists, the shear resistance by the shear key comprises coefficient C_2 which can be expressed as

$$C_2 = \frac{-B + \sqrt{B^2 - 4AC}}{2A\sigma_x f_c'} - \frac{0.2125 \cos \theta}{\sigma_x \left(\sqrt{\left(\frac{1}{2} \times \frac{7A_{key}^V}{10A_{key}^H}\right)^2 + 1} - \frac{1}{2} \times \frac{7A_{key}^V}{10A_{key}^H} \sin \theta \right)} \quad (4-7)$$

where σ_x is the normal stress due to axial pre-compression, and f_c' is concrete compressive strength; A , B and C represent the geometry coefficients (see Appendix A for the details).

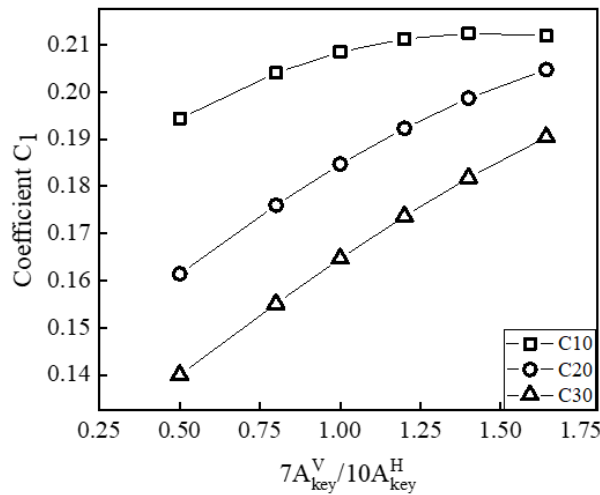


Figure 4-14. Coefficient C1 with respect to different geometries of interlocking key

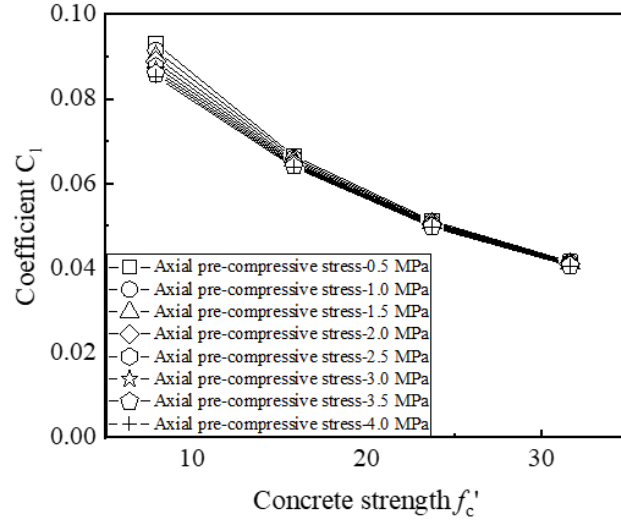


Figure 4-15. Coefficient C_2 with varying material strength

The variation of C_2 with material strength as well as axial pre-compression is shown in Figure 4-15. It is found that the coefficient C_2 changes insignificantly with axial pre-compression stress σ_n ($\sigma_x = \sigma_n$ in Eq. (4-5)). However, the coefficient C_2 decreases, as material compressive strength increases. The relationship between the coefficient C_2 and material compressive strength f'_c are linearly fitted and shown in Eq. (4-8).

$$C_2 = -0.002f'_c + 0.10076 \quad (4-8)$$

Substituting Eq. (4-8) and $C_1 = 0.14$ into Eq. (4-5), the shear capacity of interlocking brick is expressed using the following equation.

$$V_j = A_{key}^V f'_c (0.14 + (-0.002f'_c + 0.10076)\sigma_n) + uA_{sm}\sigma_n \quad (4-9)$$

It is worth noting that this equation is applicable to the interlocking brick in this study, whose geometry was optimized with proved best mechanical performance [166].

4.6.2 Modified design formula

To consider the influence of the brick surface roughness, modification is made by introducing correction factors, $f(h_{imp})$ and $g(h_{imp})$ in the analytical solution of Eq. (4-10) based on the results from simulations and laboratory tests, which account for the

influence of surface roughness on the shear resistance for the shear key and the rest flat regions. The shear capacity of an interlocking brick prism, $V_{j,imp}$, is given as follows:

$$V_{j,imp} = f(h_{imp}) \cdot A_{key}^V f'_c (0.14 + (-0.002f'_c + 0.10076)\sigma_n) + \mu \cdot g(h_{imp}) A_{sm} \sigma_n \quad (4-10)$$

Regression analysis on the simulations and laboratory testing is carried out to obtain the above modification coefficients in the proposed formula. The coefficient of determination (R^2) is found to be 95.44% for Eq. (4-11), which shows the predicted results are in good agreement with the values from the test and numerical modelling. The predicted prism shear strength is positively related to the material compressive strength, and inversely proportional to the roughness amplitude.

$$V_{j,imp} = (-0.3033h_{imp} + 1.7519)A_{key}^V f'_c (0.14 + (-0.002f'_c + 0.10076)\sigma_n) + \mu(-0.0884h_{imp} + 0.5353)A_{sm} \sigma_n \quad (4-11)$$

where h_{imp} is the surface roughness varying from 0.1 mm to 0.5 mm; f'_c denotes material compressive strength varying from 10 MPa to 30 MPa; σ_n stands for the normal stress from axial pre-compressive stress ranging from 0.54 MPa to 2.15 MPa; and μ is the friction coefficient ranging from 0.1 to 0.6.

The predicted shear strength using the above proposed formula, existing design methods, and laboratory testing data are compared in Figure 4-16. It can be observed that the proposed formula can better predict the shear strength of the interlocking brick under different conditions as compared to the AASHTO and Rombach and Specher's method.

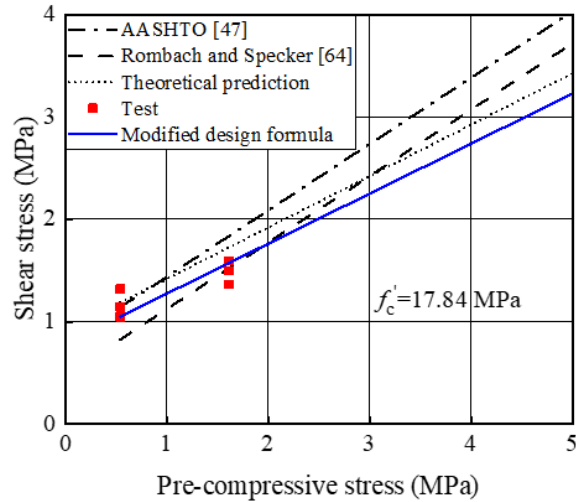


Figure 4-16. Comparison between different design models.

4.7 Summary

In this chapter, numerical modeling and laboratory tests are conducted to investigate the shear behavior of interlocking brick. The failure modes of mortar-less interlocking brick prisms are investigated. Three-dimension (3D) numerical models of the interlocking brick prism are developed using three different contact modelling approaches, which are validated against the laboratory testing results. Parametric study is conducted to evaluate the influences of friction coefficient, axial pre-compression, brick material strength and interface roughness because of brick surface unevenness on the shear capacity. Combining the testing results and numerical simulation, a modified analytical formula is proposed for prediction of the shear strength capacity of the interlocking brick prism. The following conclusions have been drawn:

1. Laboratory test and numerical modeling show the shear strength of the interlocking prism is dependent on the pre-compression level.
2. Numerical simulations with three different contact modelling approaches demonstrate that modelling the brick surface roughness is important for the reliable prediction of interlocking brick shear behavior. The simplified rough contact model is found to be able to give a good prediction of prism initial

stiffness, and shear capacities, whereas the model with perfect contact leads to large prediction error.

3. Existing design and analysis method may not accurately predict the shear strength of the interlocking brick with large keys because of the different shear failure mechanism, negligence of interface roughness, and inappropriate friction coefficient.
4. Parametric study evaluates the influences of the coefficient of friction, axial pre-compression, interface roughness, and material compressive strength on the interlocking prism shear strength.
5. A modified analysis and design formula with consideration of brick surface condition is proposed for prediction of the shear capacity of interlocking brick prism.

CHAPTER 5 INFLUENCES OF RANDOM IMPERFECTION DISTRIBUTION ON THE COMPRESSIVE PROPERTIES OF INTERLOCKING BRICK WALL

5.1 Introduction

It is known from Chapter 3 and Chapter 4 that the mechanical properties of interlocking brick assemblies are significantly influenced by the imperfections of the bricks due to construction tolerance. A systematic quantitative investigation is hence entailed for it. In this chapter, Monte-Carlo simulations are conducted to investigate the influence of spatially varying randomly distributed brick imperfections on the compressive behaviour of dry-stacking interlocking brick walls. With different imperfection distributions, the crack pattern and load path of the wall are analysed; the influences of the mean value and discreteness of imperfection sizes on the compressive strength and stiffness of the interlocking brick wall are quantified. As the structure is discrete with no bonding between the interlocking bricks, which differs from most conventional structures, extensive descriptions and discussions are made to cover the unique features of the structure, e.g., the discrete cracking patterns, the imperfection-related compressive strength, and the multi-stage stiffness development.

5.2 Numerical Model

5.2.1 Brick configuration

Figure 5-1 illustrates the interlocking bricks considered in this study, which has a width of 200 mm, a height of 180 mm and a thickness of 100 mm. It should be noted that the bricks and their material are the same as the ones described in Chapter 3.2.1. It is depicted again here because this chapter (Chapter 5) is based on a submitted

manuscript. Asymmetric interlocking shear keys are designed for the brick, where on the frontal side there is a wide shear key with a dimension of 70 mm width \times 30 mm height \times 35 mm, and on the rear side there are two smaller keys with geometric dimensions of 35 mm width \times 30 mm height \times 35 mm. The configuration of interlocking bricks is designed to provide improved shear resistance which differs from other existing interlocking bricks whose interlocking keys are usually only for self-alignment. The shear keys have inclined surfaces, which make the brick assembly easier and allows the bricks to slide on each other under high lateral force. The material of bricks is a mixture composed of sand, cement, gravel, and fly ash, therefore it has properties similar to those of concrete.

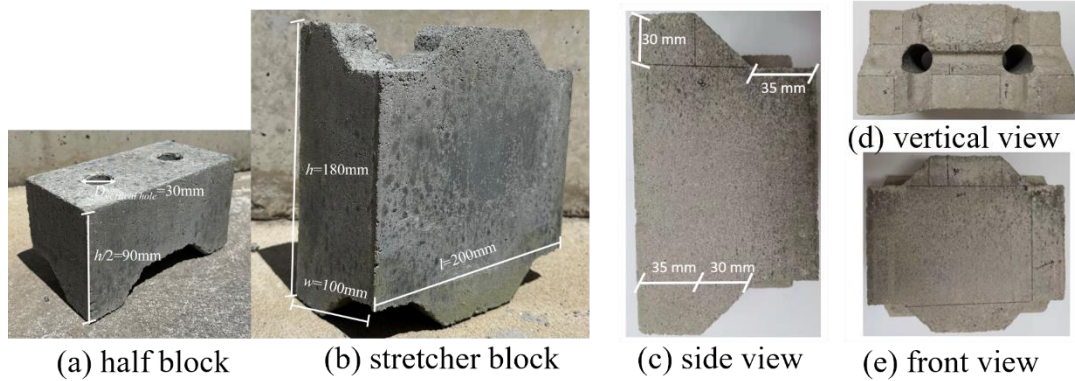


Figure 5-1. Configuration of interlocking blocks.

5.2.2 Finite element model

5.2.2.1 Model detail

A detailed three dimensional finite element model of interlocking wall with dimension 1200mm \times 800mm \times 100mm (height \times width \times thickness) is constructed using the commercial software Abaqus [167]. As mentioned above, interlocking bricks are modelled using solid element C3D8R with the Concrete Damage Plasticity (CDP) material model, in which both brick crushing in compression and cracking in tension can be considered. The material properties of the interlocking brick are shown in Table 5-1, where E_0 and ν denote the Young's modulus and the Poisson's ratio. More detailed

modelling of the interlocking brick properties and the corresponding verification can be referred to [168]. The compressive strength of brick material is 17.46 MPa. The tensile strength is assumed as $f_t=0.1 f_c$, which is a relationship commonly employed for concrete material [38, 146].

Table 5-1. Material properties of interlocking brick

Mass density (kg/m ³)	Elasticity			Plasticity			Viscosity Parameter
	Initial Young's modulus, E0 (GPa)	Poisson's ratio ν	Dilatation angle ψ (°)	Eccentricity	Biaxial stress ratio f_{ho}/f_{co}	K	
2565	13.49	0.2	30	0.1	1.16	0.67	0.0001

Note: K is the ratio between the second stress invariant on the tensile meridian and compressive meridian at initial yield.

5.2.2.2 Boundary condition and contact properties

For the interlocking brick wall, the bottom surface of the wall is fully fixed, and the lateral and rotational movements (out-of-plane) at the top of the wall are restrained while its vertical degree of freedom is enabled for the application of the vertical loading. Displacement-controlled method is used to load the interlocking brick wall till failure.

A hard contact is employed to model the contact behavior between adjacent bricks in the normal direction that the normal stress is transferred through the two surfaces. The contact surfaces will separate from each other when subjected to a normal tensile force; hence no tensile stress will be transferred across the contact surfaces. The contact behavior in the tangential direction of the interface is simulated using a finite sliding model following the Coulomb friction law. The tangential movement initiates when the surface traction stress at the connecting interface reaches the threshold shear strength τ , which is governed by the normal contact pressure p and the coefficient of friction μ ($\tau=\mu p$). The coefficient of friction between the contact surfaces of neighbouring interlocking bricks is taken as 0.3 following previous studies [38, 169].

5.2.3 Model validation

To validate the suitability and accuracy of the above numerical modelling method, it is used to model the compressive behavior of interlocking brick prisms in the authors' previous study [102]. As illustrated in Figure 5-2a, the specimen is composed of two full-sized interlocking bricks and two half blocks at both ends. The compressive load is applied using displacement-controlled loading method. The interlocking brick prism is numerically modelled using the above method in Section 2.2. Both perfect contact and imperfect contact are considered to simulate brick imperfections at the joints. There is no gap between bricks at the joint for the perfect model. For the imperfect model, gaps between bricks are modelled. Each surface imperfection height was measured using a height dial indicator (Figure 5-2b), and the measured gap sizes are applied to the numerical model with imperfect contact as shown in Figure 5-2c. An average gap width is 0.29 mm with a standard deviation of 0.16.

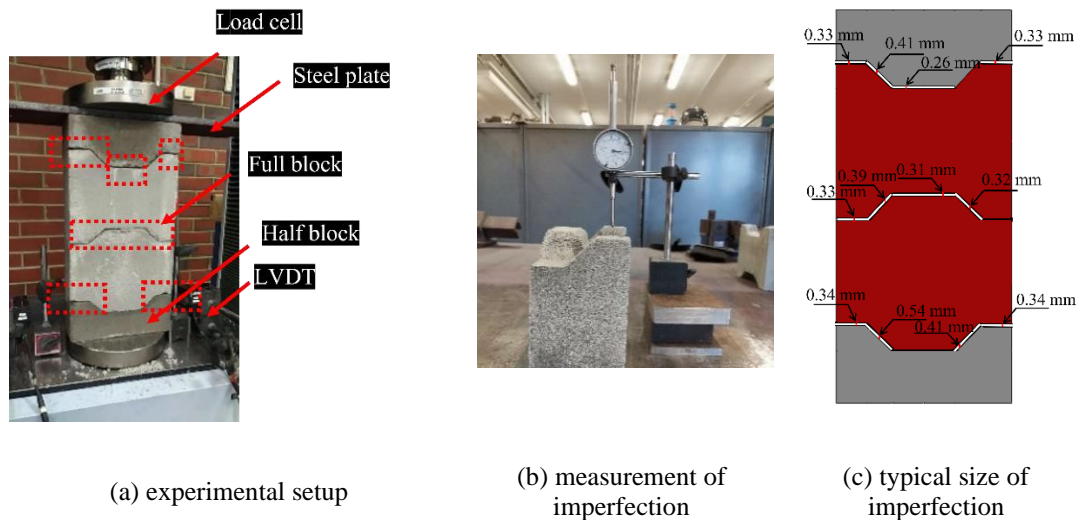


Figure 5-2. Experimental setup and numerical model

Figure 5-3 compares the compressive force versus axial displacement curves from the laboratory test and the numerical simulations. As shown, in the laboratory test the force increases gradually with the imposed displacement because of seating effect. As gaps gradually close, the force increases quicker until reaching the peak load of 112.8 kN and then plummets due to brick damage. The numerical model with perfect contact

predicts an ultimate load capacity of 113.8 kN. However, it could not model the seating effect because there are no pre-existing gaps. Moreover, an initial stiffness of 71.18 kN/mm is predicted, which is significantly larger than that of the lab test (61.85 kN/mm). The numerical model with imperfect contact predicts an ultimate capacity of 105.0 kN indicating less than 7% difference comparing to the lab testing result, while the predicted initial stiffness of 54.49 kN/mm by the numerical model with imperfect contact is much similar to that of the laboratory test.

It demonstrates that the numerical model considering brick imperfection is crucial for proper estimation of the stiffness of mortarless interlocking brick wall under compressive loading.

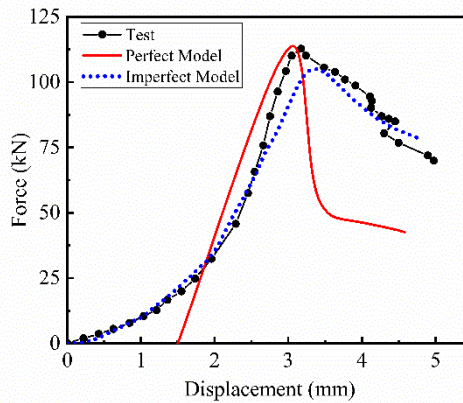


Figure 5-3. Comparison of compressive force versus axial displacement curves from laboratory test and numerical modelling

Figure 5-4 compares the failure modes of interlocking brick prisms from laboratory test and numerical simulations. In the laboratory test, wing cracks are initiated at the corner of the interlocking brick key and extend both up and down. Due to the non-perfect contact conditions between neighbouring bricks, asymmetric failure mode is observed. The numerical model with imperfect contact predicts similar damage pattern where cracks initiate on the keys of the second brick, and then extend vertically. The model with perfect contact predicts typical X-shaped failure because of the damages of shear keys due to symmetry, which could reflect the damage pattern of interlocking brick

but not able to fully represent the influence of imperfect bricks. Through the above comparison, it can be found that the developed numerical modelling method could reasonably closely represent the behavior of mortarless interlocking brick wall with consideration of brick imperfection under compressive loading.

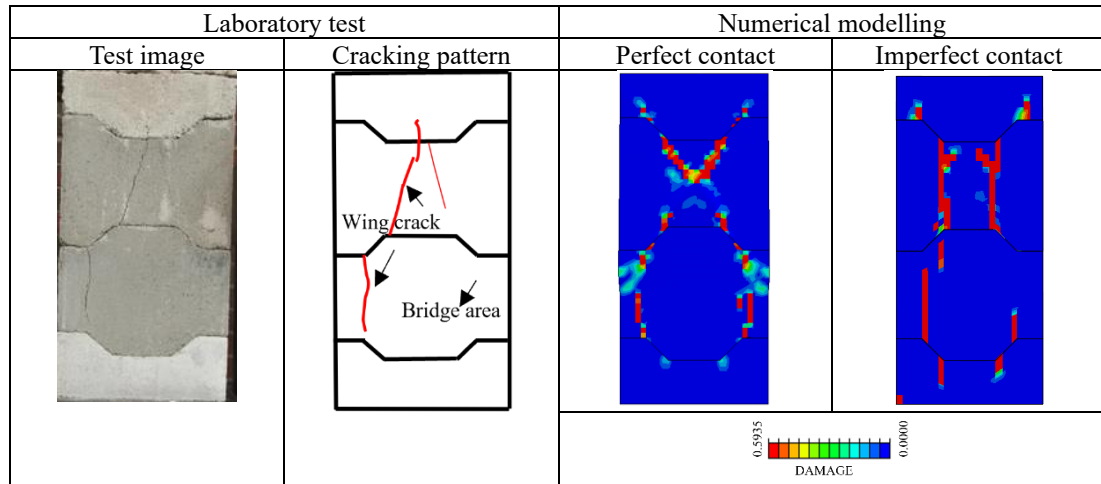


Figure 5-4. Comparison of prism damage and failure patterns

5.2.4 Size effect

The modelled wallet size (1200mm height by 800 mm width by 100 mm thickness) follows the recommendation of BS1052-1 [170] for the determination of compressive strength of the interlocking brick wall. To examine the potential size effect and to quantify its influence on the modelled compressive strength of the mortar-less interlocking brick wall, a group of masonry walls with different dimensions are numerically modelled, i.e. 600 mm × 400 mm × 100mm, 1200 mm × 800 mm × 100 mm, and 2400 mm × 1600 mm × 100mm (as shown in Figure 5-5a). For easy engineering application, axial stress and strain are used to quantify the performance of the interlocking brick wall in lieu of axial compressive load and displacement. The axial stress is the averaged compressive stress in the cross section which is calculated by dividing the measured axial compressive load by the cross-sectional area of the interlocking brick wall; and the strain is calculated by dividing the vertical displacement with the initial height of the interlocking brick wall. Figure 5-5b compares the maximum compressive strengths and the initial stiffness, from which it

can be found that varying the width and height of the wall model by four times leads to a maximum variation in the compressive strength by 3.40%, and a maximum variation in the stiffness by 0.23%. It demonstrates that the influence of model size on the compressive loading capacity is insignificant and the recommended wallet dimension by BS1052-1 is appropriate for predicting the compressive strength of mortar-less interlocking brick wall.

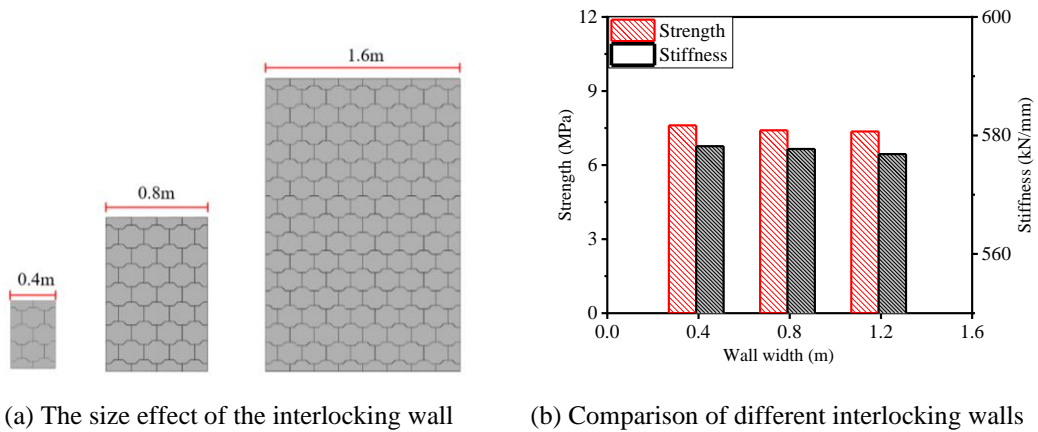


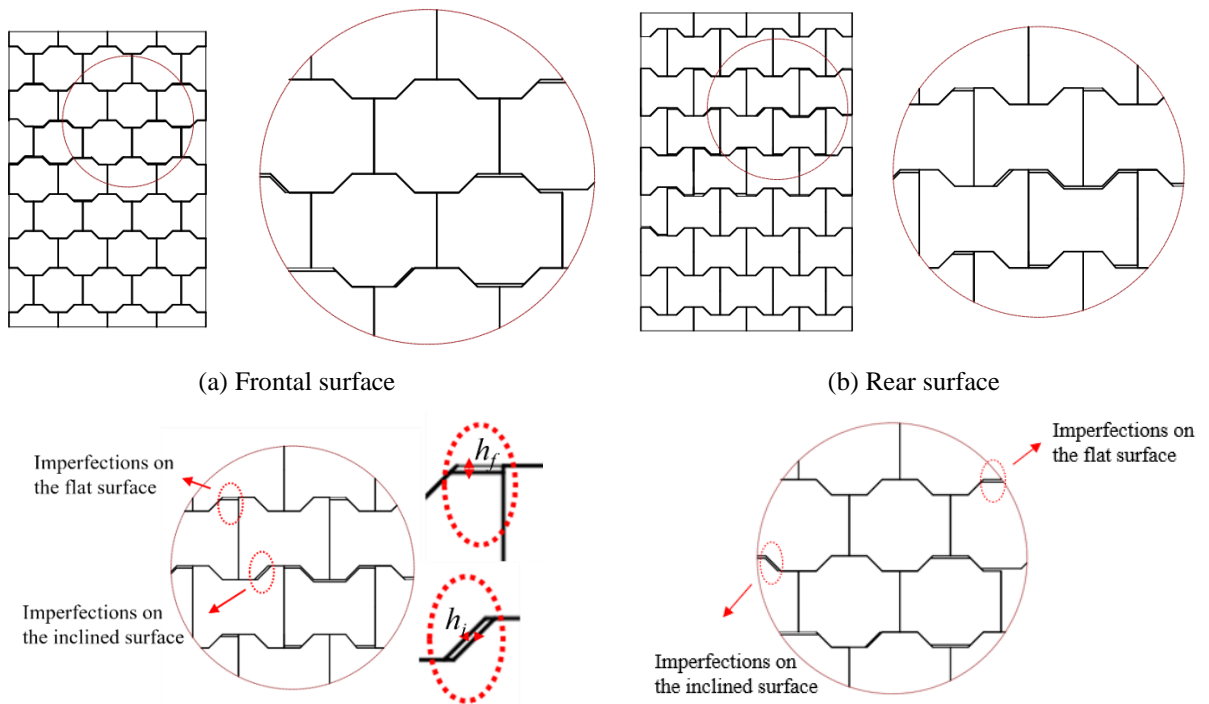
Figure 5-5. Influences of size effect.

5.3 Probabilistic Models

Compared to conventional masonry where mortar bonds bricks together leading to negligible influence of brick imperfection, dry-stacked interlocking bricks are constructed without mortar. Unavoidable imperfections in brick could potentially result in significant local stress concentration and relative movements of adjacent bricks and thus influence the mechanical performance of the masonry structure. This paper focuses on quantifying the influence of geometric imperfections on the compressive properties of interlocking brick walls, where other uncertainties such as brick material strength, are not explicitly investigated. To study the influence of random imperfection of interlocking brick on the compressive strength and axial stiffness of the interlocking brick wall, the above-selected 1200 mm × 800 mm × 100 mm interlocking brick wall with spatial brick/joint imperfection is modelled.

5.3.1 Brick and joint imperfection

Considering the manufacturing process of interlocking bricks which are pressed in mould using servo-controlled high-pressurized brick machine, imperfections could occur to the produced bricks with variation to brick heights, i.e., total brick height, and shear key height, and inclined surfaces as shown in Figure 5-1. Figure 5-6 shows the set-up of interlocking brick wall with spatial imperfections. Because of the asymmetric shear key layout on each interlocking brick unit, the wide shear key and the small keys on the frontal and rear surfaces are shown respectively in Figure 5-6a and Figure 5-6b. Considering the shape and geometry of the shear keys, imperfections could exist on the flat surfaces or the inclined surfaces of the shear keys, as seen in Figure 5-6c and 6d. As shown in Figure 5-6c, the imperfection height h means the roughness height normal to the surface of interlocking brick. It is to note that the sizes of the above imperfections are normally small, since bricks with large imperfections will be filtered out in the quality control process, and bricks with large imperfections caused during transportation will also be identified in construction and usually discarded because they will not stack properly.



(c) imperfection types on the frontal surface

(d) imperfection types on the rear surface

Figure 5-6. Illustration of interlocking wall with random spatial imperfections.

5.3.2 Stochastic analysis with Monte-Carlo simulation

The spatial variability of imperfection for interlocking brick wall is generated using the above-mentioned numerical method in stochastic analysis based on the Monte-Carlo simulations. Since bricks are manufactured in large quantities, binominal distribution is employed to describe the existence of imperfection on each brick unit. The probability of imperfection for the binominal distribution, p , depends on the quality control in brick manufacture. Following the recommendation of brick manufacturer, the probability of imperfection existence during manufacturing is stratified into four groups: high quality, high-medium quality, medium-low quality, and low quality, which correspond to 0-25%, 25-50%, 50-75%, and 75-100% possibility of each brick unit having imperfections. p is assumed to follow uniform distribution within each group. It is worth noting that Monte-Carlo simulations usually use simple random sampling, which entails a large number of simulations to achieve convergence, therefore is computationally costly. The employed stratified sampling method could help to achieve an improved convergence rate. The stratified sampling method is operated by subdividing the sample space into smaller regions and sampling within these regions. In so doing, the produced samples could more effectively fill the sample space and therefore reduce the variance of computed statistical estimators. Previous study demonstrated this sampling method could provide fast converging analysis for Monte-Carlo simulation with satisfactory accuracy [171]. The imperfection size of each brick unit is simulated following the truncated normal distribution with a mean of 0.3mm, which was determined through statistical analysis on the different batches of brick specimens [168]. The truncated normal distribution rather than the normal distribution is used herein to avoid a negative joint gap value. A python-based program is written to automatically generate interlocking brick wall models in batches in Abaqus. Despite the complex configuration of bricks due to the

random imperfections, in the numerical modelling all the initial locations of the bricks are set at the proper positions as an intact wall without considering the imperfection. The generation of spatial variability model can be expressed as follows:

(1) For a 1200 mm × 800 mm × 100 mm interlocking brick wall, it comprises of 40 bricks. Each brick is labelled with a number from 1 to 40 in the sequence from the bottom left to the top right in layers.

(2) Depending on the location of the imperfections in one brick, the imperfections of a brick are classified into four types, i.e., height imperfection on the small keys, height imperfection on the large keys, slide (side) imperfection on the front sliding surfaces, and slide imperfection on the rear sliding surfaces. The existence of imperfection is randomly determined following the Binominal distribution with a possibility of p . The brick quality is classified into four groups, i.e. high quality, high-medium quality, medium-low quality, and low quality, depending on the value of p .

(3) Once the location of imperfection in a brick is determined, the imperfection size on the surface of this brick is assumed to be uniform over the entire surface for simplicity. The imperfection size follows the truncated normal probability distribution with a mean $h_m=0.3\text{mm}$ and a specific standard deviation. The characteristic value of imperfection height is estimated using $h = h_m \pm 1.645\sigma$. Since there is very limited data on the standard deviation of imperfection size σ , the COV is assumed to vary between 0.1 and 0.5 [172].

(4) Each numerical model is established with the random spatial imperfection distribution, after which numerical modelling is carried out by loading the wall using displacement-controlled compression method till the failure of the wall. The peak compressive force and stiffness of the wall are determined through the axial load versus axial displacement curve simulated by the numerical analysis. The compressive strength of the interlocking brick wall is determined with the peak compressive force.

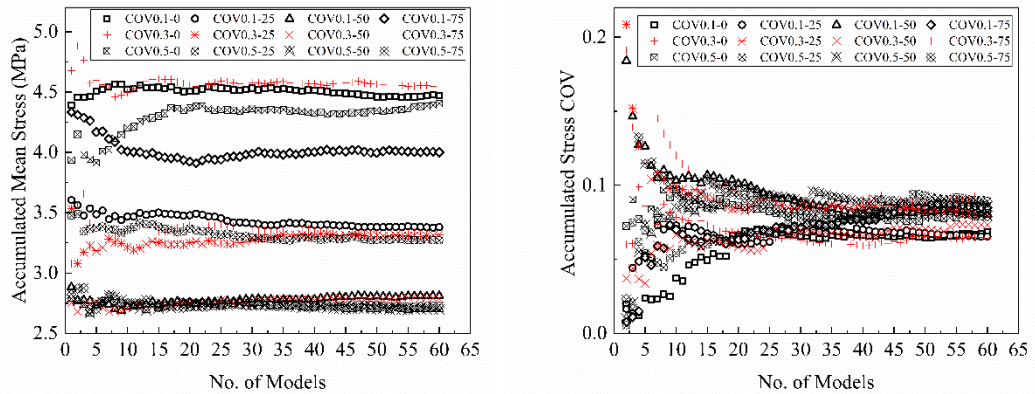
(5) Convergence analysis is performed, where the accumulated mean compressive

stress and accumulated compressive stress COV for the interlocking wall with different numbers of simulations are examined to determine the termination of numerical simulations. Repeat the above steps 1 to 4 until the statistical convergence is reached, in which the COV varies between 0.1 and 0.5. A COV of 0.1 represents the imperfection size has slight dispersion, while a COV of 0.5 represents the imperfection size has large dispersion.

(6) The average compressive stress is calculated by the ratio of the total force on the interlocking wall and the total sectional area of the brick wall. The average strain is measured by the ratio of the compressed displacement at the top surface of the interlocking wall and the height of the interlocking wall. The data are counted into different groups with different COVs and/or different range of defect rates (p) and then used for construction of the histograms of compressive strength, equivalent stiffness and linear stiffness. The probability density function is generated and compared with specific probability density functions to determine the type of distribution.

5.3.3 Convergence study

Convergence test of Monte-Carlo simulations is performed with the numerical model for interlocking brick walls of different qualities. Figure 5-7 presents the variations of the mean compressive strength of interlocking brick walls and its corresponding COV acquired from the Monte-Carlo simulations. It is found that after 60 random cases, the variations on the mean compressive strength and the corresponding COV are very small, indicating the simulations converge. Therefore, 60 simulations are needed to achieve the converged results. It is to note that the number of simulations to achieve convergence is small because the stratified sampling method is employed, which helps to unconditionally reduce the variance of statistical estimators when compared with the simple random sampling method [171].



(a) Mean compressive strength (b) COV of mean compressive strength

Figure 5-7. Convergence of Monte-Carlo simulations

5.4 Crack Development and Failure Mode

Imperfection could influence the crack pattern of individual interlocking brick unit, whose spatial distribution then influence the crack development and failure mode of the interlocking brick wall. In this section, the crack pattern of individual interlocking brick units with imperfections on different key surfaces are presented. Then, crack initiation and development of walls made of imperfect interlocking bricks are presented and analysed. The failure modes of the interlocking brick wall with spatial distributed imperfections are discussed.

5.4.1 Cracking pattern

Figure 5-8 presents typical brick cracking patterns caused by different types of brick imperfections. One single interlocking brick is modelled with its bottom fixed, and compressive load is applied gradually to its top until failure. Imperfection is introduced to different surfaces of this interlocking brick to examine the associated crack patterns of the unit brick. It is to note that there are more than dozens of combinations of imperfections on the different surfaces of an interlocking brick, which nevertheless yield similar brick cracking pattern. Therefore, only typical cases of brick unit with imperfect surfaces are listed herein with unique cracking patterns. For Case 1, imperfection exists on the tenons of the rear surface (green highlighted area) while the

other surfaces are all intact. With brick imperfections, load can only be transferred through the contacting surfaces. As a result, two vertical cracks are initiated propagated downwards on the rear surface because of the increased stress owing to smaller contact area. When more imperfections exist on the rear surface as well as the frontal surface as in Case 2, cracks also initiate on the frontal surfaces. Moreover, because of unsymmetric imperfection on the inclined surfaces, unsymmetric damages can be seen on the brick. In Case 3, imperfections exist on the inclined surfaces on the front key as well as the flat surfaces of the rear shear keys. Because of the unsymmetric load distribution on the brick, crack initiates on the right wing of the rear surface.

With more imperfections existing on more surfaces of an interlocking brick as in Case 4 where only the flat surfaces on the front shear key and one single surface on a rear key are intact, the applied compressive load can only be transferred through very limited regions in the brick. As a result, crack is developed on the edge of the load-bearing surfaces and extends from the front of the brick to the rear side of the brick. In Case 5, the flat surfaces on the right wing of the front face are intact, through which load is transferred. Under gradually increased compressive load, crack is developed on this wing. Because of partial contact on the rear face of the brick, this crack extends towards the rear surface of the brick leading to the eventual failure.

From the above illustrations it can be seen that the existence of imperfection on dry-stacked interlocking brick on different surfaces could strongly influence the cracking pattern. Those imperfections, which determines the load transfer path in one single brick, would interact with adjacent blocks when multiple bricks are stacked together to create an interlocking brick wall. The crack development and failure mode of interlocking brick walls with different quantity of imperfections, their spatial distributions and different imperfection sizes would therefore be different, which will be analyzed and discussed in the following section.

Frontal surface Rear surface Frontal surface Rear surface

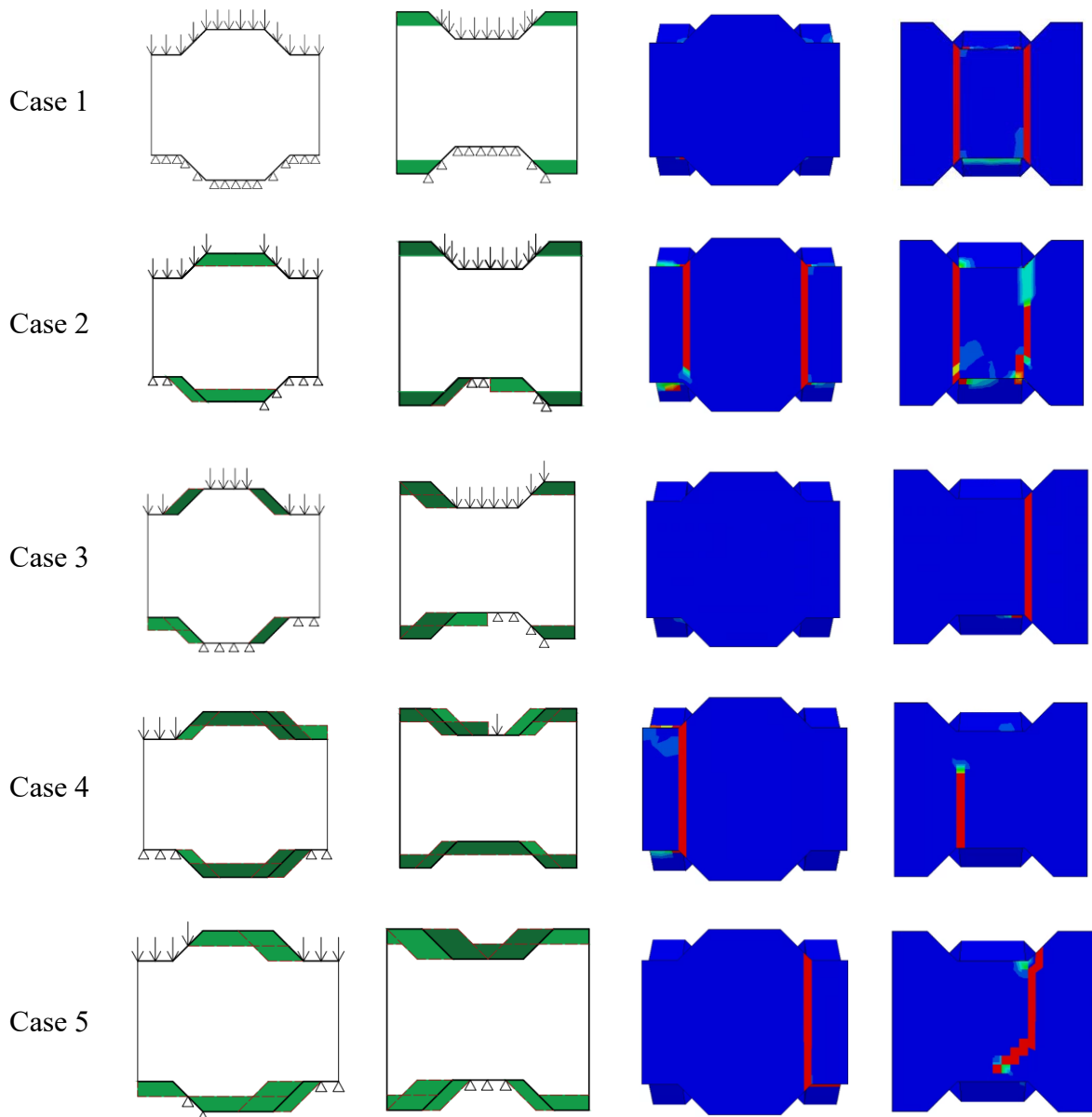


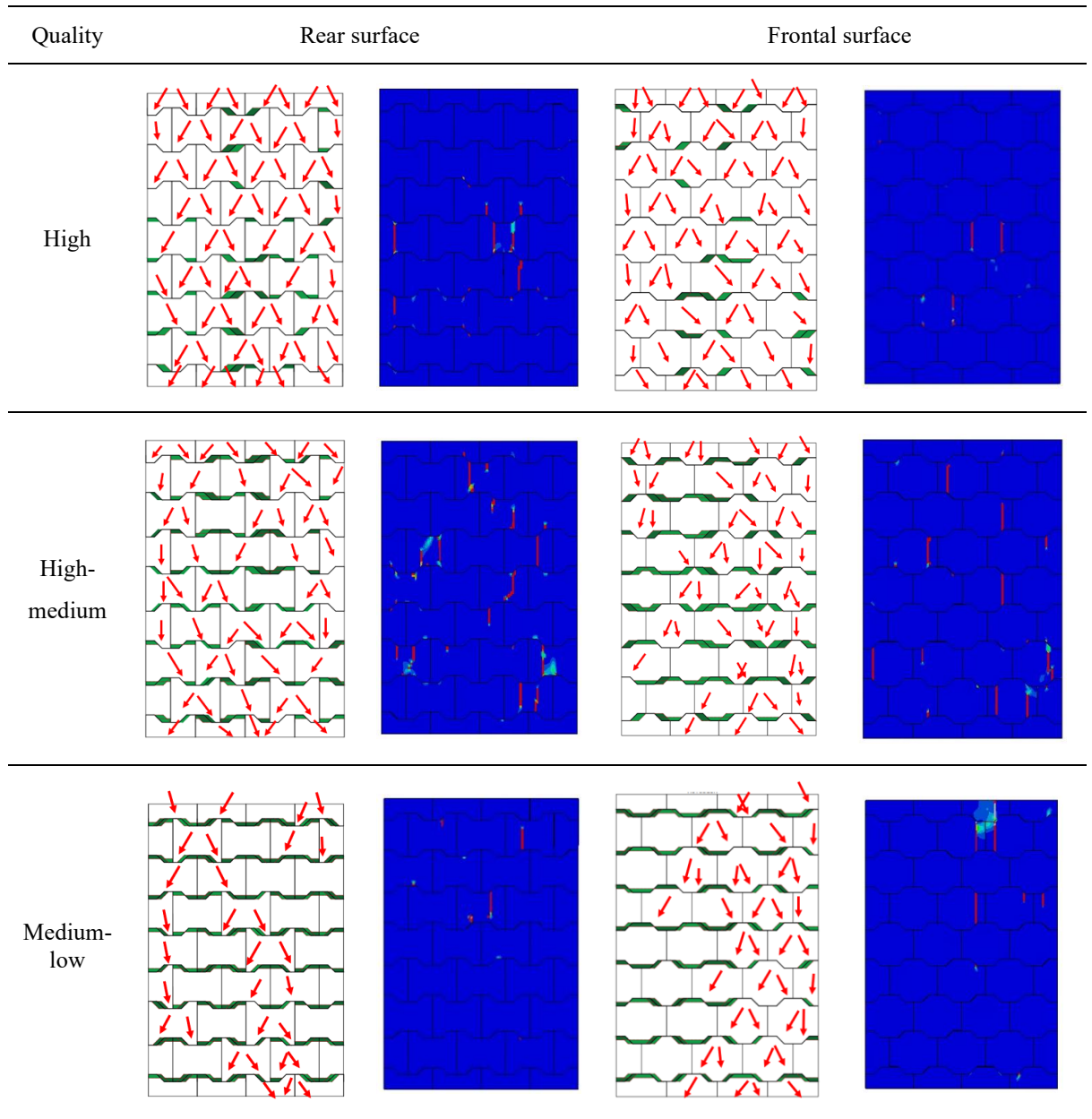
Figure 5-8. Crack patterns for interlocking brick with different imperfections

5.4.2 Initial crack and crack development in a wall

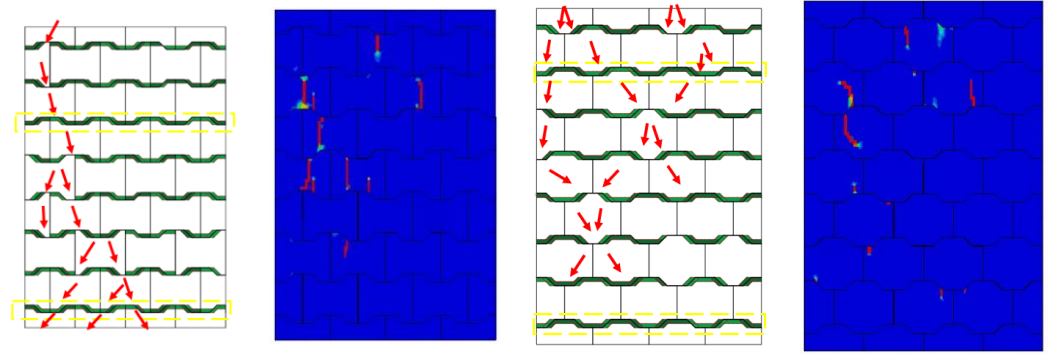
To demonstrate crack development and wall failure mode of interlocking brick walls with spatially varying imperfections, without loss of generality four typical interlocking brick walls made of high-quality, high-medium quality, medium-low quality and low-quality bricks are analysed. Figure 5-9a shows the load path, damage/crack patterns. The randomly generated imperfection locations and sizes are highlighted in green colour (darker indicates larger imperfection size). The corresponding load-displacement curves are shown in Figure 5-9b. For the high-quality

wall, the compressive load increases almost linearly with the axial displacement of the wall until Point A (more than 75% of compressive strength is achieved), when crack initiates on the wall. As can be seen in Figure 5-9a, initial cracks are developed on the interlocking bricks with large size imperfections. This is because under compressive loading, smaller joint gaps due to brick imperfections would close earlier than the larger gaps, which enables load transfer at these joints and hence more uniform stress distribution. But it also leads to non-uniform joint gaps with large brick imperfections, which causes stress concentration and hence crack initiation. For the high-medium quality wall, the compressive load that the wall could withstand increases linearly to about half of the maximum compressive strength, which is lower than that of the high-quality interlocking wall. Being similar to the high-quality wall, cracks initiate around the joints with larger size imperfections. It can be seen from Figure 5-9a that for the high-quality and high-medium quality wall, because relatively less imperfections exist and smaller imperfections would close under the imposed compressive loading first, the compressive force can then be transferred through multiple load paths over the interlocking bricks. For the low-quality wall, because of the widely spread imperfections on bricks, under the initial compressive loading, less contacts are developed between bricks resulting in seating effect (as highlighted in yellow). As a result, with the increased compressive loading, only less number of load paths are developed. Similar to the medium-low quality wall, initial cracks are developed around the load path where bricks are bearing high compressive stress. As shown, the low-quality brick wall has higher compressive strength than the medium-low and high-medium quality wall although its equivalent stiffness is small owing to a relatively large initial seating movement to close the gap between bricks. This is because the low quality wall is associated with wider spread imperfections. Under compressive loading, the gaps in brick wall close relative uniformly, whereas the medium-low and high-medium quality walls have less number of imperfections. Under compressive loading, closing of the gaps is not uniform and causes stress concentration, hence more damage

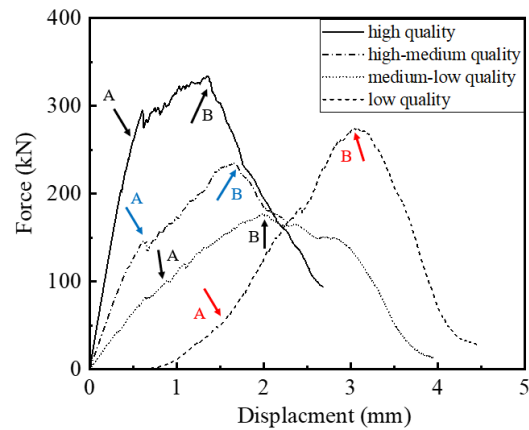
to the bricks. Therefore, their compressive loading capacity is smaller than that of the low-quality wall.



Low



(a) Load path, crack distribution and failure pattern



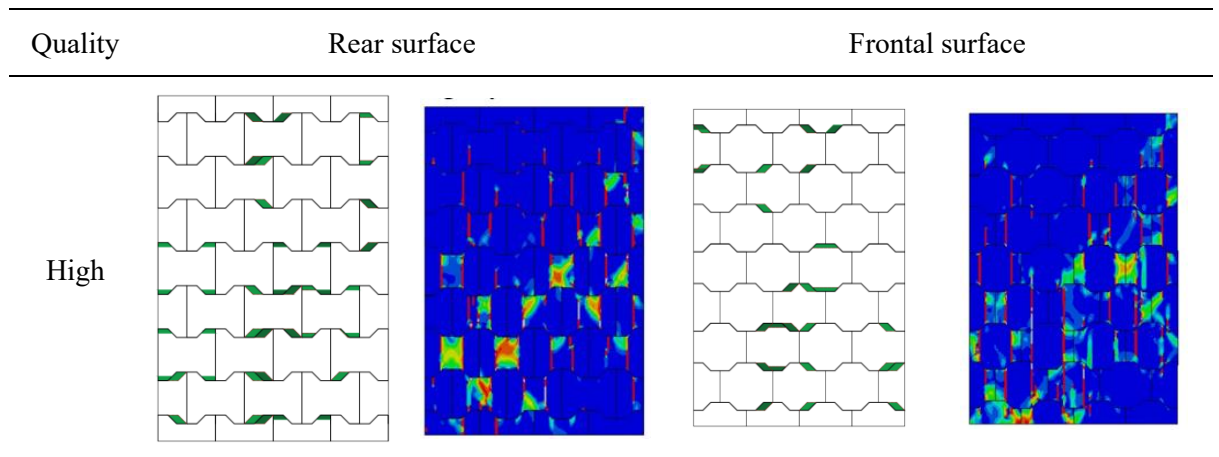
(b) Force-displacement curves

Figure 5-9. Initial crack and load path at the stage of OA

5.4.3 Failure mode

As the imposed compressive load continues to increase, these cracks extend, and more cracks are developed until the maximum compressive strengths of each wall are reached. Figure 5-10 shows the eventual damage contours of the four interlocking brick walls of different qualities. Because the distribution and size of brick imperfections are random, the crack pattern are asymmetric and random. Brick cracks widely spread among the walls. But some common cracking similarities exist in these four quality interlocking walls. Cracks initiate from the shear keys with vertical cracks indicating tensile damage [102]. Compressive damages are then developed in the cracked bricks as the wall is subjected to further increased compressive loading. It indicates that increasing the post-cracking strength of interlocking bricks would improve the mechanical performance of interlocking brick wall under compressive

loading. In the meanwhile, some differences can be observed on these four different quality interlocking brick walls: for the high-quality and high-medium quality walls, since the majority of bricks are intact thus in full contact for the compressive load to transfer through, the load distributes relatively uniformly and thus cracks are also more uniform, which leads to a higher compressive capacity and stiffness than those of the walls of the other qualities. For the medium-low quality wall with more imperfedted bricks, load is redistributed after the initial cracking of bricks around the load path. More bricks are thus to bear the compressive force. More cracks can be observed on the failed walls when the peak compressive capacity of the wall is reached. For the low-quality wall with the majority of bricks having imperfections, joint openings due to brick imperfection actually would close under the initial compressive loading, leading to a more uniform distribution of stress on the entire brick wall. As a result, on the final damage contour of the low-quality wall, cracks are distributed widely and more uniformly as compared with the medium-low quality wall.



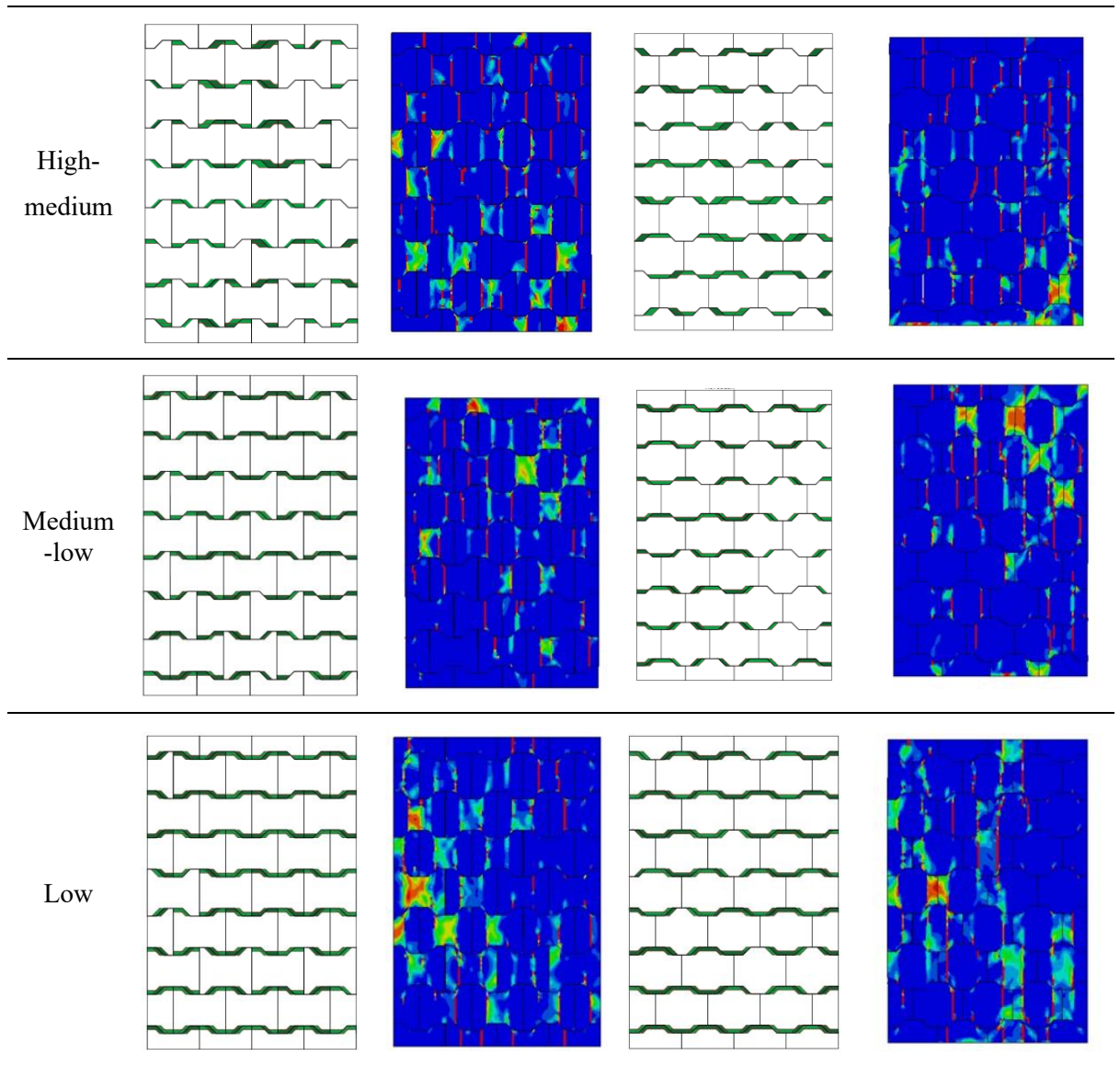


Figure 5-10. Damage contours of interlocking brick wall at peak compressive loads

5.5 Results and Analysis

The influence of random imperfections of interlocking bricks on the compressive behavior of interlocking brick wall is presented and analysed in this section. The compressive stress-strain curves are firstly presented. The compressive strength and axial stiffness of interlocking brick wall are summarized and analysed.

5.5.1 Stress-strain curves

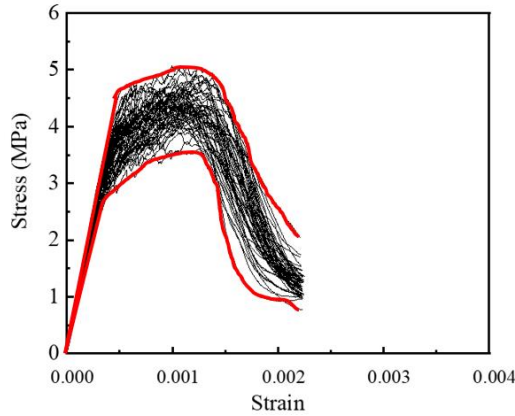
Figure 5-11 shows the compressive stress-strain curves acquired from the spatial models of interlocking brick walls with imperfections. It is noted that the engineering

stress and engineering strain of the wall through the loading process are used in the figures, which are calculated based on the net cross section area and the height of the wall, respectively. They are adopted here to have an intuitive view of how the strength and deformability of the wall are influenced by the imperfections. Figure 5-11 a-d show the stress-strain curves acquired from interlocking walls of high quality, high-medium quality, medium-low quality and low quality respectively with COV=0.1. For high quality walls, linear elastic behavior can be observed at the beginning of the compressive load until reaching about the 75% of the maximum compressive capacity. As the compressive load further increases, the slope of the curve decreases, and the compressive load increases non-linearly, after which it begins to drop, indicating the brick walls experience substantial damage. For high-medium quality walls, the load increases linearly to about 50% of the compressive capacity reflecting the linear elastic stage is shorter than that of the high quality walls. Similar non-linear stage and post-peak behaviour can be observed. As shown, the random variation of brick imperfection has minimum influence on the initial modulus of the high-quality brick wall although it has substantial influence on the stress-strain curves after yielding and the compressive strength of the wall. The random variation of brick imperfection, however, greatly affects the initial modulus of the interlocking walls with high-medium quality brick. The influence of random variations of brick imperfection on the initial modulus becomes more pronounced when the brick quality deteriorates, i.e., more prominent variation is observed. As shown, the compressive strength of the wall decreases with the deterioration of the brick quality from high-quality to medium-low quality bricks, indicating brick imperfection also affects the wall compressive strength. However, when the brick quality is low, the compressive strength increases although the initial equivalent stiffness decreases substantially. This is because, as briefly discussed above, compared to the medium-low quality bricks, the imperfection of the low-quality brick leads to more uniform imperfection distribution across the entire wall, which results in apparent seating effect, i.e., initial slippage at small compressive load. After the pre-

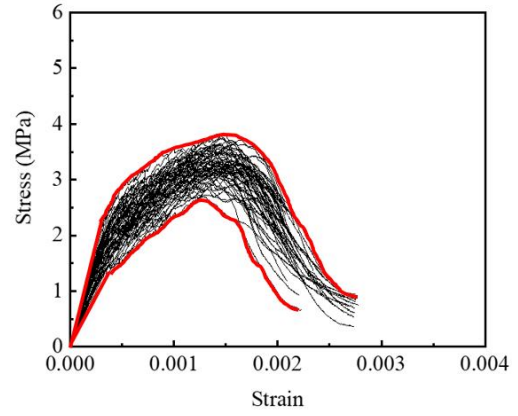
existing joint gaps due to brick imperfections close, an almost linear behavior similar to the high-quality or high-medium quality walls is observed. Comparing the stress-strain curves of low-quality walls with the other categories, it can be found that the gradual closure of joint gaps due to brick imperfections accounts for the non-linear progressive stiffening behavior of dry-stacked interlocking brick wall. Among the four categories of brick quality considered, the medium-low quality bricks lead to the smallest compressive strength. This is because the medium-low quality bricks associate with the relatively non-uniform imperfection distributions across the brick wall, which result in smaller compressive loading capacity of the wall because of the local damage induced by stress concentration related to the non-uniformly distributed imperfections. Overall, it can be found that increasing the probability of brick imperfection leads to the deteriorated wall quality and decrease in the initial compressive stiffness of the wall because of the increased number of inter-brick gaps for the first three considered quality levels of the interlocking wall. For the wall with low-quality bricks, strong seating occurs at the initial stage of load application, resulting in small equivalent stiffness of the wall. However, once the relatively uniformly distributed gaps close, the wall could resist the compressive load uniformly, resulting in similar behaviour to the wall made of high-quality bricks.

Figure 5-11 e-h and Figure 5-11 i-l show the stress-strain curves of the interlocking brick walls with $COV=0.3$ and 0.5 , respectively. For easy comparison, the upper bound and lower bound for stress-strain curves with $COV=0.1$ are sketched in these figures. As can be seen, for high-quality and high-medium quality walls, the scatter of stress-strain curves slightly increases with the rise of COV , which nevertheless appear to be insignificant because only limited numbers of bricks in these walls have imperfections. Moreover, the COV of brick imperfection has insignificant influence on the wall compressive strength. It can also be found that for low-quality walls, the seating effect decreases as the COV increases, because with a larger variation of brick imperfection, gap closure could happen earlier and easier. Also, it tends to lead to lower compressive

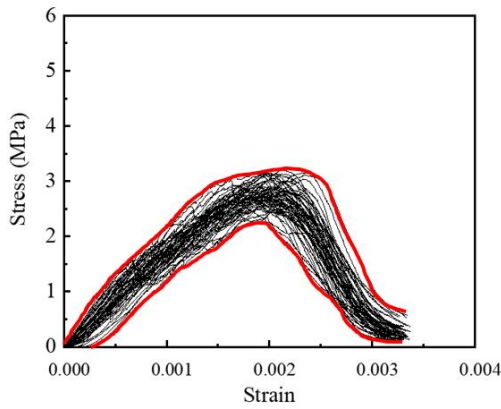
strengths through comparing Figure 5-11 d, h and l. Overall, the COV of brick imperfection size has more obvious effect on the initial stage and compressive strength of low-quality interlocking walls which however is insignificant on interlocking brick walls of other qualities.



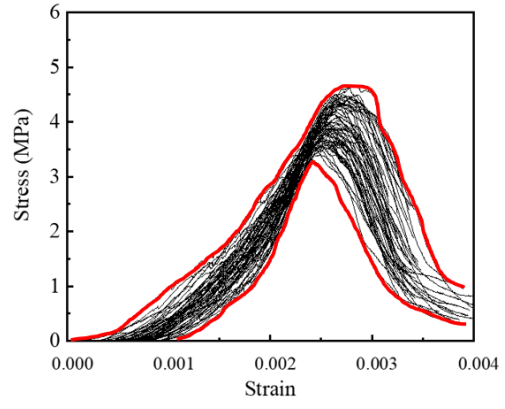
(a) High quality wall with COV=0.1



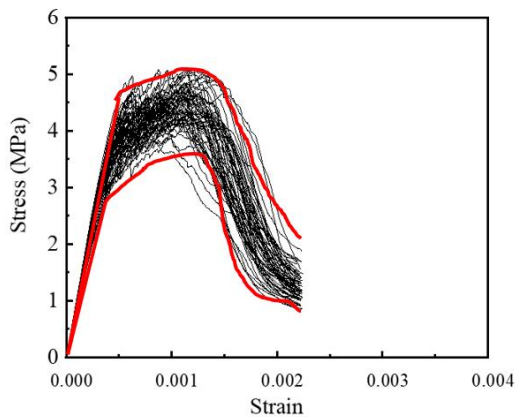
(b) High-medium quality wall with COV=0.1



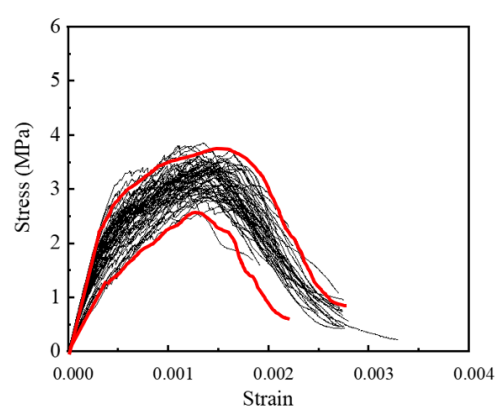
(c) Medium-low quality wall with COV=0.1



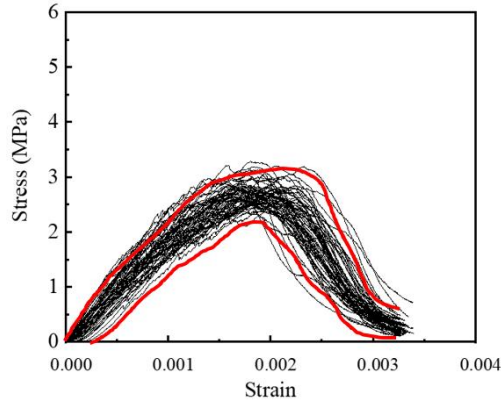
(d) Low quality wall with COV=0.1



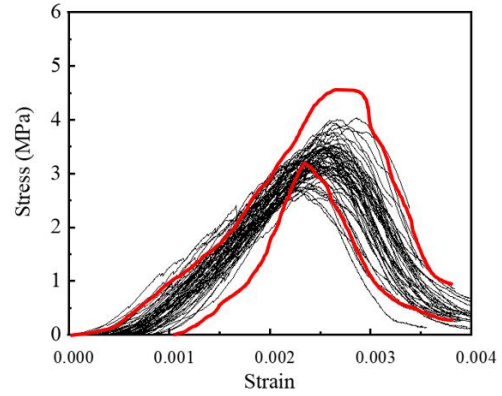
(e) High quality wall with COV=0.3



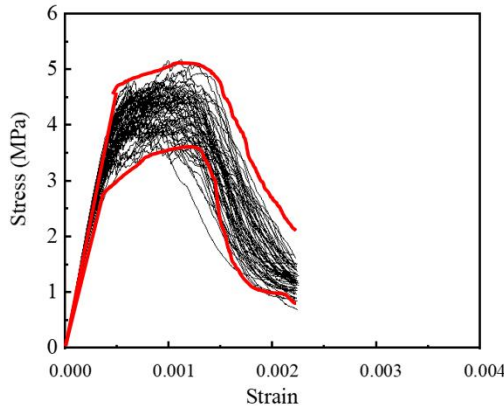
(f) High-medium quality wall with COV=0.3



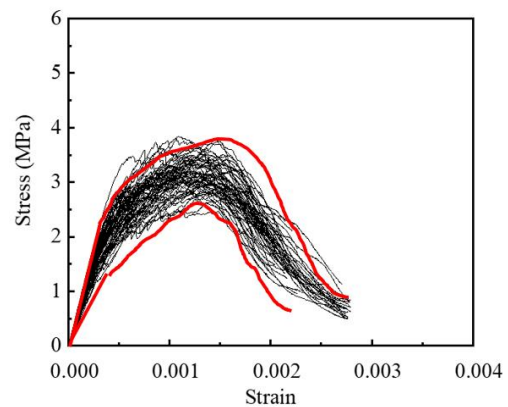
(g) Medium-low quality wall with COV=0.3



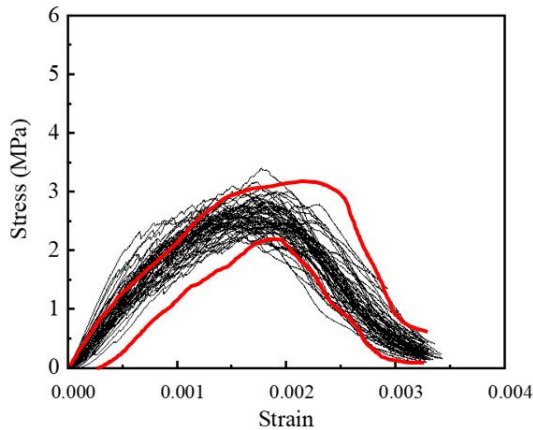
(h) Low quality wall with COV=0.3



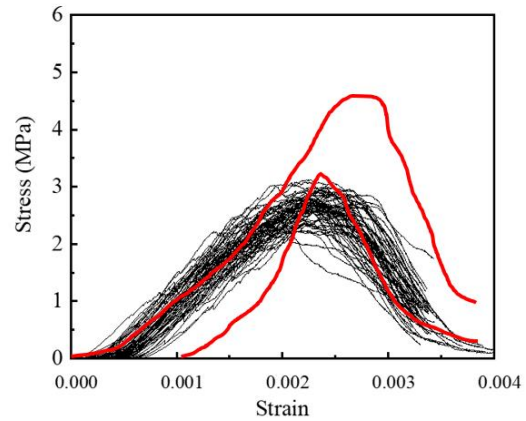
(i) High quality wall with COV=0.5



(j) High-medium quality wall with COV=0.5



(k) Medium-low quality wall with COV=0.5



(l) Low quality wall with COV=0.5

Figure 5-11. Stress-strain curves of interlocking brick walls with spatially varying imperfections

5.5.2 Compressive strength and probability distribution

The compressive strengths of interlocking brick wall from the above stress-strain curves are summarized. Table 5-2 lists the mean compressive strength, the standard deviation σ and the associated coefficient of variation (COV_f) for the four categories of

interlocking brick walls with spatially varying imperfections. Figure 5-12 shows the predicted compressive strength in the spatial analysis. With the least amount and possibility of imperfect bricks, the high-quality wall has the highest mean compressive strength. It can also be found that the COV of brick imperfection size appears to marginally influence the mean compressive strengths of high and high-medium quality walls. For example, when $COV = 0.1$, the mean compressive strengths are 4.47 MPa and 3.38 MPa for the high quality and high-medium quality interlocking brick walls, respectively; when $COV=0.5$, the mean compressive strengths are 4.40 MPa and 3.27 MPa for the high quality and high-medium quality walls. However, for the medium-low quality wall, the compressive strength declines slightly from 2.81 MPa to 2.70 MPa as COV increases from 0.1 to 0.5. For low-quality walls, the compressive strength drops significantly from 4.00 MPa to 2.72 MPa as COV increases from 0.1 to 0.5. The mean compressive strength of the low-quality walls with more number of imperfected bricks is higher than that of the high-medium and medium-low quality walls when $COV=0.1$ and $COV=0.3$. Specifically, the compressive strength increases by 42.3% from 2.81 MPa of medium-low quality wall to 4.00 MPa of low-quality walls when $COV=0.1$, and the strength increases by 19.4% from 2.79 MPa of medium-low quality wall to 3.33 MPa of low-quality wall when $COV=0.3$. As explained above, this is because more low-quality bricks lead to the imperfection distribution across the wall more uniform, which results in more significant seating effect of the wall when compressive load is applied. Once the gaps close, the wall behaves more like the one with high-quality bricks, therefore the compressive strength is higher than those with high-medium and medium-low quality bricks although the equivalent modulus is substantially smaller. However, the difference between the mean compressive strength of walls with medium-low quality and low-quality bricks when $COV=0.5$ is not obvious. This is because with more than 75% of bricks having imperfections in the low-quality walls, when subjected to compressive loading most gaps would close. When COV is small, gap closures occur more uniformly leading to better and more

proper inter-brick contacts as compared with the medium-low quality walls. When COV is large, implying more non-uniform imperfection distributions, hence more local damage owing to stress concentrations, the compressive loading capacity of the wall is therefore small. These results indicate that the compressive load-bearing capacity is less affected if the imperfections are more uniformly distributed even if the imperfection level is large. Large imperfections affect the initial equivalent stiffness of the wall. It also can be seen from Table 5-2 that for the high-quality, high-medium quality and medium-low quality interlocking walls, increasing the COV of brick imperfections would increase the COV of wall compressive strengths. For example, as COV of brick imperfection increases from 0.1 to 0.5, the COV of wall compressive strength increases from 0.065 to 0.090 and from 0.060 to 0.086 for high-medium quality and medium-low quality wall, respectively. It shows that increasing the scatter of brick imperfections will increase the fluctuation of the predicted wall compressive strengths. However, the COV of brick imperfection has insignificant influence on the COV of low-quality interlocking walls, for which the mean compressive strength and standard deviation decrease significantly and simultaneously.

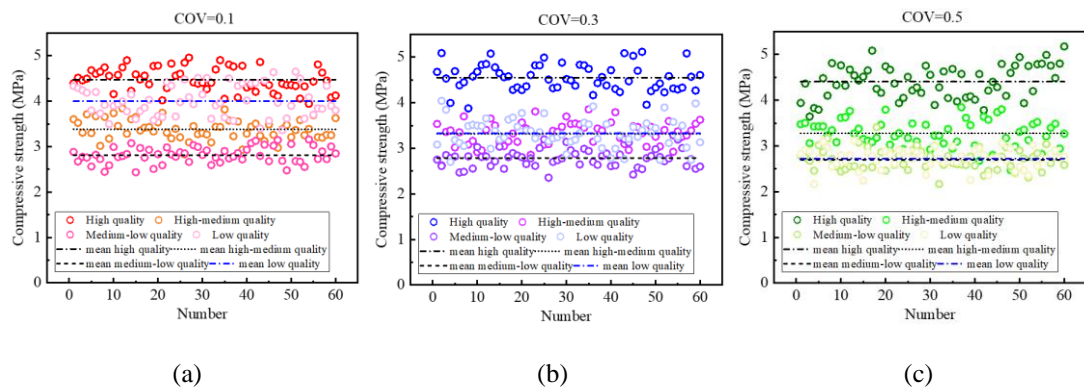


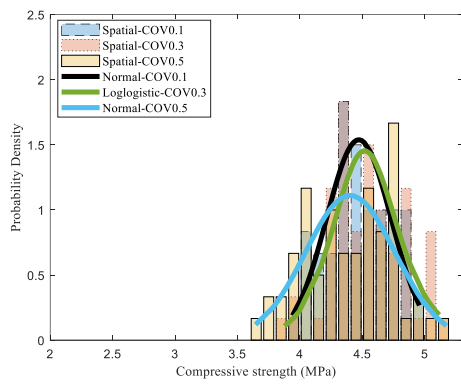
Figure 5-12. Distribution of wall compressive strengths corresponding to different COVs of brick imperfections

Table 5-2. Summary of wall compressive strengths from Monte-Carlo analysis

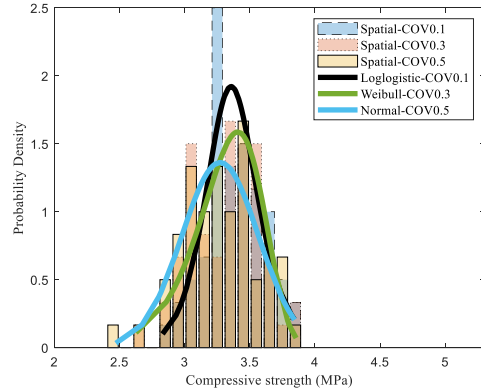
Imperfection	High-quality wall						High-medium quality wall						
	COV	f_{Max} (MPa)	f_{Min} (MPa)	f_{Mean} (MPa)	σ (MPa)	COV_f	Distribution	f_{Max} (MPa)	f_{Min} (MPa)	f_{Mean} (MPa)	σ (MPa)	COV_f	Distribution
0.1		4.96	3.94	4.47	0.26	0.058	Normal	2.83	3.84	3.38	0.22	0.065	Loglogistic
0.3		5.12	3.88	4.55	0.29	0.064	Loglogistic	3.86	2.63	3.32	0.27	0.080	Weibull

0.5	5.17	3.64	4.40	0.36	0.081	Normal	2.47	3.84	3.27	0.29	0.090	Normal
Imperfection		Medium-low quality wall					Low-quality wall					
COV	f_{Max} (MPa)	f_{Min} (MPa)	f_{Mean} (MPa)	σ (MPa)	COV _f	Distribution	f_{Max} (MPa)	f_{Min} (MPa)	f_{Mean} (MPa)	σ (MPa)	COV _f	Distribution
0.1	3.16	2.44	2.81	0.18	0.060	Normal	4.65	3.36	4.00	0.34	0.085	Normal
0.3	3.28	2.36	2.79	0.20	0.070	Loglogistic	4.04	2.70	3.33	0.32	0.095	Gamma
0.5	3.41	2.17	2.70	0.23	0.086	Loglogistic	3.12	2.17	2.72	0.22	0.079	Smallest Extreme

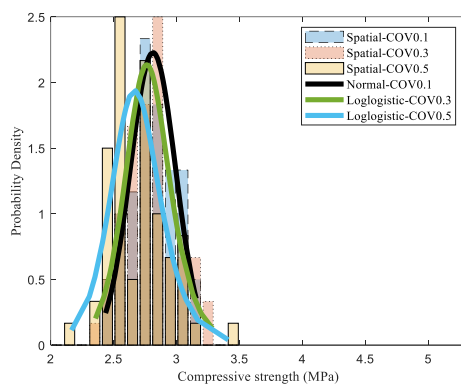
Figure 5-13 shows the histograms of wall compressive strengths. The modelled compressive strengths of the interlocking brick walls are fitted using different probability distribution functions, including Gamma, Smallest extreme value, Loglogistic, Lognormal, Normal, and Weibull [39, 93, 173]. Kolmogorov–Smirnov test is performed to select the best-fit probability distribution function as plotted in Figure 5-13. As shown, for the high-quality interlocking wall its compressive strength varies between 3.94MPa and 4.96MPa when COV=0.1, which as expected varies more significantly from 3.88MPa to 5.12MPa and from 3.64MPa to 5.17MPa when COV=0.3 and 0.5, respectively. It demonstrates that the increase of COV of imperfection size would slightly scatter the compressive strength of interlocking brick wall. Similar observation can be found on the high-medium quality interlocking walls. And it can be found that the tail of the histograms for COV=0.5 is heavier than that for COV=0.1. Therefore, the probability of wall failure will be greater for COV=0.5, in contrast to the results of COV=0.1. For the low-quality interlocking wall, the predicted compressive strength varies more significantly between 3.36MPa and 4.65MPa when COV=0.1. And when COV=0.3 and 0.5, the modelled compressive strength varies from 2.70MPa to 4.04MPa and from 2.17MPa to 3.12MPa. Therefore, the increase of COV reduces dramatically the wall strength for low-quality walls, but the influence of COV of imperfection size on the COV of compressive strength is not obvious. The results show that ignoring COV of imperfections may overestimate the compressive capacity especially when the quality of interlocking brick walls is low.



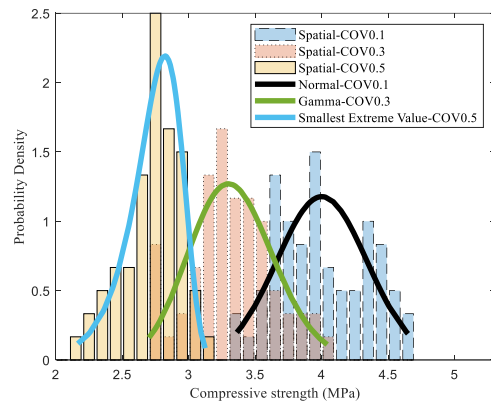
(a) High-quality wall



(b) High-medium quality wall



(c) Medium-low quality wall



(d) Low-quality wall

Figure 5-13. Histograms of compressive strength for interlocking walls

5.5.3 Equivalent stiffness and probability distribution

To depict the stiffness of the interlocking brick wall, equivalent stiffness as shown in Figure 5-14 is introduced which is defined as the slope of secant line from the origin to the peak compressive force on the modelled stress-strain curves. The distributions of the wall equivalent stiffness corresponding to the different COVs for imperfection size are illustrated in Figure 5-15. Table 5-3 summarizes the mean equivalent stiffness, the standard deviation σ and the associated coefficient of variation (COV_E) for the four quality interlocking brick walls with spatially varying imperfections. The mean equivalent stiffness decreases as the quality of the interlocking wall decreases with more imperfections, because the corresponding displacement at the peak compressive load significantly increases with the decrease in the quality of bricks. This is the reason for overestimating the stiffness of dry-stacked brick walls in numerical models without

considering existing imperfections compared to those from experimental data [38, 102]. It is worth noting that as COV of imperfection size distribution increases from 0.1 to 0.5, the mean equivalent stiffnesses of the high-quality, high-medium quality and medium-low quality walls increase. This is because the displacements at the peak compressive loads decrease significantly, while the peak compressive load varies slightly. It means the wider and more non-uniform distribution of imperfections of brick in an interlocking brick wall, the smaller the displacement of the interlocking wall at the failure point, because local damage appears earlier owing to stress concentration. However, for low-quality walls, as the COV of brick imperfection increases, the mean equivalent stiffness decreases. For instance, for the low-quality walls, the mean equivalent stiffness decreases from 92.9kN/mm to 72.6kN/mm when the COV of imperfection size increases from 0.1 to 0.5. This is because the seating effect gradually decreases with the increase of COV for imperfection size (see Figure 5-11). Overall, it can be found that the COV of brick imperfection size distribution could strongly influence the equivalent stiffness of interlocking brick walls. It is also worth noting that the mean equivalent stiffness for low-quality walls with COV=0.1 is higher than that of the medium-low quality wall. It might be because the peak compressive strength is higher than that of the medium-low quality wall as described in Section 4.2, while the increase in the wall deformation at peak compressive load of the low-quality walls is less than the increase in the peak compressive strength.

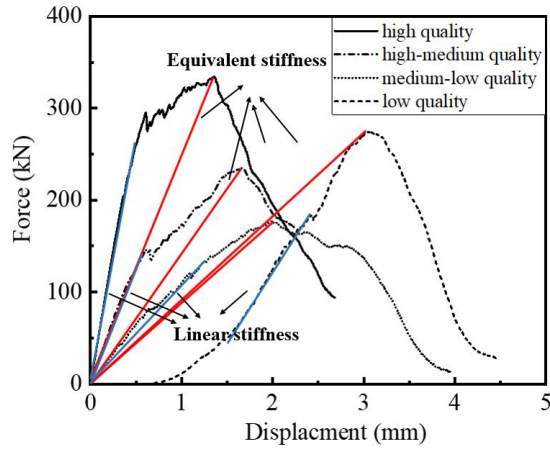


Figure 5-14. The definition of equivalent stiffness and linear stiffness

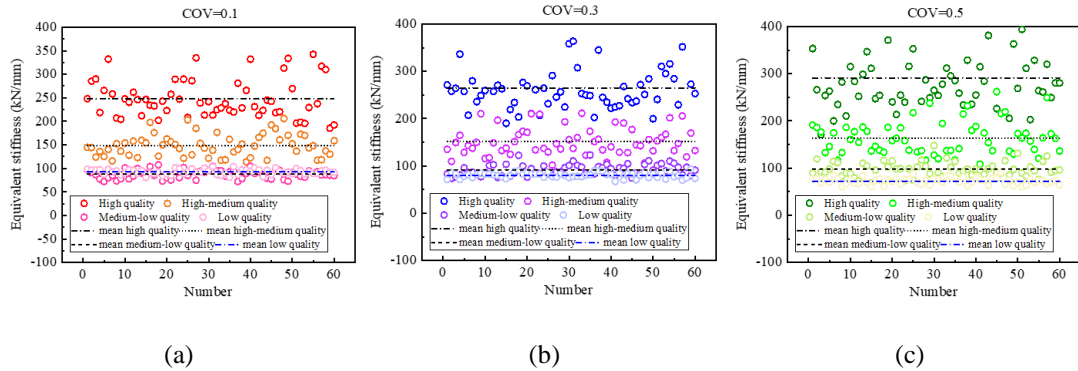
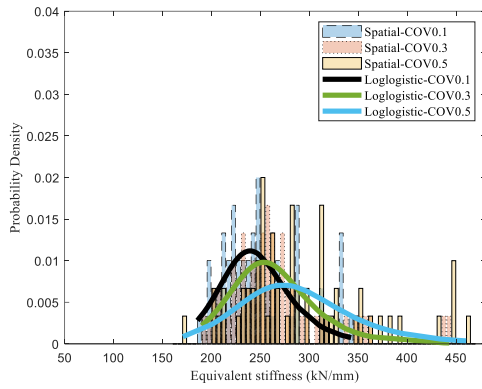


Figure 5-15. Distribution of wall equivalent stiffness corresponding to the different COVs of brick imperfection size distributions

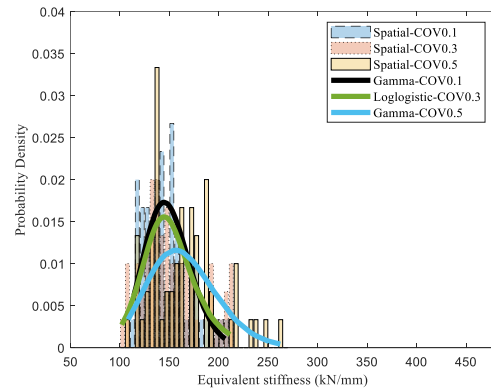
Table 5-3. Summary of wall equivalent compressive stiffness from Monte-Carlo analysis

Imperfection	High-quality wall						High-medium quality wall					
	COV	$E_{Max.}$ (kN/mm)	$E_{Min.}$ (kN/mm)	E_{Mean} (kN/mm)	σ (kN/mm)	CO V_E Distribution	$E_{Max.}$ (kN/mm)	$E_{Min.}$ (kN/mm)	E_{Mean} (kN/mm)	σ (kN/mm)	CO V_E Distribution	
0.1	0.1	342.64	185.64	247.94	40.45	0.163 Loglogistic	206.20	114.20	148.31	23.30	0.157 Gamma	
0.3	0.3	442.85	190.09	265.00	51.09	0.193 Loglogistic	211.30	101.80	151.70	28.68	0.189 Loglogistic	
0.5	0.5	460.04	170.72	291.38	66.70	0.229 Loglogistic	262.00	108.30	163.77	35.10	0.214 Gamma	
Imperfection	Medium-low quality wall						Low-quality wall					
	COV	$E_{Max.}$ (kN/mm)	$E_{Min.}$ (kN/mm)	E_{Mean} (kN/mm)	σ (kN/mm)	CO V_E Distribution	$E_{Max.}$ (kN/mm)	$E_{Min.}$ (kN/mm)	E_{Mean} (kN/mm)	σ (kN/mm)	CO V_E Distribution	
0.1	0.1	107.73	72.05	87.75	9.25	0.105 Normal	103.60	80.71	92.90	5.49	0.059 Normal	
0.3	0.3	123.20	73.79	92.21	11.65	0.126 Loglogistic	93.34	67.43	80.47	5.76	0.072 Normal	
0.5	0.5	147.86	68.49	97.68	15.39	0.106 Loglogistic	90.93	60.12	72.61	7.04	0.097 Normal	

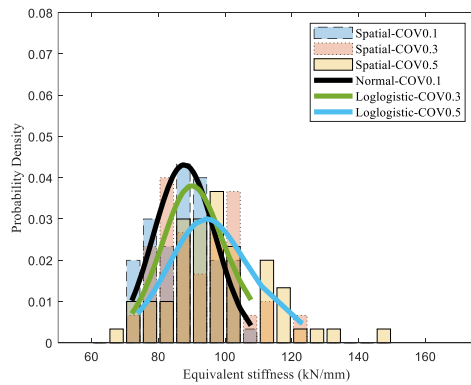
Figure 5-16 shows the histograms of the equivalent stiffness with random variation of brick imperfections and the best-fit probability distribution function. As shown in Figure 5-16a-c, as the COV of imperfection size increases, the distribution of equivalent stiffness of interlocking brick walls is gradually dispersed. For example, for the high-quality walls, its equivalent stiffness varies between 185.64 kN/mm and 342.64 kN/mm when COV=0.1, while it varies from 190.09 kN/mm to 442.85 kN/mm and from 170.72 kN/mm to 460.04 kN/mm when COV=0.3 and 0.5, respectively. This is because as the distribution of imperfection size becomes more non-uniform, local damage appears earlier owing to stress concentration. Therefore, the peak compressive strength of the wall is reached earlier with a smaller corresponding displacement although the compressive strength does not vary significantly. It also can be found that the tail of the histograms for COV=0.5 is heavier than that for COV=0.1. The probability of equivalent stiffness will be over-estimated for COV=0.5, in contrast to the results for the case of COV=0.1. As shown in Figure 5-16d, the histograms for the low-quality walls are significantly higher and narrower compared with the other three quality walls, which means the equivalent stiffness of low-quality interlocking brick walls has less variation compared with that of the walls with the other brick qualities. The predicted equivalent stiffness varies between 80.71 kN/mm and 103.60 kN/mm when COV=0.1. When COV=0.3 and 0.5, the modelled equivalent stiffness varies from 67.43 kN/mm to 93.34 kN/mm and from 60.12 kN/mm to 90.93 kN/mm, respectively. The increase of COV of brick imperfection size distribution reduces dramatically the wall equivalent stiffness for low-quality walls, but the influence on the scatter of the compressive strength is not prominent. Therefore, the stochastic analysis shows that the equivalent stiffness of the dry-stacked interlocking brick wall is significantly affected by the quality of the wall.



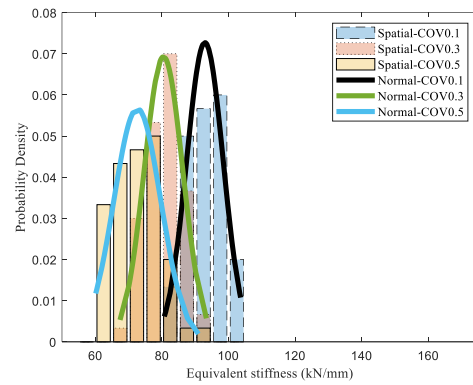
(a) High quality wall



(b) High-medium quality wall



(c) Medium-low quality wall



(d) Low quality wall

Figure 5-16. Histograms of equivalent stiffness for interlocking brick walls

5.5.4 Linear stiffness and probability distribution

For dry-stacked interlocking brick wall, because of brick imperfection, gaps inevitably exist between bricks which result in seating effect when the wall is subjected to compressive loading. When an interlocking brick wall is subjected to dead load and live load in service state, these gaps would close. Thus, linear stiffness would be important to determine the mechanical properties of interlocking brick walls. As illustrated in Figure 5-14, the linear stiffness herein is defined as the slope of secant line from the origin to the starting point of the softening stage for high quality and high-medium quality walls where seating effect is insignificant. For an interlocking brick wall with medium-low and low-quality bricks, the linear stiffness is determined as the slope of the linear portion of the load-displacement curves after seating and prior to non-linear behavior.

As shown in Table 5-4 and Figure 5-17, the mean linear stiffnesses of high quality, high-medium and medium-low quality interlocking brick walls are 511kN/mm, 320kN/mm and 119kN/mm when COV=0.1, which indicates that as the quality of wall decreases, the linear stiffness significantly decreases because the number of imperfections controls the contact areas. The mean linear stiffness for high quality, high-medium quality and medium-low quality interlocking brick walls gradually increases as the COV of brick imperfection increases. This is because with a larger variation of imperfection size, the bricks could more likely touch each other at a lower displacement, which also results in a lower peak strength but at a smaller displacement due to stress concentration. As a result, the linear stiffness increases as the COV of imperfection size distribution increases. However, the influence of COV on the linear stiffness is opposite for low-quality interlocking brick walls, where as COV increases from 0.1 to 0.5, the linear stiffness of the low-quality walls decreases from 231kN/mm to 113.5kN/mm. This is because there are widely spread imperfections existing in low-quality walls which lead to significant seating effect. When COV =0.1, most gaps would close uniformly since brick imperfection sizes are similar. This leads to a relatively larger contact area. Since the compressive stiffness is proportional to the cross-section area in contact, a larger linear stiffness is resulted.

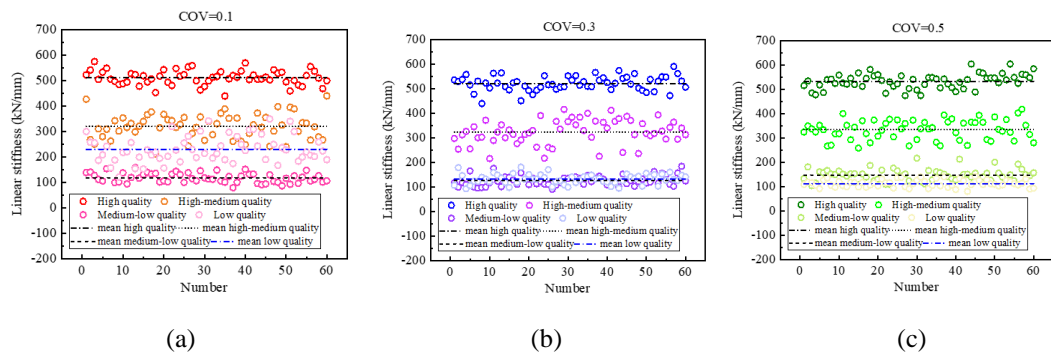


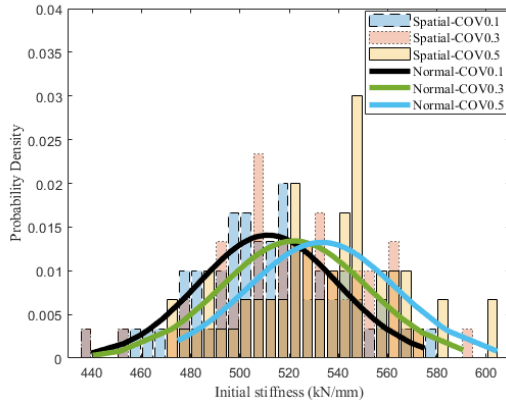
Figure 5-17. Distribution of wall linear stiffness corresponding to different COVs of brick imperfection size distributions

Table 5-4. Summary of wall linear stiffness from Monte-Carlo analysis

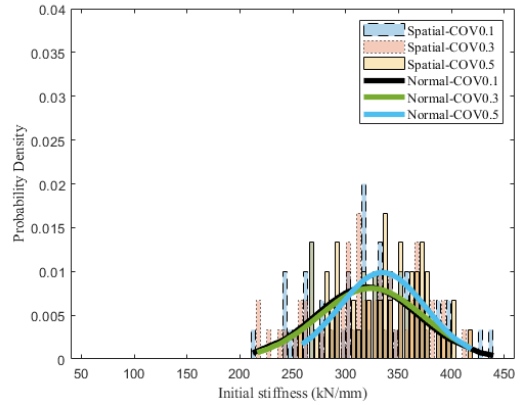
Imperfection	High-quality wall	High-medium quality wall
--------------	-------------------	--------------------------

COV	E_{Max} (kN/ mm)	E_{Min} (kN/ mm)	E_{Mean} (kN/ mm)	σ_E (kN/ mm)	CO V_E	Distrib ution	E_{Max} (kN/ mm)	E_{Min} (kN/ mm)	E_{Mean} (kN/ mm)	σ_E (kN/ mm)	CO V_E	Distrib ution
0.1	575.04	439.63	511.44	28.34	0.055	Normal	439.79	212.16	320.30	48.57	0.152	Normal
0.3	590.62	439.95	521.99	29.75	0.057	Normal	415.77	216.33	324.09	49.42	0.153	Normal
0.5	604.49	474.61	533.24	30.11	0.056	Normal	418.84	258.70	334.76	40.41	0.121	Normal
Imperfection	Medium-low quality wall						Low-quality wall					
COV	E_{Max} (kN/ mm)	E_{Min} (kN/ mm)	E_{Mean} (kN/ mm)	σ_E (kN/ mm)	CO V_E	Distrib ution	E_{Max} (kN/ mm)	E_{Min} (kN/ mm)	E_{Mean} (kN/ mm)	σ_E (kN/ mm)	CO V_E	Distrib ution
0.1	158.78	79.97	119.35	19.59	0.164	Loglog istic	350	121.79	231.04	51.35	0.22	Logno rmal
0.3	184.63	90.99	126.03	20.83	0.165	Loglog istic	181.37	93.85	132.87	20.24	0.15	Normal
0.5	217.41	104.82	148.51	24.66	0.166	Gamm a	142.68	81.37	113.53	15.01	0.13	Normal

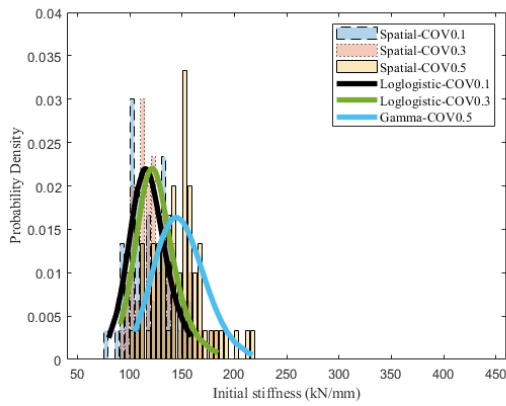
Figure 5-18 shows the histogram curves of linear stiffness. As shown, for the high-quality, high-medium quality and medium-low quality walls, as the COV increases, the distribution of linear stiffness remains relatively stable. For example, for the high-quality interlocking brick wall, its linear stiffness varies between 439.63 kN/mm and 575.04 kN/mm with COV=0.1, which is not significantly different from that with COV=0.3 and 0.5, with linear stiffness varying in the range from 439.95 kN/mm to 590.62 kN/mm and from 474.61 kN/mm to 604.49 kN/mm, respectively. Similar observations can be made on high-medium and medium-low quality interlocking walls. As for low-quality interlocking walls, the histograms of linear stiffness become more scattered as the COV decreases. The predicted linear stiffness varies between 121.79 kN/mm and 350 kN/mm when COV=0.1. However, when COV=0.3 and 0.5, the modelled linear stiffness varies from 93.85 kN/mm to 181.37 kN/mm and from 81.37 kN/mm to 142.68 kN/mm, respectively. These results indicate that when the COV of imperfection size increases, the linear stiffness in general decreases and varies in a narrower range. Overall, the quality of interlocking brick wall has a larger influence on the variation of the linear stiffness. Moreover, it is found that the imperfection distribution has a more significant influence on the linear stiffness of low-quality interlocking brick walls as compared with the other three quality interlocking walls.



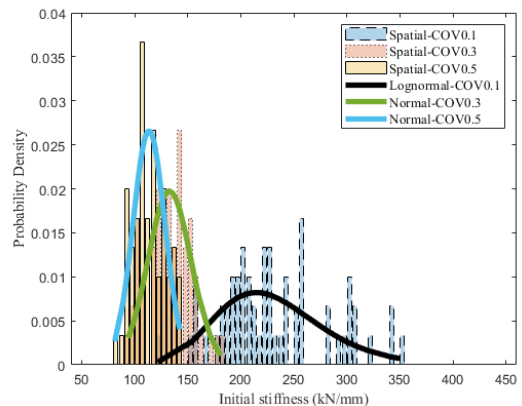
(a) High quality wall



(b) High-medium quality wall



(c) Medium-low quality wall



(d) Low quality wall

Figure 5-18. Histograms of linear stiffness for interlocking walls

5.6 Conclusion

This chapter performs stochastic analysis to investigate the compressive properties of dry-stacked interlocking brick walls with spatially varying brick imperfections. A detailed numerical model of interlocking brick walls with brick imperfection is generated. The number of brick imperfections is assumed to follow the Binominal distribution in massive brick production process. The imperfection sizes are assumed to follow the truncated normal distribution. the imperfection size on the surface of this brick is assumed to be uniform over the entire surface for simplicity. The influences of imperfection on the compressive strength, equivalent stiffness, linear stiffness of interlocking brick wall are studied. The following conclusions are derived from this study:

1. Typical crack patterns on imperfect brick units are presented, which demonstrates strong influence of imperfection on the crack patterns. It is also found that brick imperfections could strongly influence the crack initiation and development, as well as the load path of dry-stacked interlocking brick walls.
2. With less numbers of imperfect bricks, the high-quality wall has the highest mean compressive strength. The mean compressive strength of a low-quality interlocking brick wall could be higher than that of high-medium and medium-low quality walls because the low-quality brick walls have more number and wide spread gaps between bricks. Under compressive loading, these gaps would close relatively uniformly leading to improved wall strength although the initial seating length is larger and the equivalent stiffness is smaller; whereas despite less numbers of imperfect bricks, when subjected to compressive loading medium-quality walls suffer non-uniform deformation and stress concentration at joint gaps resulting in more severe localized brick damage and failures and hence lower compressive strengths.
3. The COV of brick imperfection size distribution marginally influences the mean compressive strengths of high-quality and high-medium quality walls. However, it is found to strongly influence the mean compressive strength of low-quality walls.
4. Initial seating is obvious for medium-low and low-quality brick walls under compressive load because of gap closure between imperfect bricks, and the seating displacement is prominent in the walls with relatively low-quality bricks.
5. The mean equivalent stiffness decreases as the quality of the interlocking wall decreases with more imperfections.
6. As COV of imperfection distribution increases, the mean equivalent stiffnesses of high-quality, high-medium quality and medium-low quality

walls increase because the displacements at the peak compressive loads decrease significantly, while the peak compressive load only varies slightly. But for low-quality walls, the mean equivalent stiffness decreases as the COV of brick imperfection increases.

7. The mean linear stiffnesses of high quality, high-medium and medium-low quality interlocking brick walls decrease significantly as the quality of brick decreases because the number of imperfections controls the contact areas.
8. For low-quality walls, when the COV of imperfection distributions is relatively low, their linear stiffness is a little higher than that of medium-low-quality walls after excluding the seating in determining the linear stiffness owing to the widespread relatively uniformly distributed imperfections.

CHAPTER 6 NUMERICAL DERIVATION OF HOMOGENIZED CONSTITUTIONAL RELATION FOR MASONRY WALL MADE OF MORTAR-LESS INTERLOCKING BRICKS

6.1 Introduction

In Chapter 3 to 5, intensive numerical simulations are performed to quantify the compressive and shear properties of interlocking bricks, and to carry out stochastic analysis. The numerical simulation with detailed interlocking bricks is complicated and time-consuming due to the mortar-less feature and the interlocking mechanism, which lead to convoluted contact status in an interlocking brick wall. To simplify the modelling and analysis, a representative volume element (RVE) is extracted from dry-stacking interlocking brick walls based on their periodic construction patterns. The equivalent material properties of the RVE, considering the nonlinear behaviour and damage evolution, is then derived under various stress statuses based on continuum damage mechanics. Finally, wall models made of the developed RVEs with the equivalent material model are compared with corresponding detailed models made of interlocking bricks, demonstrating the result accuracy and computation efficiency of the RVE model in predicting the behaviour of interlocking brick walls.

6.2 Methodology

To initiate the homogenization analysis, a suitable RVE needs to be defined. The RVE needs to be statistically representative in the macro-scale level of the interlocking brick wall. Specifically, an RVE of interlocking brick structure should satisfy the following requirements: (i) the RVE includes an adequate quantity of material phases; (ii) the

whole structure can be formed by continuous and periodic distributions of RVEs; and
 (iii) the RVE is small enough but satisfies the above-mentioned requirements [123].

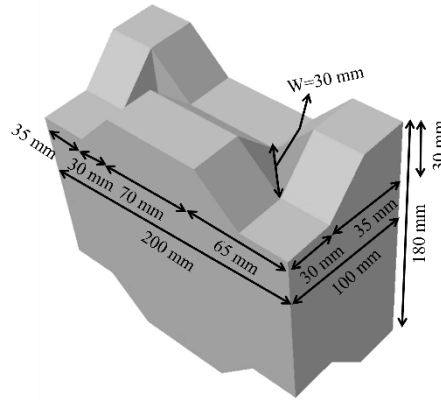


Figure 6-1. Configuration of interlocking brick

In this study, the RVE is comprised by the interlocking bricks of 200 mm × 100 mm × 180 mm (length × thickness × height) with large protruded mortise and tenon (35 mm length × 35 mm thickness × 30 mm height) (see Figure 6-1). Such shape and geometry were proved to give optimized compressive and shear resistance properties. A basic cell of dry-stacking interlocking bricks as shown in Figure 6-2 is chosen as the RVE, which is comprised of two interlocking bricks and two pieces of half bricks as top and bottom course, and 1/4 bricks are distributed at four corners. The homogenized material properties can be derived through analysing the RVE subjected to different loading conditions. To derive the constitutive stress-strain relations of the RVE in the macro-scale level, the components of the averaged stress and strain, $\bar{\sigma}_{ij}$ and $\bar{\varepsilon}_{ij}$ can be written as

$$\bar{\sigma}_{ij} = \frac{1}{V} \int_V \sigma_{ij} dV \quad (6-1)$$

$$\bar{\varepsilon}_{ij} = \frac{1}{V} \int_V \varepsilon_{ij} dV \quad (6-2)$$

where σ_{ij} and ε_{ij} are the stress and strain in an individual element in the interlocking brick in the RVE, respectively; and V is the volume of the RVE.

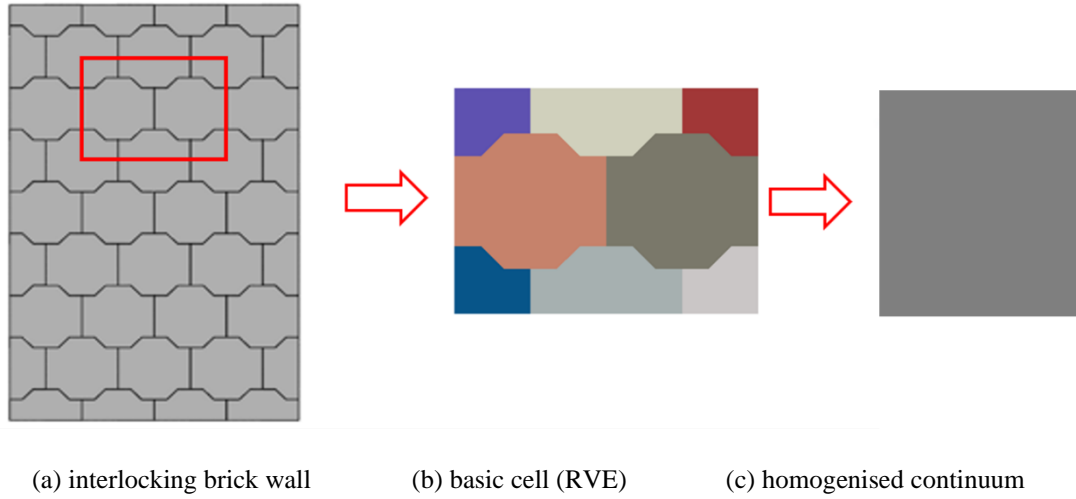


Figure 6-2. Homogenization of an interlocking wall

6.3 Numerical Modelling of Interlocking Bricks

A detailed numerical model of the RVE for the interlocking brick is generated using the commercial software ABAQUS [174], which is used to model the different stress states of the RVE to derive the homogenized material properties.

6.3.1 Material model

The material of each interlocking brick is modelled by the Concrete Damage Plasticity (CDP) model in ABAQUS. The CDP model [175] is commonly used to simulate the nonlinear behavior of concrete-like materials. Material hardening and softening in both compression and tension can be considered using Eqs. (6-3) and (6-4). As illustrated in Figure 6-3, under uniaxial compression and tension, the stress-strain relations defining the compressive stress σ_c as well as the tensile stress σ_t are derived as follows:

$$\sigma_c = (1 - d_c)E_0(\varepsilon_c - \bar{\varepsilon}_c^{pl}) \quad (6-3)$$

$$\sigma_t = (1 - d_t)E_0(\varepsilon_t - \bar{\varepsilon}_t^{pl}) \quad (6-4)$$

where d_c and d_t are the damage scalars for compression and tension; ε_c and ε_t are the total strains in compression and tension; $\bar{\varepsilon}_c^{pl}$ and $\bar{\varepsilon}_t^{pl}$ are the equivalent plastic

strains in compression and tension; and E_0 denotes the undamaged elastic modulus of the material.

The Poisson's ratio ν_c is 0.2; the Young's modulus of brick $E_0 = 13.5\text{GPa}$; the unconfined uniaxial compressive strength f_c is 17.8MPa from laboratory material testing results [168]. In the study, the tension stiffening is defined according to Martínez et al.'s study [38]. The uniaxial tensile stress for the brick material is assumed as $0.1 f_c$ [38, 102, 168, 176]. The density of brick is 2565kg/m^3 . A non-associated plastic flow rule representing the plastic potential is chosen, with a dilation angle of 30° . This is to simulate the non-dilatant behavior of brick subjected to moderate compression and shear loading [168]. f_{bo}/f_{co} denotes the ratio of biaxial compressive yield stress over the uniaxial compressive yield stress, which is taken as 1.16 for brick material. Smoothing of the tension corner is also used, which is reflected through taking into account the eccentricity parameter that equals to 0.1 [102, 177].

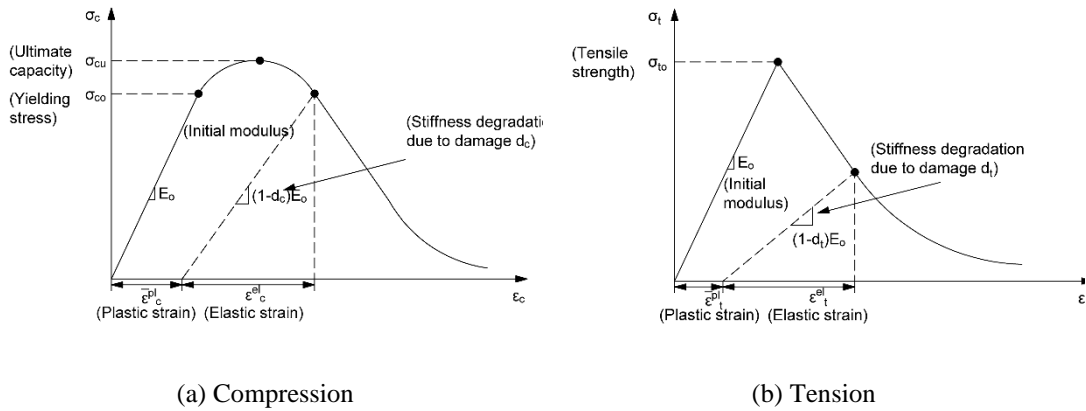


Figure 6-3. Uniaxial compressive and tensile behaviors of brick material in the CDP model

6.3.2 Contact properties

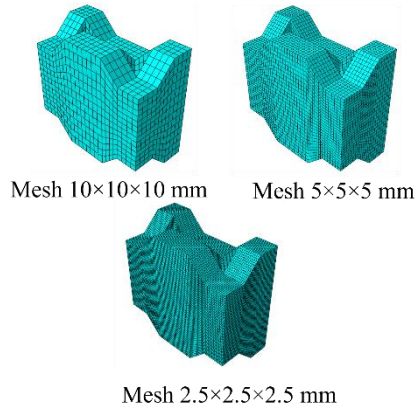
The contact between the dry-stacking bricks is assumed to be perfect without surface imperfection. The surface-to-surface contact algorithm in ABAQUS is adopted to model the contact between adjacent interlocking bricks. Mohr-Coulomb criterion is employed to define the tangential behavior, where the friction coefficient is assumed to be 0.3 [38, 148]. The hard contact is adopted to define the normal behavior at the

contact. The hard contact guarantees no penetration of the contacting surfaces.

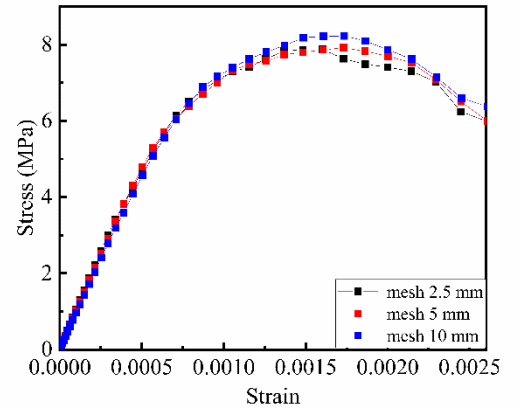
6.3.3 Mesh convergence study

Mesh convergence analysis is carried out, where 10 mm, 5 mm and 2.5 mm meshes are tested (Figure 6-4a shows the mesh of one interlocking unit in the RVE). Figure 6-4b-d) show the modelled average axial stress and strain relations of the RVE comprising of interlocking bricks with different mesh sizes that are subjected to uniaxial compression in the vertical, horizontal and out-of-plane directions, respectively. It is to note that the vertical, horizontal and out-of-plane directions correspond to the Y-, X- and Z- directions in the global coordinate systems of ABAQUS. Overall, the stress-strain curves of the three models are close to one another. As can be seen in Figure 6-4b), 5 mm mesh slightly overestimates the peak compressive strength by +0.63% as compared to 2.5 mm mesh, which also slightly underestimates that with 10mm mesh (-3.72%). Similarly, when the RVE is under uniaxial compression in the horizontal and out-of-plane directions, the RVE with 5 mm mesh only slightly overestimates the peak strengths by +3.43% and +2.91% respectively when compared to the 2.5mm mesh, which in the meanwhile slightly underestimates those from the model with 10mm mesh (-1.08% and -4.70%). As CDP model which contains damage evolution is used to model brick material, simulated material damage is also checked. Figure 6-4e) shows the relation between applied displacement and the corresponding energy dissipated by material damage (ALLDMD) obtained with different element sizes at the instant of peak strength, the energy dissipated by the three models are 5847.82 mJ for the 10mm model, 5382.76 mJ for the 5mm model and 5221.18 mJ for the 2.5mm model. The damage extent is slightly lower as the meshes become finer but there is only a small difference. The damage contours of the three models at peak strength are shown in Figure 6-4f). It can be seen that the damage patterns are also similar, with main damage concentrated around the plane connecting the central and side parts of the interlocking bricks where abrupt

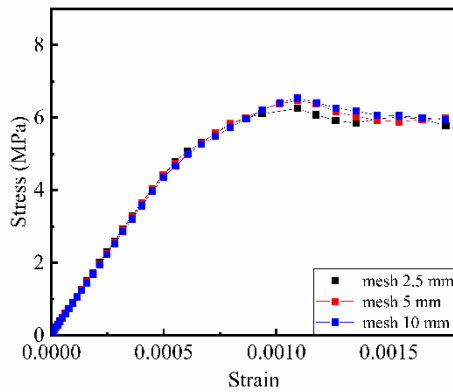
changes in geometry exist. Therefore, it is demonstrated that despite the mesh dependency of CDP model, both the stress-strain results and the damage evolution do not vary much under the studied mesh sizes. The overall response of the three meshes are very similar. Therefore, it is decided to adopt the mesh of 5 mm in the interest of computational efficiency.



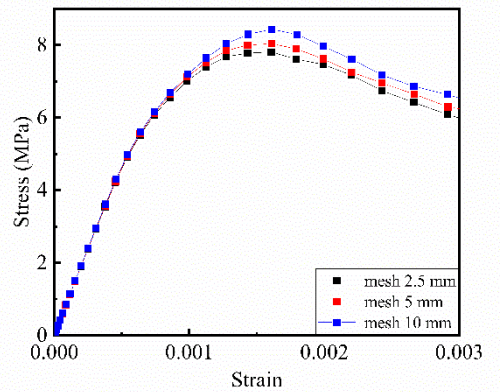
(a) Brick unit with different mesh sizes



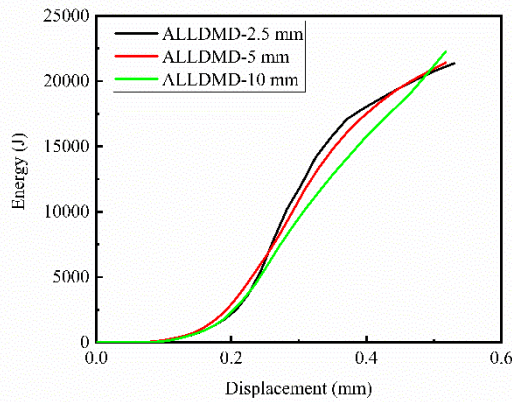
(b) Stress-strain curves of the modelled RVE under vertical loading



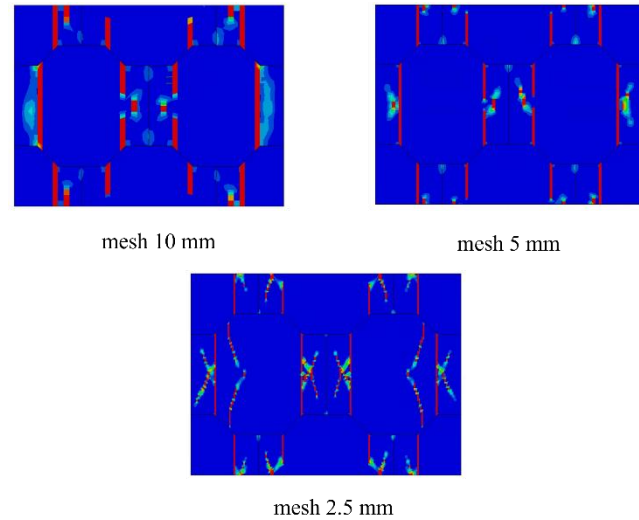
(c) Stress-strain curves of the modelled RVE under horizontal loading



(d) Stress-strain curves of the modelled RVE under out-of-plane loading



(e) Displacement and energy dissipated by material damage (ALLDMD) curve



(f) Damage mode with different mesh sizes

Figure 6-4. Mesh convergence study

6.4 Numerical Results of RVE

To derive the homogenized material properties of the RVE for interlocking bricks, responses of the basic cell is analysed under various stress states. The equivalent material properties, including the elastic properties, yield criterion, plastic flow rule, hardening/softening model and damage model, are determined using the numerical modelling results.

6.4.1 Stress-strain curves under different stress states

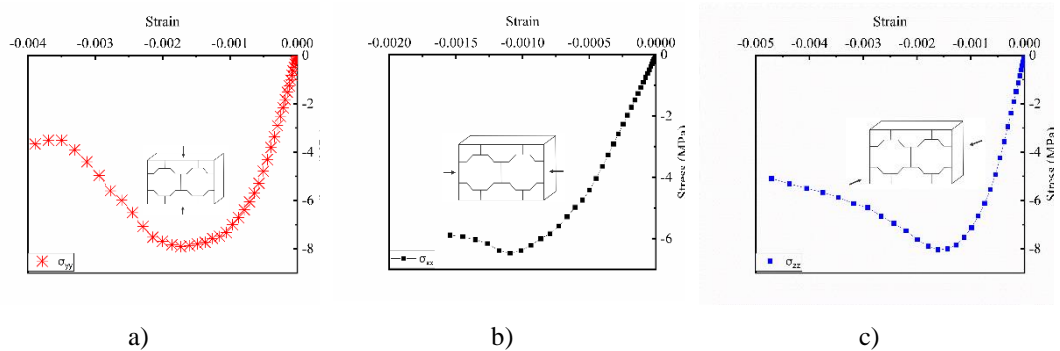
Figure 6-5 shows the homogenized stress-strain relationships of RVEs under various compressive stress states. In Figure 6-5a, a compressive loading in the Y direction is achieved by applying a Y-direction displacement on the top while constraint the displacement in the Y direction on the bottom. The lateral surfaces are not constrained. The uniaxial compressive strength of the RVE in this case is 7.92 MPa, which is much lower than the compressive strength of the interlocking brick material (17.8 MPa). It demonstrates that dry-stacking method could significantly influence the compressive strength of the interlocking brick structures. The compression in the X direction (or in the Z direction) is achieved in the same way as in the Y direction, with the applied

displacement and constraint in the corresponding direction. The uniaxial compressive strengths of the RVE subjected to compressive loading in the X direction and the out-of-plane Z direction without confinement are 6.47 MPa and 8.04 MPa, respectively. These results indicate that the material properties of the RVE are anisotropic because of the particular design of the interlocking bricks as shown in Figure 6-1. Nevertheless, anisotropy in such interlocking bricks is insignificant. As shown above, the uniaxial unconfined compressive strengths vary between 6.47MPa and 8.04MPa with a difference less than 20%. This is mainly because of the dry-stacking approach instead of mortar for inter-brick bonding, and contact imperfection for the interlocking brick is not considered either.

When the RVE is under biaxial compression, the vertical normal displacement on the top surface and the lateral normal displacement on the left surface is monotonically increased. The normal displacements on the opposite surfaces are constrained. When subjected to biaxial compression, the stress-strain relations of the RVE are shown in Figure 6-5d-f). To examine the different stress states, various ratios of displacements and thus strains in each direction are applied. Typically for $x:y=1:1$ as shown in Figure 6-5e), the compressive strengths of the RVE in the X direction and the Y direction are 9.32 MPa and 13.26 MPa, respectively, which are both higher than the corresponding unconfined uniaxial compressive strengths. The corresponding strains at the peak stresses are both similar to those subjected to unconfined uniaxial loading. It indicates that when the RVE is subjected to biaxial loading, its compressive strength increases because of the confinement. When the applied displacement in the X direction increases ($x:y=4:3$), the compressive strength in the X direction slightly improves, while the strength in the Y direction gradually decreases. This is because the nonuniform loadings in the two directions induce deviatoric stress in the RVE, besides the compressive stress. The combined compressive and shear stress lead to the reduction of the compressive strength in the Y direction. However, the compressive strength in the X direction slightly increases. According to the biaxial tensile-

compressive failure criteria for ordinary concrete developed by Kupfer [178], as one principal stress decreases, the other would increase.

Figure 6-5g-k) show the stress-strain curves of the RVE when subjected to triaxial compression. As shown in Figure 6-5g), when the RVE is restrained in both the vertical Y and the out-of-plane Z directions, the peak compressive capacity is more than 50MPa in the horizontal direction (X direction), which is significantly higher than that without constraints. Similar observations can be found in Figure 6-5h), when the RVE is constrained in the other two directions. With constraint in the X direction and loading in the Y and Z directions (Figure 6-5i), the compressive strengths of the RVE are substantially higher than those in Figure 6-5a-c). When the REV is subjected to triaxial loading (as shown in Figure 6-5k), the compressive strengths increase insignificantly comparing to the cases with one axis constrained as in Figure 6-5i). It is to note that a ‘plastic plateau’ is developed on the Z direction when the RVE is constrained in the X direction. This is because of the damage of the interlocking brick (see Figure 6-5i). The fracture of interlocking bricks leads to considerable deformation of the RVE forming the plateau. Then, stress within the RVE redistributes resulting in the compaction of the RVE, which could withstand a higher load. Similar observation was reported in a previous study on the triaxial behavior of concrete [179]. Overall, from the above observations, significant compressive strength enhancement is found on the RVE for dry-stacking interlocking brick wall under biaxial and triaxial loading.



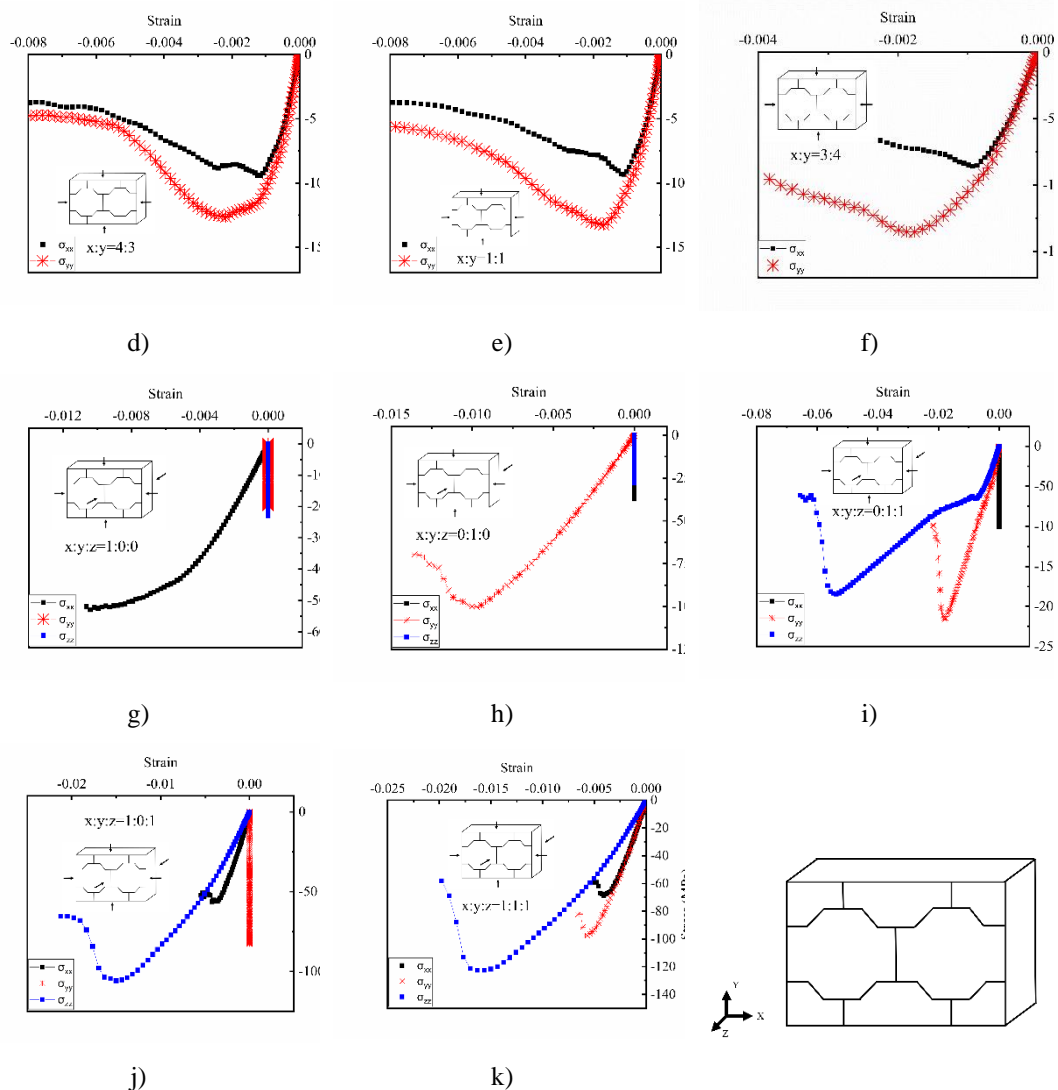
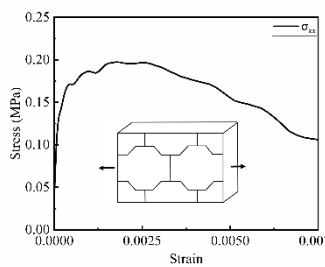


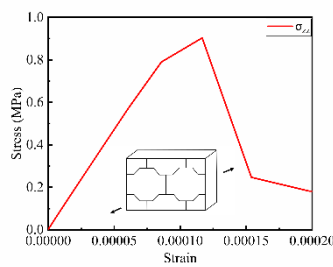
Figure 6-5. Stress-strain relations under compression-compression loadings

For the RVE under tension in the X direction, the top and bottom surfaces of the RVE are left free to move, while a non-zero displacement boundary condition in the X direction is applied at one of the lateral surfaces perpendicular to the X-axis when the opposite surface is constrained with a fixed boundary condition. Similar boundary conditions are applied in the Z direction for the RVE under tension in the Z direction. Figure 6-6a-b) show the stress-strain curves of the RVE when it is subjected to unconfined uniaxial tension in the X and Z directions, where the corresponding tensile strengths are 0.197MPa and 0.903MPa, respectively. It is to note that the tensile strength of the RVE in the Y direction without any confinement is 0. This is because for dry-stacking interlocking bricks without mortar bonding, the tensile strength is

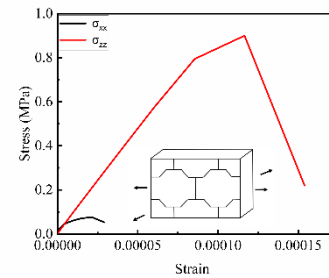
negligible. For the RVE under biaxial tensile loading, two tensile displacements normal to the left and the front surfaces of the specimen are applied and the corresponding movement in the direction on the opposite surfaces are fixed while the other surfaces are free. When the RVE is subjected to biaxial tensile loading in the horizontal X and the out-of-plane Z directions (Figure 6-6c), the maximum tensile strength in the horizontal X direction decreases substantially to below 0.1MPa, but that in the Z direction shows negligible difference comparing to that under uniaxial tension. As shown in Figure 6-6d), when confinement is applied to the Y direction, the maximum tensile strength in the X direction reduces marginally. It indicates that the constraint in the vertical direction has negligible influence on the biaxial tensile behavior of the RVE. When the RVE is subjected to the tensile-compressive loadings (see Figure 6-6e), the tensile strength also has no obvious change as compared to that under the uniaxial tension loading condition, where the failure of the RVE is resulted due to the maximum tensile strain is reached before the maximum compressive strength is met. Similar observation can be found when the RVE is subjected to the combined tensile-compression-compression loading as shown in Figure 6-6f).



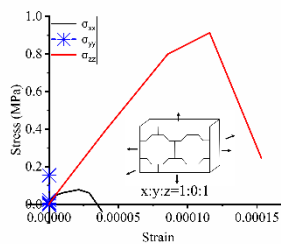
a)



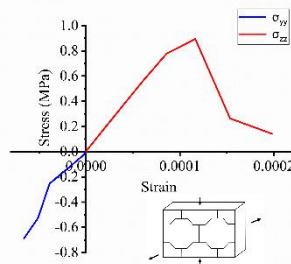
b)



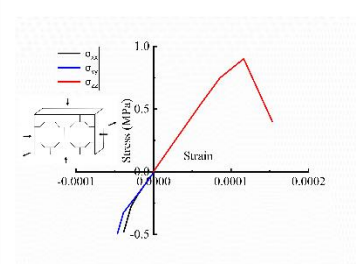
c)



d)



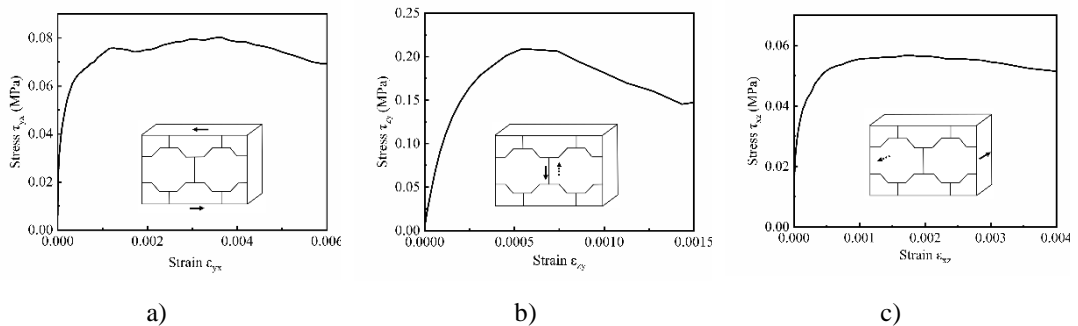
e)



f)

Figure 6-6. Stress-strain relations under compression-tension and tension-tension loadings

Figure 6-7 illustrates the stress-strain curves of the RVE when subjected to pure shear, in-plane compression-shear, and out-of-plane compression-shear loadings. For the RVE under pure shear loading, a monotonically increasing tangential displacement is applied on the top surface without any normal force, while the bottom surface of RVE is restrained for simplicity. The shear strengths of τ_{yx} , τ_{zy} and τ_{xz} are 0.08MPa, 0.209MPa and 0.057MPa, respectively, when subjected to pure shear loading (Figure 6-7a-c). It is observed that the shear stress τ_{zy} is significantly higher than τ_{yx} and τ_{xz} , because of the existence of shear keys in the interlocking bricks. Inter-brick sliding occurs when the RVE is subjected to pure shear in the YX and XZ planes. For the RVE under compression-shear loading, a monotonically increasing shear displacement is applied followed by a corresponding monotonically increasing normal (compressive) displacement on the same surface. Figure 6-7d) shows the stress-strain curves when the RVE is under the in-plane compression-shear loading. As can be seen, the shear strength significantly increases compared to that under the pure shear loading condition. Moreover, when the RVE is subjected to out-of-plane compression-shear loading, the shear strength also increases significantly (see Figure 6-7e). This demonstrates that for dry-stacking interlocking bricks, compressive stress is critical for the effective action of shear key in improving the shear resistance performance.



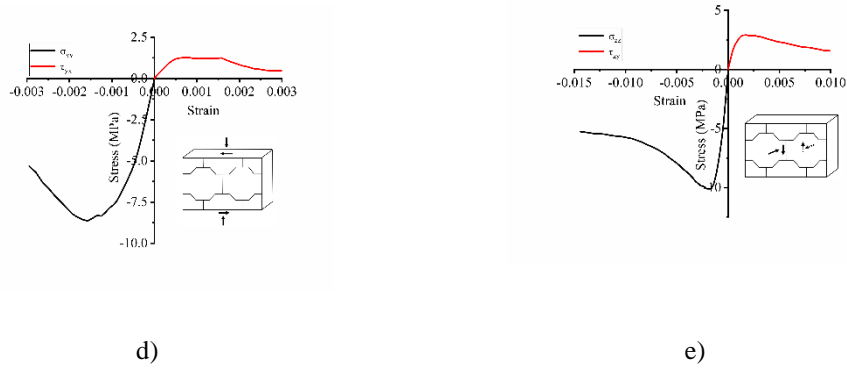


Figure 6-7. Stress-strain relations of RVE under compression-shear loadings

6.4.2 Equivalent material properties of RVE

In this section, the above numerical results of the RVE under different stress states are used to derive the equivalent material properties and the constitutive model of the RVE for interlocking brick walls, including the elastic properties, yield criterion, the plastic flow rule, hardening and softening rule, and damage model.

6.4.2.1 Elastic properties

The equivalent elastic modulus and Poisson's ratio can be derived from the stress-strain curves (Figure 6-5a-c) when the RVE is subjected to uniaxial compressive loadings. The shear modulus can be obtained from the stress-strain relations, as shown in Figure 6-7a-c) when the RVE is under pure shear loadings. From the above results, the elastic moduli of the equivalent RVE material are obtained as $E_x=9.13\text{GPa}$, $E_y=9.32\text{GPa}$, $E_z=9.13\text{GPa}$, $G_{yx}=1.02\text{GPa}$, $G_{zy}=1.06\text{GPa}$, $G_{xz}=1.07\text{GPa}$, and the Poisson's ratio can be calculated as $\nu_{yx}=0.23$, $\nu_{zx}=0.21$, and $\nu_{zy}=0.22$. Since the elastic modulus, Poisson's ratio, and the strength are very similar in the three directions, an isotropic material model is employed herein to simplify the modelling, where the equivalent material of RVE for interlocking bricks is assumed having the same elastic modulus and Poisson's ratio in the three directions. This isotropic material model is to be validated in a later section of this paper to examine its accuracy and suitability. The averaged value of elastic modulus in the three directions, i.e., $E_{eq.} = \frac{1}{3}(E_x + E_y + E_z)$,

is used as the elastic modulus, and the averaged Poisson's ratio, i.e., $v_{eq.} = \frac{1}{3}(v_{zy} + v_{yx} + v_{zx})$, is also employed for the RVE.

6.4.2.2 Yield criterion

The yield criterion of the equivalent material of the RVE for the interlocking bricks is important to simulate the homogenized continuum model. Based on the numerical results of the stress-strain relations for the RVE under different stress states (Figure 6-5-Figure 6-7), the equivalent failure envelope can be derived based on the maximum strength of the RVE.

In this material model, the yield function is assumed as follows:

$$F = \frac{1}{1-\alpha} (\sqrt{3J_2} + aI_1 + \beta \langle \bar{\sigma}_{max} \rangle - \gamma \langle -\bar{\sigma}_{max} \rangle) - \bar{\sigma}_c \leq 0 \quad (6-5)$$

where $\bar{\sigma}_{max}$ is the maximum effective stress; $\langle \cdot \rangle$ is Macauley bracket, I_1 is the first invariant of stress tensor, and J_2 is the second invariant of the stress tensor, that can be written as

$$I_1 = \sigma_1 + \sigma_2 + \sigma_3 \quad (6-6)$$

$$J_2 = \left(\frac{1}{6}\right) [(\sigma_1 - \sigma_2)^2 + (\sigma_2 - \sigma_3)^2 + (\sigma_3 - \sigma_1)^2] \quad (6-7)$$

where σ_1 , σ_2 , and σ_3 are the principal stresses.

Other parameters are defined as follows:

$$\alpha = \frac{\frac{f_{b0}}{f_{c0}} - 1}{2\left(\frac{f_{b0}}{f_{c0}}\right) - 1} \quad (6-8)$$

$$\beta = \frac{f_{c0}}{f_{t0}} (1 - \alpha) - (1 + \alpha)$$

$$\gamma = \frac{3(1 - K_c)}{2K_c - 1}$$

where f_{b0} is the biaxial compressive yield stress of the material; f_{c0} is the uniaxial compressive yield stress; f_{t0} is the tensile strength of the material. The ratio of the biaxial compressive yield stress to the uniaxial compressive yield stress, f_{b0}/f_{c0} , is calculated according to the biaxial failure envelope in the plane stress space, as shown in Figure 6-8. The ratio f_{b0}/f_{c0} for concrete is in the range of 1.10-1.16 [175]. Chi et al. [180] further widened the range of ratio f_{b0}/f_{c0} by considering fibre within concrete, which is suggested in the range of 1.32 to 1.63, whereas it is observed varying from 1.27 to 1.51 from Traina and Mansour tests [181]. From the numerical results shown in Figure 6-8, it gives $f_{b0}/f_{c0} = 1.617$.

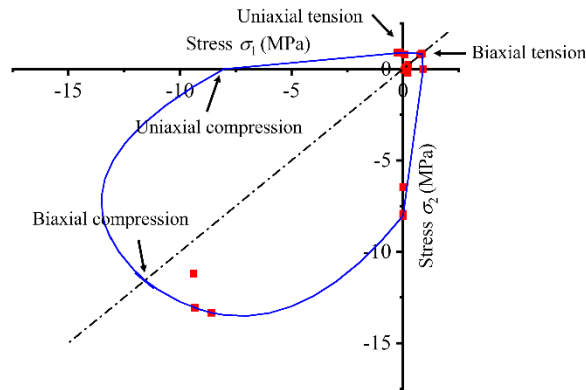


Figure 6-8. Biaxial failure envelope in plane stress space

According to the hydrostatic pressure $p = -\frac{1}{3}(\sigma_1 + \sigma_2 + \sigma_3) = -\frac{1}{3}I_1$, and the Mises equivalent stress $q = \sqrt{3J_2}$, the numerical strength points can be plotted in the p - q space. Figure 6-9 shows the strength envelope in the meridian and deviatoric planes. The shape of strength envelope in the deviatoric plane is modified through a scalar parameter K_c , denoting the ratio between the second stress invariants on the tensile meridian and the compressive meridians [113]. Typical values of K_c for

concrete are suggested to be from 0.64 by Schickert and Winkler [182] to 0.8 by Mills and Zimmerman [183]. Besides, Lubliner et al. [175] used $K_c = 2/3$ for plain concrete. It is to note that when $K_c = 1$, the strength curve in the deviatoric plane reduces to a circle, which however differs far from the strength envelope for the RVE of interlocking bricks. Since the tensile and compressive strengths of the RVE are apparently different, the value of K_c is determined according to the compressive meridian (CM) and tensile meridian (TM), where $K_c = q(TM)/q(CM)$ is a coefficient at a given state p . Tensile stresses are considered positive, and the failure surface can be described by the compressive ($\theta = 0^\circ$, $\sigma_1 = \sigma_2 < \sigma_3$) and the tensile ($\theta = 60^\circ$, $\sigma_1 = \sigma_2 > \sigma_3$) meridians [184, 185]. As shown in Figure 6-9, $K_c = 0.532$ is found to best fit the data for the RVE of interlocking bricks.

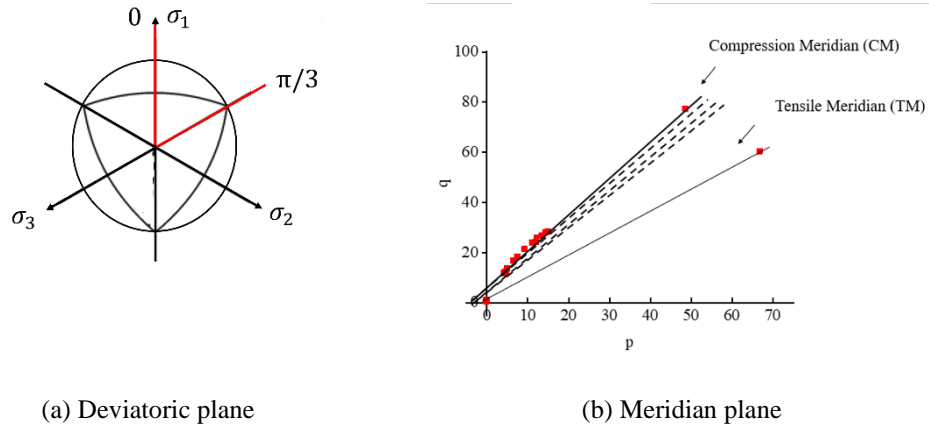


Figure 6-9. Failure surface in the deviatoric and meridian planes

6.4.2.3 Plastic flow rule

Since an associated flow rule for the yield surface gives an unrealistically high volumetric expansion in compression, which leads to an overestimated peak stress [186], the shape of the homogenised continuum loading surface at any given point is obtained by using the non-associated plastic flow rule [187]. The potential function G in Eq. (6-9) has a hyperbolic Drucker-Prager form.

$$G = \sqrt{(e\sigma_{to} \tan \psi)^2 + q^2} - p \tan \psi = 0 \quad (6-9)$$

where e is the eccentricity that defines the rate of the flow potential approaching its

corresponding linear function (the asymptote); σ_{to} denotes the strengths under uniaxial tension at failure; and ψ is the dilation angle calculated in the meridian plane [180].

The non-associated plastic potential dilation angle ψ is an important parameter, which influences the flow rule (as illustrated in Figure 6-10a). To determine the dilation angle ψ , four numerical simulations with the RVE under confined uniaxial loading condition in the Y direction with different confining pressures are conducted. The constant confining pressure is applied in the X and Z directions through the load-controlled method, and the compressive load in the Y direction is applied gradually through the displacement-controlled method. The confining pressures are 0.2 MPa, 0.4 MPa, 0.8 MPa and 1.2 MPa. The stress-strain relations obtained are shown in Figure 6-10b). The points in the stress-strain relations in terms of the maximum elastic strength are used to derive the shape of the yield surface based on previous studies [188-190]. After plotting these points in the meridian plane, $\tan \psi$ is found to be 0.688, and thus ψ is 34.53° .

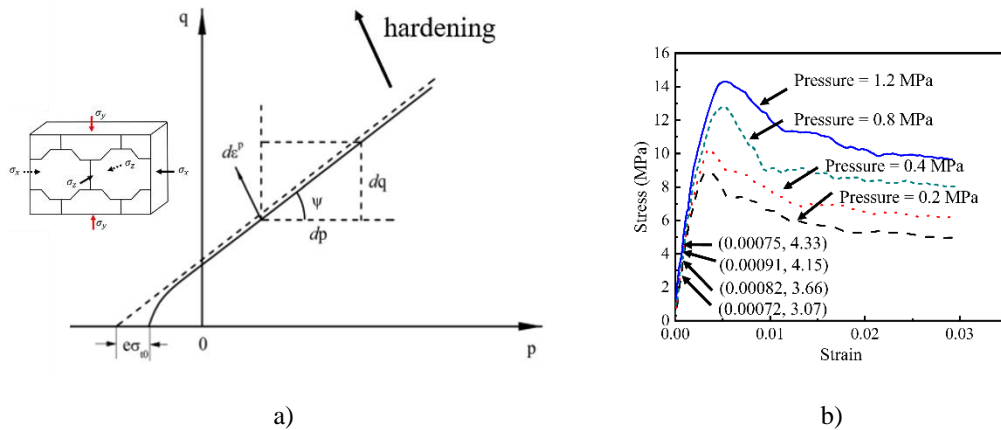


Figure 6-10. a) The plastic potential in the meridian plane; and b) confined uniaxial stress-strain relations under different pressures in the Y-direction

6.4.2.4 Hardening and softening

To depict the constitutive behavior more accurately, the hardening and softening effects are considered in the derivation of the equivalent material properties of the RVE. Without losing generality, Figure 6-11 shows the stress-strain curves of the RVE under uniaxial stress states, which comprises of an elastic stage, a hardening stage, and a softening stage. A multilinear consecutive model is used in the homogenised continuum to depict the elastic, hardening and softening behaviours as defined in Eqs. (6-10) and (6-11).

$$\sigma_c = \begin{cases} E_0 \varepsilon_c & \varepsilon_c \leq \varepsilon_{c0} \\ (\sigma_{c1} - \sigma_{c0}) \left(\frac{\varepsilon_c - \varepsilon_0}{\varepsilon_{c1} - \varepsilon_0} \right)^{\eta_1} + \sigma_{c0} & \varepsilon_{c0} \leq \varepsilon_c \leq \varepsilon_{c1} \\ (\sigma_{cu} - \sigma_{c1}) \left(\frac{\varepsilon_c - \varepsilon_{c1}}{\varepsilon_{cu} - \varepsilon_{c1}} \right)^{\eta_2} + \sigma_{c1} & \varepsilon_{c1} \leq \varepsilon_c \leq \varepsilon_{cu} \\ \sigma_{cu} \left[1 - \left(\frac{\varepsilon_c - \varepsilon_{cu}}{\beta_1 \varepsilon_{cu}} \right)^{\eta_3} \right] & \varepsilon_{cu} \leq \varepsilon_c \leq \varepsilon_{c2} \\ \sigma_{cu} \left[1 - \left(\frac{\varepsilon_c - \varepsilon_{cu}}{\beta_2 \varepsilon_{cu}} \right)^{\eta_4} \right] & \varepsilon_c \geq \varepsilon_{c2} \end{cases} \quad (6-10)$$

where $E_0 = 9.32$ GPa, is the initial elastic modulus; $\varepsilon_{c0} = 0.000567$ denotes the maximum elastic strain under compression; $\sigma_{cu} = 7.93$ MPa and $\varepsilon_{cu} = 0.00173$ represent the maximum compressive strength and the corresponding strain; $\sigma_{c1} = 7.33$ MPa and $\varepsilon_{c1} = 0.001054$ denote the turning point in the hardening region; $\sigma_{c2} = 6.52$ MPa and $\varepsilon_{c2} = 0.00245$ denote the turning point in the softening region (see Figure 6-11a); η_1 , η_2 , η_3 and η_4 describe the exponents increasing or decreasing of the curve; β_1 and β_2 are material parameters. Using the least squares method, the parameters are calculated as $\eta_1 = 0.78988$, $\eta_2 = 0.62162$, $\eta_3 = 1.90426$ and $\eta_4 = 0.9594$ and $\beta_1 = 0.80246$, $\beta_2 = 0.82954$ through curve fitting the stress-strain relations in Figure 6-11a).

$$\sigma_t = \begin{cases} E_0 \varepsilon_t & \varepsilon_t \leq \varepsilon_{t0} \\ k_1 \varepsilon_t + a_1 & \varepsilon_{t0} \leq \varepsilon_t \leq \varepsilon_{t1} \\ k_2 \varepsilon_t + a_2 & \varepsilon_{t1} \leq \varepsilon_t \leq \varepsilon_{t2} \\ k_3 \varepsilon_t + a_3 & \varepsilon_{t2} \leq \varepsilon_t \leq \varepsilon_{tu} \\ k_4 \varepsilon_t + a_4 & \varepsilon_{tu} \leq \varepsilon_t \leq \varepsilon_{t3} \\ k_5 \varepsilon_t + a_5 & \varepsilon_t \geq \varepsilon_{t3} \end{cases} \quad (6-11)$$

where k_1, k_2, k_3, k_4 and k_5 denote the slopes of the five linear parts, $k_1 = 930.17, k_2 = 149.41, k_3 = 19.97, k_4 = -1.02$ and $k_5 = -13.04$ are determined through curve fitting; a_1, a_2, a_3, a_4 and a_5 are the corresponding intercept of these linear formulae, in which $a_1 = 0.022, a_2 = 0.111, a_3 = 0.163, a_4 = 0.199$ and $a_5 = 0.229$; $\varepsilon_{t0} = 0.00000197$ is the ultimate elastic strain in tension; $\varepsilon_{t1} = 0.000113$ is the strain at the first turning point in the hardening region; $\varepsilon_{t2} = 0.00040$ is the strain at the second turning point in the hardening region; $\varepsilon_{tu} = 0.00165$ is the tensile strain at the maximum stress; and $\varepsilon_{t3} = 0.00246$ is the strain at the turning point in the softening region (as shown in Figure 6-11b).

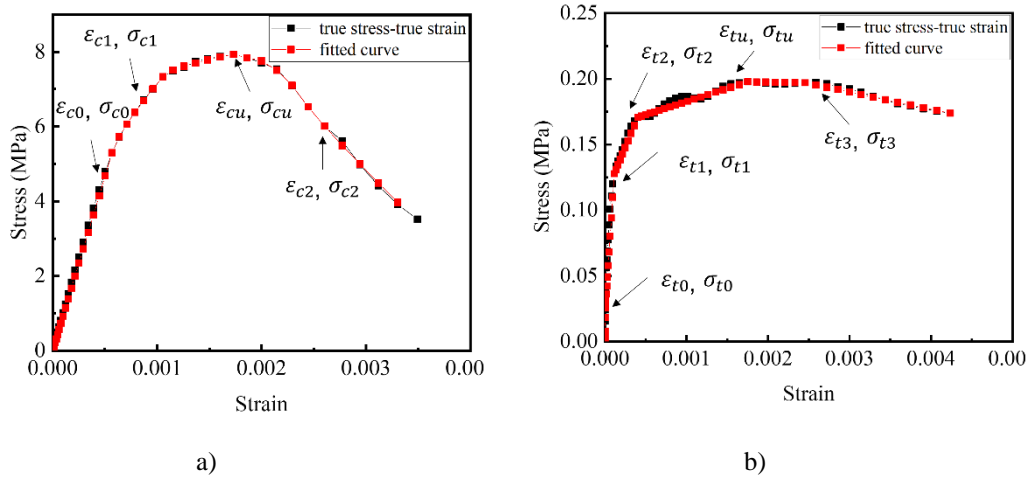


Figure 6-11. Stress-strain relations of the RVE under uniaxial stress states a) compression; b) tension

6.4.2.5 Damage model

The damage variables in this study are based on the continuum damage mechanics theory [191-193]. The damage scalar d that varies between 0 and 1 can be written as:

$$d = \frac{W_0 - W_\varepsilon}{W_0} \quad (6-12)$$

where W_0 denotes the strain energy for the undamaged element; W_ε denotes the strain energy for the damaged element (see Figure 6-12), which can be calculated by

$$W_0 = \frac{E_0 \varepsilon^2}{2} \quad (6-13)$$

and

$$W_\varepsilon = \int \sigma d\varepsilon = \int f(\varepsilon)d\varepsilon \quad (6-14)$$

where E_0 denotes the elastic modulus of the undamaged material. W_ε can be obtained through the Simpson integral approach to calculate the damaged strain energy under compression W_ε^c and the damaged strain energy under tension W_ε^t . Substituting Eqs. (6-10) and (6-11) into Eq. (6-14), respectively, the variables for W_ε^c and W_ε^t can be calculated.

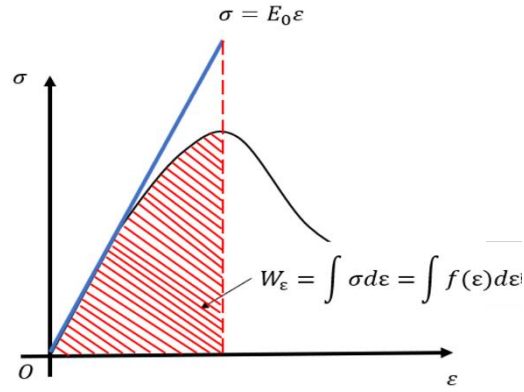


Figure 6-12. Material damage based on the continuum damage mechanics theory [191-193]

$$d_c = \begin{cases} 0 & \varepsilon_c \leq \varepsilon_{c0} \\ 1 - \frac{13.817\varepsilon_c - 219.542(0.00173 - \varepsilon_c)^{34.246} - 0.0048}{10000\varepsilon_c^2} & \varepsilon_{c0} < \varepsilon_c \leq \varepsilon_{c1} \\ 1 - \frac{16.56\varepsilon_c - 200.742(0.00173 - \varepsilon_c)^{23.924} - 0.0076}{10000\varepsilon_c^2} & \varepsilon_{c1} < \varepsilon_c \leq \varepsilon_{cu} \\ 1 - \frac{15.987\varepsilon_c - 44.30995(\varepsilon_c - 0.00173)^{22.402} - 0.0064}{10000\varepsilon_c^2} & \varepsilon_{cu} < \varepsilon_c \leq \varepsilon_{c2} \\ 1 - \frac{10.842\varepsilon_c + 37.5376(\varepsilon_c - 0.00173)^{7.73428} + 0.00659}{10000\varepsilon_c^2} & \varepsilon_c > \varepsilon_{c2} \end{cases} \quad (6-15)$$

and

$$\begin{cases} \varepsilon_t \leq \varepsilon_{t0} \\ \varepsilon_{t0} < \varepsilon_t \leq \varepsilon_{t1} \end{cases} \quad (6-16)$$

$$d_t = \begin{cases} 0 & \varepsilon_{t1} < \varepsilon_t \leq \varepsilon_{t2} \\ \frac{24443.53\varepsilon_t^2 - 0.1297\varepsilon_t + 0.00000019}{27153.215\varepsilon_t^2} & \varepsilon_{t2} < \varepsilon_t \leq \varepsilon_{tu} \\ \frac{1915.239\varepsilon_t^2 - 0.04627\varepsilon_t + 0.00000211}{1946.439\varepsilon_t^2} & \varepsilon_{tu} < \varepsilon_t \leq \varepsilon_{t3} \\ \frac{1447.969\varepsilon_t^2 - 0.05067\varepsilon_t + 0.00000482}{1451.079\varepsilon_t^2} & \\ \frac{3680.452\varepsilon_t^2 - 0.15752\varepsilon_t + 0.00003763}{3680.051\varepsilon_t^2} & \varepsilon_t > \varepsilon_{t3} \\ \frac{821.184\varepsilon_t^2 - 0.0403\varepsilon_t + 0.00001477}{820.037\varepsilon_t^2} & \end{cases}$$

where ε_c and ε_t are the compressive and tensile strains, respectively.

Substituting these variables and Eq. (6-13) into Eq. (6-12), the compressive damage scalar d_c and the tensile damage scalar d_t can be obtained as Eqs. (6-15) and (6-16). No damage exists in the elastic region but only in the inelastic region. The damage parameter under compression corresponding to the maximum compressive stress σ_{cu} is 0.295. It means that when compressive damage is more than 0.295, the strength surface begins to shrink. Based on this damage model, the damage distribution in the RVE for interlocking bricks under various loading conditions can be depicted.

It should be noted that the RVEs considered herein consist of geometrically perfect bricks, and hence there is no seating effect when the bricks are pressed against each other. As such, the derived homogenized constitutive material model does not account for the influence of the seating effect. Nevertheless, the aforementioned RVE unit and the associated homogenization derivation method are also applicable to interlocking brick assemblies with seating effects. By introducing geometric imperfections during brick modeling, the seating effect can be incorporated into the derived homogenized constitutive model.

6.5 Size Effect and Model Validation

6.5.1 Size effect

As discussed in Section 2, the selected RVE should be as small as possible to ensure the stress in the element being uniform. On the other hand, the RVE should also be

large enough to include all features of interlocking bricks. Despite the RVE selected could satisfy the basic requirements, to ensure the applicability and the reliability of the derived homogenized material properties, size effect of the RVE is examined. As shown in Figure 6-13a), the selected RVE has a width of 400 mm, a height of 300 mm, and a thickness of 100 mm. A 2×2 RVE as shown in Figure 6-13b) is numerically modelled under different stress states to evaluate the size effect.

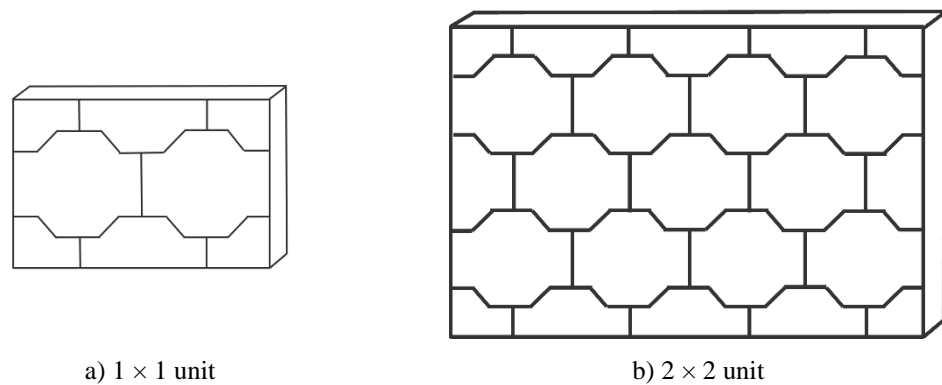
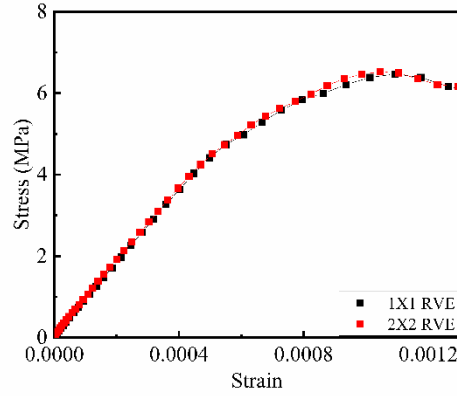


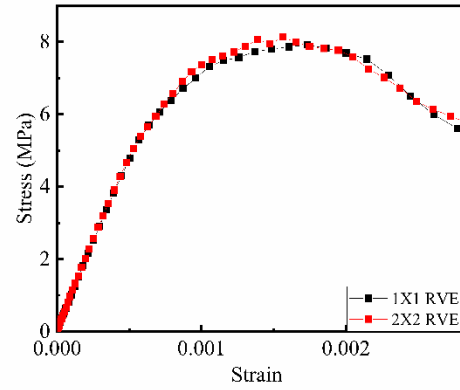
Figure 6-13. Models for examining the size effect

Figure 6-14 compares the stress-strain curves of the 1×1 unit and the 2×2 unit. When they are subjected to uniaxial compression in the X direction (see Figure 6-14a), the compressive strength of the 1×1 unit is 6.47 MPa, while that of the 2×2 unit is 6.52 MPa reflecting less than 1% difference. The initial stiffnesses of the two models also align well indicating the elastic modulus is independent of the size of the RVE when the equivalent material properties are applied to the homogenised continuum. When they are subjected to uniaxial compression in the Y direction as shown in Figure 6-14b), the compressive strength of the 1×1 unit is 7.92 MPa, while that of the 2×2 unit is 8.13 MPa with a discrepancy of 2.65%. When subjected to uniaxial tensile loading in the out-of-plane Z direction, the maximum strength of the 1×1 unit is 0.903 MPa, while that of the 2×2 unit is 0.901 MPa (as shown in Figure 6-14c). Figure 6-14d) shows the modelled stress-strain curves of the 1×1 unit and 2×2 unit subjected to compression-shear loading. The maximum shear stress of the 2×2 unit is slightly larger than that of the 1×1 unit with a difference less than 6%. Overall, the above evaluations show small

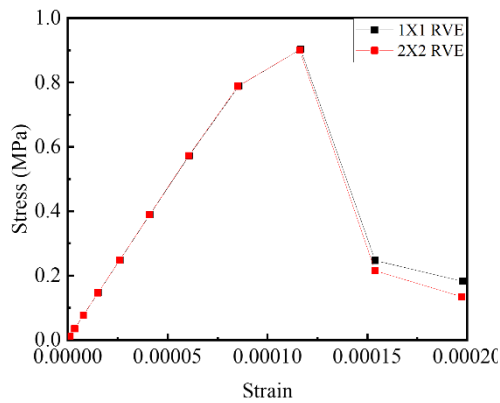
difference in the stress-strain relations between the 1×1 and the 2×2 units, demonstrating the negligible size effect on the selected RVE.



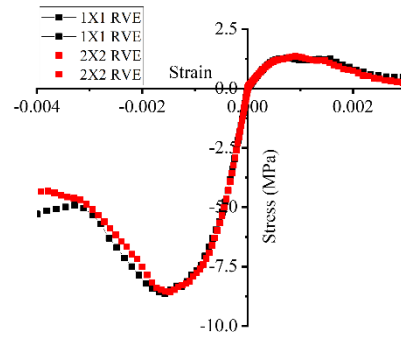
a) Uniaxial compression in the X direction



b) Uniaxial compression in the Y direction



c) Uniaxial tension in the Z direction



d) Compression-shear in the Y direction

Figure 6-14. Size effect of the RVE

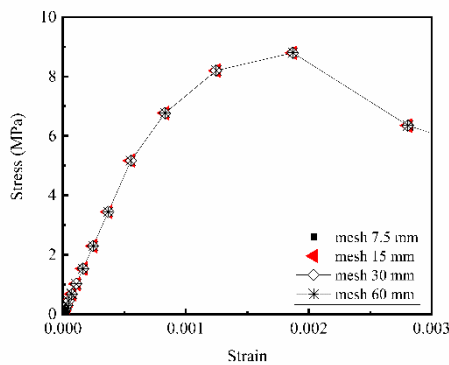
6.5.2 Model validation

To validate the suitability and accuracy of the RVE with the derived equivalent material model, the homogenized material properties are used to model the uniaxial compressive behavior and the compression-shear behaviour of an interlocking brick wall. The interlocking brick wall is 1200mm width, 900mm height, and 100mm thickness, which is fixed on the ground. It is firstly subjected to a uniaxial compressive load through displacement-controlled loading method. Then, in compression-shear case, another wall of the same size is subjected to the prescribed compressive loading and then horizontal shear loading through displacement control method. Mesh

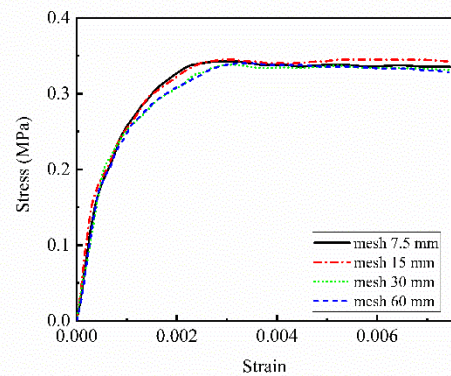
dependence study is firstly conducted to examine the influence of mesh size for the RVE. Then, the numerical modelling results are compared with data from detailed numerical modelling.

6.5.2.1 Mesh dependence

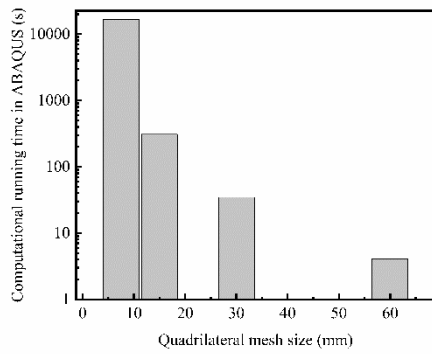
Four different mesh sizes, i.e., 7.5 mm, 15 mm, 30 mm, and 60 mm, are considered. Figure 6-15a) compares the stress-strain curves modelled using the RVE under compressive loading with different mesh sizes, where negligible difference can be seen. When the RVE wall is subjected to compression-shear loading as shown in Figure 6-15b), small variations can be found on the modelled stress-strain curves. In the meanwhile, Figure 6-15c) and d) compares the computational times using the four different mesh sizes. The numerical modelling results are obtained from a PC with Intel Core i7-7700 CPU 3.60 GHz with 16 GB RAM. As expected, the computational time reduces exponentially as the adopted mesh size increases. The above study demonstrates that when employing RVE method for interlocking brick wall, a relatively coarse mesh size could still give reasonably accurate predictions while significantly reduces the computational time. In this study, 30 mm mesh size is chosen for the subsequent numerical modelling.



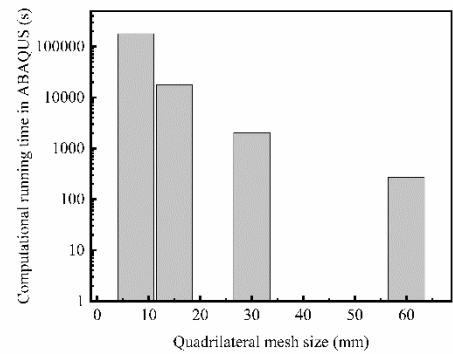
a) Stress-strain curves under compression



b) Stress-strain curves under compression-shear



c) Computational time for compression



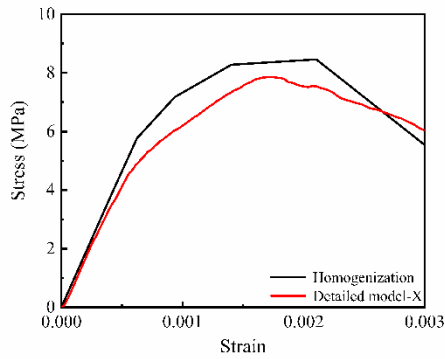
d) Computational time for compression-shear

Figure 6-15. Result comparison of mesh dependence study

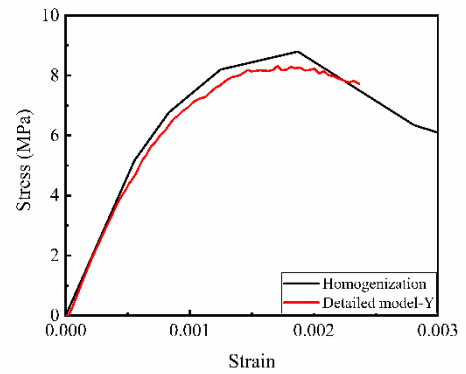
6.5.2.2 Uniaxial compression

Comparison is made between the homogenization method employing the RVE with the equivalent material properties as described above with $30\text{mm} \times 30\text{mm}$ mesh and a detailed FE method employing three-dimensional continuum elements with eight-node reduced integration (C3D8R) using $15\text{mm} \times 15\text{mm}$ mesh. Figure 6-16 shows the compressive stress-strain relations from these two models subjected to uniaxial compression in the X, Y and Z directions. It can be found that the modelling results of the homogenization method is very close to those from the detailed model. For example, the maximum compressive strengths in X and Y directions are 8.46 MPa and 8.80 MPa, with 7.63% and 5.77% error compared to the detailed modelling (7.86 MPa and 8.32 MPa). The initial moduli of the two models are also very close indicating the stiffness of the homogenization method could accurately represent that of the detailed modelling. When the interlocking brick wall is subjected to compressive loading in the Z direction, an ultimate strength of 10.71 MPa is predicted by the homogenization model. Compared to 10.73 MPa from the detailed model, the difference is 0.19%. In terms of the computational efficiency, when using a computer as described in last paragraph to model the interlocking brick wall under uniaxial compression in the Y direction, the homogenised continuum model requires 155MB memory in comparison to the 1659MB memory requirement for the detailed model.

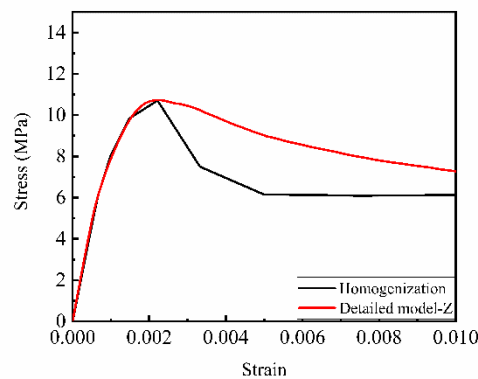
And the calculation time decreases from 100044 s to only 34.6 s, reflecting an 90.66% memory reduction and 99.97% computation time saving. It is apparent that the homogenised modelling method could substantially save the computational resource while giving reliable prediction of interlocking brick walls under vertical compressive loading.



a) Uniaxial compression in the X direction



b) Uniaxial compression in the Y direction



c) Uniaxial compression in the Z-direction

Figure 6-16. Comparison of stress-strain curves of the homogenization method and the detailed modelling method for the interlocking brick wall under uniaxial compression

6.5.2.3 Compression-shear

To further validate the homogenization method for interlocking brick wall, the interlocking brick wall subjected to compression-shear loading is modelled. The results are compared with those using detailed models. The same wall as described above is modelled with detailed and homogenized modelling for comparison. A high-strength steel plate (1400mm × 200mm × 50mm) is applied to distribute the shear load

from the loading point to the surface of the wall. Nodes of the contacting steel plate and the bricks are shared and merged together. The material properties of the high-strength steel follows previous study [168]. A uniform pressure of 0.3 MPa is applied to the interlocking brick wall in the Y direction. As above, in the homogenization method, the RVE with the equivalent material properties is employed with 30mm ×30 mm mesh size. Solid elements (C3D8R) with 15mm mesh are adopted in the detailed model. Gradually increased in-plane horizontal load controlled by displacement in the X direction is applied to the left-up corner of the wall, while the footing is fully fixed. Figure 6-17 shows the simulated shear stress versus strain curves from the two models. It can be seen that although the homogenization model slightly underestimates the initial modulus, it could reasonably replicate the behaviour of the interlocking brick wall as that of the detailed model. An ultimate shear strength of 0.338 MPa is predicted by the homogenization model, while that by the detailed model is 0.352 MPa. The difference between the predicted shear strength from the two models is 3.98%.

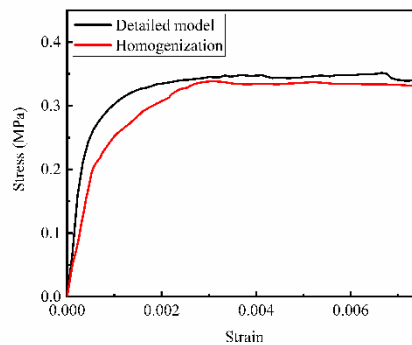


Figure 6-17. Comparison of shear stress-strain curves of the homogenization method and the detailed modelling method for the interlocking brick wall under compression-shear loading

Figure 6-18 compares the failure patterns of the detailed model and the homogenization model, where material damage is depicted by the equivalent plastic strain. At the instance when the peak shear strength is reached, damage mainly concentrates at the bottom right corner of the detailed model. In comparison, in the

homogenized model, similar damage pattern is predicted but with more severe damage. Overall, the homogenized model consumes 210 MB of memory and takes 2029.7 s to complete the numerical analysis, while the detailed model demands 2148 MB memory and requires 109218 s for the same analysis. It reflects a 90.22% memory saving and a 98.14% computation time saving, which proves the efficiency of the homogenization approach. Through the above comparisons, it can be found that the homogenized modelling method could very effectively and efficiently predict the responses of dry-stacking interlocking brick wall, significantly ease the complexity of the design analysis of such masonry structures. Since the developed approach is derived using complex stress states, which considers elastic properties, strength model, plastic flow rule, hardening and softening, and damage model, it can thus be applied to model the interlocking brick walls under complex loading conditions and stress states. Further validation and verification of the homogenized model for modelling the interlocking brick wall under dynamic loading are underway.

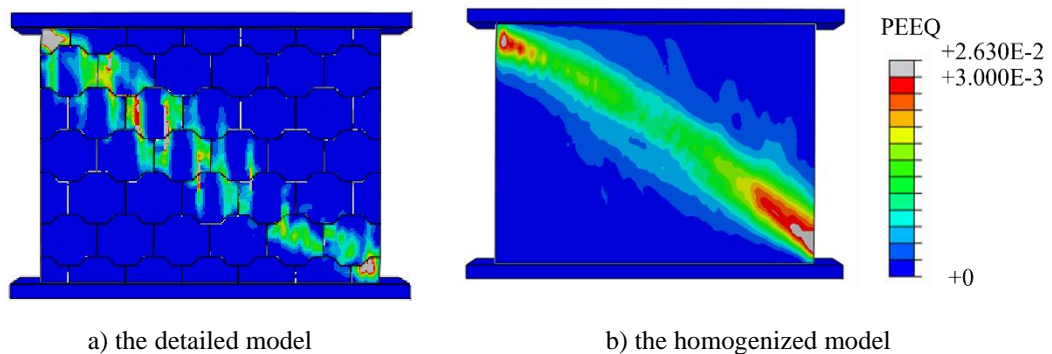


Figure 6-18. Comparison of damage contours of the homogenization method and the detailed modelling method for the interlocking brick wall under compression-shear loading

6.6 Summary

In this chapter, a homogenization modelling method for dry-stacking interlocking brick wall is developed. The different stress states of the selected RVE are numerically modelled for determination of the equivalent material properties. The equivalent

elastic properties, yield criterion, non-associative plastic flow rule, hardening and softening effects, and damage model of the RVE are determined. Size effect of the selected RVE is also examined. The accuracy and suitability of the developed homogenization method for dry-stacking interlocking brick wall are assessed through comparing the modelling results from homogenized and detailed numerical model. The following conclusions are derived from this study:

1. Numerical results from the RVE under different stress states show insignificant anisotropic material properties of dry-stacking interlocking brick wall, therefore isotropic constitutive model is developed.
2. Through modelling the RVE under different stress states, the equivalent constitutive model parameters of interlocking brick wall are derived.
3. On the selected RVE for interlocking brick wall, insignificant size effect is demonstrated. Therefore, the RVE can be applied to model the response of interlocking brick structures.
4. Model validation is performed through comparing the results from the homogenized model and detailed model of an interlocking brick wall under uniaxial compressive loadings in three directions and combined compression-shear loading. Reliable predictions of interlocking brick wall responses are obtained at less than 10% computer memory and 5% computational time as compared to the detailed modelling. The developed RVE model can be used to efficiently predict the responses of interlocking brick walls.

CHAPTER 7 NUMERICAL DERIVATION OF HOMOGENIZED CONSTITUTIONAL RELATION OF MORTAR-LESS INTERLOCKING BRICK WALL FOR DYNAMIC RESPONSE PREDICTION

7.1 Introduction

In Chapter 6, a homogenised constitutive model suitable for mortarless interlocking brick structures is proposed, and its accuracy under static loads is demonstrated. Since during the service life, a structure could be subjected to dynamic loading such as impact from vehicle crash and cyclone debris impact, as well as blast loading from gas and solid explosive detonations. In this chapter, the RVE studied in Chapter 6 is further developed to account for strain rate effect to be ready for simulating the dynamic response of interlocking brick structures under impact and impulsive loadings. Numerical simulation is performed to model the response of interlocking bricks under different stress states and various strain rates. The equivalent material properties for the RVE is determined. Model validation is then performed using the RVE to simulate the response of interlocking brick walls subjected to solid explosive blast and gas explosion. Comparison is made on the modeling results between RVE and conventional detailed FE analysis. The results demonstrate the effectiveness and efficiency of the homogenised constitutive model considering strain rate effects.

7.2 Numerical Modelling

The RVE is still modelled using the commercial software ABAQUS [174]. The shape, dimension, and material properties of the bricks are also modelled in detail as in

Chapter 6. The generated RVE is used to simulate the different stress states to derive the homogenized material properties.

7.2.1 Material model

Concrete Damage Plasticity (CDP) material model in ABAQUS is employed for the interlocking brick material, which is commonly used to model the nonlinear behavior of concrete-like materials. Material hardening and softening in both compression and tension can be considered using Eqs. (7-1) and (7-2). As illustrated in Figure 7-1, under uniaxial compression and tension, the stress-strain relations defining the compressive stress σ_c as well as the tensile stress σ_t are derived as follows:

$$\sigma_c = (1 - d_c)E_0(\varepsilon_c - \bar{\varepsilon}_c^{pl}) \quad (7-1)$$

$$\sigma_t = (1 - d_t)E_0(\varepsilon_t - \bar{\varepsilon}_t^{pl}) \quad (7-2)$$

where d_c and d_t are the damage scalars for compression and tension; ε_c and ε_t are the total strains in compression and tension; $\bar{\varepsilon}_c^{pl}$ and $\bar{\varepsilon}_t^{pl}$ are the equivalent plastic strains in compression and tension; and E_0 denotes the undamaged elastic modulus of the material.

The density of brick is 2565kg/m^3 . Laboratory test found the unconfined uniaxial compressive strength f_c is 17.8 MPa, the Young's modulus of brick E_0 is 13.5 GPa, and the Poisson's ratio ν_c is 0.2. The tension stiffening is defined following reference [38], where the uniaxial tensile stress is assumed as $0.1 f_c$. A non-associated plastic flow rule representing the plastic potential is used with a dilation angle of 30° . The ratio of biaxial compressive yield stress over the uniaxial compressive yield stress, f_{bo}/f_{co} , is taken as 1.16. The eccentricity parameter is selected to be 0.1 to smooth the tension corner [102].

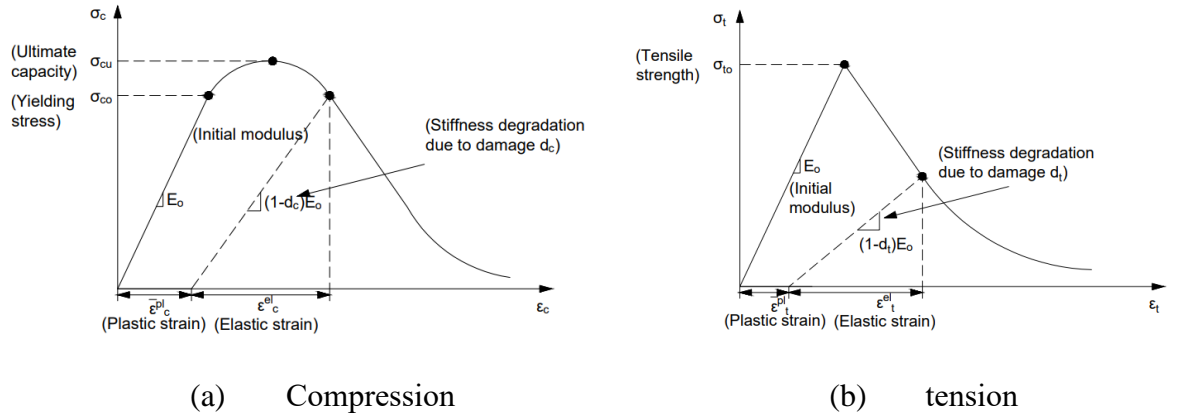


Figure 7-1. Uniaxial compressive and tensile behaviors of brick material in the CDP model

7.2.2 Strain rate effect

To account for strain rate effect, the DIF relation by Hao and Tarasov [134] are employed in this study because many previous studies have proved this relation yielding good modelling accuracy.

DIF for compressive strength σ_{c0} :

$$DIF = 0.0268 \ln \dot{\epsilon} + 1.3504 \text{ for } \dot{\epsilon} \leq 3.2 \text{ s}^{-1} \quad (7-3)$$

$$DIF = 0.2405 \ln \dot{\epsilon} + 1.1041 \text{ for } \dot{\epsilon} > 3.2 \text{ s}^{-1} \quad (7-4)$$

DIF for strain at peak compressive strength ϵ_{c0} :

$$DIF = 0.0067 \ln \dot{\epsilon} + 1.0876 \quad (7-5)$$

where $\dot{\epsilon}$ is the strain rate.

Figure 7-2 illustrates the stress-strain relation of brick when subjected to uniaxial compression at different strain rates. At a strain rate of $\dot{\epsilon} = 0.0001 \text{ s}^{-1}$, the brick exhibits an ultimate compressive strength of 17.81 MPa, and a threshold compressive strain of 0.0028. When the strain rate increases to 10 s^{-1} , the ultimate compressive strength of the brick is approximately 1.66 times its quasi-static strength. Additionally, the threshold compressive strain shows a slight increase as the strain rate increases.

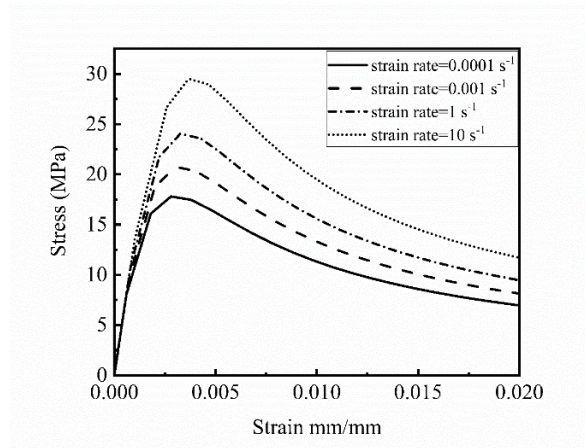


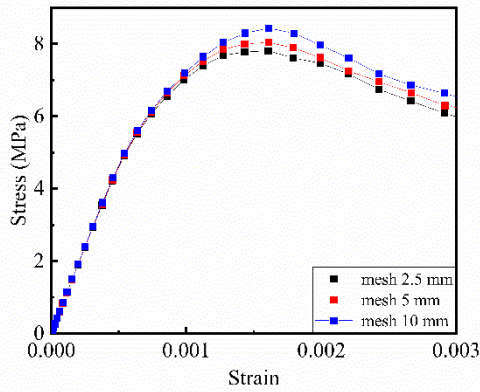
Figure 7-2. Uniaxial stress-strain curve of brick

7.2.3 Contact model

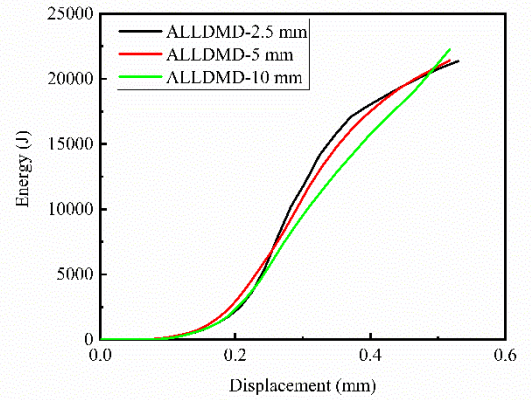
The interlocking bricks are dry-stacked without mortar or glue bonding. The surface-to-surface contact algorithm is thus adopted to model the contact between adjacent interlocking bricks. Mohr-Coulomb criterion with a friction coefficient of 0.3 is used to define the tangential behavior. Hard contact is used to define the normal behavior to avoid penetration at the contacting surfaces.

7.2.4 Mesh convergence

10 mm, 5 mm and 2.5 mm meshes are used for the interlocking bricks to examine mesh convergence. Numerical modelling results show that when subjected to out-of-plane loading, the numerical model with 5 mm mesh yields a converged prediction, which slightly overestimates the peak compressive strength with a +2.91% difference comparing to the model with 2.5 mm mesh, and a -4.70% under-prediction comparing to the model with 10mm mesh. To ensure the selected mesh size leads to converged results on brick damage, the relationship between energy dissipation due to material damage and the applied displacement is plotted in Figure 7-3b), where all mesh sizes show similar energy dissipations. The above study demonstrates 5 mm mesh is suitable for the RVE of interlocking bricks.



(a) Stress-strain curves of the modelled RVE under out-of-plane loading



(b) Material damage scalar versus applied displacement

Figure 7-3. Mesh convergence study

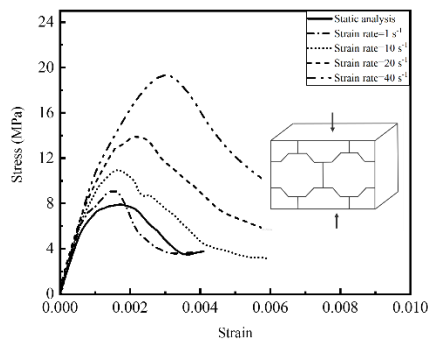
7.3 Numerical Results

Intensive numerical simulation is performed on the RVE to model its response under different stress states. The equivalent material properties, including the elastic properties, yield criterion, strain rate effect, hardening/softening model and damage model, are derived.

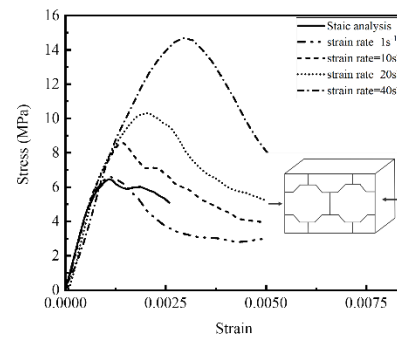
7.3.1 Stress-strain relations

Figure 7-4 depicts the stress-strain relations of the RVE under uniaxial compression at five different strain rates. It can be observed that the uniaxial compressive strength of the RVE increases with the strain rate. The uniaxial compressive strength of the RVE in the vertical direction (y-axis) at a strain rate of 0.001 s^{-1} is 9.11 MPa, which is significantly lower than the quasi-static uniaxial compressive strength of brick of 17.8 MPa. This is because under low strain rate, there is sufficient time for the brick to deform and to find the weakest position for fracture to develop, which thus leads to a lower overall strength. When the strain rate increases to 40 s^{-1} , the ultimate compressive strength increases to approximately 2.12 times of that at the strain rate of 0.001 s^{-1} , demonstrating apparent strain rate effect. When the RVE is subjected to intermediate strain rates between 1 s^{-1} and 20 s^{-1} , the equivalent compressive strength exhibits

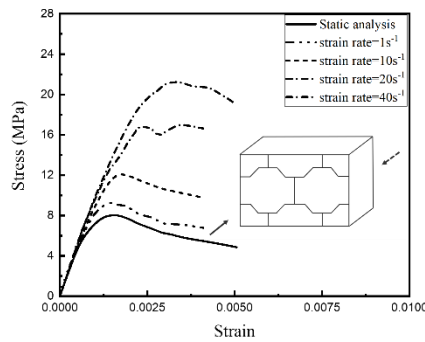
considerable increase but is still lower than the compressive strength of the brick material. Similar response can be found in Figure 7-4b) and c), where apparent strain rate effect can be observed. The dynamic compressive strength in the vertical direction (y-axis) is slightly higher than that in the horizontal direction (x-axis), while that in the out-of-plane direction (z-axis) has the highest compressive strength. This is because the layout of shear keys has minimum influence in the out-of-plane direction.



(a) Vertical direction (y-axis)



(b) Horizontal direction (x-axis)



(c) Out-of-plane direction (z-axis)

Figure 7-4. Stress-strain curves of RVE under uniaxial compressions

Figure 7-5 illustrates the stress-strain curves under uniaxial tension at five different strain rates. It can be seen that the ultimate tensile strength increases with strain rate. The tensile strength of the RVE at the same strain rate is much smaller than the corresponding compressive strength. When the strain rate is less than 1.0 s^{-1} , the

uniaxial tensile strength in the out-of-plane direction (z-axis) is larger than that in the horizontal direction. This can be attributed to the orientation of the bricks and the presence of interlocking keys, which can provide a greater resistance to the out-of-plane loading. When the strain rate increases to above 20s^{-1} , the tensile strength of the RVE in the x-axis quickly increases probably because of strain rate effect and more substantial inertial confinement. It is to note that the tensile strength in the y-axis is equivalent to zero because of no mortar/glue used to bond the interlocking bricks in the masonry wall.

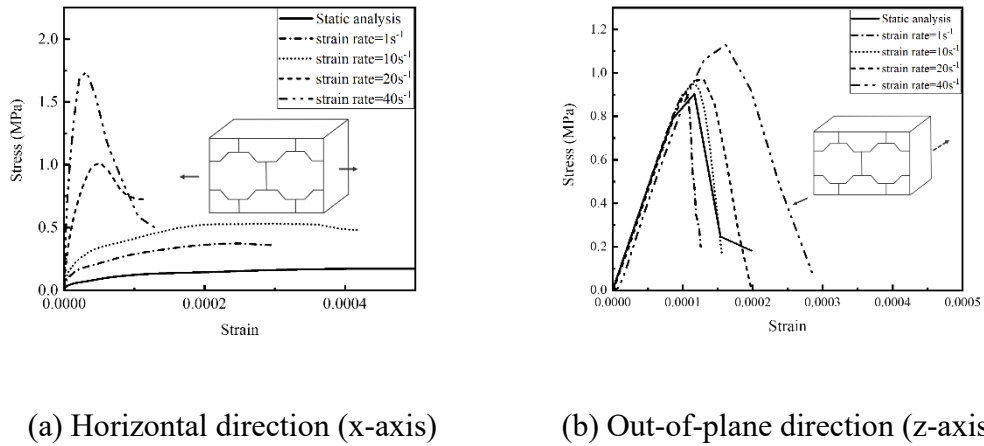
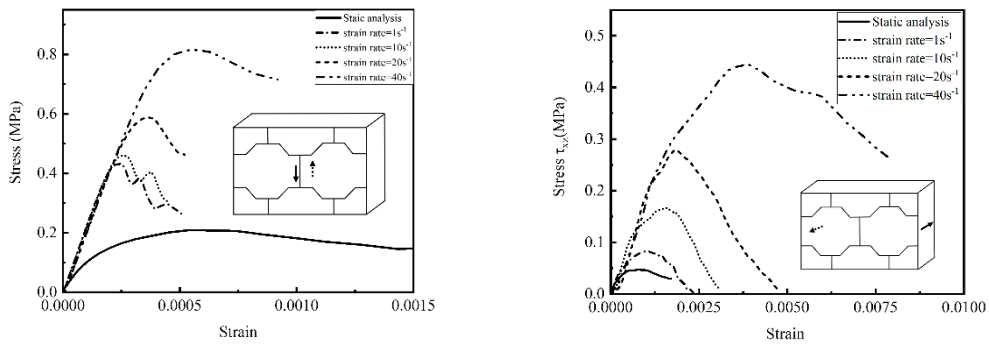


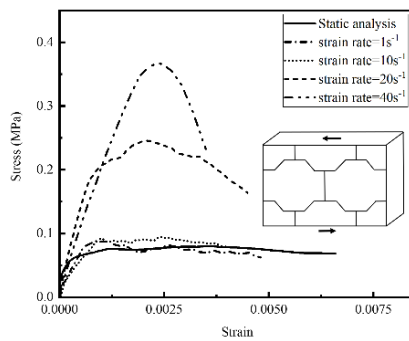
Figure 7-5. Stress-strain curves under uniaxial tension

Figure 7-6 shows the stress-strain curves of the RVE under pure shear conditions. It can be observed that the shear strength of the RVE increases with strain rate. It is to note that the shear strength is slightly lower than the tensile strength and significantly lower than the compressive strength at similar strain rates, because for dry-stacking interlocking bricks, the shear strength is strongly related to the applied normal force. The pure shear strength here only reveals the cohesion. A largest shear strength is found in the out-of-plane (z-y plane) (τ_{zy}), while the in-plane shear strength (τ_{yx}) is the smallest ($\tau_{zy} > \tau_{xz} > \tau_{yx}$).



(a) z-y plane

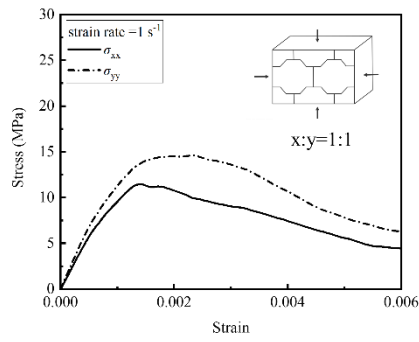
(b) x-z plane



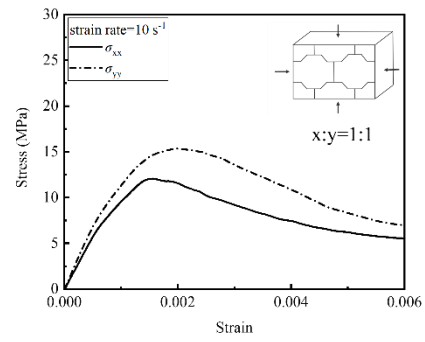
(c) y-x plane

Figure 7-6. Stress-strain curves under shear loading

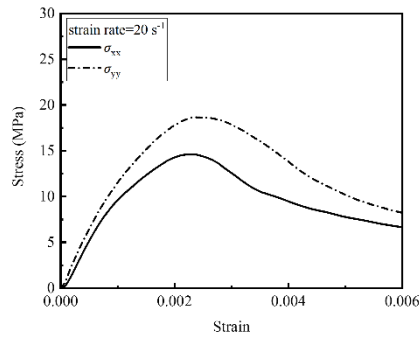
Figure 7-7 shows the stress-strain curves of the RVE when it is subjected to biaxial compression with gradually increased displacement in the y-axis and x-axis and the z-axis is unconstrained. The ratio of displacements and thus strains in each direction is $x:y=1:1$. The compressive strengths of the RVE under a strain rate of 1 s^{-1} in the x-axis and y-axis are 11.44 MPa and 14.59 MPa, respectively, which are both higher than the corresponding unconfined uniaxial compressive strengths. This behavior is attributed to the confinement effect, which provides a more efficient distribution of the load and generates more interlocking forces among the bricks, leading to an increase in the compressive strength of the RVE. Additionally, as strain rate increases, the recorded RVE compressive strength also increases accordingly, which demonstrates strain rate effect on the bi-axial strength of the RVE.



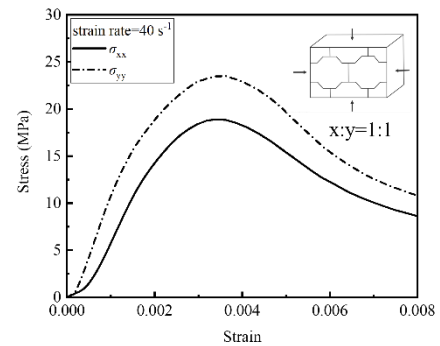
(a) Strain rate 1 s^{-1}



(b) Strain rate 10 s^{-1}



(c) Strain rate 20 s^{-1}



(d) Strain rate 40 s^{-1}

Figure 7-7. Stress-strain curves under biaxial compression

Figure 7-8 shows the stress-strain curves of the RVE under constrained compression (x-axis and z-axis constrained). The peak compressive strength of the RVE is found to be more than 100 MPa in the vertical direction (y-axis), which is substantially higher compared to the case without confinement. This indicates that confinement has a significant effect on the compressive strength of dry-stacking interlocking bricks. Figure 7-9 depicts the stress-strain curves of the RVE under bi-axial compression when the RVE is only restrained in the out-of-plane direction (z-axis). It is evident that the peak compressive capacity is more than 100 MPa in the horizontal direction (x-axis), and the peak compressive capacity is more than 180 MPa in the vertical direction (y-axis). These results demonstrate the beneficial effect of constraints in enhancing the compressive strength of the RVE. This behavior can be attributed to the confining

effect, which provides an efficient distribution of the load and generates more interlocking forces among the bricks, leading to an increase in the compressive strength of the RVE.

Figure 7-10 shows the stress-strain curves of the RVE under triaxial loading conditions. The compressive strength is found to be significantly higher than unconfined or partially confined conditions. Moreover, the ultimate compressive strengths of the RVE in both biaxial and triaxial compression states are observed to increase with increasing strain rate, indicating a pressure-dependent and rate-dependent behavior of the dry-stacking interlocking bricks under compression-compression stress states.

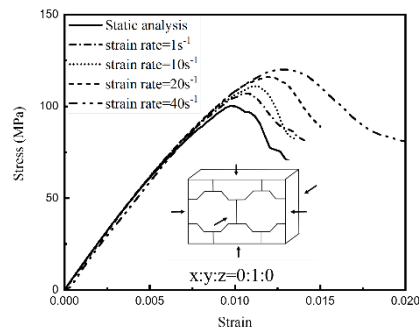
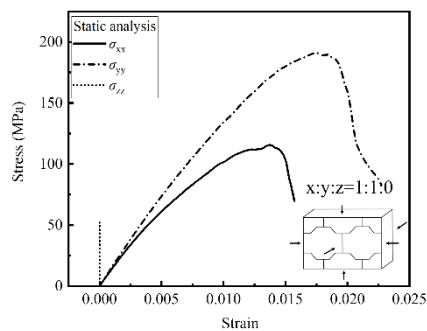
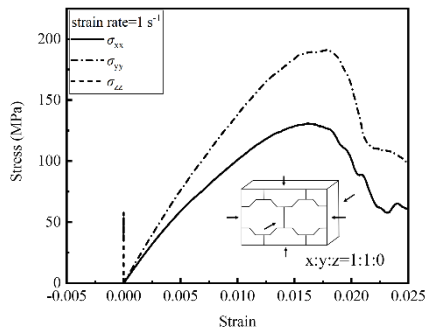


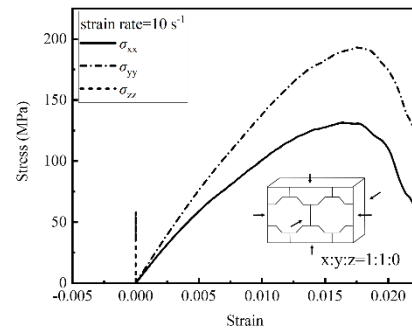
Figure 7-8. Stress-strain curves under compression with two constraints



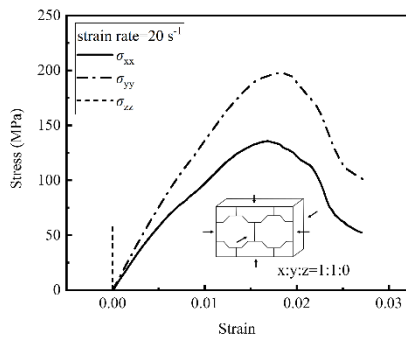
(a) quasi-static state



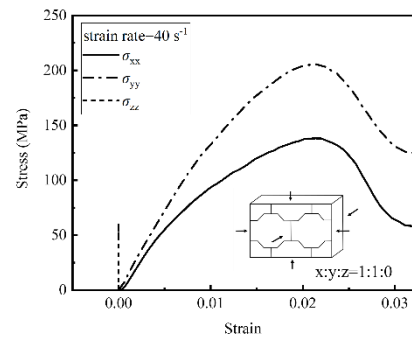
(b) Strain rate 1 s^{-1}



(c) Strain rate 10 s^{-1}

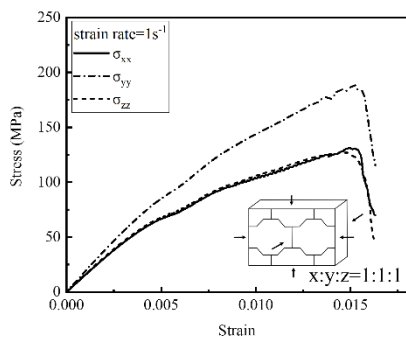


(d) Strain rate 20 s^{-1}

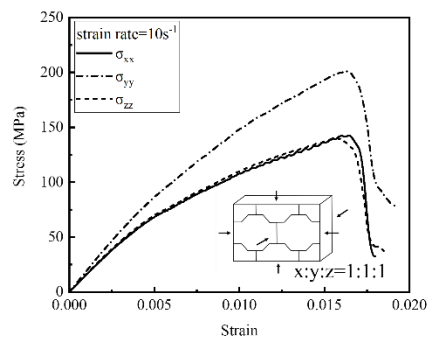


(e) Strain rate 40 s^{-1}

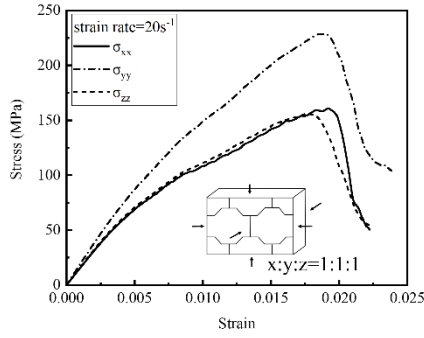
Figure 7-9. Stress-strain curves under bi-axial compression with constraint



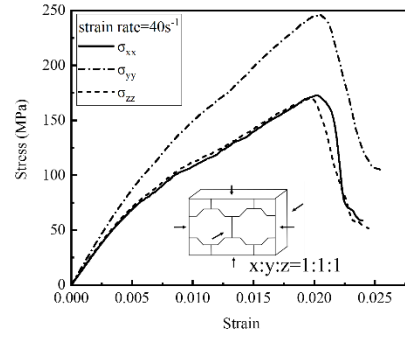
(a) Strain rate 1 s^{-1}



(b) Strain rate 10 s^{-1}



(c) Strain rate 20 s^{-1}



(d) Strain rate 40 s^{-1}

Figure 7-10. Stress-strain curves under triaxial loading

7.3.2 Derivation of equivalent properties

7.3.2.1 Elastic properties

The stress-strain curves of the RVE subjected to uniaxial compressive loadings are used to derive the equivalent elastic modulus and Poisson's ratio of the RVE. Figure 7-4 shows that the elastic modulus remains nearly constant with an increase in strain rate from 0.0001 s^{-1} to 40 s^{-1} . Based on these results, the elastic modulus of the equivalent RVE material is obtained as $E_x = 9.13 \text{ GPa}$, $E_y = 9.32 \text{ GPa}$, $E_z = 9.13 \text{ GPa}$. The shear modulus and Poisson's ratio can be calculated from the stress-strain relations when the RVE is under pure shear loadings, as shown in Figure 7-6. The values are $\nu_{yx} = 0.23$, $\nu_{zx} = 0.21$, and $\nu_{zy} = 0.22$. $G_{yx} = 1.02 \text{ GPa}$, $G_{zy} = 1.06 \text{ GPa}$, $G_{xz} = 1.07 \text{ GPa}$. Since the elastic modulus, the shear modulus and the Poisson's ratio are similar in the three directions, an isotropic material model is employed to simplify the modelling, assuming the equivalent material of the RVE for interlocking bricks has the same elastic modulus, shear modulus and Poisson's ratio in all three directions. This isotropic material model will be validated later to assess its accuracy and suitability. The average elastic modulus in the three directions, $E_{eq.} = \frac{1}{3}(E_x + E_y + E_z)$, the average shear modulus, $G_{eq.} = \frac{1}{3}(G_{xy} + G_{yz} + G_{xz})$, and the averaged Poisson's ratio, $\nu_{eq.} =$

$\frac{1}{3}(v_{zy} + v_{yx} + v_{zx})$, are used for the RVE.

7.3.2.2 Strength envelop

Based on the stress-strain curves modelled above, the equivalent strength envelope is derived for the RVE of interlocking brick wall. The yield criterion is as follows:

$$F = \frac{1}{1-a} (\sqrt{3}J_2 + aI_1 + \beta < \bar{\sigma}_{max} > -\gamma < -\bar{\sigma}_{max} >) - \bar{\sigma}_c \leq 0 \quad (7-6)$$

where $\bar{\sigma}_{max}$ represents the maximum effective stress; I_1 denotes the first invariant of stress tensor; and J_2 represents the second invariant of the stress tensor, which can be written as:

$$I_1 = \sigma_1 + \sigma_2 + \sigma_3 \quad (7-7)$$

$$J_2 = \left(\frac{1}{6}\right) [(\sigma_1 - \sigma_2)^2 + (\sigma_2 - \sigma_3)^2 + (\sigma_3 - \sigma_1)^2] \quad (7-8)$$

where σ_1 , σ_2 , and σ_3 are the 1st, 2nd and 3rd principal stresses, respectively.

The other parameters can be defined as below:

$$\alpha = \frac{\frac{f_{b0}}{f_{c0}} - 1}{2\left(\frac{f_{b0}}{f_{c0}}\right) - 1}$$

$$\beta = \frac{f_{c0}}{f_{t0}}(1 - \alpha) - (1 + \alpha) \quad (7-9)$$

$$\gamma = \frac{3(1 - K_c)}{2K_c - 1}$$

where f_{b0} represents the biaxial compressive yield stress of the material; f_{c0} denotes the uniaxial compressive yield stress; f_{t0} is the tensile strength of the material. The ratio of the biaxial compressive yield stress to the uniaxial compressive yield stress, f_{b0}/f_{c0} , is calculated based on the biaxial failure envelope in the plane stress space.

Based on the numerical results presented in Figure 7-11, the value of f_{bo}/f_{co} is 1.617.

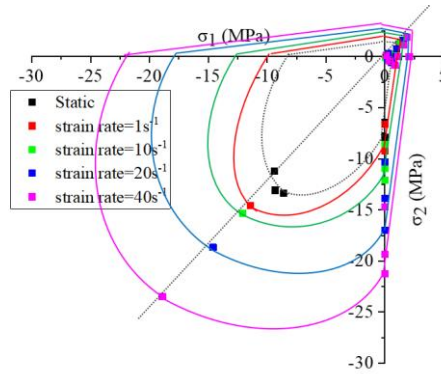
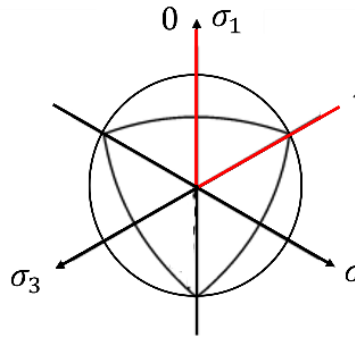
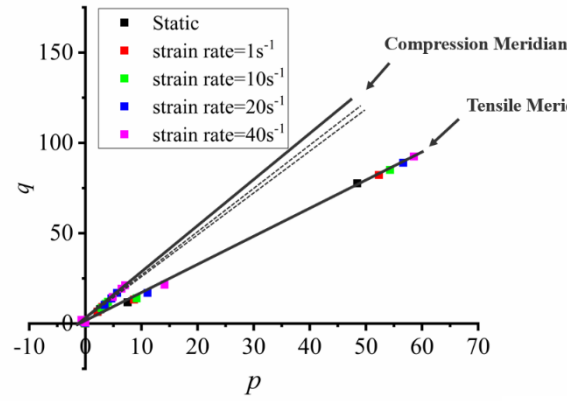


Figure 7-11. Biaxial failure envelope in plane stress space for different strain rates

The strength scatters obtained from numerical simulations can be plotted in the p - q space by employing the hydrostatic pressure $p = -\frac{1}{3}(\sigma_1 + \sigma_2 + \sigma_3) = -\frac{1}{3}I_1$ and the Mises equivalent stress $q = \sqrt{3J_2}$. The strength envelope in the meridian plane and the deviatoric plane is illustrated in Figure 7-12. The shape of the strength envelope in the deviatoric plane is adjusted by a scalar parameter K_c , which represents the ratio between the second stress invariants on the tensile meridian and compressive meridians [113]. For concrete, typical values of K_c range from 0.64 to 0.80 [182, 183]. Alternatively, Lubliner et al. [175] used $K_c = 2/3$ for plain concrete. Since the tensile and compressive strengths of the RVE are evidently different, the value of K_c is determined by considering the compressive meridian (CM) and tensile meridian (TM), where $K_c = q(TM)/q(CM)$ represents a coefficient at a given state p . The failure surface can be characterized by the compressive meridian ($\theta = 0^\circ$, $\sigma_1 = \sigma_2 < \sigma_3$) and the tensile meridian ($\theta = 60^\circ$, $\sigma_1 = \sigma_2 > \sigma_3$), where tensile stresses are considered positive [184, 185]. The numerical results indicate that a value of $K_c = 0.532$ provides the optimal fit for the strength envelope of the RVE of interlocking bricks.



(a) Deviatoric plane



(b) Meridian plane

Figure 7-12. Failure surface in the deviatoric and meridian planes

7.3.2.3 Strain rate effect

To accurately simulate the response of the RVE for interlocking brick under blast loading, strain rate effect is taken into consideration. From the numerical modelling results in Figure 7-4-Figure 7-10, the DIF of unconfined uniaxial compressive strength, uniaxial tensile strength in the strain rate range between 0.0001s^{-1} and 40 s^{-1} are derived. Figure 7-13a) shows the DIF of compressive strength of the RVE for interlocking bricks, where σ_{xc} , σ_{yc} and σ_{zc} are the compressive strengths in the x-axis, y-axis and z-axis, respectively. It can be found that the DIF of compressive strength in the z-axis is the largest, while that in the x-axis is the smallest. The DIF regression equations are derived as follows:

DIF of σ_{xc} :

$$DIF = 0.00502\log_{10}(\dot{\epsilon}) + 1.02, \dot{\epsilon} \leq 1 \quad (7-10)$$

$$DIF = -0.5997\log_{10}(\dot{\epsilon}) + 0.84663(\log_{10}(\dot{\epsilon}))^2 + 1.02495, \dot{\epsilon} > 1$$

DIF of σ_{yc} :

$$DIF = 0.03758 \log_{10}(\dot{\epsilon}) + 1.15, \dot{\epsilon} \leq 1$$

(7-11)

$$DIF = -0.788 \log_{10}(\dot{\epsilon}) + 0.9867 (\log_{10}(\dot{\epsilon}))^2 + 1.1528, \dot{\epsilon} > 1$$

DIF of σ_{zc} :

$$DIF = 0.0373 \log_{10}(\dot{\epsilon}) + 1.149, \dot{\epsilon} \leq 1$$

(7-12)

$$DIF = -0.4945 \log_{10}(\dot{\epsilon}) + 0.90472 (\log_{10}(\dot{\epsilon}))^2 + 1.14465, \dot{\epsilon} > 1$$

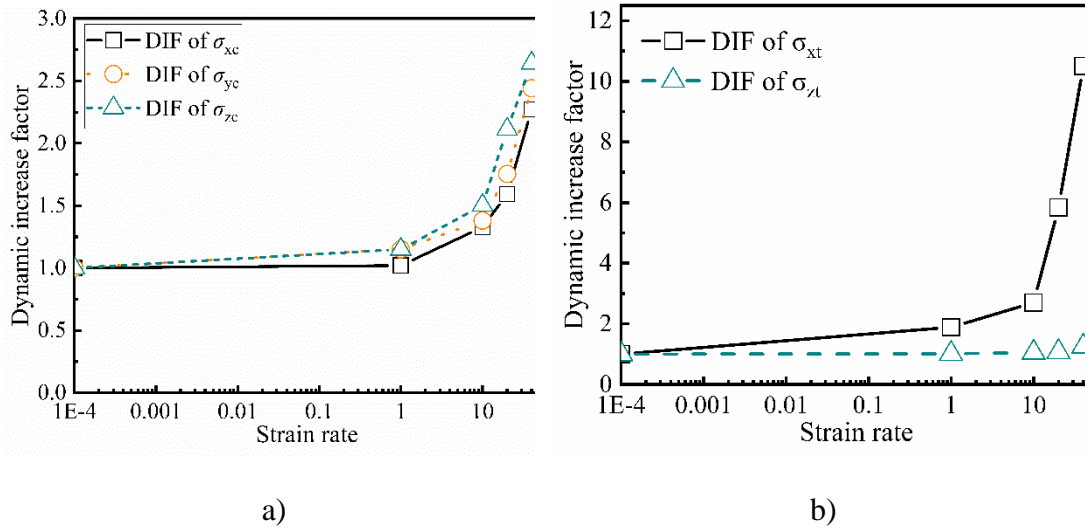


Figure 7-13. DIF of a) uniaxial compressive strength; and b) uniaxial tensile strength

Figure 7-13 b) gives the DIF of the uniaxial tensile strength of RVE. σ_{xt} and σ_{zt} are the tensile strengths in the x-axis and z-axis, respectively. The DIF regression equations are obtained as follows:

DIF of σ_{xt} :

$$DIF = 0.2225 \log_{10}(\dot{\epsilon}) + 1.89, \dot{\epsilon} \leq 1$$

$$DIF = -6.84945 \log_{10}(\dot{\epsilon}) + 7.6252 (\log_{10}(\dot{\epsilon}))^2 + 1.89274, \dot{\epsilon} > 1 \quad (7-13)$$

> 1

DIF of σ_{zt} :

$$DIF = 0.0025 \log_{10}(\dot{\varepsilon}) + 1.01, \dot{\varepsilon} \leq 1$$

$$DIF = -0.1983 \log_{10}(\dot{\varepsilon}) + 0.2101 (\log_{10}(\dot{\varepsilon}))^2 + 1.01226, \dot{\varepsilon} > 1 \quad (7-14)$$

7.3.2.4 Hardening and softening

To properly describe the constitutive behavior, the effects of hardening and softening are taken into consideration when deriving the equivalent material properties of the RVE. To illustrate this, Figure 7-14 displays the stress-strain curves of the RVE under uniaxial stress states, which includes an elastic stage, a hardening stage and a softening stage. A multilinear model is utilized in the homogenized continuum to represent the elastic, hardening, and softening behaviors as defined in Eq. (7-15).

$$\sigma_c = \begin{cases} E_0 \varepsilon_c & \varepsilon_c \leq \varepsilon_{c0} \\ (\sigma_{cu} - \sigma_{c0}) \left(\frac{\varepsilon_c - \varepsilon_{c0}}{\varepsilon_{cu} - \varepsilon_{c0}} \right)^{\eta_1} + \sigma_{c0} & \varepsilon_{c0} \leq \varepsilon_c \leq \varepsilon_{cu} \\ \sigma_{cu} \left[1 - \left(\frac{\varepsilon_c - \varepsilon_{cu}}{\beta \varepsilon_{cu}} \right)^{\eta_2} \right] & \varepsilon_c \geq \varepsilon_{cu} \end{cases} \quad (7-15)$$

$$\sigma_t = \begin{cases} E_0 \varepsilon_t & \varepsilon_t \leq \varepsilon_{t0} \\ (\sigma_{tu} - \sigma_{t0}) \left(\frac{\varepsilon_t - \varepsilon_{t0}}{\varepsilon_{tu} - \varepsilon_{t0}} \right)^{\eta_1} + \sigma_{t0} & \varepsilon_{t0} \leq \varepsilon_t \leq \varepsilon_{tu} \\ \sigma_{tu} \left[1 - \left(\frac{\varepsilon_t - \varepsilon_{tu}}{\beta \varepsilon_{tu}} \right)^{\eta_2} \right] & \varepsilon_t \geq \varepsilon_{tu} \end{cases}$$

Since the RVE shows strong strain rate sensitivity, the damage model also takes account of strain rate effect. Taking the strain rate of 0.0001 s^{-1} as an example, the initial elastic modulus is $E_0 = 9.19 \text{ GPa}$, and the maximum elastic strain under compression is $\varepsilon_{c0} = 0.000567$. The maximum compressive strength and the corresponding strain are $\sigma_{cu} = 7.93 \text{ MPa}$ and $\varepsilon_{cu} = 0.00173$, respectively. The curve is defined by exponents η_1 and η_2 to express the softening or hardening behaviors. β is a material parameter. By using the least squares method to fit the stress-strain relations,

the parameters are calculated as $\eta_1 = 0.45682$, $\eta_2 = 1.21311$, and $\beta = 1.68653$. When the strain rate is 1 s^{-1} , $\varepsilon_{t0} = 0.00000018$ denotes the maximum elastic strain under tension; $\sigma_{tu} = 0.373 \text{ MPa}$ and $\varepsilon_{tu} = 0.00025$ represent the maximum tensile strength and the corresponding strain. Using the least squares method, the parameters are calculated as $\eta_1 = 0.36$ and $\eta_2 = 0.867$ and $\beta = 10.35$ through curve fitting the stress-strain relations. As a result, σ_c and σ_t can be determined as given below:

Strain rate= 1 s^{-1}

$$\sigma_c = \begin{cases} E_0 \varepsilon_c & \varepsilon_c \leq 0.00084 \\ (\sigma_{cu} - \sigma_{c0}) \left(\frac{\varepsilon_c - \varepsilon_{c0}}{\varepsilon_{cu} - \varepsilon_{c0}} \right)^1 + \sigma_{c0} & 0.00084 \leq \varepsilon_c \leq 0.00152 \\ \sigma_{cu} \left[1 - \left(\frac{\varepsilon_c - \varepsilon_{cu}}{1.41438 \varepsilon_{cu}} \right)^{0.94767} \right] & \varepsilon_c \geq 0.00152 \end{cases}$$

Strain rate= 10 s^{-1}

$$\sigma_c = \begin{cases} E_0 \varepsilon_c & \varepsilon_c \leq 0.001009 \\ (\sigma_{cu} - \sigma_{c0}) \left(\frac{\varepsilon_c - \varepsilon_{c0}}{\varepsilon_{cu} - \varepsilon_{c0}} \right)^{0.65682} + \sigma_{c0} & 0.001009 \leq \varepsilon_c \leq 0.00164 \\ \sigma_{cu} \left[1 - \left(\frac{\varepsilon_c - \varepsilon_{cu}}{2.47893 \varepsilon_{cu}} \right)^{1.06038} \right] & \varepsilon_c \geq 0.00164 \end{cases}$$

(7-16)

Strain rate= 20 s^{-1}

$$\sigma_c = \begin{cases} E_0 \varepsilon_c & \varepsilon_c \leq 0.00136 \\ (\sigma_{cu} - \sigma_{c0}) \left(\frac{\varepsilon_c - \varepsilon_{c0}}{\varepsilon_{cu} - \varepsilon_{c0}} \right)^{0.61308} + \sigma_{c0} & 0.00136 \leq \varepsilon_c \leq 0.002128 \\ \sigma_{cu} \left[1 - \left(\frac{\varepsilon_c - \varepsilon_{cu}}{2.94649 \varepsilon_{cu}} \right)^{0.90201} \right] & \varepsilon_c \geq 0.002128 \end{cases}$$

Strain rate= 40 s^{-1}

$$\sigma_c = \begin{cases} E_0 \varepsilon_c & \varepsilon_c \leq 0.0012 \\ (\sigma_{cu} - \sigma_{c0}) \left(\frac{\varepsilon_c - \varepsilon_{c0}}{\varepsilon_{cu} - \varepsilon_{c0}} \right)^{0.73228} + \sigma_{c0} & 0.0012 \leq \varepsilon_c \leq 0.002936 \\ \sigma_{cu} \left[1 - \left(\frac{\varepsilon_c - \varepsilon_{cu}}{1.96051 \varepsilon_{cu}} \right)^{1.03627} \right] & \varepsilon_c \geq 0.002936 \end{cases}$$

Strain rate=1 s⁻¹

$$\sigma_t = \begin{cases} \frac{E_0 \varepsilon_t}{(\sigma_{tu} - \sigma_{t0}) \left(\frac{\varepsilon_t - \varepsilon_{t0}}{\varepsilon_{tu} - \varepsilon_{t0}} \right)^{0.36}} + \sigma_{t0} & \varepsilon_t \leq 0.00000018 \\ \sigma_{tu} \left[1 - \left(\frac{\varepsilon_t - \varepsilon_{tu}}{10.35 \varepsilon_{tu}} \right)^{0.867} \right] & 0.00000018 \leq \varepsilon_t \leq 0.00025 \\ & \varepsilon_t \geq 0.00025 \end{cases}$$

Strain rate=10 s⁻¹

$$\sigma_t = \begin{cases} \frac{E_0 \varepsilon_t}{(\sigma_{tu} - \sigma_{t0}) \left(\frac{\varepsilon_t - \varepsilon_{t0}}{\varepsilon_{tu} - \varepsilon_{t0}} \right)^{0.312}} + \sigma_{t0} & \varepsilon_t \leq 0.000000355 \\ \sigma_{tu} \left[1 - \left(\frac{\varepsilon_t - \varepsilon_{tu}}{1.2994 \varepsilon_{tu}} \right)^2 \right] & 0.000000355 \leq \varepsilon_t \\ & \leq 0.0002957 \\ & \varepsilon_t \geq 0.0002957 \end{cases}$$

Strain rate=20 s⁻¹

$$\sigma_t = \begin{cases} \frac{E_0 \varepsilon_t}{(\sigma_{tu} - \sigma_{t0}) \left(\frac{\varepsilon_t - \varepsilon_{t0}}{\varepsilon_{tu} - \varepsilon_{t0}} \right)^{0.46}} + \sigma_{t0} & \varepsilon_t \leq 0.0000000677 \\ \sigma_{tu} \left[1 - \left(\frac{\varepsilon_t - \varepsilon_{tu}}{2.636 \varepsilon_{tu}} \right)^{1.047} \right] & 0.0000000677 \leq \varepsilon_t \\ & \leq 0.000052 \\ & \varepsilon_t \geq 0.000052 \end{cases}$$

Strain rate=40 s⁻¹

$$\sigma_t = \begin{cases} \frac{E_0 \varepsilon_t}{(\sigma_{tu} - \sigma_{t0}) \left(\frac{\varepsilon_t - \varepsilon_{t0}}{\varepsilon_{tu} - \varepsilon_{t0}} \right)^{0.442}} + \sigma_{t0} & \varepsilon_t \leq 0.0000000674 \\ \sigma_{tu} \left[1 - \left(\frac{\varepsilon_t - \varepsilon_{tu}}{3.632 \varepsilon_{tu}} \right)^{0.867} \right] & 0.0000000674 \leq \varepsilon_t \\ & \leq 0.000032 \\ & \varepsilon_t \geq 0.000032 \end{cases}$$

(7-17)

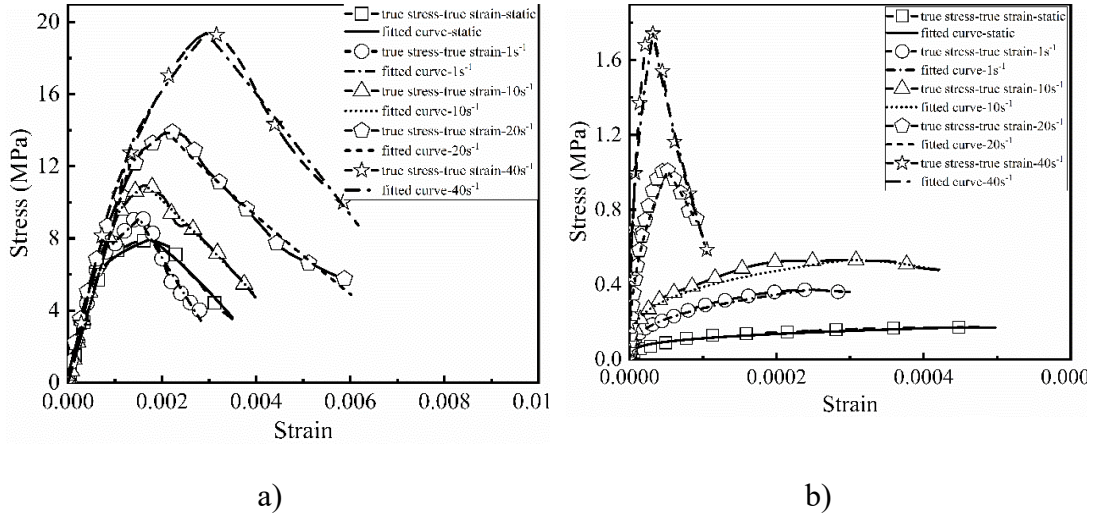


Figure 7-14. Stress-strain relations of the RVE under uniaxial stress states a) compression; b) tension

7.3.2.5 Damage model

A damage model is considered in this study for the RVE of interlocking bricks. The damage variables are based on the theory of continuum damage mechanics [191-193]. The damage scalar d is used to measure the degree of damage, and it ranges from 0 to 1. The expression for d can be written as:

$$d = \frac{W_0 - W_\varepsilon}{W_0} \quad (7-18)$$

where W_0 represents the strain energy of undamaged elements; W_ε represents the strain energy of damaged elements, which can be calculated by

$$W_0 = \frac{E_0 \varepsilon^2}{2} \quad (7-19)$$

and

$$W_\varepsilon = \int \sigma d\varepsilon = \int f(\varepsilon) d\varepsilon \quad (7-20)$$

where E_0 represents the elastic modulus of undamaged material. To calculate the damaged strain energy under compression W_ε^c and the damaged strain energy under tension W_ε^t , the Simpson integral approach is utilized to obtain W_ε . By substituting Eqs. (7-16) and (7-17) into Eq. (7-20), respectively, the variables for W_ε^c and W_ε^t can be calculated.

By substituting the variables and Eq. (7-19) into Eq. (7-18), the damage scalars under compression (d_c) and tension (d_t) can be calculated using Eqs. (7-21) and (7-22). The elastic region remains undamaged, and only the inelastic region experiences damage. For instance, at a strain rate of 1 s^{-1} , the damage parameter under compression corresponding to the peak compressive stress (σ_{cu}) is 0.126. This means that if the compressive damage exceeds 0.126, the strength surface will begin to shrink. Using the damage model, the damage distribution in the RVE for interlocking bricks under different strain rates can be described.

Strain rate = 0.00001 s^{-1}

$$d_c \begin{cases} 0 & \varepsilon_c \leq \varepsilon_{c0} \\ 1 - \frac{16.229\varepsilon_c - 213.984(0.00173 - \varepsilon_c)^{28.467} - 0.0068}{10000\varepsilon_c^2} & \varepsilon_{c0} < \varepsilon_c \leq \varepsilon_{cu} \\ 1 - \frac{-253.872\varepsilon_c + 242.558(\varepsilon_c - 0.00173)^{0.9844} + 0.4593}{10000\varepsilon_c^2} & \varepsilon_c > \varepsilon_{cu} \end{cases}$$

Strain rate = 1 s^{-1}

$$d_c \begin{cases} 0 & \varepsilon_c \leq \varepsilon_{c0} \\ 1 - \frac{-369.308\varepsilon_c - 380.604(0.00152 - \varepsilon_c)^{0.9973} + 0.5811}{10000\varepsilon_c^2} & \varepsilon_{c0} < \varepsilon_c \leq \varepsilon_{cu} \\ 1 - \frac{14.175\varepsilon_c + 13.4365(\varepsilon_c - 0.00152)^{12.7675} - 0.0000806}{10000\varepsilon_c^2} & \varepsilon_c > \varepsilon_{cu} \end{cases} \quad (7-21)$$

Strain rate = 10 s^{-1}

$$\varepsilon_c \leq \varepsilon_{c0}$$

$$d_c \begin{cases} 1 - \frac{0}{23.4676\varepsilon_c - 160.7248(0.00164 - \varepsilon_c)^{25.0393} - 0.0133} & \varepsilon_{c0} < \varepsilon_c \leq \varepsilon_{cu} \\ 1 - \frac{10000\varepsilon_c^2}{-417.74\varepsilon_c + 412.2514(\varepsilon_c - 0.00164)^{0.9907} + 0.7091} & \varepsilon_c > \varepsilon_{cu} \end{cases}$$

Strain rate=20 s⁻¹

$$d_c \begin{cases} 1 - \frac{0}{31.075\varepsilon_c - 150.286(0.00213 - \varepsilon_c)^{17.867} - 0.0234} & \varepsilon_c \leq \varepsilon_{c0} \\ 1 - \frac{10000\varepsilon_c^2}{-435.106\varepsilon_c + 420.972(\varepsilon_c - 0.00213)^{0.9855} + 0.9664} & \varepsilon_{c0} < \varepsilon_c \leq \varepsilon_{cu} \\ & \varepsilon_c > \varepsilon_{cu} \end{cases}$$

Strain rate=40 s⁻¹

$$d_c \begin{cases} 1 - \frac{0}{-143.886\varepsilon_c - 181.82(0.00294 - \varepsilon_c)^{0.9968} + 0.6293} & \varepsilon_c \leq \varepsilon_{c0} \\ 1 - \frac{10000\varepsilon_c^2}{-278.89\varepsilon_c + 259.772(\varepsilon_c - 0.00294)^{0.9683} + 0.89346} & \varepsilon_{c0} < \varepsilon_c \leq \varepsilon_{cu} \\ & \varepsilon_c > \varepsilon_{cu} \end{cases}$$

and

Strain rate = 0.00001s⁻¹

$$d_t = \begin{cases} \frac{0}{11323.57\varepsilon_t^2 - 0.1171\varepsilon_t + 3.2482 * 10^{-7}} & \varepsilon_t \leq \varepsilon_{t0} \\ \frac{12223.706\varepsilon_t^2}{107.0596\varepsilon_t + 0.8846} & \varepsilon_{t0} < \varepsilon_t \leq \varepsilon_{tu} \\ & \varepsilon_t > \varepsilon_{tu} \end{cases} \quad (7-22)$$

Strain rate=1 s⁻¹

$$d_t = \begin{cases} \frac{0}{3947.663\varepsilon_t^2 - 0.1557\varepsilon_t + 1.2486 * 10^{-6}} & \varepsilon_t \leq \varepsilon_{t0} \\ \frac{4539.41\varepsilon_t^2}{652.178\varepsilon_t + 0.586} & \varepsilon_{t0} < \varepsilon_t \leq \varepsilon_{tu} \\ & \varepsilon_t > \varepsilon_{tu} \end{cases}$$

Strain rate=10 s⁻¹

$$d_t = \begin{cases} 0 & \varepsilon_t \leq \varepsilon_{t0} \\ \frac{4010.244\varepsilon_t^2 - 0.2959\varepsilon_t + 4.1306 * 10^{-6}}{4569.605\varepsilon_t^2} & \varepsilon_{t0} < \varepsilon_t \leq \varepsilon_{tu} \\ 667.277\varepsilon_t + 0.484 & \varepsilon_t > \varepsilon_{tu} \end{cases}$$

Strain rate=20 s⁻¹

$$d_t = \begin{cases} 0 & \varepsilon_t \leq \varepsilon_{t0} \\ \frac{36683.02\varepsilon_t^2 - 1.144\varepsilon_t + 8.3699 * 10^{-6}}{47319.74\varepsilon_t^2} & \varepsilon_{t0} < \varepsilon_t \leq \varepsilon_{tu} \\ 6104.414\varepsilon_t + 0.0695 & \varepsilon_t > \varepsilon_{tu} \end{cases}$$

Strain rate=40 s⁻¹

$$d_t = \begin{cases} 0 & \varepsilon_t \leq \varepsilon_{t0} \\ \frac{36683.02\varepsilon_t^2 - 1.144\varepsilon_t + 8.3699 * 10^{-6}}{47319.74\varepsilon_t^2} & \varepsilon_{t0} < \varepsilon_t \leq \varepsilon_{tu} \\ 6104.414\varepsilon_t + 0.0695 & \varepsilon_t > \varepsilon_{tu} \end{cases}$$

where ε_c and ε_t are the compressive and tensile strains, respectively.

7.4 Model Validation

To examine the suitability and accuracy of the RVE with the equivalent material model, the RVE is used to simulate the responses of mortarless interlocking brick walls under dynamic loading. The numerical results with the homogenised material model are compared with those of the detailed model. Full-scale dry-stacking interlocking brick walls of 3000mm height, 2000mm width and 100mm thickness are generated following [195]. The interlocking wall is made from the interlocking bricks and the size of interlocking brick has a width of 200 mm, height of 180 mm and thickness of 100 mm. Numerical models of the interlocking brick walls are firstly generated using the RVE with the above derived material model. For comparison, detailed numerical

models of the two interlocking brick walls are also generated using detailed micro modelling approach. The material models are the same as those detailed above in Section 3 to maintain the same material properties for a fair comparison.

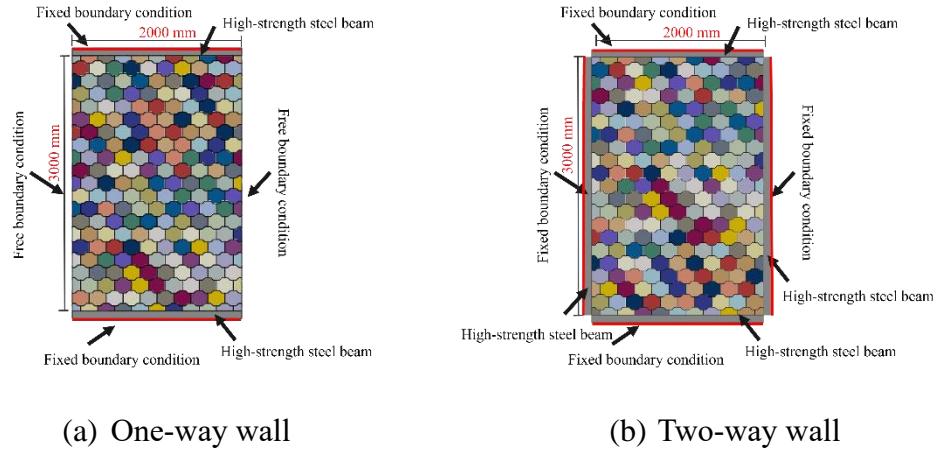


Figure 7-15. An overview of the interlocking brick wall models

7.4.1 TNT explosion

Numerical simulation is firstly performed to examine the response of interlocking brick walls under TNT explosion. As illustrated in Figure 7-16, the brick wall is constrained on its four boundaries, making it a two-way wall. 40kg TNT with a stand-off distance of 5m (case 1) and 10kg TNT with a stand-off distance of 1m (case 2) are considered, respectively. The TNT is positioned at a height of 1.5m above the ground. The Conwep function in ABAQUS is utilized to estimate the blast loads acting on the frontal surface of the wall.

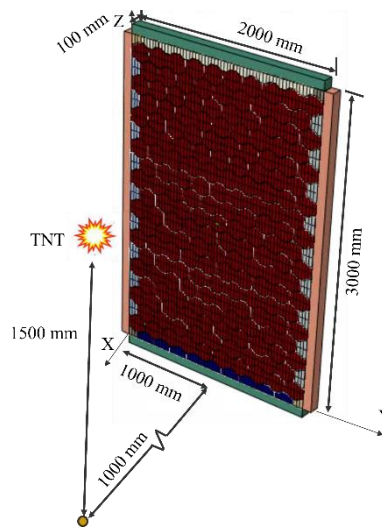
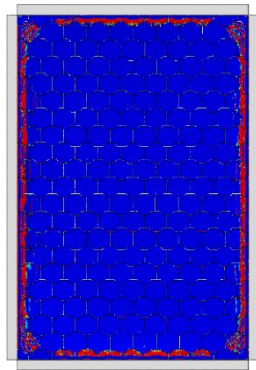


Figure 7-16. Illustration of interlocking brick wall under TNT explosion (Case 2)

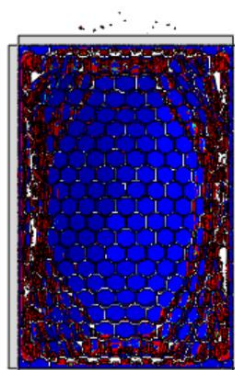
7.4.1.1 Case 1 (40kg TNT at 5m stand-off distance)

Figure 7-17 shows the failure mode of the interlocking brick wall with the RVE and the detailed model at their damage initiation and at the time when damage has fully developed. As shown in Figure 7-17a, under the action of blast loading, the boundary of the detailed model exhibits noticeable shear failure, which progresses from the boundary into the wall(Figure 7-17b). Simultaneously, a typical flexural damage pattern of the two-way slab is observed on the backside of the wall with flexural cracks (Figure 7-17c). As seen in Figure 7-17d-e, the homogenised model successfully predicts the shear failure around the boundary of the mortarless interlocking brick wall under blast loading from 40 kg TNT detonated at a 5 m stand-off distance. Also, on the backside of the homogenised wall (Figure 7-17f), a diffused flexural damage pattern similar to that of the detailed model is observed. Figure 7-17g displays the deflection-time comparison of the wall centre in both models. It can be seen that the predicted deflection by the homogenized model is only slightly lower than that in the detailed model. At 0.2 s, the deflection of the centre point in the detailed model is 1089.7 mm, while that in the homogenized model is 1042.8 mm, indicating only 4.3 % lower than the former. It should be noted that Figure 7-17g presents a comparison of displacements of the two wall models within the first 0.2 seconds, and since the

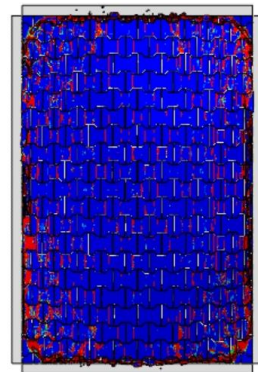
rebound of the wall occurs after this period, a decrease in wall displacement is not observed in Figure 7-17g. Using a workstation of 64-CPU 2.8 GHz Intel Xeon Platinum 8362 and 256 GB DDR4 RAM for the above simulation, the homogenised model only takes 307 sec to complete the simulation, which is only 1% of simulation time by using the detailed model (32347 sec). It demonstrates that the developed homogenized model has great advantages of computation efficiency comparing to the conventional detailed modelling method.



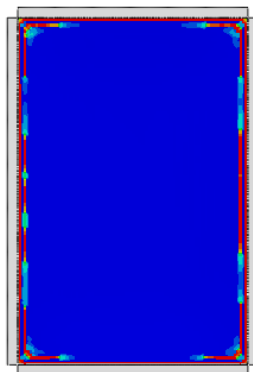
(a) Initial damage on front side (detailed model)



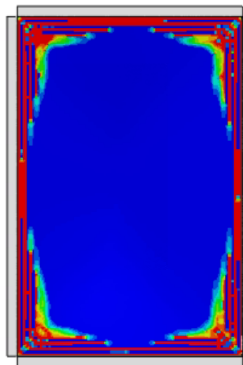
(b) Failure mode on front side (detailed model)



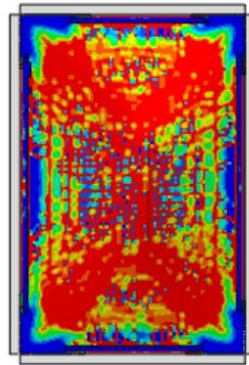
(c) Failure mode on rear side (detailed model)



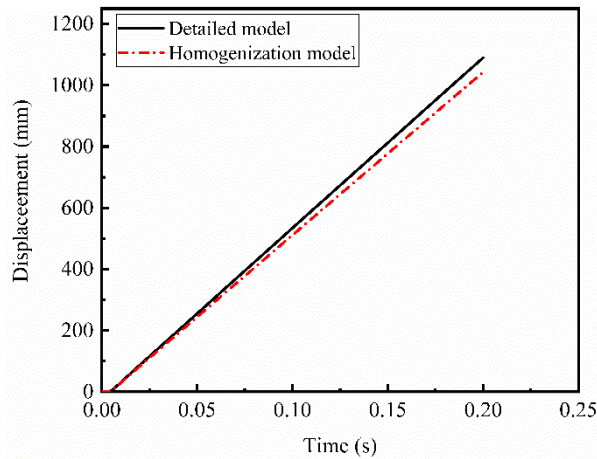
(d) Initial damage on front side (RVE)



(e) Failure mode on front side (RVE)



(f) Failure mode on rear side (RVE)



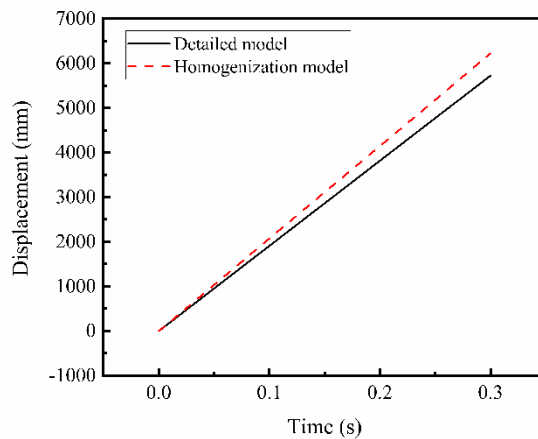
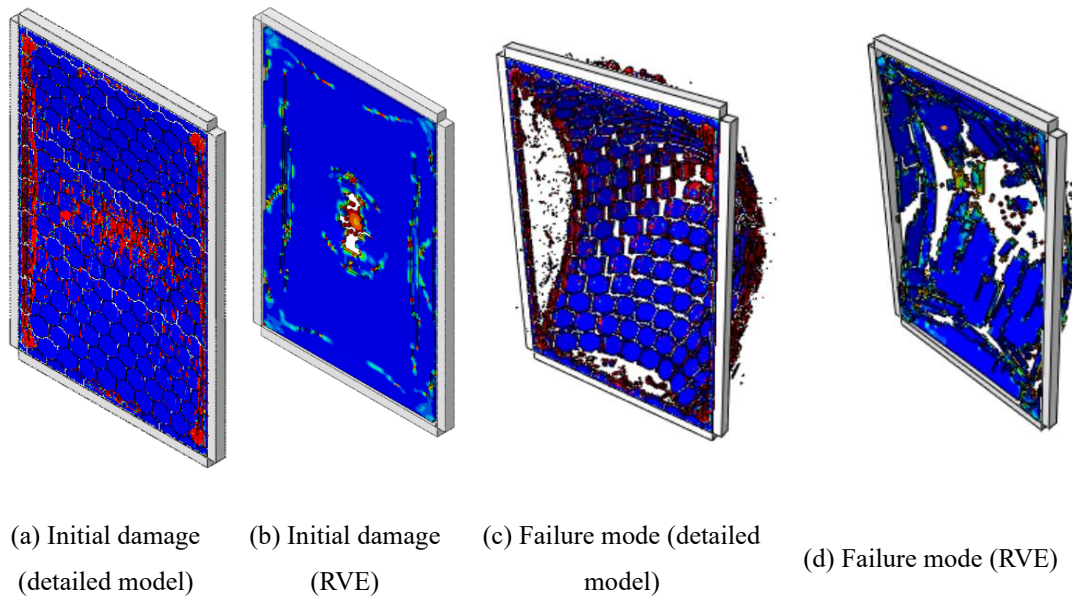
(g) Comparison of displacement response time histories

Figure 7-17. Comparison of damage contours under 40kg TNT at 5m stand-off distance

7.4.1.2 Case 2 (10kg TNT at 1m stand-off distance)

The comparison is further carried out to model the interlocking brick walls subjected to the more intensive blast loading, where stress waves induced by the explosion can lead to extreme material compaction resulting in compressive failure of bricks [196]. As shown in Figure 7-18a, under the action of the reflected overpressure from 10 kg TNT detonated at a 1 m stand-off distance, the wall in the detailed model exhibits shear failure at the boundary and local compressive damage at the centre position as a result of the intensive blast overpressure. Both of these failure modes are predicted in the homogenized model (Figure 7-18b). With the development of damage in the detailed model, the wall detaches from the boundary, and the entire wall surface exhibits noticeable bending deformations; the individual bricks separate due to the absence of mortar bonding, becoming high-speed debris (Figure 7-18c). A similar damage pattern is predicted by the homogenized model (Figure 7-18d), where the entire wall surface breaks free from the boundary constraint due to severe shear failure at the boundary, and the internal elements of the wall separate and scatter due to the bending-induced tensile stresses exceeding the low tensile strength of the homogenized material, also resulting in flying high-speed debris. Figure 7-18e compares the deflection-time histories of the wall centres in both models. It can be seen that under the more intense

blast loading, the central deflection in the homogenized model is slightly larger than that in the detailed model. However, the difference is small. At 0.3 s, the central deflection of homogenized model is 6224.15 mm, while that of detailed model is 5722.2 mm, resulting in a difference of less than 10% (8.77%). Because of the complex contact algorithm in the detailed model, it takes 28301sec to complete the above simulation, while the homogenization model only required 332.9 sec (-98.82% less time) for the simulation with similar accuracy.



(e) Comparison of displacement response time histories

Figure 7-18. Comparison of damage contours under 10kg TNT at 1m stand-off distance

7.4.2 Gas explosion loading

To further examine the performance of the developed homogenized model, it is used to simulate the response of interlocking brick walls subjected to gas explosion. Two cases are considered here, where the 3000mm height by 2000mm width by 100mm thickness wall is restrained only at its top and bottom boundaries as a one-way wall shown in Figure 7-15a, and in the 2nd case, the four edges of the wall are all restrained to achieve a two-way wall shown in Figure 7-15b. The blast overpressure from gas explosion is applied to the frontal surface of the wall. Previous field testing data on autoclaved aerated concrete masonry wall is employed in this study considering the similarity of structural form [195]. Figure 7-19 shows the recorded blast overpressure time histories of 3 tests listed in [195], among which the data of Test 9 is chosen for the numerical simulation in this study. The information of Test 9 is listed in Table 7-1. ΔP_i stands for the i th peak in the pressure-time histories. It is noted that the detailed information of ΔP_2 and ΔP_3 is not provided in [195].

Table 7-1. Information of selected tests [195]

Test no.	Wall no.	Gas concentration	Boundary condition	Vent cover	ΔP_1		ΔP_4	
					Peak (kPa)	Rise duration (ms)	Peak (kPa)	Rise duration (ms)
9	W3	9.50%	Two-way	1.5 μ m film	1.23	130	85.88	80

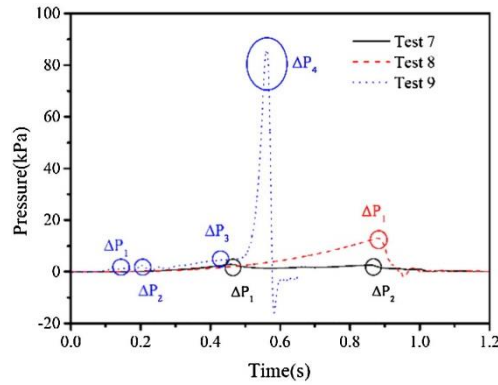
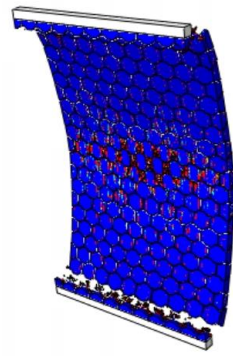


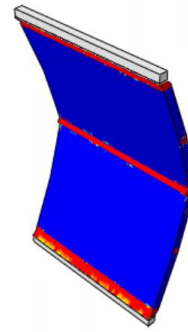
Figure 7-19. Recorded pressure-time histories [195].

7.4.2.1 One-way wall

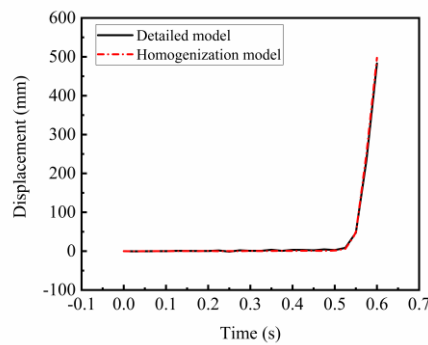
Figure 7-20a) and b) show the damage patterns of the one-way interlocking brick walls from the detailed model and the homogenized model. It can be found that when subjected to blast overpressure, the detailed model simulates a typical flexural bending failure with bricks fail at both mid-span and along the top and bottom boundaries. This is expected for one-way wall where the maximum bending moments are developed at both mid-span and near the boundaries. The homogenized model predicts a similar failure pattern with observed flexural bending failure at mid-span and near boundaries. Figure 7-20c) compares the simulated wall central displacement time histories from the detailed model and the homogenized model, which shows almost identical central displacement time histories. For example, the predicted displacement from the homogenized model at 0.6 s is 497.51 mm, which is only marginally higher (+2.9%) than that by the detailed model of 483.04 mm. The numerical modelling using the homogenised method takes only 1243.1 sec comparing to 50370 sec of the detailed model for the simulation when using a workstation of 64 CPUs 2.8 GHz Intel Xeon Platinum 8362 and 256 GB DDR4 RAM. It proves that the developed homogenized model has great efficiency and good accuracy for simulating the behavior of interlocking brick wall under gas explosion.



a) Detailed model



b) Homogenised model



c) Comparison of displacement response time histories

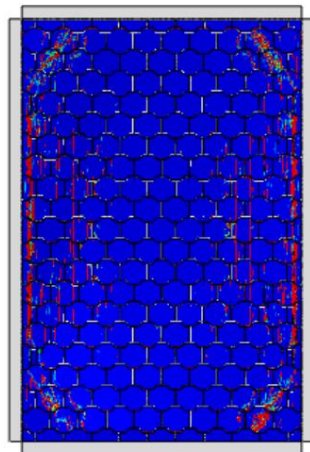
Figure 7-20. Comparison of damage contours and central displacement time histories for one-way wall under gas explosion

7.4.2.2 Two-way wall

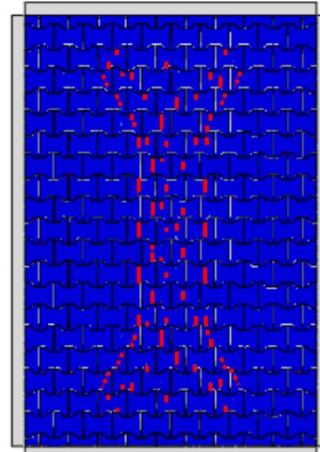
Figure 7-21 compares the responses of a two-way interlocking brick wall when subjected to gas explosion by using the homogenized model and the detailed model. As can be seen, in the detailed model, on the frontal surface the interlocking brick wall experiences severe damage around its four boundaries, while on the rear surface flexural damages are observed on the interlocking brick wall which follows the pattern of yield-line theory along the maximum bending moment. Figure 7-21 c) and d) show the simulated wall damage pattern by the homogenized model. It can be seen that the homogenized model predicts a wall damage pattern very similar to that of the detailed

model. Figure 7-21e) compares the wall central displacement time histories using the two models, where very similar displacement response time histories from the two models are observed. The detailed model predicts a maximum displacement of 253.7 mm, while the homogenized model yields a maximum central displacement of 220.7 mm, i.e., a -13% underprediction. This is primarily because the dry-stacking interlocking bricks have no tensile strength when the wall deflects, leading to bricks disintegration under large deformation. The homogenized model takes 1519.7 sec for the performed numerical simulation, corresponding to a saving of over 97% in computation time comparing to the detailed model (51917 sec).

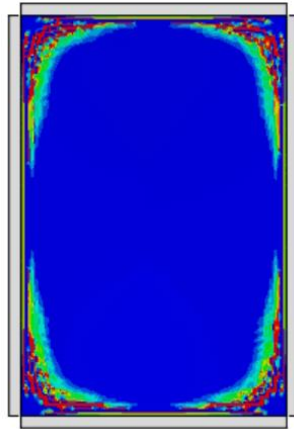
Overall, the above numerical simulations and comparisons demonstrate that the developed homogenized model for interlocking brick wall can provide a reasonably accurate prediction of the structural response of dry-stacking interlocking masonry walls subjected to both TNT explosion and gas explosion loadings. In the meanwhile, comparing to the conventional detailed micro model, the homogenized modelling approach shows superior computational efficiency.



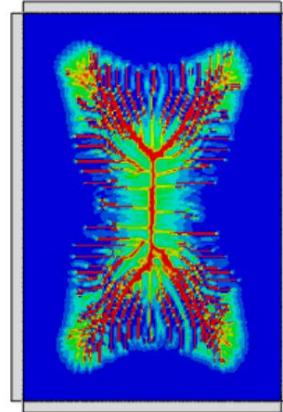
a) Front side (detailed model)



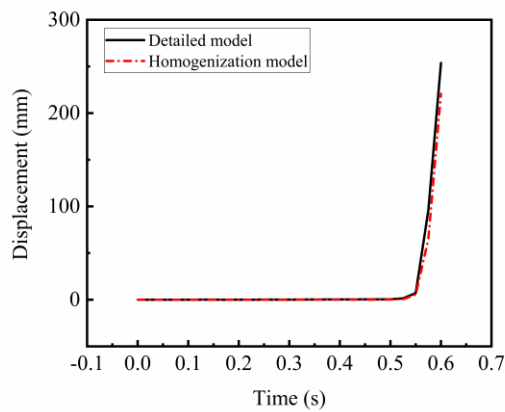
b) Rear side (detailed model)



c) Front side (RVE)



d) Rear side (RVE)



e) Comparison of displacement response time histories

Figure 7-21. Comparison of damage contours and central displacement time histories for two-way wall under gas explosion

7.5 Summary

This chapter develops a homogenization modelling method for dry-stacking interlocking brick walls with consideration of strain rate effect for predicting the response of interlocking brick walls under blast loading. A RVE is selected based on the periodic pattern of interlocking brick walls. The equivalent material properties are determined through numerically modelling of the RVE under different stress states. The equivalent elastic properties, strength model, strain rate effect and damage model

are all derived with numerical modelling results. The accuracy and suitability of the developed homogenization method for simulating the response of dry-stacking interlocking brick walls under TNT explosion and gas explosion are assessed by comparing the modelling results obtained from the detailed numerical models. Based on the numerical results, the following conclusive remarks can be drawn:

1. The equivalent constitutive model parameters of interlocking brick walls are determined by modelling the RVE under different stress states and strain rates.
2. The RVE of interlocking bricks show insignificant anisotropic material properties.
3. Model validation shows the developed homogenized model could yield a reasonable prediction accuracy when the interlocking brick walls are subjected to TNT blasting and gas explosion. In the meanwhile, comparing with the traditional detailed model, the developed homogenized model could save over 90% of the computational time, thus showing superior efficiency.

CHAPTER 8 CONCLUSIONS AND RECOMMENDATIONS

8.1 Main findings

This thesis investigates the mechanical properties of an innovative type of interlocking brick and the constructed masonry wall and develops a homogenised constitutive approach for analysis of dry-stacking interlocking brick structures. The compressive and shear properties of interlocking brick prisms and walls are investigated through analytical analysis, laboratory testing, and numerical modeling. The research explores various influence factors, including the number of bricks, joint roughness amplitude, brick material strength, friction coefficient, and axial pre-compression on the compressive and shear capacities. Modified formulas and semi-empirical prediction methods are derived for estimating the compressive strength, axial stiffness, and shear strength of interlocking brick prisms. A stochastic analysis is conducted to examine the effects of spatially varying brick imperfections on the compressive properties of dry-stacked interlocking brick walls. It is found that brick imperfections strongly influence crack patterns, crack initiation, crack development, and load paths in these walls. The quality of bricks and the coefficient of variation of brick imperfection sizes have significant impacts on wall performance. Using representative volume elements (RVEs) to determine equivalent material properties, homogenization modeling methods are developed for dry-stacked interlocking brick walls. The strain rate effect is also considered in the development of the homogenized RVE constitutive models for predicting the response of interlocking brick walls under blast loading. Detailed findings are summarized as follows:

1. To predict the compressive strength of unit interlocking brick, existing fracture mechanism based analytical solution could provide good estimation. However, because the strength of prism is strongly influenced by the number of blocks, the

analytical solution based on a unit interlocking block could not well predict the compressive strength of the prism. Laboratory compressive tests revealed strong seating effect of the dry-stacking interlocking brick prisms on their compression performance. It is found that the ultimate strength decreases with the increase in the number of blocks because of the increased number of interlocking joints. Detailed numerical models using different contact modelling methods are generated which could reasonably predict the behaviour of interlocking brick prisms. The imperfect contact model gives the closest prediction considering the initial stiffness, the ultimate compressive load-carrying capacity and damage modes. However, none of these methods could replicate the seating effect. Parametric study quantifies the influence of the number of bricks, joint roughness amplitudes and material compressive strength on the prism compressive capacity. A modified formula is derived to predict the compressive strength of interlocking brick prisms with consideration of the number of blocks, joint roughness amplitudes, and material strength. A semi-empirical prediction method is also derived to predict the axial stiffness of the interlocking brick prisms.

2. To quantify the shear strength of interlocking bricks, both laboratory test and numerical modeling are performed, which show the shear strength of the interlocking prism is dependent on the pre-compression level. Numerical simulations with three different contact modelling approaches demonstrate that modelling the brick surface roughness is important for the reliable prediction of interlocking brick shear behavior. The simplified rough contact model is found to be able to give a good prediction of prism initial stiffness, and shear capacities, whereas the model with perfect contact leads to large prediction error. Existing design and analysis method may not accurately predict the shear strength of the interlocking brick with large keys because of the different shear failure mechanism, negligence of interface roughness, and inappropriate friction coefficient. Parametric study evaluates the influences of the coefficient of friction, axial pre-

compression, interface roughness, and material compressive strength on the interlocking prism shear strength. A modified analysis and design formula with consideration of brick surface condition is proposed for prediction of the shear capacity of interlocking brick prism.

3. Intensive numerical simulation is performed on interlocking brick walls with randomly distributed joint imperfections. Typical crack patterns on imperfect brick units are presented, which demonstrate strong influence of imperfection on the crack patterns. It is also found that brick imperfections could strongly influence the crack initiation and development, as well as the load path of dry-stacked interlocking brick walls. With less numbers of imperfect bricks, the high-quality wall has the highest mean compressive strength. The mean compressive strength of a low-quality interlocking brick wall could be higher than that of high-medium and medium-low quality walls because the low-quality brick walls have more and wider-spread gaps between bricks. Under compressive loading, these gaps would close relatively uniformly leading to improved wall strength although the initial seating length is larger and the equivalent stiffness is smaller; whereas despite the less numbers of imperfect bricks, when subjected to compressive loading, medium-quality walls suffer non-uniform deformation and stress concentration at joint gaps resulting in more severe localized brick damage and failures and hence lower compressive strengths. The COV of brick imperfection size distribution marginally influences the mean compressive strengths of high-quality and high-medium quality walls. However, it is found to strongly influence the mean compressive strength of low-quality walls. Initial seating is obvious for medium-low and low-quality brick walls under compressive load because of gap closure between imperfect bricks, and the seating displacement is prominent in the walls with relatively low-quality bricks. The mean equivalent stiffness decreases as the quality of the interlocking wall decreases with more imperfections. As COV of imperfection distribution increases, the mean equivalent stiffnesses of high-quality,

high-medium quality and medium-low quality walls increase because the displacements at the peak compressive loads decrease significantly, while the peak compressive load only varies slightly. But for low-quality walls, the mean equivalent stiffness decreases as the COV of brick imperfection increases. The mean linear stiffnesses of high quality, high-medium and medium-low quality interlocking brick walls decrease significantly as the quality of brick decreases because the number of imperfections controls the contact areas. For low-quality walls, when the COV of imperfection distributions is relatively low, their linear stiffness is a little higher than that of medium-low-quality walls after excluding the seating in determining the linear stiffness owing to the widespread relative uniformly distributed imperfections.

4. Based on periodic pattern, a representative volumetric element is derived for dry-stacking interlocking brick structures. Numerical modeling is carried out to simulate the response of RVE under different stress states, which show insignificant anisotropic material properties of dry-stacking interlocking brick wall, therefore isotropic constitutive model is developed. Through modelling the RVE under different stress states, the equivalent constitutive model parameters of interlocking brick wall are derived. On the selected RVE for interlocking brick wall, insignificant size effect is demonstrated. Therefore, the RVE can be applied to model the response of interlocking brick structures. Model validation is performed through comparing the results from the homogenized model and detailed model of an interlocking brick wall under uniaxial compressive loadings in three directions and combined compression-shear loading. Reliable predictions of interlocking brick wall responses are obtained at less than 10% computer memory and 5% computational time as compared to the detailed modelling. The developed RVE model can be used to efficiently predict the responses of interlocking brick walls.
5. The homogenized approach with RVE is extended to consider strain rate effect.

The equivalent constitutive model parameters of interlocking brick walls are determined by modelling the RVE under different stress states and strain rates. The RVE of interlocking bricks show insignificant anisotropic material properties. Model validation shows the developed homogenized model could yield a reasonable prediction accuracy when the interlocking brick walls are subjected to TNT blasting and gas explosion. In the meanwhile, comparing with the traditional detailed model, the developed homogenized model could save over 90% of the computational time, thus showing superior efficiency.

8.2 Recommendations

Based on the studies, there are the following recommendations for further investigations:

1. Random imperfections on the contact surfaces between bricks in mortarless interlocking masonry structures have a significant impact on the overall performance of the structures. Based on the research conducted in this thesis on the influence of these random imperfections on the compressive performance of mortarless interlocking masonry, future studies could investigate the potential impact of these random imperfections on the shear performance of such structures.
2. The imperfections investigated in this thesis are geometric in nature. Due to variations in production materials and curing conditions, material properties of different bricks may also vary. Future research could consider introducing randomness in material properties and examine their influence on structural performance under various loading conditions.
3. When deriving the homogenised constitutive model in this thesis, perfect interlocking bricks are assumed. With the introduction of imperfections, adjustments to the homogenised constitutive model could be investigated.
4. This thesis focuses on the study of unreinforced mortarless interlocking masonry

structures. In engineering practise, reinforcement is often introduced to masonry structures to improve its load-bearing performance and ductility. Further study could be performed to incorporate reinforcement and validate the developed homogenized methods for interlocking bricks.

5. This study focuses on one type of interlocking brick provided by the industry partner. The employed methods in this thesis could be extended to other types of interlocking bricks. Optimization could be performed to improve the structural performance of interlocking bricks with consideration of unavoidable imperfections.

REFERENCES

- [1] Ngapeya GGC, Waldmann D, Scholzen F. Impact of the height imperfections of masonry blocks on the load bearing capacity of dry-stack masonry walls. *Construction and Building Materials*. 2018;165:898-913.
- [2] Bui T, Limam A, Sarhosis V, Hjiat M. Discrete element modelling of the in-plane and out-of-plane behaviour of dry-joint masonry wall constructions. *Eng Struct*. 2017;136:277-94.
- [3] Casapulla C, Mousavian E, Zarghani M. A digital tool to design structurally feasible semi-circular masonry arches composed of interlocking blocks. *Computers & Structures*. 2019;221:111-26.
- [4] Dyskin AV, Pasternak E, Estrin Y. Mortarless structures based on topological interlocking. *Frontiers of Structural and Civil Engineering*. 2012;6:188-97.
- [5] Liu H, Liu P, Lin K, Zhao S. Cyclic behavior of mortarless brick joints with different interlocking shapes. *Materials*. 2016;9:166.
- [6] Sturm T, Ramos LF, Lourenço PB. Characterization of dry-stack interlocking compressed earth blocks. *Materials and Structures*. 2015;48:3059-74.
- [7] Ali M. Use of coconut fibre reinforced concrete and coconut-fibre ropes for seismic-resistant construction. *Materiales de Construcción*. 2016;66:073.
- [8] Thanoon WA, Jaafar MS, Kadir MRA, Ali AAA, Trikha D, Najm AM. Development of an innovative interlocking load bearing hollow block system in Malaysia. *Construction and Building Materials*. 2004;18:445-54.
- [9] Bragança L, Pinheiro M. Portugal SB10: sustainable building affordable to all: low cost sustainable solutions. *Portugal SB10: sustainable building affordable to all: low cost sustainable solutions: Universidade do Minho*; 2010. p. 1-870.
- [10] Edwards J, Gayed M, Pyra M, Rodriguez T. Design and Construction of Interlocking Mortarless Block Masonry. 2nd MASONRY MINI SYMPOSIUM EDMONTON, ALBERTA2010. p. 4.
- [11] Gallegos HJIJoHS, Applications i. Mortarless masonry: the Mecano system. 1988;12:145-57.
- [12] Drysdale R, Gazzola EJB, Masonry B. STRENGTH AND DEFORMATION PROPERTIES OF A GROUTED, DRY- STACKED, INTERLOCKING, CONCRETE BLOCK SYSTEM. 1991;1:164-71.
- [13] Jaafar MS, Thanoon WA, Najm AM, Abdulkadir MR, Ali AAA. Strength correlation between individual block, prism and basic wall panel for load bearing interlocking mortarless hollow block masonry. *Construction and Building Materials*. 2006;20:492-8.

- [14] Drysdale RG, Eng P. Properties of AZAR dry-stack block-IV™ construction. Hamilton, Ontario: McMaster University; 2005.
- [15] Anand K, Ramamurthy KJTMSJ. Development and evaluation of hollow concrete interlocking block masonry system. 2005;23:11-9.
- [16] Al-Fakih A, Mohammed BS, Liew MSJCERJ. Behavior of the Dry Bed Joint in the Mortarless Interlocking Masonry System: an Overview. 2018;4.
- [17] Anand K, Ramamurthy K. Development and performance evaluation of interlocking-block masonry. Journal of Architectural Engineering. 2000;6:45-51.
- [18] Ramamurthy K, Kunhanandan Nambiar E. Accelerated masonry construction review and future prospects. Progress in Structural Engineering and Materials. 2004;6:1-9.
- [19] Wang G, Li Y, Zheng N, Ingham JM. Testing and modelling the in-plane seismic response of clay brick masonry walls with boundary columns made of precast concrete interlocking blocks. Engineering Structures. 2017;131:513-29.
- [20] Beall C. New masonry products and materials. Progress in Structural Engineering and Materials. 2000;2:296-303.
- [21] Ramamurthy K, Kunhanandan Nambiar EK. Accelerated masonry construction review and future prospects. Progress in Structural Engineering and Materials. 2004;6:1-9.
- [22] Murray EB. Dry Stacked Surface Bonded Masonry-Structural Testing and Evaluation. 2007.
- [23] Anand KB, Ramamurthy K. Development and performance evaluation of interlocking-block masonry. Journal of Architectural Engineering. 2000;6:45-51.
- [24] Alwathaf AH, Thanoon WA, Jaafar MS, Noorzai J, Kadir MRA. Shear characteristic of interlocking mortarless block masonry joints. Masonry International. 2005;18:39-44.
- [25] Oikonomopoulou F, Bristogianni T, Barou L, Jacobs E, Frigo G, Veera FA et al. Interlocking cast glass components, Exploring a demountable dry-assembly structural glass system. Heron. 2018;63:103.
- [26] Ali M, Gultom RJ, Chouw N. Capacity of innovative interlocking blocks under monotonic loading. Construction and Building Materials. 2012;37:812-21.
- [27] Tang Z, Ali M, Chouw N. Residual compressive and shear strengths of novel coconut-fibre-reinforced-concrete interlocking blocks. Construction and Building Materials. 2014;66:533-40.
- [28] Rekik A, Allaoui S, Gasser A, Blond E, Andreev K, Sinnema S. Experiments and nonlinear homogenization sustaining mean-field theories for refractory mortarless masonry: The classical secant procedure and its improved variants. European Journal

of Mechanics-A/Solids. 2015;49:67-81.

[29] Thanoon WA, Alwathaf AH, Noorzaei J, Jaafar MS, Abdulkadir MR. Nonlinear finite element analysis of grouted and ungrouted hollow interlocking mortarless block masonry system. *Engineering Structures*. 2008;30:1560-72.

[30] Ayed HB, Limam O, Aidi M, Jelidi A. Experimental and numerical study of interlocking stabilized earth blocks mechanical behavior. *Journal of Building Engineering*. 2016;7:207-16.

[31] Jaafar MS, Alwathaf AH, Thanoon WA, Noorzaei J, Abdulkadir MR. Behaviour of interlocking mortarless block masonry. *Proceedings of the Institution of Civil Engineers-Construction Materials*. 2006;159:111-7.

[32] Lee YH, Shek PN, Mohammad S. Structural performance of reinforced interlocking blocks column. *Construction and Building Materials*. 2017;142:469-81.

[33] Jaafar MS, Thanoon WA, Najm AMS, Abdulkadir MR, Ali AAA. Strength correlation between individual block, prism and basic wall panel for load bearing interlocking mortarless hollow block masonry. *Construction and Building Materials*. 2006;20:492-8.

[34] Zhang X, Hao H, Zheng J, Hernandez F. The mechanical performance of concrete shear key for prefabricated structures. *Advances in Structural Engineering*. 2020:1369433220950618.

[35] Sokairge H, Rashad A, Elshafie H. Behavior of post-tensioned dry-stack interlocking masonry walls under out of plane loading. *Construction and Building Materials*. 2017;133:348-57.

[36] Shi TW, Zhang XH, Hao H, Chen C. Experimental and numerical investigation on the compressive properties of interlocking blocks. *Engineering Structures*. 2022;228:111561.

[37] Ngapeya GGC, Waldmann D, Scholzen F. Impact of the height imperfections of masonry blocks on the load bearing capacity of dry-stack masonry walls. 2018;165:898-913.

[38] Martínez M, Atamturktur S, Ross B, Thompson J. Assessing the Compressive Behavior of Dry-Stacked Concrete Masonry with Experimentally Informed Numerical Models. *Journal of Structural Engineering*. 2018;144:04018080.

[39] Sahu S, Sarkar P, Davis R. Quantification of uncertainty in compressive strength of fly ash brick masonry. *Journal of Building Engineering*. 2019;26:100843.

[40] Zhang X, Biswas WK. Development of eco-efficient bricks—A life cycle assessment approach. *Journal of Building Engineering*. 2021;42:102429.

[41] Jaafar MS, Alwathaf AH, Thanoon WA, Noorzaei J, Abdulkadir M. Behaviour of interlocking mortarless block masonry. *Proceedings of the Institution of Civil*

Engineers-Construction Materials. 2006;159:111-7.

[42] Sarfarazi V, Haeri H. Effect of number and configuration of bridges on shear properties of sliding surface. *Journal of Mining Science*. 2016;52:245-57.

[43] Shemirani AB, Haeri H, Sarfarazi V, Hedayat A. A review paper about experimental investigations on failure behaviour of non-persistent joint. *Geomechanics and Engineering*. 2017;13:535-70.

[44] Casapulla C, Mousavian E, Argiento L, Ceraldi C, Bagi K. Torsion-shear behaviour at the interfaces of rigid interlocking blocks in masonry assemblages: experimental investigation and analytical approaches. *Materials and Structures*. 2021;54:1-20.

[45] Tang ZH, Ali M, Chouw N. Residual compressive and shear strengths of novel coconut-fibre-reinforced-concrete interlocking blocks. *Construction and Building Materials*. 2014;66:533-40.

[46] Li C, Hao H, Bi KM. Numerical study on the seismic performance of precast segmental concrete columns under cyclic loading. *Engineering Structures*. 2017;148:373-86.

[47] Li C, Hao H, Zhang XH, Bi KM. Experimental study of precast segmental columns with unbonded tendons under cyclic loading. *Advances in Structural Engineering*. 2017:319-34.

[48] Askar OF, Aziz AH, Al-Shaarbaf IA. Experimental study on the shear transfer in joints of precast segmental bridge. *Journal of Engineering and Sustainable Development*. 2012;16:88-106.

[49] Ahmed GH, Aziz OQ. Stresses, deformations and damages of various joints in precast concrete segmental box girder bridges subjected to direct shear loading. *Engineering Structures*. 2020;206:110151.

[50] Bu ZY, Wu WY. Inter shear transfer of unbonded prestressing precast segmental bridge column dry joints. *Engineering Structures*. 2018;154:52-65.

[51] Ahmed GH, Aziz OQ. Shear strength of joints in precast posttensioned segmental bridges during 1959–2019, review and analysis. *Structures* 2019;20:527-42.

[52] Alcalde M, Cifuentes H, Medina F. Influence of the number of keys on the shear strength of post-tensioned dry joints. *Materiales de Construcción*. 2013;63:297-307.

[53] Zhou XM, Mickleborough N, Li ZJ. Shear strength of joints in precast concrete segmental bridges. *ACI Structural Journal*. 2005;102:3.

[54] Jiang HB, Wei RB, Ma ZJ, Li YH, Jing Y. Shear strength of steel fiber-reinforced concrete dry joints in precast segmental bridges. *Journal of Bridge Engineering*. 2016;21:04016085.

[55] Jiang HB, Chen L, Ma ZJ, Feng WX. Shear behavior of dry joints with castellated

- keys in precast concrete segmental bridges. *Journal of Bridge Engineering*. 2015;20:04014062.
- [56] Zhang XH, Hao H, Zheng JB, Hernandez F. The mechanical performance of concrete shear key for prefabricated structures. *Advances in Structural Engineering*. 2020;24:291-306.
- [57] Buyukozturk O, Bakhoun MM, Beattie SM. Shear behavior of joints in precast concrete segmental bridges. *Journal of Structural Engineering*. 1990;116:3380-401.
- [58] Jiang HB, Wang SD, Fang ZC, Chen GF, Li JH. Numerical analysis on the shear behavior of single-keyed dry joints in precast high-strength concrete segmental bridges. *Mathematical Biosciences and Engineering*. 2019;16:3144-68.
- [59] Liu TX, Wang Z, Guo J, Wang JQ. Shear strength of dry joints in precast UHPC segmental bridges: experimental and theoretical research. *Journal of Bridge Engineering*. 2019;24:04018100.
- [60] Gopal BA, Hejazi F, Hafezolghorani M, Lei VY. Numerical analysis and experimental testing of ultra-high performance fibre reinforced concrete keyed dry and epoxy joints in precast segmental bridge girders. *International Journal of Advanced Structural Engineering*. 2019;11:463-72.
- [61] Shamass R, Zhou XM, Alfano G. Finite-element analysis of shear-off failure of keyed dry joints in precast concrete segmental bridges. *Journal of Bridge Engineering*. 2015;20:04014084.
- [62] Ahmed GH, Aziz OQ. Influence of intensity & eccentricity of posttensioning force and concrete strength on shear behavior of epoxied joints in segmental box girder bridges. *Construction and Building Materials*. 2019;197:117-29.
- [63] Agaajani S, Waldmann D. Stabilité de systèmes de murs en blocs de béton emboîtables sans joints en mortier. 2012.
- [64] Agaajani S. Development and investigation of a new dry-stacked wall system [Ph.D]: University of Luxembourg; 2015.
- [65] Fan WC, Cao P, Tang GD. Experimental and numerical study on the damage evolution of random rock joint surface during direct shear under CNL condition. *Geotechnical and Geological Engineering*. 2019;37:975-83.
- [66] Thompson MK. Methods for generating rough surfaces in ANSYS. Proceedings of the 2006 International ANSYS Users Conference & Exhibition, Pittsburgh, PA2006.
- [67] Thompson MK, Thompson J. Methods for generating probabilistic rough surfaces in ANSYS. Proc 20th Korea ANSYS User's Conf2010. p. 9-10.
- [68] Thompson MK. A comparison of methods to evaluate the behavior of finite element models with rough surfaces. *Scanning*. 2011;33:353-69.
- [69] Bahaaddini M, Sharrock G, Hebblewhite BK. Numerical direct shear tests to

model the shear behaviour of rock joints. *Computers and Geotechnics*. 2013;51:101-15.

[70] Boutoutaou H, Bouaziz M, Fontaine JF. Modelling of interference fits with taking into account surfaces roughness with homogenization technique. *International Journal of Mechanical Sciences*. 2013;69:21-31.

[71] Hyun S, Pei L, Molinari JF, Robbins MO. Finite-element analysis of contact between elastic self-affine surfaces. *Physical Review E*. 2004;70:026117.

[72] Roberts CL, Breen JE, Kreger ME. Measurement based revisions for segmental bridge design and construction criteria. Austin (TX): The University of Texas at Austin: Center for Transportation Research, Bureau of Engineering Research; 1993.

[73] Turmo J, Ramos G, Aparicio AC. Shear strength of dry joints of concrete panels with and without steel fibres: Application to precast segmental bridges. *Engineering Structures*. 2006;28:23-33.

[74] Bakhoum MM. Shear behavior and design of joints in precast concrete segmental bridges [Ph.D]: Massachusetts Institute of Technology; 1990.

[75] Foure B, Bouafia Y, Soubret R, Thomas P. Shear test on keyed joints between precast segments. *Proceedings of the Workshop AFPC External Prestressing in Structures, Saint-Rémy-lès-Chevreuse*1993. p. 297-319.

[76] AASHTO. Guide specifications for design and construction of segmental concrete bridges. Section. 2nd ed; ed. 2003 interim revisions2003.

[77] Ahmed GH, Aziz OQ. Shear behavior of dry and epoxied joints in precast concrete segmental box girder bridges under direct shear loading. *Engineering Structures*. 2019;182:89-100.

[78] Casapulla C, Portioli F. Experimental tests on the limit states of dry-jointed tuff blocks. *Materials and Structures*. 2016;49:751-67.

[79] Zahra T, Dhanasekar M. Characterisation and strategies for mitigation of the contact surface unevenness in dry-stack masonry. *Construction and Building Materials*. 2018;169:612-28.

[80] Yang GM, Coquille JC, Fontaine JF, Lambertin M. Contact pressure between two rough surfaces of a cylindrical fit. *Journal of Materials Processing Technology*. 2002;123:490-7.

[81] Bolhassani M, Hamid AA, Lau ACW, Moon F. Simplified micro modeling of partially grouted masonry assemblages. *Construction and Building Materials*. 2015;83:159-73.

[82] Bosro MZM, Samad AAA, Mohamad N, Ali N, Inn GW, Tambichik MA et al. Computational Study of Mortarless Masonry Block System Under Uniaxial Compression Load. *International Journal of Integrated Engineering*. 2018;10:74-9.

- [83] Ngapeya GGC, Waldmann D. Experimental and analytical analysis of the load-bearing capacity P_u of improved dry-stacked masonry. *Journal of Building Engineering*. 2020;27:100927.
- [84] Silva RA, Soares E, Oliveira DV, Miranda T, Cristelo NM, Leitão D. Mechanical characterisation of dry-stack masonry made of CEBs stabilised with alkaline activation. *Construction and Building Materials*. 2015;75:349-58.
- [85] Andreev K, Sinnema S, Rekik A, Allaoui S, Blond E, Gasser A. Compressive behaviour of dry joints in refractory ceramic masonry. *Construction and Building Materials*. 2012;34:402-8.
- [86] Lourenço PB, Oliveira DV, Roca P, Orduña A. Dry joint stone masonry walls subjected to in-plane combined loading. *Journal of Structural Engineering*. 2005;131:1665-73.
- [87] Al-Fakih A, Mohammed BS, Liew MS. Behavior of the Dry Bed Joint in the Mortarless Interlocking Masonry System: an Overview. *Civil Engineering Research Journal*. 2018;4:1-5.
- [88] Zahra T, Yin Z, Dhanasekar M. Experimental investigation of dry joint surface and closure characteristics of interlocking blocks under compression. *Brick and Block Masonry*. 2016:2003-9.
- [89] Thanoon WAM, Alwathaf AH, Noorzaei J, Jaafar MS, Abdulkadir MR. Finite element analysis of interlocking mortarless hollow block masonry prism. *Computers & Structures*. 2008;86:520-8.
- [90] Safiee NA, Jaafar MS, Alwathaf AH, Noorzaei J, Abdulkadir MR. Structural behavior of mortarless interlocking load bearing hollow block wall panel under out-of-plane loading. *Advances in structural engineering*. 2011;14:1185-96.
- [91] Mousavian E, Casapulla C. Structurally informed design of interlocking block assemblages using limit analysis. *Journal of Computational Design and Engineering*. 2020.
- [92] Chan C, Hover KC, Folliard KJ. Spatial variations in material properties of segmental retaining wall (SRW) units, part II: sampling considerations for absorption tests. *Journal of ASTM International*. 2005;2:1-18.
- [93] Lawrence S. Random variations in brickwork properties. *Proc, 7th Int Brick Masonry Conf1985*. p. 537-47.
- [94] Stewart MG. Spatial variability of pitting corrosion and its influence on structural fragility and reliability of RC beams in flexure. *Structural Safety*. 2004;26:453-70.
- [95] Zhu F, Zhou Q, Wang F, Yang X. Spatial variability and sensitivity analysis on the compressive strength of hollow concrete block masonry wallettes. *Construction and Building Materials*. 2017;140:129-38.

- [96] Stewart M, Lawrence S. Model error, structural reliability and partial safety factors for structural masonry in compression. *Masonry International*. 2007;20:107-16.
- [97] Standard A. AS 3700: masonry structures. Sydney; 2001.
- [98] Heffler L, Stewart M, Masia M, Correa M. Statistical analysis and spatial correlation of flexural bond strength for masonry walls. *Masonry Int*. 2008;21:59-70.
- [99] Li J, Masia MJ, Stewart MG, Lawrence SJ. Spatial variability and stochastic strength prediction of unreinforced masonry walls in vertical bending. *Engineering Structures*. 2014;59:787-97.
- [100] Fyfe A, Middleton J, Pande G. Numerical evaluation of the influence of some workmanship defects on the partial factor of safety (GAMMA M) for masonry. *Masonry International*. 2000;13:48-53.
- [101] Stewart MG, Lawrence S. Structural reliability of masonry walls in flexure. *Masonry International*. 2002;15:48-52.
- [102] Shi T, Zhang X, Hao H, Chen C. Experimental and numerical investigation on the compressive properties of interlocking blocks. *Engineering Structures*. 2021;228:111561.
- [103] Gooch LJ, Masia MJ, Stewart MG. Application of stochastic numerical analyses in the assessment of spatially variable unreinforced masonry walls subjected to in-plane shear loading. *Engineering Structures*. 2021;235:112095.
- [104] Lourenço PJBB. Computational strategies for masonry structures. 1997.
- [105] Sacco E, Toti J. Interface elements for the analysis of masonry structures. *International Journal for Computational Methods in Engineering Science and Mechanics*. 2010;11:354-73.
- [106] Rekić A, Lebon F. Homogenization methods for interface modeling in damaged masonry. *Advances in Engineering Software*. 2012;46:35-42.
- [107] Alforno M, Monaco A, Venuti F, Calderini C. Validation of simplified micro-models for the static analysis of masonry arches and vaults. *International Journal of Architectural Heritage*. 2021;15:1196-212.
- [108] Silva LC, Lourenço PB, Milani G. Rigid block and spring homogenized model (HRBSM) for masonry subjected to impact and blast loading. *International journal of impact engineering*. 2017;109:14-28.
- [109] Gambarotta L, Lagomarsino S. Damage models for the seismic response of brick masonry shear walls. Part I: the mortar joint model and its applications. *Earthquake engineering & structural dynamics*. 1997;26:423-39.
- [110] Casolo S, Milani G. Simplified out-of-plane modelling of three-leaf masonry walls accounting for the material texture. *Construction and Building Materials*. 2013;40:330-51.

- [111] Yang CX, Shen JM, Yang WJ. Study on homogenization process of masonry using numerical simulation based on periodic boundary conditions. *Applied Mechanics and Materials: Trans Tech Publ*; 2012. p. 768-73.
- [112] Pande G, Liang J, Middleton J. Equivalent elastic moduli for brick masonry. *Computers and Geotechnics*. 1989;8:243-65.
- [113] Choudhury T, Milani G, Kaushik HB. Experimental and numerical analyses of unreinforced masonry wall components and building. *Construction and Building Materials*. 2020;257:119599.
- [114] Kouris LAS, Bournas DA, Akintayo OT, Konstantinidis AA, Aifantis EC. A gradient elastic homogenisation model for brick masonry. *Engineering Structures*. 2020;208:110311.
- [115] Drougkas A, Roca P, Molins C. Analytical micro-modeling of masonry periodic unit cells–Elastic properties. *International Journal of Solids and Structures*. 2015;69:169-88.
- [116] Cecchi A, Milani G, Tralli A. A Reissner–Mindlin limit analysis model for out-of-plane loaded running bond masonry walls. *International journal of solids and structures*. 2007;44:1438-60.
- [117] Di Nino S, Luongo A. A simple homogenized orthotropic model for in-plane analysis of regular masonry walls. *International Journal of Solids and Structures*. 2019;167:156-69.
- [118] Cecchi A, Sab K. A multi-parameter homogenization study for modeling elastic masonry. *European Journal of Mechanics-A/Solids*. 2002;21:249-68.
- [119] Gabor A, Bennani A, Jacquelin E, Lebon F. Modelling approaches of the in-plane shear behaviour of unreinforced and FRP strengthened masonry panels. *Composite structures*. 2006;74:277-88.
- [120] Wu C, Hao H. Derivation of a multi-axial yield function for orthotropic hollow concrete block masonry. *Australian Structural Engineering Conference 2005: Engineers Australia*; 2005. p. 144.
- [121] Wu C, Hao H. Numerical derivation of averaged material properties of hollow concrete block masonry. *Engineering Structures*. 2008;30:870-83.
- [122] Ma G, Hao H, Lu Y. Homogenization of masonry using numerical simulations. *Journal of engineering mechanics*. 2001;127:421-31.
- [123] Wei X, Hao H. Numerical derivation of homogenized dynamic masonry material properties with strain rate effects. *International Journal of Impact Engineering*. 2009;36:522-36.
- [124] Peng B, Wang D, Zong G, Zhang Y. Homogenization strategy for brick masonry walls under in-plane loading. *Construction and Building Materials*. 2018;163:656-67.

- [125] Silva LC, Lourenço PB, Milani G. Nonlinear discrete homogenized model for out-of-plane loaded masonry walls. *Journal of Structural Engineering*. 2017;143:04017099.
- [126] Silva LC, Lourenço PB, Milani G. Numerical homogenization-based seismic assessment of an English-bond masonry prototype: Structural level application. *Earthquake Engineering & Structural Dynamics*. 2020;49:841-62.
- [127] Bertolesi E, Milani G, Lourenço PB. Implementation and validation of a total displacement non-linear homogenization approach for in-plane loaded masonry. *Computers & Structures*. 2016;176:13-33.
- [128] Milani G, Bertolesi E. Quasi-analytical homogenization approach for the non-linear analysis of in-plane loaded masonry panels. *Construction and Building Materials*. 2017;146:723-43.
- [129] Wu C, Hao H. Derivation of 3D masonry properties using numerical homogenization technique. *International Journal for Numerical Methods in Engineering*. 2006;66:1717-37.
- [130] Hopkinson B. X. A method of measuring the pressure produced in the detonation of high explosives or by the impact of bullets. *Philosophical Transactions of the Royal Society of London Series A, Containing Papers of a Mathematical or Physical Character*. 1914;213:437-56.
- [131] Rafsanjani SH, Lourenço PB, Peixinho N. Implementation and validation of a strain rate dependent anisotropic continuum model for masonry. *International Journal of Mechanical Sciences*. 2015;104:24-43.
- [132] Sahli G, Ben Ayed H, Limam O, Aidi M. Derivation of in-plane macroscopic elastoplastic behavior of ISEB masonry walls. *Structures*. 2022;44:84-100.
- [133] Larcher M, Peroni M, Solomos G, Gebbeken N, Bieber P, Wandelt J et al. Dynamic increase factor of masonry materials: experimental investigations. *ISIEMS/ICPS*. 2013.
- [134] Hao H, Tarasov B. Experimental study of dynamic material properties of clay brick and mortar at different strain rates. *Australian Journal of Structural Engineering*. 2008;8:117-32.
- [135] Zhang X, Chiu Y-W, Hao H, Hsieh A, Salter N, Cui J. Dynamic compressive material properties of clay bricks at different strain rates. *Construction and Building Materials*. 2018;192:754-67.
- [136] Zhang X, Chiu Y-W, Hao H. Dynamic tensile properties of clay bricks. *Mechanics of Materials*. 2022;165:104157.
- [137] Wong RHC, Chau KT, Tang CA, Lin P. Analysis of crack coalescence in rock-like materials containing three flaws—part I: experimental approach. *International*

Journal of Rock Mechanics and Mining Sciences. 2001;38:909-24.

[138] Zhang K, Cao P, Ma G, Wang W, Fan W, Li K. Strength, fragmentation and fractal properties of mixed flaws. *Acta Geotechnica*. 2016;11:901-12.

[139] Wong RHC, Chau KT. Crack coalescence in a rock-like material containing two cracks. *International Journal of Rock Mechanics and Mining Sciences*. 1998;35:147-64.

[140] Tasdemir MA, Maji AK, Shah SP. Crack propagation in concrete under compression. *Journal of engineering mechanics*. 1990;116:1058-76.

[141] Wu Z, Zhao G, Huang C. Fracture toughness and fracture energy for different concrete strength. *Journal of Dalian University of technology*. 1993;33:73-7.

[142] ASTM. Standard test methods for sampling and testing concrete masonry units and related units. ASTM C140-10. 2008.

[143] EN C. 1052-1: Methods of test for masonry, Part 1: Determination of compressive strength. British Standards Institution, London. 1999.

[144] Systèmes D. ABAQUS Documentation (Dassault Systèmes, Providence, RI). Version; 2014.

[145] Lubliner J, Oliver J, Oller S, Oñate E. A plastic-damage model for concrete. *International Journal of Solids and Structures*. 1989;25:299-326.

[146] Simulia. Abaqus Analysis User's Guide, Version 6.14. Dassault Systemes Providence, RI; 2014.

[147] Prabhu S, Atamturktur S, Brosnan D, Messier P, Dorrance R. Foundation settlement analysis of Fort Sumter National Monument: Model development and predictive assessment. *Engineering Structures*. 2014;65:1-12.

[148] Gorst NJS, Williamson SJ, Pallett PF, Clark LA. Friction in temporary works. *Research Rep*. 2003;71.

[149] Vasconcelos G, Lourenço PB. Experimental characterization of stone masonry in shear and compression. *Construction and Building Materials*. 2009;23:3337-45.

[150] Park CH, Bobet A. Crack coalescence in specimens with open and closed flaws: a comparison. *International Journal of Rock Mechanics and Mining Sciences*. 2009;46:819-29.

[151] Ashby MF, Hallam SD. The failure of brittle solids containing small cracks under compressive stress states. *Acta Metallurgica*. 1986;34:497-510.

[152] Sarhat SR, Sherwood EG. The prediction of compressive strength of ungrouted hollow concrete block masonry. *Construction and Building Materials*. 2014;58:111-21.

[153] BS EN 1052-3: 2002: Methods of test for masonry- Part 3: determination of initial shear strength. British Standards Institution. 2002.

- [154] Chahrour AH, Soudki KA, Straube J. RBS polymer encased concrete wall part I: experimental study and theoretical provisions for flexure and shear. *Construction and Building Materials*. 2005;19:550-63.
- [155] Kaneko Y, Connor JJ, Triantafillou TC, Leung CK. Fracture mechanics approach for failure of concrete shear key. I: Theory. *Journal of Engineering Mechanics*. 1993;119:681-700.
- [156] Freund L. Stress intensity factor calculations based on a conservation integral. *International Journal of Solids and Structures*. 1978;14:241-50.
- [157] Cholewicki A. Loadbearing capacity and deformability of vertical joints in structural walls of large panel buildings. *Building Science*. 1971;6:163-84.
- [158] Koseki K, Breen JE. Exploratory study of shear strength of joints for precast segmental bridges. University of Texas, Austin, 1983.
- [159] Bakhom MM. Shear behavior and design of joints in precast concrete segmental bridges: Massachusetts Institute of Technology; 1990.
- [160] Wong RH, Chau KT. Crack coalescence in a rock-like material containing two cracks. *International Journal of Rock Mechanics and Mining Sciences*. 1998;35:147-64.
- [161] Rombach GA, Specker A. Segmentbrücken. *Beton-Kalender*, Teil 1, Ernst & Sohn. 2004:177-212.
- [162] Specker A, Rombach GA. Design of joints in segmental hollow box girder bridges. 1st FIB Kongress. Osaka, Japan, 2002.
- [163] Specker A. Der Einfluss der Fugen auf die Querkraft-und Torsionstragfähigkeit extern vorgespannter Segmentbrücken [Ph.D]: Technische Universität Hamburg; 2001.
- [164] Sandoval C, Calderón S, Almazán JL. Experimental cyclic response assessment of partially grouted reinforced clay brick masonry walls. *Bulletin of Earthquake Engineering*. 2018;16:3127-52.
- [165] Hofbeck JA, Ibrahim IO, Mattock AH. Shear transfer in reinforced concrete. *Journal Proceedings* 1969. p. 119-28.
- [166] Yong HTD. Utilisation of topologically-interlocking osteomorphic blocks for multi-purpose civil construction [Ph.D]: The University of Western Australia; 2011.
- [167] ABAQUS A. 6.14, Dassault Systèmes Simulia Corp. Provid RI, USA. 2014.
- [168] Shi T, Zhang X, Hao H, Xie G. Experimental and numerical studies of the shear resistance capacities of interlocking blocks. *Journal of Building Engineering*. 2021;44:103230.
- [169] Gorst N, Williamson S, Pallett P, Clark L. Friction in temporary works. *Research Rep*. 2003;71.

- [170] EN B. 1052-1 (1999) British Standard. Methods of test for masonry—Part 1: Determination of compressive strength. CEN European Committee for Standardization. Central Secretariat: rue de Stassart 36, B-1050 Brussels, September, 1998.
- [171] Shields MD, Teferra K, Hapij A, Daddazio RP. Refined stratified sampling for efficient Monte Carlo based uncertainty quantification. *Reliability Engineering & System Safety*. 2015;142:310-25.
- [172] Tabbakhha M, Modaressi-Farahmand-Razavi A. Analyzing the effect of workmanship quality on performance of unreinforced masonry walls through numerical methods. *Computers & Structures*. 2016;167:1-14.
- [173] Montazerolghaem M. Analysis of unreinforced masonry structures with uncertain data. 2015.
- [174] ABAQUS D. Abaqus theory manual. Dessault Systèmes. 2014.
- [175] Lubliner J, Oliver J, Oller S, Onate E. A plastic-damage model for concrete. *International Journal of solids and structures*. 1989;25:299-326.
- [176] Klingner RE. *Masonry structural design*: McGraw-Hill Education; 2017.
- [177] Milani G, Lourenço PB, Tralli A. Homogenised limit analysis of masonry walls, Part I: Failure surfaces. *Computers & structures*. 2006;84:166-80.
- [178] Kupfer H, Hilsdorf HK, Rusch H. Behavior of concrete under biaxial stresses. *Journal proceedings*1969. p. 656-66.
- [179] Wang L-c, Song Y-p. Mechanical behavior and failure criterion of the gangue-based haydite concrete under triaxial loading. *Materials and Structures*. 2015;48:1419-33.
- [180] Chi Y, Yu M, Huang L, Xu L. Finite element modeling of steel-polypropylene hybrid fiber reinforced concrete using modified concrete damaged plasticity. *Engineering Structures*. 2017;148:23-35.
- [181] Traina LA, Mansour SA. Biaxial strength and deformational behavior of plain and steel fiber concrete. *ACI Materials Journal*. 1991;88.
- [182] Schickert G, Winkler H. Results of test concerning strength and strain of concrete subjected to multi-axial compressive stress. 1977.
- [183] Mills LL, Zimmerman RM. Compressive strength of plain concrete under multiaxial loading conditions. *Journal Proceedings*1970. p. 802-7.
- [184] Li Q, Ansari F. Mechanics of damage and constitutive relationships for high-strength concrete in triaxial compression. *Journal of engineering mechanics*. 1999;125:1-10.
- [185] AlGohi BH, Baluch MH, Rahman MK, Al-Gadhib AH, Demir C. Plastic-

Damage Modeling of Unreinforced Masonry Walls (URM) Subject to Lateral Loading. *Arabian Journal for Science and Engineering*. 2017;42:4201-20.

[186] Chen W-F, Han D-J. *Plasticity for structural engineers*: J. Ross Publishing; 2007.

[187] Voyiadjis GZ, Taqieddin ZN. Elastic plastic and damage model for concrete materials: Part I-theoretical formulation. *The International Journal of Structural Changes in Solids*. 2009;1:31-59.

[188] Cheng H, Paz CM, Pinheiro BC, Estefen SF. Experimentally based parameters applied to concrete damage plasticity model for strain hardening cementitious composite in sandwich pipes. *Materials and Structures*. 2020;53:1-17.

[189] Babanajad SK, Farnam Y, Shekarchi M. Failure criteria and triaxial behaviour of HPFRC containing high reactivity metakaolin and silica fume. *Construction and Building Materials*. 2012;29:215-29.

[190] Öztekin E, Pul S, Hüsem M. Experimental determination of Drucker-Prager yield criterion parameters for normal and high strength concretes under triaxial compression. *Construction and Building Materials*. 2016;112:725-32.

[191] Voyiadjis GZ, Kattan PI. Investigation of the damage variable basic issues in continuum damage and healing mechanics. *Mechanics Research Communications*. 2015;68:89-94.

[192] Voyiadjis GZ, Kattan PI. A comparative study of damage variables in continuum damage mechanics. *International Journal of Damage Mechanics*. 2009;18:315-40.

[193] Walton CA, Horstemeyer M, Martin HJ, Francis D. Formulation of a macroscale corrosion damage internal state variable model. *International Journal of Solids and Structures*. 2014;51:1235-45.

[194] Yong HTD. *Utilisation of topologically-interlocking osteomorphic blocks for multi-purpose civil construction*. 2011.

[195] Li Z, Chen L, Fang Q, Hao H, Zhang Y, Chen W et al. Study of autoclaved aerated concrete masonry walls under vented gas explosions. *Engineering Structures*. 2017;141:444-60.

[196] Michaloudis G, Gebbeken N. Modeling masonry walls under far-field and contact detonations. *International journal of impact engineering*. 2019;123:84-97.

[197] AASHTO LRFD bridge design specifications. American Association of State Highway and Transportation Officials, Washington, DC. 2012.

APPENDIX I INTERLOCKING SHEAR RESISTANCE MODEL

The shear resistant mechanism of the interlocking brick prism comprises of two parts, i.e., shear keys and interface friction, which can be expressed as

$$V_j = A_{key}^V f'_c (C_1 + C_2 \sigma_n) + u A_{sm} \sigma_n \quad (A-1)$$

The contribution of shear key is influenced by material strength f'_c , normal stress from axial pre-compression σ_n , and shear key geometry. To determine coefficient C_1 and C_2 , the influence of material shear strength on shear key resistance is analysed first. Figure A-1(a) illustrates the free body diagram of the interlocking brick prism. V is the applied vertical force on the brick prism. The force on each interlocking brick joint is $V/2$ due to symmetry. Since there are two shear keys on each joint bearing this force, the shear force F_s on each shear key equals to $V/4$. Take a typical element on the shear key for stress analysis which experiences axial compressive stress σ_x from axial pre-compression, shear stress τ and normal stress σ_y , which can be calculated with the applied forces on the prism as

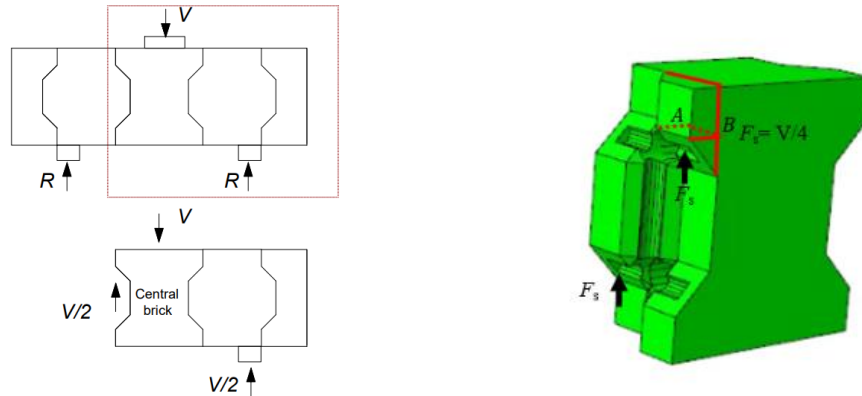
$$\tau = \frac{F_s}{A_{key}^V} = \frac{V}{4A_{key}^V} \quad (A-2)$$

$$\sigma_x = \frac{N}{A_{brick}} \quad (A-3)$$

$$\sigma_y = \frac{7F_s}{10A_{key}^H} = \frac{7V}{40A_{key}^H} \quad (A-4)$$

where V is the applied vertical force on the brick prisms, N is the axial pre-compression force, A_{key}^H is the horizontal projection area of the interlocking key along the direction of pre-compressive force, and A_{key}^V is the vertical projection area of the interlocking key along the direction of the applied vertical shear force, A_{brick} is the cross-sectional area of the interlocking brick perpendicular to the axial pre-compression direction, as

shown in Figure A-1(c). Detailed derivation of σ_y is provided in Figure A-1.



Central brick

(a) Free body diagram

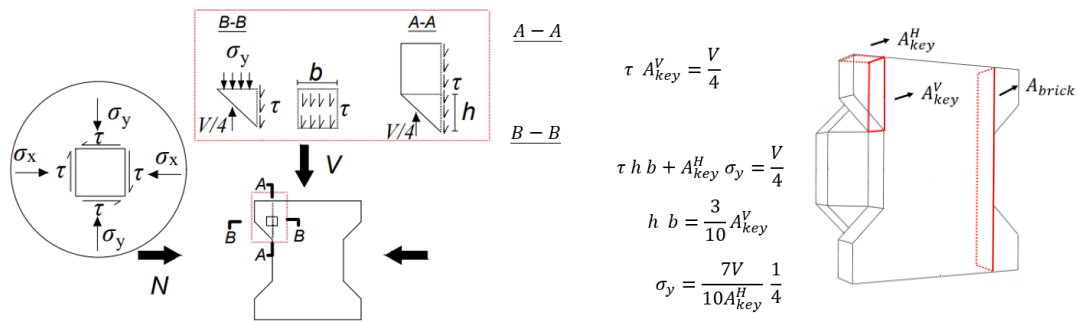


Figure A-1. Free body diagram and stress state

uniaxial tensile failure. The tangent angle θ is relative to stress axis. The centre coordinate of the uniaxial tensile strength circle is $(x_3, y_3) = (-f_t/2, 0)$. The angle of the line connecting point (x_2, y_2) and (x_3, y_3) relative to σ axis is β , which can be calculated by

$$\tan\beta = \frac{|y_2|}{|x_3|} = \frac{0.25f_c}{f_t/2} = 0.5 \frac{f_c}{f_t} \quad (\text{A-7a})$$

$$\beta = \tan^{-1}(0.5 \frac{f_c}{f_t}) \quad (\text{A-7b})$$

Typically for concrete-like material, the uniaxial compression strength f_c is taken as $0.85 f_c'$ and the tensile strength f_t is taken as $0.604\sqrt{f_c'}$ MPa [197]. Therefore,

$$\beta = \tan^{-1}(0.7\sqrt{f_c'}) \quad (\text{A-8})$$

The angle for the modified failure envelop can be calculated by

$$\theta = 2\beta - 90^\circ \quad (\text{A-9})$$

To determine C_I in Eq. A-1, take a stress state of non-confinement $\sigma_x=0$, when the stress reaches the failure state under gradually increased shear load, line L_2 is tangent to the Mohr's circle, and runs across line OD at point $(\sigma_y, -\tau)$. The point of intersection of the Mohr's circle with the τ axis is $(0, \tau)$. The distance from centre of the Mohr's circle, i.e., point $(\sigma_y/2, 0)$, to Line L_2 is

$$R_2 = \left(\frac{y_2}{\tan\theta} + \frac{\sigma_y}{2} \right) \sin\theta \quad (\text{A-10a})$$

where R_2 is radius of the Mohr's circle.

Substituting Eqs. A-2, A-4 and A-6 into A-10 together with $\alpha=37^\circ$, it yields

$$R_2 = 0.25 \cdot f_c \cdot \cos\theta + \left(\frac{7A_{key}^V}{10A_{key}^H} \right) \cdot \frac{\tau}{2} \cdot \sin\theta \quad (\text{A-10b})$$

Since the radius of the stress circle R_2 can also be written as

$$R_2 = \sqrt{(\sigma_y - \frac{\sigma_y}{2})^2 + (-\tau - 0)^2} \quad (\text{A-11a})$$

Substituting Eq. A-2 and A-4 in,

$$R_2 = \left(\sqrt{\left(\frac{1}{2} \times \frac{7A_{key}^V}{10A_{key}^H}\right)^2 + 1} + 1 \right) \tau \quad (\text{A-11b})$$

With Eqs. A-10b and A-11b, the shear stress τ is expressed using the following equation.

$$\begin{aligned} \tau &= \frac{0.25 \cdot f_c \cdot \cos\theta}{\sqrt{\left(\frac{1}{2} \times \frac{7A_{key}^V}{10A_{key}^H}\right)^2 + 1} - \frac{1}{2} \times \frac{7A_{key}^V}{10A_{key}^H} \sin\theta} \\ &= \frac{0.2125f_c' \cos\theta}{\sqrt{\left(\frac{1}{2} \times \frac{7A_{key}^V}{10A_{key}^H}\right)^2 + 1} - \frac{1}{2} \times \frac{7A_{key}^V}{10A_{key}^H} \sin\theta} \end{aligned} \quad (\text{A-12})$$

Using Eq. A-12, the coefficient C_1 in Eq. A-1 can be expressed with variables A_{key}^V , A_{key}^H related to shear key geometry and concrete failure angle θ .

$$C_1 = \frac{0.2125 \cos\theta}{\sqrt{\left(\frac{1}{2} \times \frac{7A_{key}^V}{10A_{key}^H}\right)^2 + 1} - \frac{1}{2} \times \frac{7A_{key}^V}{10A_{key}^H} \sin\theta} \quad (\text{A-13})$$

To determine the coefficient C_2 , when the interlocking brick is subjected to axial pre-compressive stress, σ_x is introduced and the corresponding Mohr's circle enlarges, which is nevertheless still tangent to the strength envelope line L_2 . As shown in Figure A-2b, The stresses on two normal planes are (σ'_x, τ') and $(\sigma'_y, -\tau')$, respectively. The line connects these two points diametrically. The centre coordinates of the Mohr's circle is $(\frac{\sigma'_x + \sigma'_y}{2}, 0)$. The radius of the circle can be calculated as

$$R_3 = \sqrt{\tau'^2 + \left(\frac{\sigma'_x}{2} - \frac{\sigma'_y}{2}\right)^2} \quad (\text{A-14})$$

Similar to Eq. A-10, line L_2 is tangent to the Mohr's circle. So the radius can also be calculated as

$$R_3 = \left(\frac{y_2}{\tan\theta} + \frac{\sigma'_x + \sigma'_y}{2} \right) \sin\theta = 0.25 \cdot f_c \cdot \cos\theta + \left(\frac{\sigma'_x}{2} + \frac{\sigma'_y}{2} \right) \sin\theta \quad (\text{A-15})$$

With Eq. A-14 and A-15, the quadratic equation of shear stress τ is expressed using the following equation.

$$A\tau^2 + B\tau + C = 0 \quad (\text{A-16})$$

where the coefficient A, B and C can be written as

$$A = 1 + \left(\frac{1}{2} \times \frac{7A_{key}^V}{10A_{key}^H}\right)^2 \cdot \cos^2\theta \quad (\text{A-17a})$$

$$B = -[\sigma_x(1 + \sin^2\theta) + (0.5f_c \cdot \sin\theta\cos\theta)] \cdot \left(\frac{1}{2} \times \frac{7A_{key}^V}{10A_{key}^H}\right) \quad (\text{A-17b})$$

$$C = \left(\frac{\sigma_x^2}{4}\right) \cos^2\theta - 0.25\sigma_x \cdot f_c \cdot \sin\theta\cos\theta - 0.0625f_c^2 \cdot \cos^2\theta \quad (\text{A-17c})$$

The root of Eq. A-16 is expressed as follows:

$$\tau = \frac{-B + \sqrt{B^2 - 4AC}}{2A} \quad (\text{A-18})$$

The shear stress under pre-compression can be written as

$$\tau = \frac{-B + \sqrt{B^2 - 4AC}}{2A} - \frac{0.2125f_c' \cos\theta}{\sqrt{\left(\frac{1}{2} \times \frac{7A_{key}^V}{10A_{key}^H}\right)^2 + 1 - \frac{1}{2} \times \frac{7A_{key}^V}{10A_{key}^H} \sin\theta}} \quad (\text{A-19})$$

Referring to Eq. (A-1), the coefficient C_2 is expressed using the following equation.

$$C_2 = \frac{-B + \sqrt{B^2 - 4AC}}{2A\sigma_x f_c'} - \frac{0.2125\cos\theta}{\sigma_x \left(\sqrt{\left(\frac{1}{2} \times \frac{7A_{key}^V}{10A_{key}^H}\right)^2 + 1 - \frac{1}{2} \times \frac{7A_{key}^V}{10A_{key}^H} \sin\theta} \right)} \quad (\text{A-20})$$

APPENDIX II STATEMENT OF CONTRIBUTION OF CO-AUTHORS

To whom it may concern,

I, Tingwei Shi, conducted experimental, numerical and analytical investigations, data processing and analysis, and wrote the manuscripts of the papers entitled as follows, which were reviewed and edited by the co-authors. They also provided insights on experimental preparation, data processing and data analysis.

- 1. Experimental and numerical investigation on the compressive properties of interlocking blocks**
- 2. Experimental and numerical studies of the shear resistance capacities of interlocking blocks**
- 3. Influences of Random Imperfection Distribution on the Compressive Properties of Interlocking Brick Wall.**
- 4. Numerical Derivation of Homogenized Constitutional Relation for Masonry Wall Made of Mortar-less Interlocking Bricks. (Under review)**
- 5. Numerical Derivation of Homogenized Constitutional Relation for Masonry Wall Made of Mortar-less Interlocking Bricks under Dynamic Loading. (Under review)**

Tingwei Shi

I, as a co-author, endorse that this level of contribution by the candidate indicated above is appropriate.

Prof. Hong Hao

Dr. Xihong Zhang

Mr. Guanyu Xie

Mr. Chong Chen

APPENDIX III COPYRIGHT CLEARANCE

The proof of the rights, granted by publisher for the publications that form the chapters of this thesis are attached below.

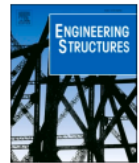
Engineering Structures 228 (2021) 111561



Contents lists available at [ScienceDirect](#)

Engineering Structures

journal homepage: www.elsevier.com/locate/engstruct



Experimental and numerical investigation on the compressive properties of interlocking blocks



Tingwei Shi, Xihong Zhang^{*}, Hong Hao, Chong Chen

Centre for Infrastructural Monitoring and Protection, School of Civil and Mechanical Engineering, Curtin University, Australia

Shi T, Zhang X, Hao H, et al. *Experimental and numerical investigation on the compressive properties of interlocking blocks*. Engineering Structures, 2021, 228: 111561.

Journal of Building Engineering 44 (2021) 103230



Contents lists available at [ScienceDirect](#)

Journal of Building Engineering

journal homepage: www.elsevier.com/locate/job



Experimental and numerical studies of the shear resistance capacities of interlocking blocks



Tingwei Shi, Xihong Zhang^{*}, Hong Hao, Guanyu Xie

Centre for Infrastructural Monitoring and Protection, School of Civil and Mechanical Engineering, Curtin University, Australia

Shi T, Zhang X, Hao H, et al. *Experimental and numerical studies of the shear resistance capacities of interlocking blocks*. Journal of Building Engineering, 2021, 44: 103230.



Contents lists available at ScienceDirect

Structures

journal homepage: www.elsevier.com/locate/structures



Influences of random imperfection distribution on the compressive properties of interlocking block wall

Tingwei Shi ^a, Xihong Zhang ^{a,*}, Hong Hao ^{a,b}, Guanyu Xie ^a

^a Centre for Infrastructural Monitoring and Protection, School of Civil and Mechanical Engineering, Curtin University, Bentley, WA 6102, Australia

^b Earthquake Engineering Research and Test Centre, Guangzhou University, Guangzhou, China

Shi T, Zhang X, Hao H, et al. *Influences of random imperfection distribution on the compressive properties of interlocking block wall*. Structures. 2023, 56: 104875.